



## Coordinated control of wind power and energy storage

Zhao, Haoran; Wu, Qiuwei; Rasmussen, Claus Nygaard; Xu, Honghua

*Publication date:*  
2014

*Document Version*  
Publisher's PDF, also known as Version of record

[Link back to DTU Orbit](#)

*Citation (APA):*  
Zhao, H., Wu, Q., Rasmussen, C. N., & Xu, H. (2014). Coordinated control of wind power and energy storage. Technical University of Denmark, Department of Electrical Engineering.

## DTU Library

Technical Information Center of Denmark

---

### General rights

Copyright and moral rights for the publications made accessible in the public portal are retained by the authors and/or other copyright owners and it is a condition of accessing publications that users recognise and abide by the legal requirements associated with these rights.

- Users may download and print one copy of any publication from the public portal for the purpose of private study or research.
- You may not further distribute the material or use it for any profit-making activity or commercial gain
- You may freely distribute the URL identifying the publication in the public portal

If you believe that this document breaches copyright please contact us providing details, and we will remove access to the work immediately and investigate your claim.

# Coordinated control of wind power and energy storage

Haoran Zhao

DTU



Kongens Lyngby 2014  
CEE-PhD-2014

# Coordinated control of wind power and energy storage

**Author:**

Haoran Zhao

**Supervisors:**

Associate Professor Qiuwei Wu, CEE, DTU.

Dr. Claus Nygaard Rasmussen, R&D, Siemens Wind Power.

Professor Honghua Xu, IEE, CAS.

**Funding:**

Technical University of Denmark

Sino-Danish Center for Education and Research

**Center for Electric Power and Energy**

Richard Petersens Plads, Building 322, 2.

2800 Kgs. Lyngby

Denmark

**Sino-Danish Center for Education and Research**

Niels Jensens Vej 2

8000 Aarhus C

Denmark

**Release date:** October 2014

**Class:** 1 (public)

**Edition:** First

**Comments:** This report is a part of the requirements to achieve PhD in Electrical Engineering at Technical University of Denmark.

**Rights:** © Haoran Zhao, 2014

**ISBN:** 000-00-00000-00-0

*“Knowledge is power.”*

*—Francis Bacon.*

“知识就是力量。”

*To my parents, especially my father.*

献给我的父母，尤其缅怀我的父亲。

d

---

# Abstract (English)

---

Nowadays, wind power has become one of the fastest growing sources of electricity in the world. Due to the inherent variability and uncertainty, wind power integration into the grid brings challenges for power systems, particularly when the wind power penetration level is high. The challenges exist in many aspects, such as reliability, power quality and stability. With the rapid development of energy storage technology, the application of Energy Storage System (ESS) is considered as an effective solution to handle the aforementioned challenges.

The main objective of this study is to investigate the coordinated control of wind power and ESS. Due to the different technical characteristics, such as power and energy density, ESS can play different roles either in generation-side, grid-side or demand side. This thesis focuses on the following two scenarios:

- Scenario 1: As a part of wind farm, the ESS plays a generation-side role which aims to improve the grid-friendliness of the wind farm.
- Scenario 2: As a part of microgrid, the ESS is used to efficiently accommodate the wind power fluctuation.

Around the main objective, the relevant research fields including the wind turbine modeling and control, wind farm modeling and control, planning of ESS are also studied in this thesis.

The implementation and validation of the International Electrotechnical Commission (IEC) generic Type 1A are presented in this thesis. It is shown that the

implemented IEC generic Type 1 models in PowerFactory (PF) can represent the relevant dynamics during normal operation and fault conditions. The model against measurements validation was carried out to verify the implemented wind turbine generator model.

For the wind turbine control strategy, the  $\mathcal{L}_1$  adaptive controller for Maximum Power Point Tracking (MPPT) of a small variable speed Wind Energy Conversion System (WECS) is developed. It showed good tracking performance towards the optimum Tip Speed Ratio (TSR) and robustness with fast adaptation to uncertainties and disturbances.

For the wind farm control, the optimal active power control based on Distributed Model Predictive Control (D-MPC) is proposed. With the developed D-MPC, most of computation tasks are distributed to the local D-MPCs equipped at each actuator (wind turbine or ESS). This control structure is independent from the scale of the wind farm.

The algorithms for optimal siting and sizing of ESS in the grid with a significant penetration of wind power are studied and implemented in a test network. For the point of view the grid operator, the optimal sizing and siting of ESS are analyzed, which enhance the controllability and derive the global benefit of the whole grid.

# Abstract (Danish)

---

Vindkraft er nu den hurtigst voksende energikilde inden for elektricitetsproduktion. Men vindens varierende natur og den tilhørende uforudsigelighed giver visse udfordringer i forhold til el-systemet, specielt hvis andelen af vindkraft i systemet er høj. Udfordringerne relaterer sig eksempelvis til forsyningssikkerhed, systemstabilitet og spændingskvalitet. Som følge af den hurtige udvikling inden for energilagringsteknologier overvejes energilagring nu som et effektivt middel til at håndtere disse udfordringer.

Hovedformålet med dette studie har været en analyse af koordineret kontrol mellem vindkraft og energilagring. På grund af lagringsteknologiernes forskellige tekniske karakteristika, fx. forskellige effekt- og energitætheder, kan energilagring indgå i forskellige sammenhænge; i forbindelse med generering, på netsiden eller på forbrugssiden. Denne afhandling fokuserer på de følgende to scenarier:

- Scenario 1: I en vind-park kan energilagring indgå som en integreret del af genereringen og forbedre vindparkens karakteristika i forhold til el-systemet.
- Scenario 2: Som en del af et mindre isoleret el-system (microgrid) kan energilagring anvendes til at håndtere vind-fluktuationerne på en effektiv måde.

I relation til hovedformålet er de relevante forskningsområder modellering af vindmøller, kontrol og modellering af vind-parker og planlægning af energilagringssystemer.



Implementering og validering af vindmølle-modeller Type 1A i henhold til den Internationale Elektrotekniske Kommission (IEC) er præsenteret i denne afhandling. Det vises hvordan den generiske IEC Type 1 model implementeret i Powerfactory (PF) kan præsentere den relevante dynamiske opførsel under normal drift såvel som i fejlsituationer. Den implementerede model er verificeret vha. måledata.

I relation til kontrolstrategien for vindmøller er der udviklet en adaptiv kontrol strategi til maksimal-effekt styring (Maximum Power Point Tracking – MPPT) af vindmøller der kører med variabel hastighed. Kontrolstrategien viste gode resultater i forhold til at opretholde et optimalt forhold mellem vindhastighed og rotationshastighed (Tip Speed Ratio – TSR) og var desuden robust med hensyn til regulering i forbindelse med forstyrrelser.

I forbindelse med kontrol af vind-parker er optimal aktiv effektkontrol baseret på ”Distributed Model Predictive Control” (D-MPC) foreslået og behandlet i denne afhandling. Den udviklede D-MPC strategi fordeler det meste af beregningsarbejdet mellem lokale D-MPC enheder der hver især er udstyret med en aktuator (i forbindelse med vindmøllen eller et tilhørende energilagere). Kontrolstrukturen er uafhængig af vind-parkens størrelse.

Afhandlingen indeholder desuden et studie af algoritmer der kan bruges til at finde frem til den optimale størrelse og placering af energilagring i el-systemer med en betydelig andel vindkraft. I forbindelse med dette studie er de udviklede algoritmer implementeret i et modelbaseret test-netværk. Analysen tager sigte på at finde den optimale størrelse og placering der giver systemoperatøren forøget kontrol og flest mulige fordele i forhold til el-systemet som helhed.

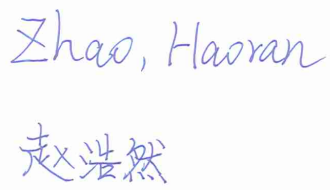
# Preface

---

This thesis was prepared in partial fulfillment of the requirements for acquiring the PhD degree in engineering. It was conducted under the PhD program of Sino-Danish Center for Education and Research, which provided partial funding.

This project summarizes the work of the author during his PhD study. It was carried out from October 2011 to October 2014. During this period, the author was hired at Technical University of Denmark (DTU), where he was a PhD student at the Center for Electric Power and Energy (CEE).

Lyngby, 30-September-2014



Zhao, Haoran  
赵浩然

Haoran Zhao



# Acknowledgements

---

I am greatly thankful to my supervisors; to my main supervisor Associate Prof. Qiuwei Wu for his kind supervision, patience and mentoring during my PhD study. He has always been a source of guidance and inspiration during the research and writing of this thesis as well as on philosophy of science, engineering and life in general; to my co-supervisor Claus Nygaard Rasmussen, who was Associate professor in CEE and now as R&D engineer in Siemens Wind Power, for his motivation, instructive supervision, knowledge sharing and guidance during my PhD study.

I would like to express my gratitude to all my colleagues, especially Dr. Shi You, Dr. Junjie Hu for their enthusiastic help which lets me adapt to the life in Denmark, PhD student Han Xue, Zhaoxi Liu, Dr. Seung-Tae Cha for the interesting joint work and thoughtful discussion, PhD student Xiaowei Song for his encouragement and company in the office during the last several months of my PhD study and PhD student Alessandro Pensini, Daniel Esterbahn Bondy, Dr. Kai Heussian, Dr. Anna Candela Garolera for sharing many interesting discussions on various topics related to our common interests of research and study.

I am particular thankful to my external supervisor and friends in Institute of Electrical Engineering, Chinese Academy of Science, especially Prof. Honghua Xu, Dr. Shuju Hu, Dr. Weihuang Huang, Bin Song, Fenglin Li, Ya Deng, Lingling Wang, Rui Ma for their support in research and life during my five-month wonderful external stay in Beijing, China.

I am also thankful to my ex-colleagues and ex-managers at DIGSILENT GmbH, especially Dr. Menghua Zhao, Dr. Jochen Alber, Dr. Bernd Weise, Sabine

Seeger, Ralf Hoeschele for their knowledge sharing, technical support, friendship and very nice time together in Germany.

I would like to thank to the Centre for Electric Power and Energy at the Technical University of Denmark, for the opportunity of doing a work in this area, providing also a working place and academic material.

Equally, I would like to express my gratitude to “Sino-Danish Center for Education and Research”. Without their financial support, it would not have been possible to perform the study resulting in this thesis.

Most importantly, I am greatly thankful to my parents for their support, understanding, patience and love; to my girlfriend Ya Tang for all her immense love; to my friends for being there, always, cross the distance, time and languages.

# Contents

---

<b>Abstract (English)</b>	<b>i</b>
<b>Abstract (Danish)</b>	<b>iii</b>
<b>Preface</b>	<b>v</b>
<b>Acknowledgements</b>	<b>vii</b>
<b>Acronyms</b>	<b>xix</b>
<b>1 Introduction</b>	<b>1</b>
1.1 Background . . . . .	1
1.2 Objectives and research problems . . . . .	8
1.3 Contributions . . . . .	9
1.4 Structure of the thesis . . . . .	10
1.5 Publications . . . . .	11
<b>2 Roles of Wind Power Plants in Modern Power Systems</b>	<b>15</b>
2.1 Wind turbine generator technology . . . . .	15
2.2 Grid-side roles of wind power plant . . . . .	19
2.3 Discussion and conclusion . . . . .	31
<b>3 Roles of Energy Storage Systems in Modern Power Systems</b>	<b>33</b>
3.1 Energy storage technology . . . . .	34
3.2 Generation-side roles of ESS . . . . .	39
3.3 Grid-side roles of ESS . . . . .	41
3.4 Demand-side roles of ESS . . . . .	44
3.5 ESS type selection . . . . .	44
3.6 Operation and control of ESS . . . . .	45

---

3.7	Discussion and conclusion . . . . .	48
<b>4</b>	<b>Implementation and Validation of Generic Wind Turbine Model (Type 1)</b>	<b>51</b>
4.1	Background and basic knowledge . . . . .	52
4.2	Model description . . . . .	52
4.3	Implementation . . . . .	56
4.4	Simulation and results . . . . .	59
4.5	Model validation against the field measurement . . . . .	68
4.6	Discussion and conclusion . . . . .	72
<b>5</b>	<b>Advanced Wind Turbine Control: <math>\mathcal{L}_1</math> Adaptive Control Approach</b>	<b>75</b>
5.1	Background and basic knowledge . . . . .	75
5.2	Generator control system of WECSs . . . . .	79
5.3	Design of $\mathcal{L}_1$ adaptive controller . . . . .	85
5.4	Simulation and results . . . . .	89
5.5	Discussion and conclusion . . . . .	98
<b>6</b>	<b>Advanced Wind Power Plant Control: D-MPC Approach</b>	<b>99</b>
6.1	Background and basic knowledge . . . . .	99
6.2	Linearization of wind turbine model . . . . .	102
6.3	D-MPC without energy storage . . . . .	115
6.4	D-MPC with energy storage . . . . .	125
6.5	Simulation and results . . . . .	128
6.6	Discussion and conclusion . . . . .	143
<b>7</b>	<b>Optimal Siting and Sizing of Energy Storage System</b>	<b>145</b>
7.1	Background and basic knowledge . . . . .	146
7.2	Operation of ESS for wind power dispatch . . . . .	148
7.3	Methodology for optimal siting and sizing . . . . .	148
7.4	Generation of Wind Power Time Series . . . . .	151
7.5	Periodical optimization problem . . . . .	154
7.6	Simulation and results . . . . .	159
7.7	Discussion and conclusion . . . . .	169
<b>8</b>	<b>Coordinated Control Strategies for Microgrid Application</b>	<b>171</b>
8.1	Background and basic knowledge . . . . .	172
8.2	Modeling of DG units . . . . .	173
8.3	Control strategies of VSI-interfaced DG units . . . . .	179
8.4	Control topology of microgrid . . . . .	185
8.5	Coordinated control strategy (Case 1) . . . . .	186
8.6	Coordinated control strategy (Case 2) . . . . .	188
8.7	Simulation and results . . . . .	196

---

8.8 Discussion and conclusion . . . . .	204
<b>9 Conclusion and scope for future work</b>	<b>209</b>
9.1 Conclusions . . . . .	209
9.2 Future work . . . . .	211
<b>Appendices</b>	<b>212</b>
<b>A Parameter for case studies</b>	<b>213</b>
A.1 Test case for IEC Generic WTG model . . . . .	213
A.2 Parameter for 6 kW WECS . . . . .	216
A.3 NREL 5 MW wind turbine model . . . . .	217
A.4 Parameter for Microrgrid . . . . .	218
<b>B Theoretical background</b>	<b>221</b>
B.1 Projection operator for adaptation laws . . . . .	221
B.2 Model discretization . . . . .	223
B.3 Empirical copulas and families of copulas . . . . .	224
<b>Bibliography</b>	<b>227</b>





# List of Figures

---

1.1	Global cumulative installed wind capacity 2003-2013 [3]	2
1.2	Top 10 new installed capacity Jan.–Dec. 2013	2
1.3	Wind power penetration in leading wind markets 2012	3
2.1	General structure of Type 1 WTG	16
2.2	General structure of Type 2 WTG	17
2.3	General structure of Type 3 WTG	17
2.4	General structure of Type 4 WTG	19
2.5	Inertial control loop	22
2.6	Droop control loop	22
2.7	Combination of inertial control and droop control	23
2.8	Relation between pitch angle, power and deloading coefficients	25
2.9	Rotor speed control	26
2.10	Deloaded optimal active power curve	26
2.11	wind power plant control level	28
2.12	Block diagram of AGC main processing modules	29
3.1	Energy storage classification	34
3.2	Technical maturity of ESS systems [76]	38
3.3	Comparison of rated power energy content of different ESS technologies	40
3.4	Principle of using LPF algorithm for power fluctuation mitigation	47
4.1	Runtime WTG model structure of Type 1A	53
4.2	Block diagram for constant aerodynamic torque model	54
4.3	Block diagram for two-mass model in IEC standard	54
4.4	Block diagram for grid protection model	55
4.5	Runtime wind turbine model structure of Type 1B	57

4.6	Block diagram for blade angle FRT control model . . . . .	58
4.7	Modified block diagram in PF and RTDS . . . . .	58
4.8	Modified runtime wind turbine model structure of Type 1A . . . . .	59
4.9	Initialization with different induction models . . . . .	60
4.10	Single line diagram of test case . . . . .	60
4.11	Simulation results in normal operation (Type 1A) . . . . .	62
4.12	Simulation results in normal operation (Type 1B) . . . . .	63
4.13	Generator speed $\omega_{\text{gen}}$ . . . . .	64
4.14	Filtered voltage of WTT $u_{\text{WTT}}$ during FRT . . . . .	65
4.15	Power outputs during FRT. Above: PF RMS results; Below: PF EMT results . . . . .	66
4.16	Dynamic responses of the $\omega_{\text{gen}}$ , $i_s$ and $T_{\text{gen}}$ during the fault . . . . .	67
4.17	Voltage dip windows . . . . .	69
4.18	Comparison of simulated active power against measurements . . . . .	70
4.19	Comparison of simulated active current against measurements . . . . .	70
4.20	Comparison of simulated reactive power against measurements . . . . .	71
4.21	Comparison of simulated reactive current against measurements . . . . .	71
5.1	Control system for variable speed WECS . . . . .	76
5.2	ORC of variable speed WECS . . . . .	77
5.3	Generator control system based on TSR concept. . . . .	79
5.4	Block diagram of differentiation based estimator. . . . .	81
5.5	ORC curve for 6kW WECS. . . . .	82
5.6	SCIG Vector Control. . . . .	83
5.7	The closed loop $\mathcal{L}_1$ Adaptive Controller. . . . .	86
5.8	Root locus, (a) for decision of $w$ ; (b) for decision of $\Gamma$ . . . . .	90
5.9	Step responses of $\lambda$ and $C_p$ . . . . .	91
5.10	Comparison of actual wind and wind estimation. . . . .	92
5.11	Friction disturbances. . . . .	93
5.12	Comparison of $\lambda$ variation during the operation in Scenario 1: (a) in time series format; (b) $\lambda$ in density format. . . . .	94
5.13	Efficiency comparison during the operation in Scenario 1. (a) Full time frame; (b) Zoomed in time frame (100 s $\sim$ 150 s). . . . .	95
5.14	Comparison of $\lambda$ variation during the operation in Scenario 2: (a) in time series format; (b) $\lambda$ in density format. . . . .	96
5.15	Efficiency comparison during the operation in Scenario 2. (a) Full time frame; (b) Zoomed in time frame (100 s $\sim$ 150 s). . . . .	97
6.1	Wind field in the offshore wind power plant Horn Rev 1 . . . . .	100
6.2	Power controlled wind turbine [156] . . . . .	102
6.3	Wind turbine model by NREL. . . . .	103
6.4	Operation areas in $\omega_r - \theta - v_w$ space . . . . .	104
6.5	Regressors for identification of $T_a$ . . . . .	110
6.6	Regions $\chi_{T_a}^i$ of $T_a$ identification . . . . .	111

6.7	Regions $\chi_{T_g}^i$ of $T_g$ identification . . . . .	112
6.8	Regions $\chi_{F_t}^i$ of $F_t$ identification . . . . .	113
6.9	Control structure of wind power plant based on D-MPC . . . . .	116
6.10	Control structure of wind power plant with ESS . . . . .	126
6.11	Power reference during simulation . . . . .	128
6.12	Wind speed variation in the low speed condition . . . . .	129
6.13	State variable comparison . . . . .	129
6.14	Output variable comparison . . . . .	130
6.15	Wind speed variation in the high speed condition . . . . .	131
6.16	State variable comparison . . . . .	131
6.17	Output variable comparison . . . . .	132
6.18	Convergence comparison with different $\mathbf{L}$ . . . . .	133
6.19	Wind speed variation of WT 05 . . . . .	134
6.20	Active power of the wind power plant $P_{\text{gen}}^{\text{wfc}}$ , (a) represents the high wind condition; (b) represents the low wind condition. . . . .	135
6.21	Simulation results of WT 05 under the high wind condition . . . . .	136
6.22	Simulation results of WT 05 under the low wind condition . . . . .	137
7.1	Flow chart of optimal siting and sizing algorithms . . . . .	149
7.2	Single line diagram of IEEE 14 buses system . . . . .	160
7.3	P-P plot for the WSTS: (a) WF 1, (b) WF 2 . . . . .	161
7.4	Wind power productions . . . . .	163
7.5	Power exchange comparison between Scenario 1 and 2 . . . . .	163
7.6	Power exchange comparison between Scenario 1 and 3 . . . . .	164
7.7	Power exchange in percent . . . . .	165
7.8	ECDF for power rating at different buses, (a) Bus 6, (b) Bus 9, (c) Bus 13 . . . . .	166
7.9	ECDF for energy rating at different buses, (a) Bus 6, (b) Bus 9, (c) Bus 13 . . . . .	168
8.1	DG types and technologies [16] . . . . .	172
8.2	Battery Electric Equivalent: (a) simple (b) with parasitic reaction . . . . .	173
8.3	BESS Configuration . . . . .	174
8.4	Generation System . . . . .	175
8.5	Configuration of a PMSG wind turbine . . . . .	176
8.6	Control strategy of chopper . . . . .	178
8.7	Pitch angle control . . . . .	179
8.8	Structure of $P/Q$ control . . . . .	180
8.9	Dual-loop control block of inverter controller ( $P/Q$ ) . . . . .	181
8.10	Dual-loop control block of inverter controller ( $P/Q$ ) . . . . .	182
8.11	Structure of $U/f$ control . . . . .	183
8.12	Dual-loop control block of inverter controller $U/f$ . . . . .	183
8.13	Structure of droop control . . . . .	184
8.14	Droop control . . . . .	184

---

8.15	The hierarchical control topology of microgrid . . . . .	186
8.16	Islanded control . . . . .	187
8.17	Fuzzy rule surface plot . . . . .	189
8.18	Rotor side converter control . . . . .	191
8.19	Grid side converter control for grid-connected mode . . . . .	192
8.20	Damping controller . . . . .	193
8.21	Bode diagram for band-pass filter design . . . . .	194
8.22	Comparison between overspeeding and underspeeding operations . . . . .	195
8.23	Coordinated control strategy . . . . .	196
8.24	Test case configuration . . . . .	197
8.25	Wind and load power profile . . . . .	198
8.26	Voltage at PCC . . . . .	198
8.27	Frequency at PCC . . . . .	199
8.28	Results of BESS in islanded operation . . . . .	199
8.29	Results of dispatchable DGs in islanded operation . . . . .	200
8.30	Microgrid test system . . . . .	201
8.31	$U_{DC}$ during transition . . . . .	202
8.32	Transients during the transition between grid-connected mode and islanded mode . . . . .	203
8.33	Active power comparison during islanded operation . . . . .	204
8.34	Simulation results of PMSG in islanded operation . . . . .	205
8.35	Simulation results of PMSG in islanded operation . . . . .	206
B.1	Projection operator . . . . .	223

# List of Tables

---

1.1	Wind power plant interconnection standards . . . . .	6
3.1	Capital cost of ESS . . . . .	39
3.2	Technical features of ESS . . . . .	39
3.3	Grid-side roles of ESS . . . . .	42
4.1	Parameter For Constant Aerodynamic Torque Model . . . . .	54
4.2	Parameter For Two-Mass Model . . . . .	55
4.3	Parameter For Grid Protection Model . . . . .	55
4.4	Parameter For Blade Angle FRT Control Model . . . . .	57
4.5	Case Study Scenarios . . . . .	61
4.6	Characteristic quantities of active current . . . . .	72
4.7	Characteristic quantities of reactive current . . . . .	72
5.1	Energy production comparison . . . . .	97
6.1	Simulation statistics %RMSE . . . . .	130
6.2	Simulation Statistics $\sigma(P_{\text{gen}}^{\text{wfc}})$ in MW . . . . .	135
6.3	Simulation Statistics $\sigma(T_s)$ in 0.01MNm . . . . .	138
6.4	Simulation Statistics $\sigma(\Delta F_t)$ in 0.01MN . . . . .	138
6.5	Simulation Statistics $\sigma(T_s)$ in 0.01MNm . . . . .	139
6.6	Simulation Statistics $\sigma(\Delta F_t)$ in 0.01MN . . . . .	139
6.7	Simulation Statistics $\sigma(T_s)$ in 0.01MNm . . . . .	141
6.8	Simulation Statistics $\sigma(\Delta F_t)$ in 0.01MN . . . . .	142
6.9	Simulation Statistics $\sigma(T_s)$ in 0.01MNm . . . . .	142
6.10	Simulation Statistics $\sigma(\Delta F_t)$ in 0.01MN . . . . .	143
7.1	Euclidean distance between empirical and theoretical copulas . .	161
7.2	Comparison of the correlation coefficients . . . . .	162

---

7.3	Case scenario definition . . . . .	162
7.4	Case scenario definition . . . . .	165
7.5	Power comparison . . . . .	167
7.6	Energy comparison . . . . .	167
8.1	Model . . . . .	175
8.2	Fuzzy rules . . . . .	188
8.3	Case study specification . . . . .	197
8.4	Case study specification . . . . .	201
A.1	Parameter for external rid . . . . .	213
A.2	Parameter for 50/10 kV transformer Tr1 . . . . .	214
A.3	Parameter for 10 kV collection cable . . . . .	215
A.4	Parameter for 10/0.96 kV transformer Tr2 . . . . .	215
A.5	Parameter for SCIG . . . . .	216
A.6	Parameter for mechanical part . . . . .	216
A.7	Parameter for mechanical part . . . . .	216
A.8	Parameter for SCIG . . . . .	217
A.9	Parameter for mechanical part . . . . .	217
A.10	Parameter for generator . . . . .	218
A.11	Model parameter . . . . .	218
A.12	Parameter for mechanical part . . . . .	219
A.13	Parameter for pitch controller and actuator . . . . .	219
A.14	Parameter for PMSG . . . . .	220
B.1	Generators of Archimedean copulas . . . . .	226

# Acronyms

---

<b>ACE</b>	Area Control Error
<b>AGC</b>	Automatic Generation Control
<b>ARMA</b>	Autoregressive Moving Average
<b>BESS</b>	Battery Energy Storage System
<b>CAES</b>	Compressed Air Energy Storage
<b>CDF</b>	Cumulative Distribution Function
<b>CES</b>	Cryogenic Energy Storage
<b>C-MPC</b>	Centralized Model Predictive Control
<b>DD-MPSG</b>	Direct Driven Permanent-Magnet Synchronous Generator
<b>DFIG</b>	Double-Fed Induction Generator
<b>DG</b>	Distributed Generator
<b>D-MPC</b>	Distributed Model Predictive Control
<b>ECDF</b>	Empirical Cumulative Distribution Function
<b>ED</b>	Economic Dispatch
<b>EMT</b>	Electro-Magnetic Transient
<b>ENTSO-E</b>	European Network of Transmission System Operators for Electricity



<b>ESS</b>	Energy Storage System
<b>EV</b>	Electrical Vehicle
<b>FACTS</b>	Flexible Alternating Current Transmission System
<b>FC</b>	Fuel Cell
<b>FERC</b>	Federal Energy Regulatory Commission
<b>FES</b>	Flywheel Energy Storage
<b>FRT</b>	Fault Ride Through
<b>FSWT</b>	Fixed Speed Wind Turbine
<b>GDB</b>	Generator Dead Band
<b>GHG</b>	Green House Gas
<b>GRC</b>	Generation Ramp Constraint
<b>GSC</b>	Grid Side Converter
<b>GWEC</b>	Global Wind Energy Council
<b>HCS</b>	Hill-Climbing Search
<b>IEA</b>	International Energy Agency
<b>IEC</b>	International Electrotechnical Commission
<b>IG</b>	Induction Generator
<b>LA</b>	Lead Acid
<b>LFC</b>	Load-frequency Control
<b>LPF</b>	Low Pass Filter
<b>LQG</b>	Linear Quadratic Gaussian
<b>LQR</b>	Linear Quadratic Regulator
<b>LVRT</b>	Low Voltage Ride Through
<b>MA</b>	Metal-Air
<b>MGCC</b>	MicroGrid Central Controller
<b>MIMO</b>	Multiple Input and Multiple Output
<b>MPC</b>	Model Predictive Control

<b>MPPT</b>	Maximum Power Point Tracking
<b>NaS</b>	Sodium Sulphur
<b>NiCd</b>	Nickel Cadmium
<b>NiMH</b>	Nickel Metal Hybrid
<b>NREL</b>	National Renewable Energy Laboratory
<b>OPF</b>	Opimal Power Flow
<b>ORC</b>	Optimal Regmies Characteristic
<b>PCC</b>	Point of Common Coupling
<b>PF</b>	DIgSILENT/PowerFactory
<b>PHS</b>	Pumped Hydro Storage
<b>PLL</b>	Phase Locked Loop
<b>PMSG</b>	Permanent-Magnet Synchronous Generator
<b>PSD</b>	Power Spectrum Density
<b>PSF</b>	Power Signal Feedback
<b>PSO</b>	Paritcle Swarm Optimization
<b>PWA</b>	Piece-Wise Affine
<b>PWM</b>	Pulse Width Modulation
<b>QP</b>	Quadratic Programming
<b>RES</b>	Renewable Energy Source
<b>RMS</b>	Root Mean Square
<b>ROCOF</b>	Rate of Change Of Frequency
<b>RSC</b>	Rotor Side Converter
<b>SC</b>	Super-capacitor
<b>SCIG</b>	Squirrel Cage Induction Generator
<b>SGCC</b>	State Grid Corporation of China
<b>SISO</b>	Single Input Single Output
<b>SMC</b>	Sliding Mode Control

---

<b>SMES</b>	Superconducting Magnetic Energy Storage
<b>SNG</b>	Synthetic Natural Gas
<b>SOC</b>	State of Charge
<b>STATCOM</b>	Static Synchronous Compensator
<b>SVC</b>	Static Var Compensator
<b>TES</b>	Thermal Energy Storage
<b>TSO</b>	Transmission System Operator
<b>TSR</b>	Tip Speed Ratio
<b>UCTE</b>	Union for the Co-ordination of Transmission of Electricity
<b>V2G</b>	Vehicle-To-Grid
<b>VPP</b>	Virtual Power Plant
<b>VRB</b>	Vanadium Redox Battery
<b>VRR</b>	Variable Rotor Resistance
<b>VSC</b>	Voltage Source Converter
<b>VSI</b>	Voltage Source Inverter
<b>VSWT</b>	Variable Speed Wind Turbine
<b>WECC</b>	Western Electricity Coordinating Council
<b>WECS</b>	Wind Energy Conversion System
<b>WPP</b>	Wind Power Plant
<b>WPTS</b>	Wind Power Time Series
<b>WRSG</b>	Wound-Rotor Synchronous Generator
<b>WSTS</b>	Wind Speed Time Series
<b>WTG</b>	Wind Turbine Generator
<b>WTR</b>	Wind Turbine Rotor
<b>ZnBr</b>	Zinc Bromine
<b>ZOH</b>	Zero-Order-Hold

# Introduction

---

## 1.1 Background

### 1.1.1 Wind power development

Wind power, as an alternative to fossil fuels, is plentiful, renewable, widely distributed and clean, and produces no Green House Gas (GHG) emissions during operation [1]. Recently, it has achieved rapid development due to the fast increase of energy demand and accelerating depletion of the world fossil fuels.

From the global capacity point of view, according to the the statistics from Global Wind Energy Council (GWEC), the worldwide cumulative installed wind capacities in the past 10 years are illustrated in Fig. 1.1. The total installed capacity has reached 318,137 MW. By the end of 2010, wind energy was over 2.5% of total worldwide electricity usage, growing more than 25% per annum. As estimated by International Energy Agency (IEA), that figure will reach 2,182 TWh by 2030 [2].

From the development point of view in each country, more than 83 countries around the world had been using wind power on a commercial basis by 2010. The

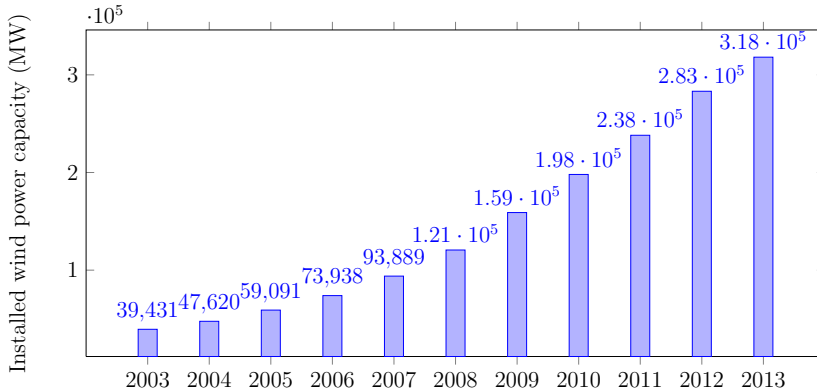


**Figure 1.1:** Global cumulative installed wind capacity 2003-2013 [3]

top 10 countries with new installed wind power capacity in 2013 are illustrated in Fig. 1.2. It shows that more than half of the new installed wind power was added outside the traditional markets of Europe and North America. The value of China accounted for nearly half of the installations at 45.6%.

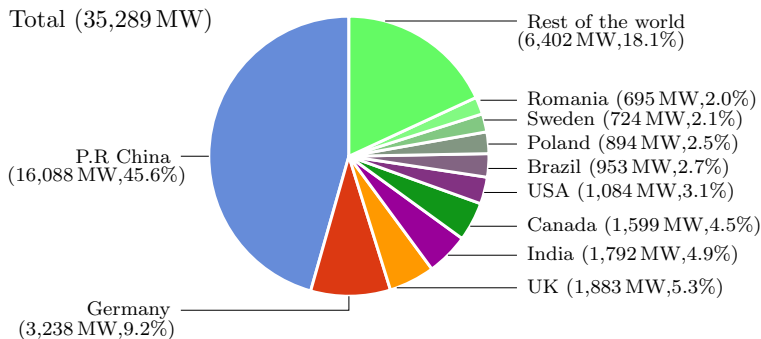


**Figure 1.2:** Top 10 new installed capacity Jan.–Dec. 2013

In several countries, relatively high levels of wind power penetration have been achieved. As shown in Fig. 1.3, the penetration level of Denmark has reached 28.5%, followed by Portugal with 18.8% and Spain with 18.4%, according to the report of US Department of Energy. Denmark has an ambitious target of 50% in 2020.

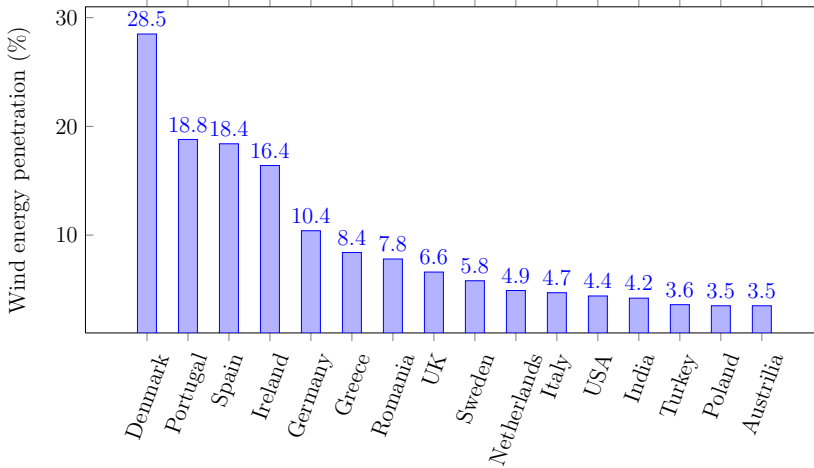


**Figure 1.3:** Wind power penetration in leading wind markets 2012

### 1.1.2 Challenges with wind power integration

Due to the inherent variability and uncertainty, wind power integration into the grid brings impact on different aspects of power system, such as reliability, power quality, stability and planning. The impact is largely dependent on the penetration level [4].

#### 1.1.2.1 Impact on system reliability

Wind power generation is often faced with difficulties regarding the reliability in terms of the generation, planning and scheduling of the power supply. Although no power system is 100% reliable, the intermittent wind generation will increase the level of uncertainty as well as the capacity of operating reserve which in turn increases the generation costs. At the low penetration level, the additional wind power fluctuation is comparable to existing load fluctuations [5]. The committed Conventional Generators (CGs), such as thermal or hydro units, have sufficient load tracking capability without additional operating reserve. However, it becomes challenging at a high penetration level. The response time of CGs should be fast enough during sudden and large change of wind power due to random failures or gust of wind. Besides, more operating reserve is required. An extra reserve of 3-6% of the rated capacity of the wind plant is required for 10% wind integration and approximately 4-8% for 20% wind integration.

### 1.1.2.2 Impact on power quality

The power quality transmitted to the grid is evaluated by the deviation from the normal sinusoidal voltage and current waveforms in a power system network. Power quality components of a power system mainly include flickers, harmonic distortions and etc.

Harmonics can be injected both at the generation and the consumer sides. At the consumer side, harmonics are caused by nonlinear loads. At the generation side, sources of harmonics include the Flexible Alternating Current Transmission System (FACTS) such as reactive power compensators and power electronics devices. The power electronic converters used by the variable speed Wind Energy Conversion System (WECS) are considered as a sources of harmonics.

Flickers are the periodic voltage frequency variations typically between 0.5 and 25 Hz. The oscillatory output power produced by wind turbine generators could cause flickers in the power system. Besides, the fluctuation due to the tower shadow and turbulence effect in wind may cause flickers. IEC 61400-21 defines the measurement procedure to calculate the flicker impact of wind turbines.

### 1.1.2.3 Impact on system stability

Power system transient stability is related to the ability to maintain synchronism when subjected to a severe disturbance, such as tripping of transmission lines, loss of production capacity (generator unit failure) and short circuits.

The conventional power system mainly consists of synchronous generators for electricity production whose inertia plays a significant role in maintaining the stability of power system under a transient condition. The inertia dictates how large the frequency deviations would be due to a sudden change in the generation and load power balance. It influences the eigenvalues and vectors that determine the stability and mode shape of transient response [6]. This type of response of the traditional synchronous generators is called inertia response. The contributions to the system inertia by Wind Turbine Generators (WTGs) are dependent on the WTG type. Due to the direct connection the power system, fixed-speed induction generators can provide inertia response. The modern variable-speed wind turbines whose rotation speed is normally decoupled from grid frequency by power electronic converters, may decrease the system inertia [7]. With high wind power penetration, this decrease aggravates the grid frequency stability.

Many power system faults are cleared by the relay protection of the transmission

system either by disconnection or by disconnection and fast reclosure. There exists a short period with voltage drop beyond a specified threshold, followed by a period when the voltage returns. It is called voltage dip. In early days, only a few wind turbines were connected to the grid. As the voltage dip occurred, the wind turbine was simply disconnected from the grid and was reconnected when the fault was cleared and the voltage returned to normal. It did not cause a significant impact on the stability of the power system. However, with the increasing penetration of wind energy, the power contribution by a wind power plant to the grid is significant. If the entire wind power plant is suddenly disconnected at full generation, the system will lose further production capability [6]. It can further lead to a large frequency and voltage drop and possibly complete loss of power. It is very important to keep the WTGs connected under disturbances in the network. Therefore, the new generation of WTGs are required to have the Fault Ride Through (FRT) capability specified by grid codes.

#### 1.1.2.4 Impact on system planning

As wind resources are often located in remote locations, far from load centers, it is critical to develop sufficient transmission to transport wind power to load centers [8].

Accordingly, transmission planning processes are highly varying and tend to be influenced by regional politics. It may happen that energy production is in one country or state, and consumed in another. The generation capacity, transmission location and load size are different from locations. These disparities make the development of transmission for wind power contentious and complex. Besides, in order to carry the variable, partially unpredictable wind power, new technical requirements arise regarding the transmission technology to be used.

Based on the distribution of wind resources, an alternative vision of the future grid–microgrid is provided, where energy is generated and consumed locally. It can reduce the cost of line losses and the high capital cost of transmission lines. In such schema, the electricity grid could be conceptualized as a collection of independent microgrids with significantly reduced long-distance energy transmission requirements.

#### 1.1.3 Requirements of the TSO

To fulfill the requirements of fast-growing wind generation, wind power plant integration standards are made or updated according to the different developments



of wind power and grid statues. The specific wind power plant interconnection standards in the countries with large installed wind power capacity are listed in Table 1.1.

**Table 1.1:** Wind power plant interconnection standards

Country	Issued by	Year	Title
UK	National Grid	2010	The grid code
Canada	Manitoba Hydro	2009	Transmission system interconnection requirements
	Hydro Québec	2009	Transmission provider requirements for the connection of power plants to the Hydro Quebec transmission system
	BTBC	2008	60 kV to 500 kV technical inter-connection requirements to power generators
	CanWEA	2006	CanWEA base code
	AESO Alberta	2004	Wind power facility technical requirements
Denmark	Elkraft and Eltra	2004	Technical regulation for the properties and the regulation of wind turbines connected to grids with voltage above 100 kV
Germany	E.ON Netz	2006	Grid code high and extra high voltage
Spain	REE	2006	Installations connected to a power transmission system and generating equipment
USA	FERC	2005	Interconnection for wind energy
China	AQSIQ	2011	Technical rules for connecting wind power plant to power system GB/T 19963-2011
	SGCC	2009	Technical rules for connecting wind power plant to power system Q/GDW 392-2009

The Danish Grid Code requires the output power of individual wind generators to be controlled by an automatic frequency regulation controller. Transmission System Operator (TSO) may demand primary response from 47 Hz to 50 Hz and high frequency response from 50 Hz to 53 Hz with a deadband of 49.9 Hz-50.1 Hz [9].

In Great Britain, all wind power plants are required to be capable of meeting the frequency response requirements of primary, secondary and high frequency response [10]. Moreover, the wind power plants should have the technical capability of providing balancing services similar with conventional power plants. To be specific, in the event of a frequency drop ( $> 0.5$  Hz), the primary response should be activated within 0 s to 10 s and sustain for 20 s. The generators should maintain power output at the secondary response from 30 s to 30 min in order

to stabilize the frequency. In the event of a frequency increase, the generator output power should decrease within 0 s to 10 s.

Hydro-Québec grid code states that wind power plants with rated power greater than 10 MW must have frequency control system that helps to reduce large ( $> 0.5$  Hz) and short-term ( $< 10$  s) frequency deviations in power system [11].

The German Grid Code requires wind power plants to reduce their available power production when the network frequency is higher than normal values. wind power plant with a rated capacity less than 100 MW can provide primary response by an agreement with TSO. Given a frequency deviation of 0.2 Hz, the primary response of the generating plant should be able to change by 2% of the rated power output evenly in 30 s and be maintained for at least 15 min. When the frequency increases more than 50.5 Hz, TSO can request a reduction of the active power [12].

In Spain, there are plans to implement in a new operative procedure to strengthen requirements for the power and frequency control contribution from wind generators. This includes the participation in the power and frequency control schemes and in addition requirements for inertia provision by emulation from wind energy converters [13].

In China, the relevant state standard and rules are made by government and State Grid Corporation of China (SGCC) and revised in 2009 and 2011, respectively [14], [15]. The active power ramp rates of 1 min and 30 min are limited based on the capacity of the wind power plant. When the frequency is higher than 50.2 Hz, the wind power plant must follow the dispatch order by TSO.

#### 1.1.4 Application of ESS for wind integration support

The Energy Storage System (ESS) is considered as an effective solution to handle the aforementioned challenges of future power systems with large scale wind power integration.

According to the requirements by specific wind power plants, grid operators or consumers, the specific applications of ESS can be described in different aspects:

- For the generation-side roles of the ESS, it aims to improve the grid-friendliness of wind power plants to dispatch wind power such that they could be controlled like conventional power plants.

- For the grid-side roles of the ESS, it can provide ancillary services to mitigate variability and uncertainty of the entire grid.
- For the demand-side roles of the ESS, it can fulfill the requirements of both consumers and grid operators.

### 1.1.5 Microgrid

Currently, the energy sector is being driven into a new era by environmental concern, electricity business restructuring, and recent development of small scale power generation. Large portions of increases in electrical energy demand will be met through widespread installations of Distributed Generation (DG). Renewable Energy Sources (RESs) and other environmental-friendly energy sources such as wind turbines, photovoltaic arrays, hydro turbines, ESS are commonly used to power DG systems. Also, conventional synchronous generators powered by gas-fired or diesel engines can be used in DG systems [16].

As an efficient solution to improve the utilization of DG, the microgrid concept has attracted more and more attentions due to its great benefits and control flexibility [17]. The microgrid can operate in the grid-connected mode and islanded mode. Since the RESs have an intermittent nature, i.e. wind and sun, they cannot ensure constant power supply required by loads. In addition, the DG units with relatively slow response have insufficient dynamic performance in terms of load tracking [18]. ESS can play important roles in microgrid, such as enabling fast load pick-up, enhancing the reliability, and smoothing the generation profile in non-dispatchable sources.

## 1.2 Objectives and research problems

The main objective of the PhD project is the coordinated control between wind power and ESS. The control objectives are defined according to the roles that the ESS plays. The PhD project focuses on the following two scenarios:

- Scenario 1: As a part of a wind power plant, the ESS plays a generation-side role which aims to improve the grid-friendliness of the wind power plant. The control objectives include:
  1. To smooth the wind power production in order to improve the power quality.

2. To track the reference power from the system operator.
  3. To minimize the mechanical loads experienced by the wind turbines.
- Scenario 2: As a part of microgrid, the ESS is used to compensate the mismatch between power generation and consumption in the islanded operation. Two microgrid configurations are considered:
    1. In the islanded operation, the voltage and frequency are maintained by synchronous generators. The ESS is coordinated with dispatchable generators for frequency support.
    2. In the islanded operation, the wind power penetration is high. The voltage and frequency are maintained by a Voltage Source Converter (VSC) interfaced WTG. As the master DG unit, the WTG is regulated for the load following. As the slave, the ESS is used as a complementary component and activated only if necessary.

To achieve the objectives of the PhD project, other relevant problems have been investigated, including:

- Modeling and control of modern wind turbine.
- Active power control of modern wind power plant.
- Planning problem of ESS for the optimal sizing and siting.

## 1.3 Contributions

The main contributions of this PhD work are listed below:

- Review of the roles that wind power plays in the modern power system, especially the control for frequency support.
- Review of the roles that ESS plays in the modern power system from different stakeholders: the wind power plant owner, the grid operator and the energy consumer.
- Modeling and validation of International Electrotechnical Commission (IEC) generic wind turbine model (Type 1) in DIgSILENT/PowerFactory according to the committee draft of IEC 61400-27.

- Development of a Maximum Power Point Tracking (MPPT) control algorithm for variable speed WECS based on  $\mathcal{L}_1$  adaptive control theory.
- Development of two coordinate control algorithms for active power control of wind power plant based on Distributed Model Predictive Control (D-MPC) theory. The two control algorithms correspond to two cases—with and without ESS, respectively.
- Development of a heuristic optimal sizing and siting algorithm for ESS in a grid considering the network constraints, ESS and committed CG characteristics for the benefit of the whole system.
- Development of two coordinate control algorithms between wind power and ESS for microgrid application, which correspond to the two scenarios described in Section 1.2.

## 1.4 Structure of the thesis

The thesis is organized as follows:

**Chapter 2:** This chapter presents an overview of wind turbine generator technologies and the roles that wind power plant plays in modern power system. Among different ancillary services, the short-term frequency control support and inertia response are described. Their implementations in the wind power control are reviewed.

**Chapter 3:** This chapter reviews the state of the art of the ESS technologies for wind power integration support from different aspects, including the modern ESS technologies, their potential applications for wind power integration support, the planning problem and the present operation and control strategies of the ESS.

**Chapter 4:** This chapter presents the implementation of the IEC generic Type 1 WTG model in DIgSILENT/Power Factory (PF) and the validation of the implemented model against field measurements.

**Chapter 5:** This chapter presents the design of an  $\mathcal{L}_1$  speed adaptive controller for MPPT of a small variable speed WECS.

**Chapter 6:** This chapter presents the optimal active power control of wind power plant based on D-MPC. The control objective includes tracking the power reference from the system operator and minimizing the mechanic loads of wind

turbines. As the prediction model for D-MPC, a discrete-time Piece-Wise Affine (PWA) model of wind turbine is developed. The D-MPC algorithm is implemented by using the fast dual gradient method.

**Chapter 7:** This chapter proposes a heuristic algorithm of optimal sizing and siting of ESS which is used for the operation-based planning of the power system with large wind power integration. The statistics from simulated system operations are then coupled to the planning process to determine the optimal siting and sizing of storage throughout the network.

**Chapter 8:** In this chapter, two coordinate control strategies are developed for islanded operation of microgrid with wind power integration. These two strategies are based on the roles that ESS and wind turbine play and aim to handle different situations.

## 1.5 Publications

The main publications during the PhD study are listed:

### Journal Paper (Accepted)

1. H. Zhao, Q. Wu, C.N. Rasmussen, and M. Blanke.  $\mathcal{L}_1$  Adaptive Speed Control of a Small Wind Energy Conversion System for Maximum Power Point Tracking. *IEEE Transaction on Energy Conversion*, 2014.
2. H. Zhao, Q. Wu, I. Margaris, J. Bech, P.E. Sørensen, and B. Andresen. Implementation and Validation of IEC Generic Type 1A Wind Turbine Generator Model. *International Transaction on Electrical Energy Systems*, 2014.
3. H. Zhao, Q. Wu, S. Hu, H. Xu, and C.N. Rasmussen. Review of Energy Storage System of Wind Power Integration Support. *Applied Energy*, 2014.
4. H. Zhao, Q. Wu, I. Margaris, and P.E. Sørensen. Implementation of IEC Generic Model of Type 1 Wind Turbine Generator in DIgSILENT PowerFactory. *Automation of Electric Power Systems*, 2014.
5. S.T. Cha, Q. Wu, H. Zhao, and C. Wang. Frequency Control for Island Operation of Bornholm Power System. *Energy Procedia*, 2014.

### Journal Paper (Submitted)

1. H. Zhao, Q. Wu, S. Hu, and H. Xu. Review of Wind Power Control for Short-term Frequency Control Support.
2. H. Zhao, Q. Wu, Q. Guo, H. Sun and Y. Xue. Distributed Model Predictive Control of A wind power plant for Optimal Active Power Control, Part I: Clustering-based Wind Turbine Model Linearization.
3. H. Zhao, Q. Wu, Q. Guo, H. Sun and Y. Xue. Distributed Model Predictive Control of A wind power plant for Optimal Active Power Control, Part II: Implementation with Clustering-based Piece-Wise Affine Wind Turbine Model.
4. H. Zhao, Q. Wu. Optimal Sizing and Siting of Energy Storage System for Short-term Dispatch in Power System with Wind Power Integration.
5. H. Zhao, Q. Wu, W. Huang, J.M. Guerrero and C.N. Rasmussen. Converter Controller Design of PMSG Wind Turbines and Coordinate Control Strategy with BESS for Microgrid Application.

### Conference Paper (Published)

1. H. Zhao, S.T. Cha, C.N. Rasmussen, Q. Wu. Cooperative Operation of Battery Energy Storage System and Dispatchable Distributed Generation in Microgrid System. *International Conference on Wind Energy Grid-Adaptive Technologies (WeGAT 2012)*, 2012, Jeju, Korea.
2. S.T. Cha, H. Zhao, Q. Wu, J. Østergaard, T. Nielsen, and H. Madsen. Evaluation of Energy Storage System to Support Danish Island of Bornholm Power Grid. *10th International Power and Energy Conference (IPEC 2012)*, 2012, Ho Chi Minh City, Vietnam.
3. S.T. Cha, H. Zhao, Q. Wu, J. Østergaard, A. Saleem, and J. Østergaard. Coordinated Control Scheme of Battery Energy Storage System (BESS) and Distributed Generators (DGs) for Electric Distribution Grid Operation. *38th Annual Conference on the IEEE Industrial Electronics Society, (IECON 2012)*, 2012, Montreal, Canada.
4. H. Zhao, Q. Wu, P.E. Sørensen, J. Bech, and B. Andresen. Implementation of draft IEC Generic Model of Type 1 Wind Turbine Generator in PowerFactory and Simulink. *12th International Workshop on Large-scale Integration of Wind Power into Power Systems as well as on Transmission Networks for Offshore Wind Power Plants*, 2013, London, United Kingdom.

- 
5. H. Zhao, Q. Wu, C.N. Rasmussen, Q. Guo, and H. Sun. Distributed Model Predictive Control for Active Power Control of wind power plant. *5th IEEE PES Innovative Smart Grid Technologies (ISGT) European 2014 Conference, 2014, Istanbul, Turkey.*





## CHAPTER 2

# Roles of Wind Power Plants in Modern Power Systems

---

At the early stage of its development, wind power generation technology focused more on extracting the maximum power from wind resources. It was often considered nondispatchable and had limited contribution to strengthen the system stability and reliability. As long as the wind power penetration level is low, the wind power is manageable and can be accepted by system operators. As the wind power penetration level grows, especially as the capacity of wind power plants becomes larger, it will have a serious impact on the system operation.

Recently, due to the development of power electronic technologies, mechanical engineering technologies and proper control strategies, the controllability of an individual wind turbine and a wind power plant has been largely improved. Therefore, wind generation should play a greater role in maintaining the system reliability and stability.

## 2.1 Wind turbine generator technology

The present WTG based WECS can be generally divided into the following four types [19].

### 2.1.1 Type 1

This type represents the wind turbine with directly grid connected Induction Generator (IG) with fixed rotor resistance (typically Squirrel Cage Induction Generator (SCIG)). As illustrated in Fig. 2.1, the Wind Turbine Rotor (WTR) is connected to the IG via a Gearbox (GB). The capacitor bank provides reactive power compensation. Most Type 1 WTGs are equipped with Mechanically Switched Capacitor (MSC) banks. As the protection device, the main Circuit Breaker (CB) disconnects generator and capacitor from the grid during the fault.

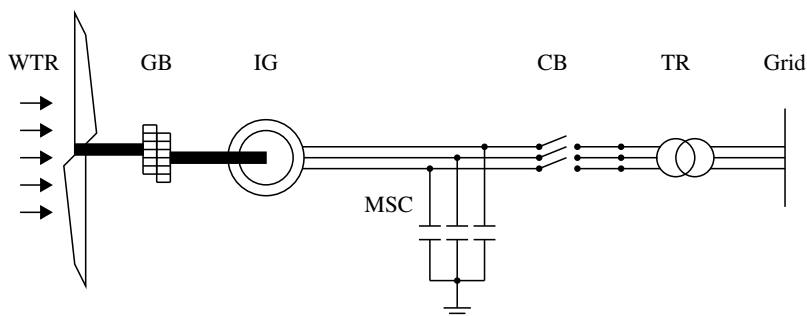


**Figure 2.1:** General structure of Type 1 WTG

Due to the direct connection to the grid, the IG works on its natural mechanical characteristic having an accentuated slope (corresponding to a small slip, normally 1%-2%) given by the rotor resistance [20]. The rotational speed of IG is very close to the synchronous speed imposed by the grid frequency and not affected significantly by the wind variations.

### 2.1.2 Type 2

This type represents the wind turbine with directly grid connected IG with Variable Rotor Resistance (VRR). The general structure of Type 2 WTG is illustrated in Fig. 2.2. As an evolution of Type 1 WTG, the total (internal plus external) rotor resistance is adjustable by regulation of power electronics. In such way, the slip of the generator can be controlled which affects the slope of the mechanical characteristic. The range of the dynamic speed control is determined by how large the additional resistance is. Usually the control range is up to 10% over the synchronous speed.

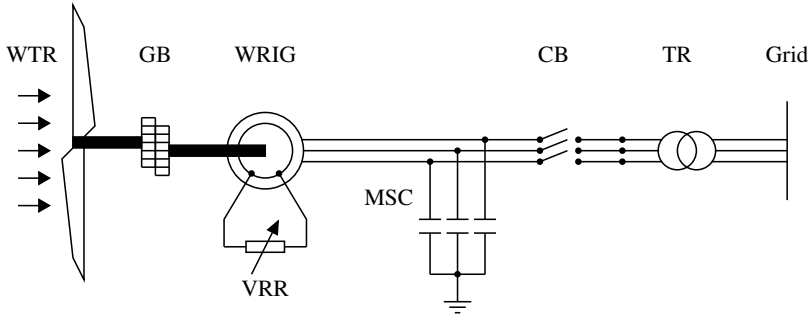


**Figure 2.2:** General structure of Type 2 WTG

### 2.1.3 Type 3

This type represents the wind turbine with Double-Fed Induction Generator (DFIG). As illustrated in Fig. 2.3, the DFIG is a WRIG with the stator windings connected directly to the three-phase, constant frequency grid and the rotor windings connected to a back-to-back VSCs—Rotor Side Converter (RSC) and Grid Side Converter (GSC) [21]. They are decoupled with a Direct Current (DC) link. The main idea is that the RSC controls the generator in terms of active and reactive power, while the GSC controls the DC-link voltage and ensures operation at a large power factor.

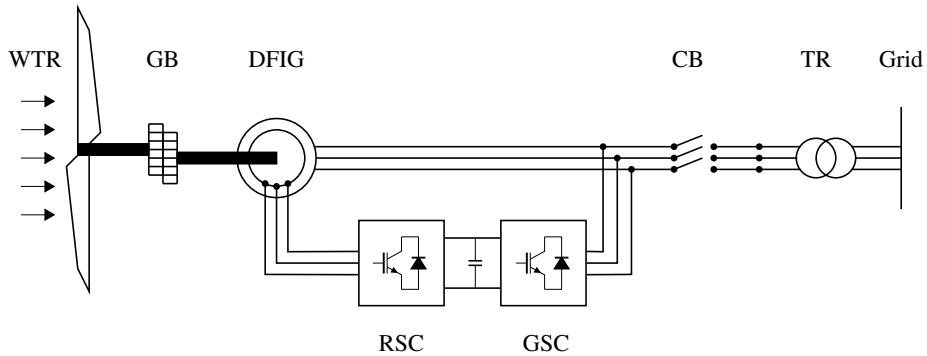


**Figure 2.3:** General structure of Type 3 WTG

The stator delivers power into the grid all the time. The power flow of the rotor is dependent on the operating point:

- If the slip is negative (over-synchronous operation), it feeds power into the

grid.

- If the slip is positive (sub-synchronous operation), it absorbs power from the grid.

In both cases, the power flow in the rotor is approximately proportional to the slip. By regulation of the generator behavior through the GSC controller, the rotation speed is allowed to operate over a large, but still restricted range (normally 40%).

#### 2.1.4 Type 4

This type represents the wind turbine connected fully through a power converter. The general structure of Type 4 WTG based WECS is shown in Fig. 2.4. The generator type is flexible. It can be equipped with either an induction generator or a synchronous generator. Furthermore, the synchronous generator can be either a Wound-Rotor Synchronous Generator (WRSG) or a Permanent-Magnet Synchronous Generator (PMSG), the latter being the one mostly used by the wind turbine industry. The back-to-back VSC configuration is applied. Its RSC ensures the rotational speed adjusted within a large range, whereas the GSC transfers the active power to the grid and control the reactive power.

The PMSG is considered a good option to be used in WECS. Firstly, due to its self-excitation property, its operation is allowed at high power factor and efficiency. As it is supplied by the permanent magnets, PMSG does not require energy supply for excitation. Secondly, the salient pole of PMSG operates at low speeds, and thus the gearbox (Fig. 2.4) can be removed. This is a big advantage of PMSG-based WECS as the gearbox is a sensitive device in wind power systems. The same objective can be achieved using Direct Driven multipole PMSG (DD-PMSG) with large diameter. Due to the synchronous nature of PMSG, problems exist during start-up, synchronization and voltage regulation. Moreover, since the magnetic materials are sensitive to temperature, a cooling system is required. Otherwise, these materials will lose their magnetic properties if exposed to high temperatures [20], [21].

#### 2.1.5 Comparison

These four types can be further classified into two categories according to the speed control criterion: Fixed Speed Wind Turbines (FSWTs) including Type 1 and Variable Speed Wind Turbines (VSWTs) including Type 2, Type 3 and

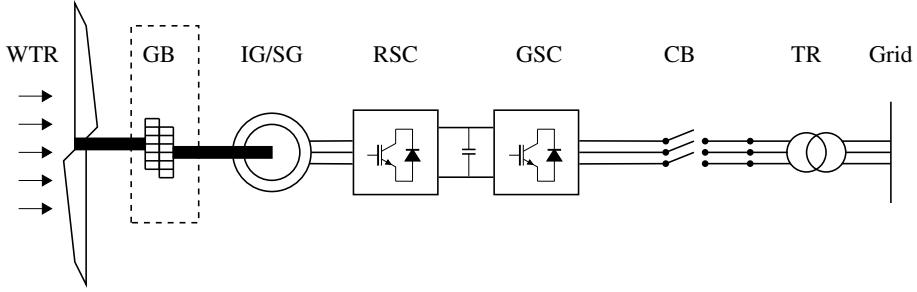


**Figure 2.4:** General structure of Type 4 WTG

Type 4 [22]. Since the speed variability of Type 2 is small, VSWTs mainly refer to Type 3 and Type 4 in this thesis.

FSWTs have the advantage of being simple, robust and reliable, with simple and inexpensive electric systems and well proven operation. Besides, they can naturally provide the inertia response. However, as FSWTs have limited controllability in terms of rotational speed, the captured aerodynamic efficiency is restricted. Due to the fixed-speed operation, the mechanical stress is important. All fluctuations in wind speed are transmitted into the mechanical torque and further, as electrical fluctuations, into the grid.

Due to the regulation of rotor speed within a larger range, VSWTs are highly controllable, allowing maximum power extraction over a large range of wind speeds. Furthermore, the active and reactive power control can be fully decoupled and implemented independently. Currently, they are more advantageous and predominate in market shares, especially in MW class. Type 3 WTGs (DFIGs) are partially connected through the electronic converter. For Type 4 WTGs, the intermediate DC voltage bus between the back-to-back converters creates an electrical decoupling between the generator and the grid. There is no contribution to the power system apparent inertia [23]. An attempt to emulate this kind of response can be realized by adding in the maximum power tracking control loop. More details are described in the following sections.

## 2.2 Grid-side roles of wind power plant

Due to the development of power electronics, mechanical engineering technologies and control strategies, modern WTGs have been enabled to possess performance comparable or even superior to those of conventional thermal or hydro

generating units [8]. Modern Wind Power Plants (WPPs) have become more grid-friendly and are capable of providing ancillary services for the system stability and reliability. As summarized in [24], [25], some advanced operational capabilities are listed as follows.

- Reactive power and voltage control support. For Type 3 and Type 4 WTGs, they have the built-in capability of providing such support through reactive power controller. For the transmission lines with Flexible AC Transmission System (FACTS) installation, this support can also be provided through a combination of switched capacitor banks and FACTS devices such as Static Var Compensator (SVC) and Static Synchronous Compensator (STATCOM).
- Fault Ride-Through (FRT) ability. This ability enables WTGs to survive in (ride through) specific low and high voltage/frequency range and duration, caused by faults or disturbances in the power system. Through modifications to the controls, voltage ride-through can be achieved with all modern wind generating units.
- Active power and frequency control support. According to the requirements of danish TSO, different types of power control are involved including absolute power limitation, delta limitation, balance control, stop control, ramp and fast down regulation to support system protection. On top of that, frequency control is required. This can be achieved through unit control mechanisms for wind turbine units.
- Inertial response. As summarized in Section 2.1.5, inertial response is inherent in Type 1 and Type 2 units, and can be achieved through supplemental controls in the converter to emulate the inertial behavior for Type 3 and Type 4 units.

The following sections concentrate on the the frequency control support. Frequency control is an important ancillary service provided by TSO [26]. A common framework is defined by coordinating authorities like Union for the Co-ordination of Transmission of Electricity (UCTE, now ENTSO-E) in mainland Europe or Federal Energy Regulatory Commission (FERC) in North America. The aim of frequency control is to maintain the balance between load and generation within a synchronous area. It is generally based on three control actions performed with distinct features:

- Primary frequency control. It is a local automatic control that stabilizes the frequency after a large disturbance.

- Secondary frequency control. It is a centralized automatic generation control which aims to bring frequency back to its nominal value. Following an imbalance, it restores the interchanges with surrounding power systems in each control area.
- Tertiary frequency control, by which the primary and secondary reserves are restored. This control is done by manual changes in the dispatching of generating units [27], [28].

The reviewed frequency control support consists of inertial response, primary frequency control and secondary frequency control.

## 2.2.1 Wind turbine control for inertial response and primary frequency control

### 2.2.1.1 Inertial control loop

An important feature of VSWTs is the possibility for their active and reactive power outputs to be controlled as required by system operators. Although the steady-state active power delivered to the grid depends on the mechanical energy transferred from the wind, the electric power can be transiently controlled by resorting to the mechanical system kinetic energy. Thus, one solution to tackle the inertia issue of VSWTs is adding a supplementary loop in their control system to provide so-called synthetic or virtual inertia from the power conversion system of these units [22], [29], [30], [31]. The supplementary loop can be either added into a active power control loop or a torque control loop [22], depending on the reference signal required for the converter controller. For the former case, the active control scheme of VSWTs is depicted in Fig. 2.5. The additional power  $p_{df}$  is proportional to frequency derivative. In this way, VSWTs can respond to frequency derivative that is equal to the inherent behavior of the synchronous machine. The frequency derivative is filtered by a high-pass filter with time constant  $T_R$ . Permanent frequency deviation has no effect on the control strategy.  $p_{df}$  is calculated as,

$$p_{df} = \frac{K_{df}s}{T_{RS} + 1} f_{meas}, \quad (2.1)$$

where  $K_{df}$  is a constant weighting the frequency derivative and equals to the term  $2H$ .  $H$  is the total extra virtual inertia constant of the wind turbine [32].  $p_{ref}^{cmd}$  is the reference command derived by wind power plant control.

The typical inertia constant of the generators of the large power plants are in the range of 2~9s [28], while values for wind turbines have roughly the



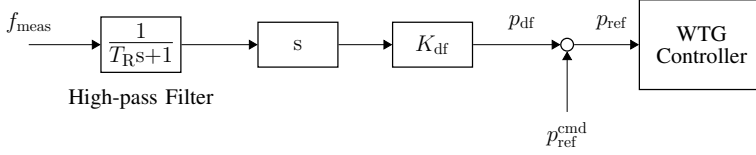


**Figure 2.5:** Inertial control loop

same value about 2~6s [33], [34]. The introduction of wind turbines in the grid therefore doesn't necessarily reduce the amount of available kinetic energy. Actually, the variable speed wind turbine can operate in a wide range of speed changes. With the same rating and inertial constant, the variable wind turbines can considerably release greater kinetic energy (about 4.12 times [29]) than fixed speed wind turbines and conventional generators [35]. These conclusions are validated by the simulation results derived in [22] and [31]. However, too much kinetic energy extraction from the rotor may result in stalling. Since the inertial control feature only acts when needed, it does not adversely impact annual energy production [36].

### 2.2.1.2 Droop control loop

The droop control is to adjust the active power output which is proportional to the frequency deviation [34]. Similarly with the inertial loop, the droop control loop can either be added into active power control loop or torque control loop [22] depending on the reference signal required for the converter controller of VSWTs [29]. The droop control loop is illustrated in Fig. 2.6.

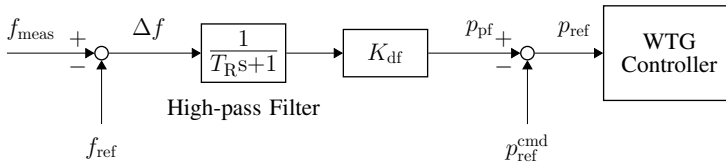


**Figure 2.6:** Droop control loop

Compared with the inertial control, the droop control does not affect much Rate Of Change Of Frequency (ROCOF) but greatly influences the frequency nadir [31]. The droop constant  $K_{pf}$  affects the steady state frequency deviation [28].

As proposed in [22] and [34], both inertia response control and droop control are combined together. The control scheme is illustrated in Fig. 2.7.

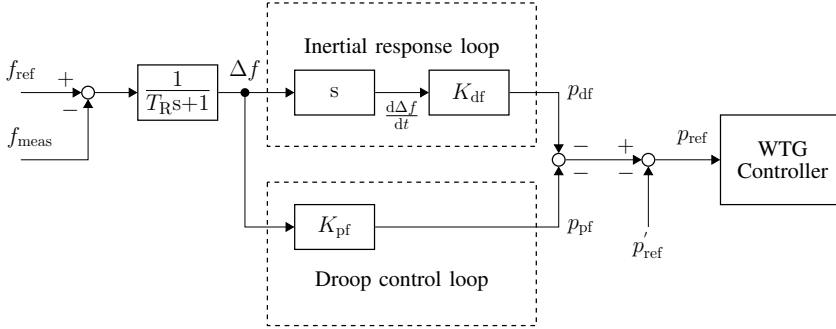


**Figure 2.7:** Combination of inertial control and droop control

In [30], frequency responses of conventional power plants and wind turbines to the load increase are tested and compared. The response and settling time of mechanical power of hydro, thermal and steam unit are 4~25 s and 20~48 s, respectively. The response and settling time of the wind turbine are shorter, 3~9 s and 8~38 s respectively. In [37] and [38], the capability of providing a short-term excess active power support of a commercial multi-megawatt VSWT is quantified. In [37], a GE 3.6 MW model was used to show that the WTG can provide an extra 0.1 p.u. of active power for more than 10 s quite easily without hitting the minimum speed limit, which is twice the Hydro-Québec requirement. In [38], a 2 MW DFIG was investigated to show an active power overproduction of 0.2 p.u. for at least 10 s. These results are helpful for the grid operator for restoring a critical situation of grid frequency dip, especially in power systems with slow primary movers response or low inertia.

Although both inertial and droop control methods can contribute to improving the frequency performance during a frequency event, it still requires further studies on synthetic inertia by wind turbines limited by speed and power ratings, recovered period etc. Firstly, it should be noticed that releasing or storing kinetic energy can only be considered as a part of primary control. Indeed, the wind persistence being limited, this power reserve cannot be guaranteed further to short-term. Secondly, the inertial control mentioned above did not investigate limitations of VSWTs, like current and voltage rating of converters. Thirdly, most inertial control methods allow a temporary overload of the machine when operating at a high wind speed [23]. This would require generators rated for greater than nominal power and torque. The peak torque is 130% which may cause mechanical stress and the rotor currents may not be handled by the RSC [31].

### 2.2.1.3 Deloading Control

VSWTs normally operate for maximization of revenue and resource utilization. In that case, they are not available to provide a sustained increase in power output and participate in primary frequency regulation. It is generally necessary to force the wind turbine to operate in a non-optimal power point [39]. Assuming the available maximum active power is  $P_{\text{avi}}$ , the reserve factor  $f_p$  is used to quantify the reserved power. The maximum operation power can be expressed as  $P_{\text{max}} = P_{\text{avi}}(1 - f_p)$ . The operation point could vary continuously within the band  $[P_{\text{min}}, P_{\text{max}}]$ . The reserve factor is dependent on the reserve requirement, typically 10% [40]. This control methodology of wind turbine is called deloading control. The ways to deload wind turbine are classified into two categories. One is pitch angle increase and the other is driving the wind turbine operation at increased speed. Both methods can be used simultaneously to optimize the control performance [29], [41].

**Pitch control** As depicted in Fig. 2.8(a), increasing the pitch angle could reduce the power coefficient  $C_p$ . As proposed in [41], there is an optimal turbine rotational speed  $\omega_t^{\text{opt}}$  for any given wind speed corresponding to the MPPT strategy. It is desirable to maintain  $\omega_t^{\text{opt}}$  in the deloading operation through pitching. The relation between required pitch angle and desired deloading is illustrated in Fig. 2.8(b).

In [42], the droop controller is implemented through pitch control. The reference pitch angle  $\theta_{\text{ref}}$  can be derived by,

$$C_p(\lambda_{\text{opt}}, \theta_{\text{ref}}) = (1 - f_p)C_p(\lambda_{\text{opt}}, \theta_{\text{min}}). \quad (2.2)$$

where  $\lambda_{\text{opt}}$  indicates the optimal tip speed ratio.

Since the optimal speed  $\omega_t^{\text{opt}}$  is determined, a simple two-dimensional look-up table reflecting the function shown in Fig. 2.8(b) is adopted. The pitch control is available for both FSWTs and VSWTs. Due to the servo time constant, the response of pitch control is slower than the rotor speed control.

**Rotor speed control** Another way to deload the wind turbine is to drive wind turbine to operate differently from the optimum curve. It is only available for VSWTs. Theoretically, both decreasing (underspeeding) and increasing (overspeeding) rotation speed are possible, as depicted in Fig. 2.9. However, underspeeding may decrease the small signal stability [43]. Consequently, VSWTs normally operate under the overspeeding condition.

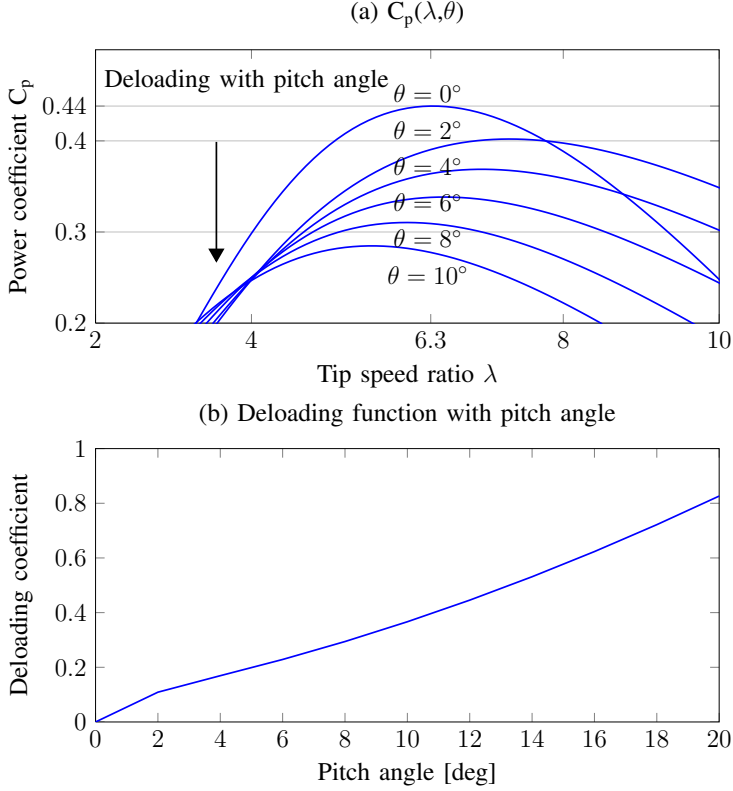


**Figure 2.8:** Relation between pitch angle, power and deloading coefficients

As depicted in Fig. 2.5, the power reference  $p_{\text{ref}}^{\text{cmd}}$  is the command signal for converter control. According to [44], [45], the power reference can be defined as Eqn. 2.3 based on the measured rotor speed  $\omega_r$  and wind speed  $v_w$  (shown in Fig. 2.10),

$$p_{\text{ref}}^{\text{cmd}} = p_1 + \frac{p_0 - p_1}{\omega_{r1} - \omega_{r0}} (\omega_{r1} - \omega_r), \quad (2.3)$$

where  $p_0$  and  $p_1$  are the maximum and deloaded active powers for a given wind speed, respectively,  $\omega_{r0}$  and  $\omega_{r1}$  are the minimum and maximum rotor speeds referred to the generator side, respectively. In the control approach proposed by [45], the converter control and pitch control are combined together to provide primary frequency regulation.

Compared with the aforementioned pitch control, rotor speed control is realized by the power electronic converter and can response to the frequency variation in a faster manner. Therefore, it is more convenient applied [46]. It should be

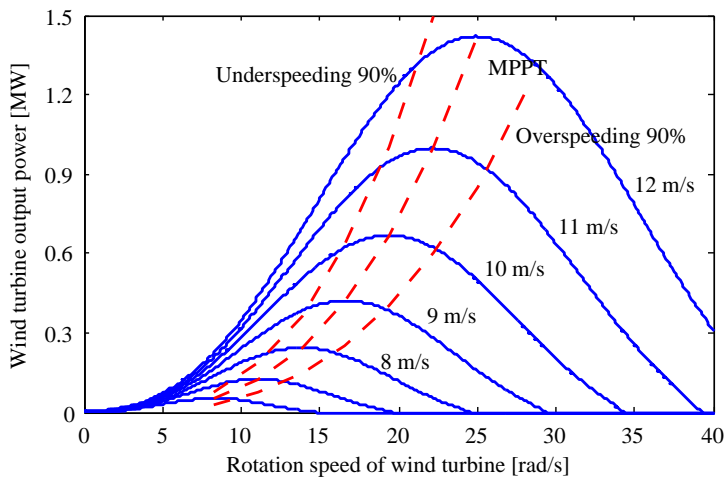


**Figure 2.9:** Rotor speed control

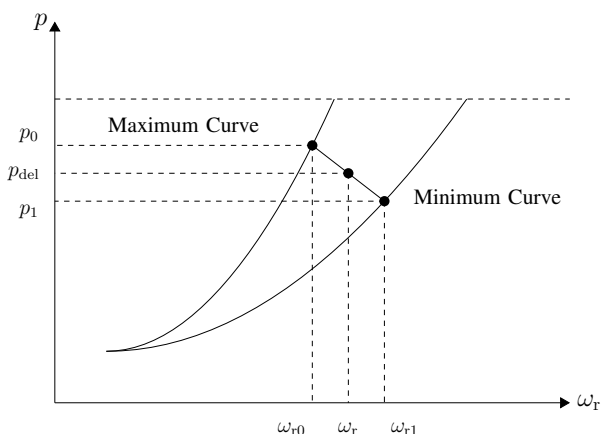


**Figure 2.10:** Deloaded optimal active power curve

noticed that at medium to high wind speeds,  $\omega_r$  required for deloading purposes is often greater than maximum rotation speed  $\omega_{max}$ . Consequently, as far as rotor speed control is concerned, three wind speed regimes can be identified: a low wind speed regime where deloading is achieved through rotational speed increase, a medium wind speed regime where a coordinated use of speed control and pitching is required and the high wind speed regime where speed control essentially degenerates into pitching.

Another important observation concerns rotor speed control when applied in

DFIGs. The percentage of the total power transferred to the grid and the power through the converter depends on the generator slip. The higher the slip is, the higher the power through the converter. Consequently when speed control at near-nominal wind speeds, a converter sized for optimum operation might not be adequate. This is another constraint that has to be taken into account [41].

### 2.2.2 wind power plant control for inertial response and primary frequency support

Besides the control implemented at the wind turbines to provide inertial response and primary frequency control support, it is possible to program the wind power plant control to provide a form of inertial response (e.g., GE's WindINERTIA control feature)[36]. Furthermore, in order to coordinate each wind turbine of the wind power plant and make it behave as a single centralized unit, the wind power plant level control should be built up. The centralized frequency control seems to be the most robust and consistent solution from a control point of view [25]. The overall diagram with a hierarchical structure of central control and local control is shown in Fig. 2.11 [47]. The wind turbine controllers should not respond to the frequency variation but only deliver the reference power. The structure may utilize either a separate (external) energy storage device or a power reserve achieved through deloading of one or more turbines in a wind power plant [48]. There are two main functions for the active power control: firstly, receiving operator's request and distributing power reference signal to each machine for the desired generation. Secondly, calculating each machine's deloaded condition and come up with a desired generating margin [40].

As illustrated in Fig. 2.11, the active power reference signal  $P_{\text{ref}}^{\text{wfc}}$  is determined in the control function block, based on one or several control functions required by system operator.  $P_{\text{ref}}^{\text{wfc}}$  can be adjusted with some correction  $\Delta P_{\text{freq}}$  from subordinate frequency control loop which provide inertial response and primary frequency regulation [44], [49]. The power reference  $P_{\text{out}}^{\text{wfc}}$  is further fed into a dispatch function block, where it is converted into power reference  $P_{\text{ref}}^{\text{WT}_i}$  for each individual wind turbine of the wind power plant.  $\alpha_i$  is the distribution factor, thus  $P_{\text{ref}}^{\text{WT}_i} = P_{\text{out}}^{\text{wfc}} \cdot \alpha_i$ . There are different dispatch algorithms. In [47],  $\alpha_i$  is proportional to the available active power. Another dispatch method is introduced in [40].  $P_{\text{ref}}^{\text{WT}_i}$  is dependent on the wind speed. Generally, the higher the wind is, the larger the set point is weighted. For the given wind velocity  $v_w$ ,  $DF_{\text{WT}_i}$  is expressed as follows,

$$\alpha_i = \frac{W(v_w)N(v_w)}{\sum[W(v_w)N(v_w)]} \frac{1}{N(v_w)}, \quad (2.4)$$

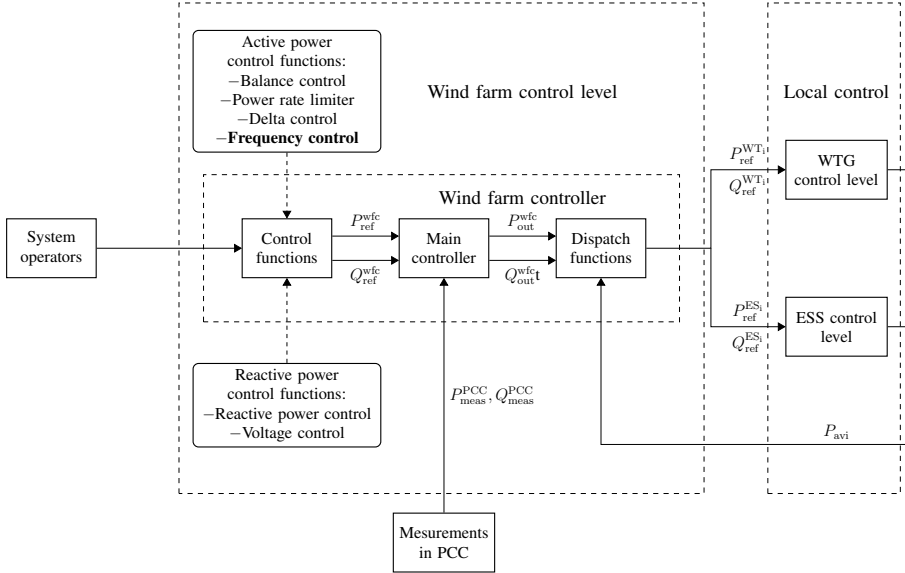


**Figure 2.11:** wind power plant control level

where  $W(v_w)$  is the weighting factor for each level of wind speed,  $N(v_w)$  is the number of wind turbine operating at  $v_w$  within the wind power plant.

The recovery strategy for wind power plant control after frequency support was studied in [34], [35]. If all the wind turbines are allowed to accelerate simultaneously, the sudden decrease of wind power will cause another sudden reduction in power system frequency. A method of restoring the full-converter WTGs to their initial operating point after providing frequency support was proposed in [23]. A better way to turn off the wind power plant control is to instruct each wind turbine to switch off their control at different times.

### 2.2.3 Secondary frequency control from wind power control

A steady-state frequency deviation still remains after primary frequency regulation due to the droop characteristic and frequency sensitivity of load [28]. The secondary frequency control (also called Automatic Generation Control (AGC)) is a centralized automatic control that adjusts the active power production of the generating units to restore the frequency and the interchanges with other systems to their scheduled values following an imbalance [27], [50], [51]. In Eu-

rope, secondary frequency control is also called load-frequency control (LFC) [52].

### 2.2.3.1 Conventional AGC

The conventional AGC model is well discussed in [27], [28], [53]. AGC is realized through Area Control Error (ACE). The ACE signal is defined as a linear combination of frequency and tie-line power changes to present the net active power imbalance of a control area. It is calculated as follows according to UCTE ( $ACE_{UCTE}$ ) or NERC ( $ACE_{NERC}$ ) [27],

$$ACE_{UCTE} = P_{me} - P_{se} + K_{ri}(f_m - f_t), \quad (2.5)$$

$$ACE_{NERC} = P_{me} - P_{se} - 10B(f_m - f_t) - I_{ME}, \quad (2.6)$$

where  $K_{ri}$  is the constant proportional factor of the control area (positive and in MW/Hz),  $B$  is the frequency bias setting (negative and in MW/0.1Hz),  $P_{me}$  is the measured value of total power exchanged by the zone with other zones,  $P_{se}$  represents the scheduled power exchange from the zone to all neighboring zones,  $f_m$  and  $f_t$  are measured network frequency and target frequency, respectively. Because of the simple structure and robust performance, PI control is the widely used type of controller for the AGC, while the control parameters (gains) obtained through extensive field testing and tuning, and usually using a trial-and-error approach [54], [55]. As illustrated in Fig. 2.12, when ACE signal exceeds a standard limit, it should be filtered to remove noise effect. Then it is applied through the PI control block, Generator Dead Band (GDB) and Generation Ramp Constraint (GRC). The output  $\Delta P_c$  is sent to generating units.

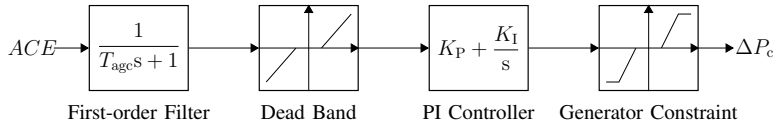


**Figure 2.12:** Block diagram of AGC main processing modules

### 2.2.3.2 Impact of AGC with large-scale wind integration

The current form of AGC may not be well suited to the future power system with large-scale wind integration [54]. Most of the conventional AGC synthesis methodologies provide model based controllers that are difficult to use for large-scale power systems with nonlinearities (e.g. GDB and GRC) and uncertain parameters. On the other hand, most of the applied linear modern/robust



control techniques to the AGC problem suggest complex control structure with high order dynamic controllers, which are not practical for industry practices [56]. Conventional AGC is based on equilibrium assumption. However, frequency regulation in systems with fluctuations caused by wind can no longer be viewed as equilibria problems. According to [57], persistent fluctuation of wind power creates constantly changing conditions requiring frequency regulation to be formulated as a control design problem which accounts for generator dynamics. To accommodate the variation of the wind power, the area control Area Control Error (ACE) signal is also proposed to be updated to represent the impacts of wind power on the scheduled flow over the tie lines [58]. Also, existing AGC algorithms need to be modified based on wind power forecasts to address the variability and uncertainty of wind generation [8].

### 2.2.3.3 New AGC Algorithm

To handle the aforementioned problems, several new AGC control methods have been proposed to accommodate their dynamics and effects on overall system dynamic performance [59].

A Linear Quadratic Regulator (LQR) based full state feedback control was proposed in [60]. However, with large system size, it would require complex sensing and communications. Moreover, some information for control areas are private and could hardly be revealed. As the sharing information becomes less desirable, it is necessary to resort to minimally coordinated solutions in order for the industry to accept the proposed enhancements. [61] introduced Enhanced Automatic Generation Control (E-AGC) approach to frequency regulation in multi-area electric energy systems to overcome the above limitations. This new approach utilizes the concept of an interactions variable (IntV) for monitoring and control purposes.

Model Predictive Control (MPC) is a control scheme based on the system model, where in each sampling interval, an optimization procedure is performed in order to calculate optimal control action. An attractive attribute of MPC technology is its ability to systematically account for process constraints. [54] proposed a fully decentralized MPC control architecture that uses the ACE signal as an input. This controller satisfies NERC's performance standards CPS1 and CPS2 [62], moreover it reduces generating units wear and tear. Centralized MPC is not well suited for the control of a large-scale, geographically expansive system. However, performance benefits obtained with centralized MPC can be realized through distributed MPC strategies, as described in [63]. The effectiveness of MPC is dependent on a model of acceptable accuracy and the availability of sufficiently fast computational resources. These requirements limit the application

base for MPC.

Most of the AGC scheme mentioned above are based on the linear models which are only valid within specific operating ranges. The nonlinear models of conventional plants (e.g. GDB and GRC), wind power generation and insufficient knowledge about system. The most recent advancement in this area is the application of Artificial Intelligent (AI) algorithm (such as neural networks [64], fuzzy logic [65], [66] and genetic algorithms [67]) to tackle the difficulties [59]. Dealing with complex dynamic systems, such as large-scale power systems, that can be described with the terms uncertainty, non-linearity, information structure constraints, and dimensionality. It is very difficult to satisfy all requirements with an intelligent control system. However, the application of Multi-Agent System (MAS) could be considered as an approach to design an intelligent control system to autonomously achieve a high level of control objectives. The Multi-Agent Reinforcement Learning (MARL)-based AGC design was proposed by [68] and [69]. Another intelligent agent-based control scheme, using Bayesian Network (BN), was addressed to design AGC system in a multi-area power system [58]. The proposed BN-based multi-agent AGC framework includes two agents in each control area to estimate the amount of power imbalance and provide an appropriate control action signal according to the load disturbances and tie-line power changes.

## 2.3 Discussion and conclusion

This chapter presents a review of wind turbine generator technologies and the roles of wind power plants in the modern power system. Among the different ancillary services, the short-term frequency control support and inertia response with their implementations in the wind power control are reviewed.

The control strategies of providing inertial response and primary frequency control from wind power can either be implemented at the local wind turbine control level or the wind power plant control level. From the control point of view, the latter one seems to be the most robust and consistent solution. To perform active power control, the deloading control is proposed, either through pitch angle adjustment or increasing rotor speed. Besides, the other aspects including the overproduction for inertial control, recovery strategy after frequency restoration are reviewed.

The secondary frequency control, also called AGC or LFC, is the centralized automatic control to restore the frequency and power interchanges. Several new AGC algorithms are presented which use LQR, MPC, AI, etc. They can deal

with the uncertainty and variability of wind power more efficiently. For a wind power plant itself, it is also desirable to make the wind power plant operate as a conventional power plant. This object could be achieved by introducing advanced control strategy and external ESS which is described in Chapter 3.

## CHAPTER 3

# Roles of Energy Storage Systems in Modern Power Systems

---

It is a big challenge to operate the power system with high wind power penetration securely and reliably due to the inherent variability and uncertainty of wind power. With the flexible charging-discharging characteristic, Energy Storage System (ESS) is considered as an effective tool to enhance the flexibility and controllability not only of a specific wind power plant, but also of the entire grid.

This chapter reviews the state of the art of ESS technologies for wind power integration support from different aspects. Firstly, modern ESS technologies and their potential applications for wind power integration support are introduced. Secondly, the planning problem in relation to the ESS application for wind power integration is reviewed, including the selection of the ESS type, and the optimal sizing and siting of the ESS. Finally, the proposed operation and control strategies of the ESS for different application purposes in relation to the wind power integration support are summarized.

### 3.1 Energy storage technology

According to energy forms in which electrical energy can be stored, energy storage can be classified into different types, as illustrated in Fig. 3.1. A short description regarding the working principles and potential capability of several commonly applied ESS types for wind power integration support are presented in this following section.

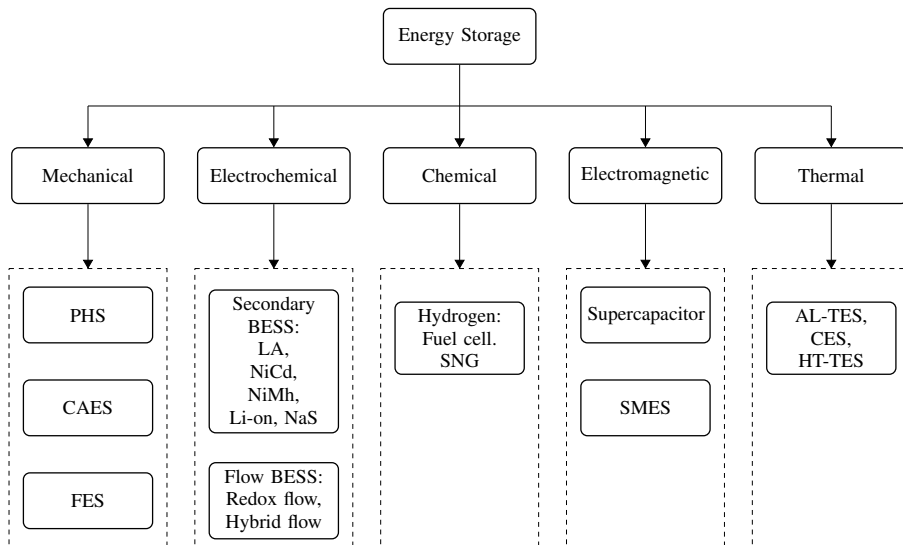


**Figure 3.1:** Energy storage classification

#### 3.1.1 Pumped Hydro Storage (PHS)

As the largest and the most mature energy storage technology available, PHS represents nearly 99% of world-side installed electrical storage capacity, with over 120 GWh [70], [71], [72]. It generally consists of two water reservoirs. The body of water at a relatively high elevation represents potential or stored energy. During off-peak hours, it pumps water from the lower to upper reservoir, considered as the charging process. In the discharging process, water from upper reservoir is released and flows through hydro turbines which are connected to generators, producing electrical energy [73].

The PHS has the largest power and energy rating, long lifetime, high round-trip

efficiency and very small discharge losses. The main applications for PHS with wind power integration are energy management via time-shifting, frequency control and non-spinning reserve supply. The installation of PHS is dependent on geographical conditions and has the impact in the nature environment. Therefore the flexibility of its application is restricted.

### 3.1.2 Compressed Air Energy Storage (CAES)

The CAES is a technology for different industrial applications. By means of electrical compressors, the air is compressed and stored in either an underground structure (salt cavern, abandon mines, rock structures) or an above-ground system of vessels or pipes. If required, the compressed air is released and mixed with natural gas, burned and expanded in a modified gas turbine. Current researches in CAES are focused on the development of systems with fabricated storage tanks which will remove the geological dependency and compressed air will be stored with a higher pressure. So far, there are only two CAES units in operation, which are located in Huntorf, Germany and Alabama, USA [74]. However, there are also several CAES units being planned or under construction [75].

Due to the high power and energy capacity rating, CAES is another choice of wind power plants for energy management purposes. The storage period can be over a year due to very small self-charge losses [76]. Similarly to the PHS, the CAES installation is also limited by topographical conditions.

### 3.1.3 Flywheel Energy Storage (FES)

The first generation of FES has been available since 1970s which uses a large steel rotating body on mechanical bearings. In the FES, the rotational energy is stored in an accelerated rotor, a massive rotating cylinder (comprised of a rim attached to a shaft) in a compartment, the bearings and a shaft. To reduce windage losses, The whole structure is placed in a vacuum enclosure. During the charging process, rotor is accelerated to a very high speed which can reach from 20,000 to over 50,000 rpm. By keeping the rotating body at a constant speed, the energy is stored in the FES. During the discharging process, the FES releases energy and drives the machine as a generator.

The main advantages of the FES are the excellent cycle stability, a long life of providing full charge-discharge cycles, little maintenance cost, high power density and high efficiency. The FES is mainly applied to suppress fast wind

power fluctuation, to provide ride-through interruptions of several seconds or to bridge the shift between two sources [76]. Moreover, it is also designed to provide damping enhancement [77]. The main drawbacks are the short operation duration and high self-discharge losses.

### 3.1.4 Battery Energy Storage System (BESS)

The BESS stores electricity in the form of chemical energy [78]. A general secondary battery consists of a set of low-voltage/power battery cells connected in parallel and series to achieve a desired electrical characteristic. Each cell is made up of a liquid, paste or solid electrolyte together with anode and cathode [76]. A battery is charged by an internal chemical reaction under a potential applied to both electrodes. The reaction is reversible and let the battery deliver the absorbed energy for discharging. Various types of second batteries have been developed for commercial use, including Lead Acid (LA) battery, Nickel Cadmium (NiCd) battery, Nickel Metal Hydride (NiMH) battery, Lithium Ion (Li-ion) battery and Sodium Sulphur (NaS) battery.

As a whole, secondary batteries have the ability to track load changes for system stability enhancement as its response time is very fast (<sec). The self-discharge loss is small and the round-trip efficiency is high. Due to the high power and energy densities, the BESS construction is facilitated by the short lead time, potential convenient sitting and technology modularity [76]. However, the disposal of the toxic materials contained in most batteries leads to ecological problem.

For inter-comparison, the limited number of cycle lifetime restricts the application of LA as large-scale storage devices. The life span of NiCd is seriously dependent on the cycle depth. A deep cycle can reduce lifetime of NiCd battery significantly. Besides, this technology suffers from memory effect [70]. Li-ion has the highest power and energy densities among them. The research related to the Li-ion battery focuses on its application of electrical vehicles. The high capital cost limits its large-scale application for wind power integration support. The NaS battery is an economical solution for power quality improvement and peak-shaving applications. However, its operation temperature is high (300 ~ 340°C) and the stored energy is partly for heating which affects the operation performance. The high cost is another barrier.

The flow battery is another form of battery. The energy is stored in one or more electro-active species which are dissolved in liquid electrolytes [71]. Additional electrolyte is stored externally, generally in tanks and is usually pumped through the cells of the reactor. The energy rating is determined by the quantity of electrolyte whereas the power rating is dependent on active area of the cell

stack [76]. The typical flow batteries are Vanadium Redox Battery (VRB), Polysulphide Bromide (PSB) and Zinc Bromine (ZnBr).

Flow batteries have been installed in MW class and can play more important roles for future large-scale application. In [79], a washout filter-based scheme was adopted to smooth out short-term power fluctuations of a wind power plant with VRBs. The ZnBr battery was used to dispatch the wind power based on the optimal method [80].

### 3.1.5 Superconducting Magnetic Energy Storage (SMES)

The SMES is made up of superconductive coil, power conditioning system, refrigerator and vacuum [70]. The energy is stored in the magnetic field created by DC current circulating through a superconducting coil [71]. In order to avoid the losses by the current flow, the coil should be kept in superconducting state.

The SMES has very rapid response time. The requested power is available almost instantaneously [71]. The SMES is very promising as a power storage system for load leveling or a power stabilizer [81], [82]. The SMES can be incorporated into a back-to-back DC link [82], where the back-to-back system is used as a power conditioning system for the SMES coils. It can also be utilized by cooperation with wind power plant for power quality improvement [81], [83], [84], [85] and dynamic stability enhancement [77], [86]. The drawbacks are that superconductive coil is very sensitive to temperature changes and the operational reliability is crucially dependent on the refrigeration system. Thus, only a few SMES with small capacity are available for commercial application.

### 3.1.6 Super-capacitor (SC)

So far, great progress has been achieved in capacitor storage technologies. Instead of common arrangement of a solid dielectric between the electrodes, an electrolyte solution is placed between two solid conductors for SC. Compared with conventional capacitors, it has much larger capacitance and energy density which enables a compact design [76], [71].

Due to extraordinarily low inner resistance, the SC has almost unlimited cycle stability. as well as extremely high power density and fast charges and discharges. Other advantages include long durability, high reliability, no maintenance, long lifetime, and operation over a wide temperature range and in diverse



environments. They are environmentally friendly and easily recycled or neutralized. The efficiency is typically around 90% and the discharge time is in the range of seconds to hours. Currently, the research for wind power integration support focuses on the power leveling of wind power plants [87], cooperation with batteries for smoothing fast fluctuations [88].

Other ESS technologies, including Fuel Cell (FC), Metal-Air (MA) battery, Solar Fuel, Cryogenic Energy Storage (CES), Synthetic Natural Gas (SNG) and Thermal Energy Storage (TES) are either still under development or technically developed but still not being used. The technical maturity of ESS types is shown in Fig. 3.2.

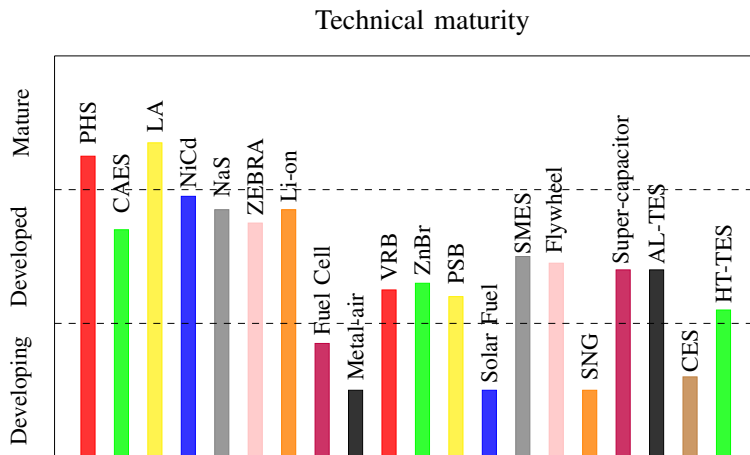


Figure 3.2: Technical maturity of ESS systems [76]

Various characteristics of ESS should be taken into consideration for application, including capital cost, power and energy rating, power and energy density, ramp rate, round-trip efficiency, response time, self-discharge losses, life and cycle time are summarized and listed in Table 3.1 and 3.2, respectively.

Different applications require different technical features of ESS. Among them, energy and power ratings are two main factors. In [71], a comparison of several storage technologies based on these factors are illustrated in a double-logarithmic chart (Fig. 3.3).

**Table 3.1:** Capital cost of ESS

System	Capital cost		
	\$/kW	\$/kWh	\$/kWh-Per cycle
PHS	600~2000	5~100	0.1~1.4
CAES	400~8000	2~50	2~4
FES	250~350	1000~5000	3~25
LA	300~600	200~400	20~100
NiCd	500~1500	800~1500	20~100
Li-ion	1200~4000	600~2500	15~100
NaS	1000~3000	300~500	8~20
VRB	600~1500	150~1000	5~80
ZnBr	700~2500	150~1000	5~80
FC	10000+	—	6000~20000
SC	100~300	300~2000	2~20
SMES	200~300	1000~10000	—

**Table 3.2:** Technical features of ESS

System	Rating		Density		Response time	Efficiency [%]	Self-discharge per day [%]	Lifetime	
	Power rating [MW]	Discharge time typical	Power density [W/l]	Energy density [Wh/l]				in [years]	in [cycles]
PHS	100~5000	1~24 h+	0.1~0.2	0.2~2	min	70~80	Very small	> 50	>15000
CAES	5~300	1~24 h+	0.2~0.6	2~6	min	41~75	Small	> 25	>10000
FES	0~0.25	sec~hours	5000	20~80	<sec	80~90	100	15~20	10 <sup>1</sup> ~ 10 <sup>7</sup>
LA	0~20	sec~hours	90~700	50~80	<sec	75~90	0.1~0.3	3~15	250~1500
NiCd	0~40	sec~hours	75~700	15~80	<sec	60~80	0.2~0.6	5~20	1500~3000
Li-on	0~0.1	min~hours	1300~10000	200~400	<sec	65~75	0.1~0.3	5~100	600~1200
NaS	0.05~8	sec~hours	120~160	15~300	<sec	70~85	~20	10~15	2500~4500
VRB	0.03~3	sec~10 h	0.5~2	20~70	sec	60~75	Small	5~20	>10000
ZnBr	0.05~2	sec~10 h	1~25	65	sec	65~75	Small	5~10	1000~3650
FC	0~50	sec~24 h+	0.2~20	600 (200bar)	sec~min	34~44	0	10~30	10 <sup>3</sup> ~ 10 <sup>4</sup>
SC	0~0.3	ms~1 h	40000~120000	10~20	<sec	85~98	20~40	4~12	10 <sup>1</sup> ~ 10 <sup>5</sup>
SMES	0.1~10	ms~8 s	2600	6	<sec	75~80	10~15	—	—

## 3.2 Generation-side roles of ESS

The ESS applications related to wind power integration can be summarized and categorized in terms of roles that plays for different stakeholders: the wind power plant owner, the grid operator and the energy consumer.

The generator-side role of the ESS aims to improve the grid-friendliness of wind

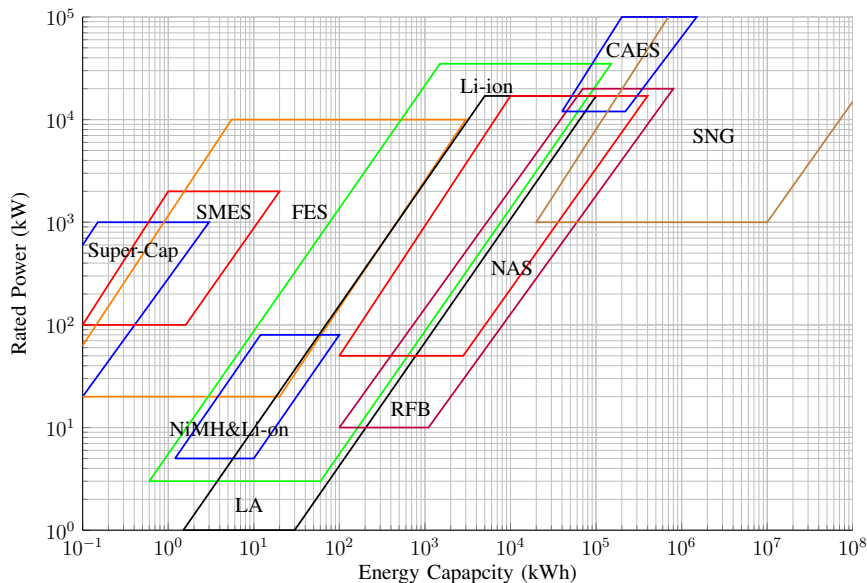


**Figure 3.3:** Comparison of rated power energy content of different ESS technologies

power plant to dispatch wind energy so that they can be controlled like conventional generator, e.g. thermal or hydro power plant. Besides, it shall be controlled to effectively utilize limited transmission capacity.

### 3.2.1 Time shifting

Due to the stochastic characteristic of wind, wind power production demonstrates an anti-peak feature, e.g. high wind power during off-peak demand or low wind power during peak demand. The time shifting is to store extra wind energy during periods of low demand and stands ready to dispatch energy to the grid during periods of high demand. The benefit of storing electricity is expected to be larger with the large gap of demand between peak and off-peak. To satisfy the time shifting function, large quantities of energy for significant periods of time (from hours to days) are required for the ESS facility. Besides, the storage efficiency is another key factor to be considered for the economical operation of time shifting, as significant losses occur for an inefficient storage system.

### 3.2.2 Output smoothing

The inherently variable nature of wind power leads to the fluctuations in frequency and voltage [8]. The ESS can be used to smooth out these fluctuations to keep system stable. Accordingly, the output power of ESS needs to be rapidly regulated for absorbing the excess energy during output spikes and releasing energy during output drop. The ramping capability is very important for the smoothing function. The output smoothing at the plant level reduces the need for power quality and ancillary services at the system level [89].

### 3.2.3 Transmission utilization efficiency

Rich wind resources are often located in rural areas far from existing high capacity transmission lines [90]. Due to transmission constraints, the produced energy may not be transferred to load. Addition ESS can reduce transmission congestion, defer or avoid transmission and distribution upgrades.

## 3.3 Grid-side roles of ESS

Nowadays, the ESS is also required by the grid operator to provide ancillary services to mitigate variability and uncertainty of the entire grid, rather than specific loads or wind power plants. These applications are listed in Table 3.3. Due to the geographical distribution of wind resources, the net variability and uncertainty are less. Accordingly, the need for service overall is reduced [8].

### 3.3.1 Energy arbitrage/Load leveling

In the power market, the electricity price varies from time to time, normally hourly [73]. ESS can be used to store low-cost off-peak energy and releases when the price is higher. It can reduce market risk exposure to volatile on-peak prices and manage high cost energy imbalance charges [91].

**Table 3.3:** Grid-side roles of ESS

Application	Time scales	Example of ESS
Energy Arbitrage, Load leveling	Hours to days	PHS, NaS, CAES,VRB
Frequency regulation	seconds to minutes	Li-ion, NaS, FES, VRB
Inertia emulation, Oscillation damping, Voltage support LVRT	<1 sec	LA, NAS, FES, VRB
Primary reserves	~10 min	PHS, FES, BES
Secondary reserves	Minutes to hours	PHS
Efficiency use of transmission network	Minutes to hours	Li-ion
Emergency power supply, Black start	Minutes to hours	LA

### 3.3.2 Frequency regulation

Modern wind power plants are required to provide frequency regulation by the grid operator. With the high wind penetration level, providing frequency response from a wind power plant is technically feasible by utilizing additional droop control. However, when using a WTG for primary control, it is required to keep a power reserve and not all the available energy can be fed into the grid. It leads to a considerably amount of energy loss. Besides, it may cause fatigue of wind turbines and instability problem [92], [93]. Another effective solution is the use of ESS. For the primary frequency control, a local droop control loop can be added to the active power controller of the ESS. For secondary frequency control, the active power command is generated by AGC.

### 3.3.3 Inertia emulation

The grid inertia reduces frequency variability and makes the grid less sensitive to sudden generation changes. The instantaneous inertial response determines ROCOF [7]. Since modern wind turbines (such as DFIGs and PMSGs) are partly or fully decoupled from grid, the contribution to the power system apparent inertia is restricted. Additional ESS can significantly increase apparent inertia of grid which improve the frequency stability. The supplementary loop can be added into the active power control of ESS.

### 3.3.4 Oscillation damping

In an interconnected system, sudden changes of power in tie-line might cause oscillations with frequency range between 0.5 and 1 Hz [73]. It may further result in a synchronism loss of several machines. Application of a damping controller is an effective control scheme to simultaneously solve the inherent power fluctuations and enhance system stability for a large wind power plant [83]. SMES and FES were utilized in [86] and [77] to damp the system oscillation. The tie-line power deviation was used as a feedback signal to generate the phase component for the converter control.

### 3.3.5 Voltage control support

The wind power variability can degrade grid voltage stability [80]. The installed ESS can provide adequate reactive power to maintain the local voltage level. This service can be obtained by the converter of ESS connected to the grid [94].

### 3.3.6 Reserve application

Since there exists error in the wind power forecasting, additional reserves are needed for emergency support. Based on the response time, reserve can be generally classified into primary, secondary and tertiary reserves [73]. According to the power and energy densities, the corresponding ESS types can be utilized as the operation reserves.

### 3.3.7 Emergency power supply/Black start

The ESS can be used to restart from shut-down condition without the assistance from the electrical grid and energize the power system in the event of a catastrophic failure [8], [73].

### 3.3.8 Transmission utilization efficiency

The ESS can help grid operators efficiently use the transmission system capacity, defer transmission system upgrades in order to reduce transmission costs and mitigate local dependency challenges of wind power.

### 3.4 Demand-side roles of ESS

So far, most existing ESS applications for energy consumer are related more to the energy requirement than solving particular challenges related to the integration of large-scale RES [95]. One application that significantly assists the wind integration is Vehicle-To-Grid (V2G) [8], [96].

Due to the aggregation effect of many Electrical Vehicles (EVs) plugged into the grid, these EVs can be regarded as a Virtual Power Plant (VPP) with relative large capacity. This EV VPP (EVPP) has to fulfill the requirements of both vehicle owners and grid operators. Since all the EVs are controlled as a whole, individual vehicle will not be locked in the charging station and its owner has the full convenience. The grid operator can treat this VPP as a conventional provider of ancillary services [97], such as time-shifting, operation reserve, frequency regulation and etc.

Currently, many efforts have been made to investigate the EVPP feasibility and possible architecture [98]. One finished project is the EDISON project financed by the Danish TSO—Energienet DK. The Danish island, Bornholm was used as a test site. This project aims to coordinate charging and discharging of EVs so as to optimize the utilization of wind energy in the island grid.

Since the ESS is a costly solution, it is not economically viable for the ESS to work for single application service. In [48], the installed ESS was mainly used for the output smoothing. It can also contribute to system wide controls such as frequency regulation or oscillation damping. In [92], the applied BESS had the ability to provide both frequency response service and energy time-shifting.

### 3.5 ESS type selection

The power fluctuation density caused by wind power integration at different time scales is a key factor for ESS selection to satisfy specific application purpose. Low frequency fluctuation, ranged from minutes to hours, is related to generation reserve and the energy dispatch of power system, while high frequency fluctuation, ranged from seconds to minutes, affects power system frequency control [99]. Based on the local wind data, the corresponding Power Spectrum Density (PSD) can be derived [100]. According to the PSD analysis, some technical requirements of the ESS can be determined, including charging-discharging cycle, power and energy density classes. It is observed that the dominant power components concentrate over the low-frequency band, especially in the dc and

day cycle [101]. Although this observation is obtained from the local data, it has implication. Similar results are derived in [76]. The high frequency fluctuations (above 1 Hz) are insignificant due to the absorption by the turbine generator inertia [102].

In [103], the PSD derived from wind speed measurements from Changi, Singapore, was analyzed. For maximizing the energy capture, the low frequency band was taken into account. The selected storage medium was required to have the capability to fully charge–discharge in hours and have high specific density. Combined with other technical and economical consideration, the NaS was selected for the daily dispatch purpose.

The rated capacity of modern wind power plant can reach to several hundreds MWs. For the energy management purpose, large-scale storage medium should be applied, such as BESS, PHS and CAES [104]. Since PHS and CAES are limited by topographical constraints, the BESS is considered a more competitive option for large-scale ESS application due to high power and energy density, scalability, fast response time, simple maintenance requirement and high cycle life for both technical and economical consideration [103], [105].

For the power quality improvement purpose, the high frequency band of the PSD should be studied. The response time and ramp rate capability are the main concerns for this purpose. The storage mediums with fast response and small energy capacity, such as FES, super-capacitor, SMES, are potential options.

Since no single storage technology can provide the benefits of both high power density and energy density, a hybrid ESS with the combination of multilevel storage devices can be used to deliver desired power time series [106]. The high energy density storage medium, normally BESS, is adopted for low frequency fluctuation mitigation [107], [88], [108], and the high power density store medium which can be SC([88]), SMES([108]), FES ([107]), are used for smoothing high-frequency fluctuations.

## 3.6 Operation and control of ESS

### 3.6.1 Operation of ESS for wind power dispatch

A properly designed ESS is proved to bring additional economic benefit. If wind power output can be scheduled in a manner similar to that of a conventional power plant, the prospect of wind power will be much improved as optimal



economic dispatch can then be achieved [101].

The operation modes for wind power plant utilized with the ESS participating in modern power market are described in [109], [103] and [101]. Wind power for next few hours are estimated based on wind speed forecast. The power dispatch schedule for wind power plant has to be submitted in advance to the grid operator. The grid operator adjusts the system operating state leading to economic dispatch and power flow regulation. The schedule beyond the certain hours would be allowed to be adjusted to compensate the forecast errors. Once the output power of wind power plant differs from the schedule submitted, the wind power plant operator will be financially punished. Therefore, a lot of researches concentrate on the daily optimal scheduling scheme design for wind power plants by taking advantage of flexible charging-discharging ability of ESS.

In [110], the expected dispatch power was estimated based on the hourly average forecast wind power without consideration of economic benefit. In [111] and [112], the generation scheduling was based on the forecast of electricity price, load and wind generation. It aims to maximize the expected profit from participating in a day ahead power market. In [113], wind power plant operator was assumed to participant in Nord Pool market. The wind forecasting error was regarded as stochastic variable. The ESS was adjusted hourly based on stochastic programming, seeking for the maximum benefits of wind power plant and the ESS. [111] introduced a dynamic algorithm applied for daily scheduling in a power market. The objective of the online operation strategy was to follow a given generation schedule as close as possible. A statistical approach was proposed in [101] to determine output power of hybrid wind-BESS system. The developed new dispatch strategy ensures the BESS go through full charge-discharge cycle to maximize the lifetime worth of BESS. [114] proposed an hourly discretized optimization algorithm to identify the optimum daily operation strategy to be followed by the wind turbines and PHS, assuming that a wind-power is perfectly forecasted.

The aforementioned are the use of single-unit ESS. In [115], a dual BESS (one in service and one in standby) which allows more flexibility in terms of the design of the dispatch pattern was proposed. The dispatched power from WTG-BESS power station can be treated as a firm commitment. It can be determined based on the long-term historical wind power data, the likelihood of success of the power delivery and BESS capacity. With a similar dual-ESS configuration, [103] developed an optimum switch-over dispatch scheme for dual-BESS, by considering wind speed forecast and charging-discharging characteristics of installed BESS. The primary operation objective of WTG-BESS scheme was to harness the energy available in the wind as much as possible.

### 3.6.2 Operation of ESS for fluctuation mitigation

Wind power filtering algorithms are widely applied by means of fast and short-term ESS to mitigate the output fluctuation of wind power plant. The block diagram of a simplified model for filtering control of hybrid WPP-ESS is shown in Fig. 3.4. Through the Low-Pass Filter (LPF) with time constant  $T_f$ , the high-frequency part  $P_{\text{out}}^{\text{exp}}$  is filtered as charging or discharging command of ESS. Since the ESS inevitably accompanies a control lag, losses and an output limiter, an actual output doesn't match the target output. However, due to its simplicity and fast computation speed, it is easy to be implemented and suitable for the application in real-time operation.

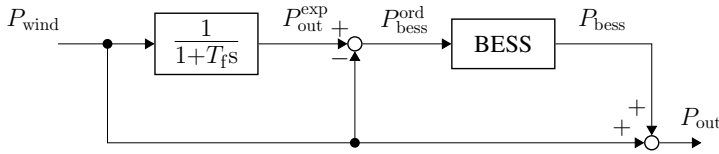


**Figure 3.4:** Principle of using LPF algorithm for power fluctuation mitigation

As proposed in [79] and [99], the power output reference of the ESS  $P_{\text{bess}}^{\text{ord}}$  is determined by,

$$P_{\text{bess}}^{\text{ord}} = \frac{-sT_f}{1 + sT_f} P_{\text{wind}}. \quad (3.1)$$

The Remaining Energy Level (REL) of ESS can be calculated as,

$$\text{REL} = \frac{P_{\text{bess}}^{\text{ord}}}{s} = \frac{T_f}{1 + sT_f} P_{\text{wind}}. \quad (3.2)$$

Eqn. 3.2 shows that a larger time constant  $T_f$  has higher smoothing effect but also results in a larger ESS power and capacity. It is very important to select proper  $T_f$  for the controller design. Normally,  $T_f$  is decided by local wind profile and the ESS capacity, and is kept constant during operation [79], [48], [102], [116]. [99] proposed a flexible LPF with an optimization of  $T_f$ .  $T_f$  is regulated based on Particle Swarm Optimization (PSO) algorithm in real-time. The maximum fluctuation of combined power in any 1 min and 30 min time window is kept within predefined constraints.

With large output variation of wind power plant, it is easy to reach capacity limits of ESS by the mere smoothing method without consideration of charging

level. Therefore, State Of Charge (SOC) is introduced as feed-back signal to keep the charging level within its proper range [79], [99]. In [102] additional coefficient  $k$  was introduced to protect ESS from over-limiting, as shown in the following equation.  $k$  was changed according to the predefined curve based on SOC.

$$P_{\text{bess}}^{\text{ord}} = k \frac{-sT_f}{1 + sT_f} P_{\text{wind}}. \quad (3.3)$$

Due to the measurement delay, phase of measured power signal is shifted. To compensate this lag, an additional lead-lag compensator was introduced for LPF in [48].

### 3.6.3 Operation of hybrid ESS

The previous subsections describe the operation of single type ESS. Since single type storage technology can hardly meet the requirement of both fast response and large energy capacity [8], the logical solution is a hybrid ESS system, which combines multiple storage devices into several levels that can be used to deliver required power. In [106], a knowledge-based Artificial Neural Network (ANN) control with washout-filter was used for two-level storage for wind power dispatch.

For the grid with many installed ESSs dispersed in large area, the integration of these ESSs will have much more capability compared with the individual ESS. By gathered into a virtual assembly and controlled centrally, they can be used for many utility applications, such as frequency regulation, load leveling and control of transmission power flow. A concrete example of an implementation based on aggregated energy storage systems using BESS is proposed in Japan, called Battery SCADA [71]. Demonstration of this technology has been started in 2012 in Yokohama, Japan.

## 3.7 Discussion and conclusion

The ESS is considered as an effective solution to handle the reliability and stability challenges of future power systems with large scale wind power integration. Various ESSs with different technical features are available in the market.

The ESS can be used for different applications required by specific wind power plants, grid operators or consumers. For the generation-side, it can aim to

---

improve the grid-friendliness of wind power plants to dispatch wind energy such that they could be controlled like conventional power plants. For the grid-side roles of the ESS, it can provide ancillary services to mitigate variability and uncertainty of the entire grid. For the demand-side roles, the aggregated EVPP can fulfill the requirements of both vehicle owners and grid operators.

The recent research of the ESS operation and control focuses on the daily dispatch scheme of the ESS with wind power plants and fluctuation mitigation. Different factors, including wind power forecast error, technical constraints, market rules, and energy price, are taken into consideration to determine the optimal operation strategy for single or multiple ESSs. For the output smoothing purpose, the high frequency component is filtered and compensated by the ESS. The time constant is the key factor to strike a balance among the smoothing effect, the required ESS power and capacity rating.



## CHAPTER 4

# Implementation and Validation of Generic Wind Turbine Model (Type 1)

---

In this chapter, the implementation of International Electrotechnical Commission (IEC) generic Type 1 WTG model in DIgSILENT/Power Factory (PF) and the validation of the implemented model against field measurements are presented. The model topology, details of the blocks of the model and how to implement them in PF are described. Both normal and fault conditions have been conducted with the implemented IEC Type 1 WTG model. The dynamic responses were captured and analyzed. Based on the simulation results, the EMT and RMS models were compared and evaluated.

To validate the implemented model, the model to field measurement validation method is employed. The “play-back” approach and the measurement data from Siemens Wind Power are used. The results show that there is a good agreement between the simulation results and the measurements. The errors between the simulation results and measurements are calculated according to the voltage dip windows and the index definition specified in the IEC 61400-27-1 committee draft.

## 4.1 Background and basic knowledge

According to the classification of wind turbine generators in Chapter 2, the Wind Generation Modeling Group (WGMG) of the Western Electricity Coordinating Council (WECC) and the IEEE Working Group on Dynamic Performance of Wind Power Generation (DPWG) have developed the generic WTG models. The joint report describing the current version of generic models was published in [117]. The WECC generic models were developed by simplifying a detailed transient stability model. Instead of addressing electromagnetic transients, the generic positive sequence models are of main concern. These models have been released in the latest versions of two commercial software packages GE PSLF and Siemens PTI PSS/E.

International Electrotechnical Commission (IEC) started the standardization work—IEC 61400-27 to define standard, public dynamic simulation models for wind turbines and wind power plants. It consists of both modeling and validation subgroups. The working group “WG27” held the first meeting in October 2009 [118]. The committee draft specifying wind turbine models and validation procedures has been finished at the end of 2011. These models aim to be applicable for dynamic simulations of power system events such as short circuits (low voltage ride through), loss of generation or loads, and typical switching events [118].

Although the modeling part of the IEC standard draft has a substantial overlap with WECC WGMG, it considers the inputs from other sources including the publications from European researchers and vendors. The aim is that the generic models should have a reasonable coverage of the actual wind turbines.

DIgSILENT PowerFactory (PF) is a widely used commercial power system analysis software, especially in Europe. The customers cover Transmission System Operators (TSOs), universities and research institutes. It is necessary to implement IEC generic WTG models in PF to serve the needs of both industry and academia.

## 4.2 Model description

The configuration of Type 1 WTG has been described in Chapter 2 and not repeated. One thing to be noticed is that the blade pitch angles of the Type 1 WTG can either be fixed or controllable. The latter one is used for Fault-Ride Through (FRT) control. In the initial IEC committee draft, Type 1 WTGs are

accordingly divided into two subgroups:

- Type 1A: without FRT control.
- Type 1B: with blade angle FRT control.

The Type 1B model is removed from the newly modified IEC committee draft. However, it is also studied in this thesis.

### 4.2.1 Structure of generic Type 1A WTG model

The structure of the generic Type 1A WTG model is illustrated in Fig. 4.1, which is comprised of aerodynamic, mechanical, generator system, electrical equipment and grid protection blocks.

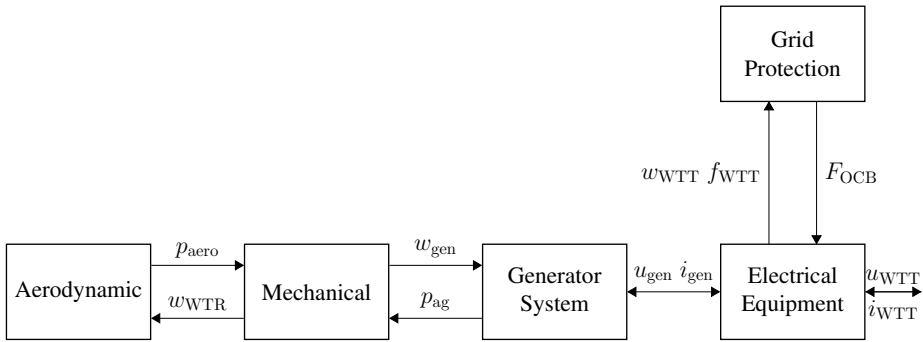


**Figure 4.1:** Runtime WTG model structure of Type 1A

#### 4.2.1.1 Aerodynamic block

The aerodynamic torque is considered to be constant during the short time period. Therefore, constant aerodynamic torque model is used instead of pseudo governor model described in [117]. The model parameters are given in Table 4.1 and the runtime block diagram is given in Fig. 4.2.



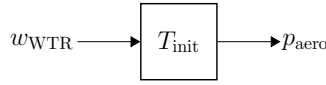


**Figure 4.2:** Block diagram for constant aerodynamic torque model

**Table 4.1:** Parameter For Constant Aerodynamic Torque Model

Symbol	Unit	Description	Source
$T_{init}$	p.u.	Initial steady state torque	Initialization

#### 4.2.1.2 Mechanical block

The mechanical part is implemented by a two-mass model which represents the low-speed turbine rotor and the high-speed generator, respectively. The connecting resilient shaft is modeled as a spring and a damper. The block diagram of IEC standard model is shown in Fig. 4.3. The parameters of the two-mass block are listed in Table 4.2.

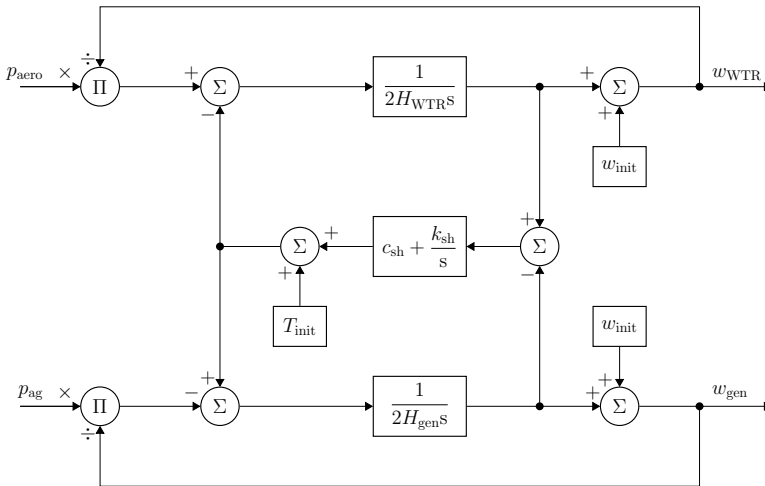


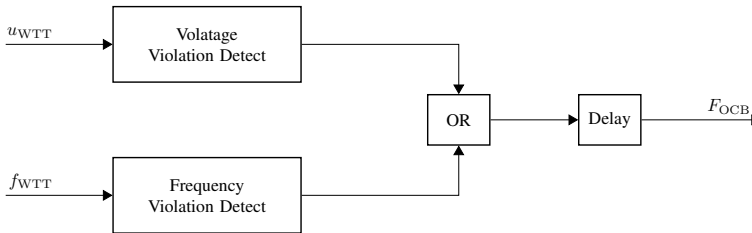
**Figure 4.3:** Block diagram for two-mass model in IEC standard

**Table 4.2:** Parameter For Two-Mass Model

Symbol	Unit	Description	Source
$H_{WTR}$	p.u.	Inertia constant of wind turbine rotor	Manufacturer
$H_{gen}$	p.u.	Inertia constant of generator	Manufacturer
$k_{sh}$	p.u.	Shaft stiffness	Manufacturer
$c_{sh}$	p.u.	Shaft damping	Manufacturer
$w_{init}$	p.u.	Initial steady state shaft rotor speed	Initialization
$T_{init}$	p.u.	Initial steady state shaft torque	Initialization

### 4.2.1.3 Grid protection

The existing implementation of WECC generic WTG models doesn't have protection modules [117]. According to [19] and [119], the protection levels and disconnection time should be determined based on the measured voltage and frequency of WTT. Once voltage or frequency violates the range constraint and this violation lasts more than disconnection time  $t_{disc}$ , grid protection will work and disconnect WTG through CB, as depicted in Fig. 4.4. The parameters are listed in Table 4.3.

**Figure 4.4:** Block diagram for grid protection model**Table 4.3:** Parameter For Grid Protection Model

Symbol	Unit	Description	Source
$u_{over}$	p.u.	Wind turbine over voltage protection setting	Manufacturer
$u_{under}$	p.u.	Wind turbine under voltage protection setting	Manufacturer
$f_{over}$	p.u.	Wind turbine over frequency setting	Manufacturer
$f_{under}$	p.u.	Wind turbine under frequency setting	Manufacturer
$t_{disc}$	sec	Delay time for opening the circuit breaker	Manufacturer

#### 4.2.1.4 Generator System

The standard induction generator model in the simulation tools is used to represent the generator system. In PF, different detailed levels of induction generator model are used according to the simulation types—Root Mean Square (RMS) and Electro-Magnetic Transient (EMT). In RMS simulation, simplified electromechanical transient model is adopted where the stator transients are neglected [120]. In EMT simulation, the detailed electromagnetic transient model is adopted [121].

### 4.2.2 Structure of generic Type 1B WTG model

The structure of the generic Type 1B WTG model is shown in Fig. 4.5. Compared with the Type 1A model, Type 1B model has no independent aerodynamic block. Instead, the aerodynamic power is generated by blade angle FRT control model shown in Fig. 4.6. A similar model is used by WECC WTG model (pseudo governor model) which was designed and developed following a thorough investigation of aerodynamic characteristics and pitch control of several vendor detail WTG models [117]. Moreover, the IEC model takes the FRT into consideration.

In normal operation, the controller regulates the output power  $p_{\text{aero}}$  following the power reference  $p_{\text{WTref}}$ . When the fault happens, it can be detected by comparing the filtered wind turbine terminal voltage  $u_{\text{WT}}$  and voltage threshold  $u_{\text{dip}}$ . The operation is changed into FRT mode. Then the controller adjusts the blade angle to constraint  $p_{\text{aero}}$  by Proportional-Integral controller. Because of the limitation of the blade angle adjustment, there are maximum and minimum values of the output:  $p_{\text{Amax}}$  and  $p_{\text{Amin}}$ . The ramping rate is also constrained within the range  $[dp_{\text{Amin}}, dp_{\text{Amax}}]$ . The wind turbine is still kept in connection with the grid. The parameters of the blade angle FRT control are listed in Table 4.4.

## 4.3 Implementation

### 4.3.1 Modification of IEC model in PF

According to the IEC committee draft, the built-in induction generator model in simulation software is assumed to exclude its inertia equation. Actually in

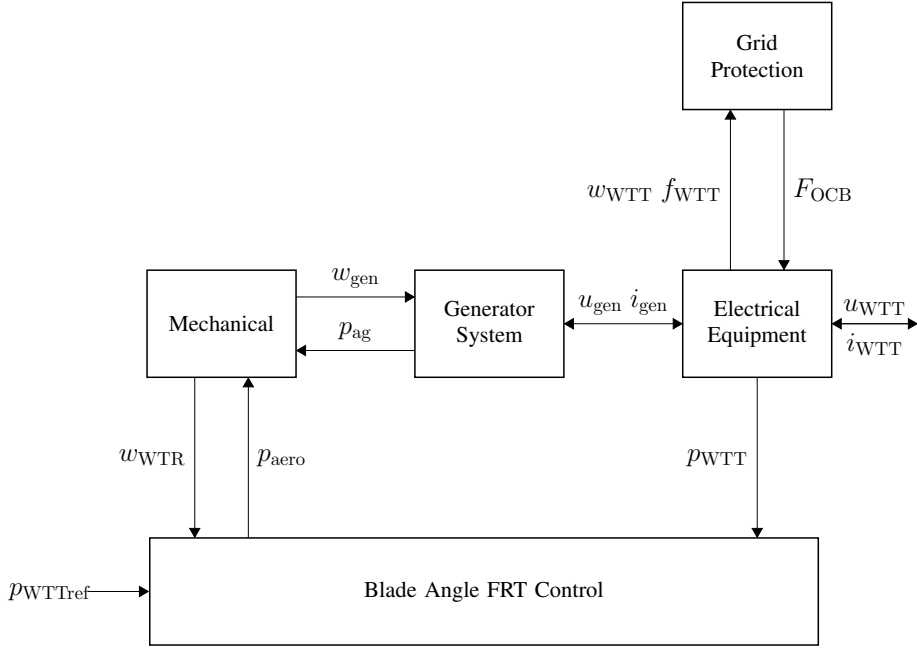


**Figure 4.5:** Runtime wind turbine model structure of Type 1B

**Table 4.4:** Parameter For Blade Angle FRT Control Model

Symbol	Unit	Description	Source
$T_{P\text{filt}}$	p.u.	Filter time constant for power measurement	Manufacturer
$T_{U\text{filt}}$	p.u.	Filter time constant for voltage measurement	Manufacturer
$u_{\text{dip}}$	p.u.	Voltage threshold for LVRT detection	Manufacturer
$p_{A\text{max}}$	p.u.	Maximum power allowed by LVRT control	Manufacturer
$p_{A\text{min}}$	p.u.	Minimum power allowed by LVRT control	Manufacturer
$p_{\text{LVRTref}}$	p.u.	Power reference during LVRT	Manufacturer
$dp_{A\text{max}}$	p.u.	Maximum power ramp rate during LVRT	Manufacturer
$dp_{A\text{min}}$	p.u.	Minimum power ramp rate during LVRT	Manufacturer
$K_{p\text{gov}}$	p.u.	Pseudo governor proportional constant	Manufacturer
$K_{i\text{gov}}$	p.u.	Pseudo governor integral constant	Manufacturer

PF, the inertia part is integrated in the induction generator. Moreover, instead of generator rotation speed  $\omega_{\text{gen}}$ , the mechanical power is the input. Therefore, a modified mechanical block diagram and runtime diagram are shown in Fig.

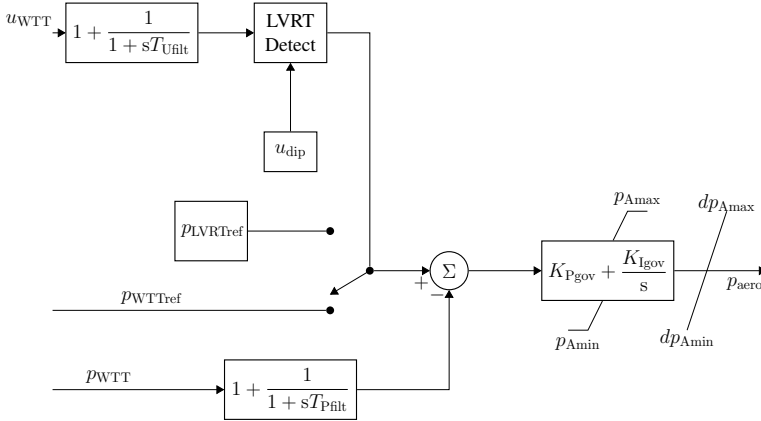


Figure 4.6: Block diagram for blade angle FRT control model

4.7 and Fig. 4.8, respectively.

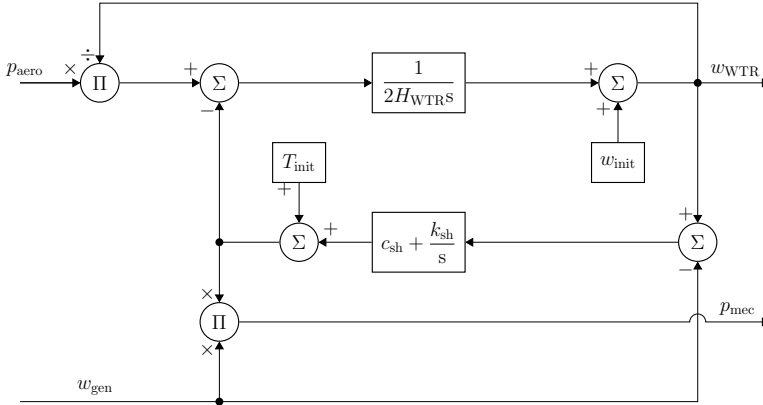


Figure 4.7: Modified block diagram in PF and RTDS

This modification doesn't cause any difference of the simulation results, as there are still two masses as a whole. Compared with one-mass lumped model, the interaction between the two masses will result in the torsional oscillation and has a significant impact on the dynamic behavior of WTG. The torsional oscillation is typically between 0.2 to 4 Hz. This dynamic response is presented in the simulation part. The nature frequencies can be calculated in [122].

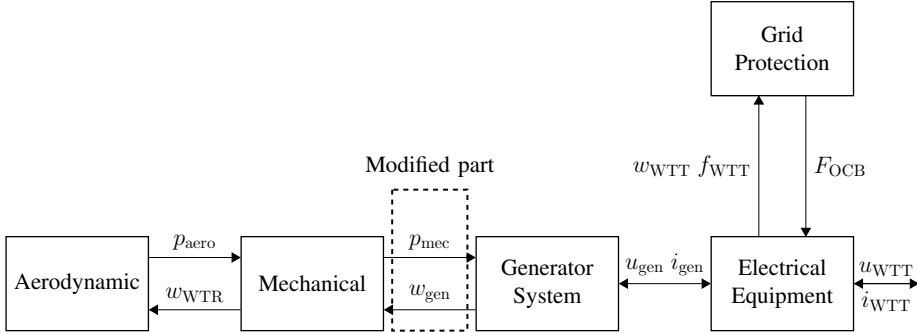


Figure 4.8: Modified runtime wind turbine model structure of Type 1A

### 4.3.2 Initialization

Initialization of electrical devices and control system is very important for the power system simulation. Correct initialization avoids the fictitious electrical transients and makes it possible to evaluate correctly the real dynamic performance of the system [123]. If the initialization is not done properly, the state variables do not stay at the value at which they were initialized, but start changing at the start of the dynamic simulation. In this case, it may take time to reach a steady state, and even numerical instability. In PF, the initialization is executed in the following two steps:

- Step 1: Initialization of the built-in electrical models through load flow calculation. These models include induction generator and other electrical equipments. PF has alternative RX model (slip iteration) which is based on the equivalent circuit. It is more precise method of representing induction machine and suitable for initializing a transient analysis [121]. The comparison of the performances with PQ model and RX model is depicted in Fig. 4.9. Obviously, with RX model, the system gets into the steady state in a faster manner.
- Step 2: Initialization of control blocks: aerodynamic model, mechanical model and blade angle FRT control model.

## 4.4 Simulation and results

The test system from [124] was used to carry out case studies. The single line diagram of the test system is shown in Fig. 4.10. The test system is comprised

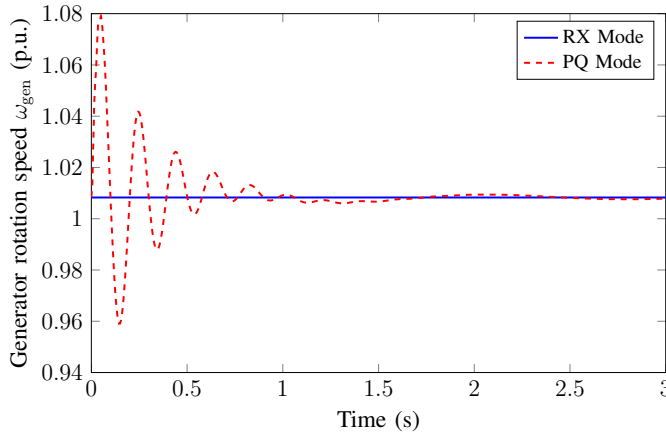


**Figure 4.9:** Initialization with different induction models

of an external grid using a Thevenin equivalent model, two step-up transformers TR1 and TR2, the collection cable, circuit breaker CB, reactive power compensation and wind turbine generator WTG. This test system represents a reduced wind power installation and is used for both Type 1A and Type 1B. The parameters of the electrical components are listed in Appendix A.1.

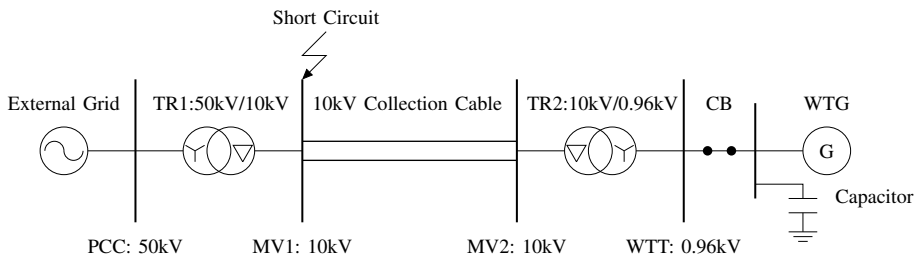


**Figure 4.10:** Single line diagram of test case

#### 4.4.1 Normal operation

For Type 1A, the blade angle is fixed. The output active power  $p_{WTT}$  can only be affected by the aerodynamic torque  $T_{init}$ .  $T_{init}$  can be specified as a linear piece-wise function to simulate the wind variation. The simulation settings are listed in Table 4.5.

**Table 4.5:** Case Study Scenarios

Study Scenario	Event	
Normal operation	Wind variation	
	Simulation time	50 s
	For Type 1A, aerodynamic torque $T_{\text{init}}$ is specified as piece-wise function.	0 ~ 10 s $T_{\text{init}} = 1.0836$ .
		10 ~ 25 s, $T_{\text{init}} = 0.9$ .
		25 ~ 50 s, $T_{\text{init}} = 1.1$ .
	For Type 1B, reference $p_{\text{WTTref}}$ is specified as piece-wise function.	0 ~ 10 s, $p_{\text{WTTref}} = 0.8894$ .
		10 ~ 25 s, $p_{\text{WTTref}} = 0.8$ .
		0 ~ 10 s, $p_{\text{WTTref}} = 1$ .
	Fault condition	3-phase short circuit on terminal MV
Simulation time		20 s
Low frequency oscillation (Type 1A,B).		The short circuit is at 5 s, cleared at 5.1 s.
FRT control (Type 1B).		

For Type 1B, the blade angle is controllable. The active power  $p_{\text{WTT}}$  can be regulated by reference  $p_{\text{WTTref}}$  through adjusting the blade angle. During the normal operation, this reference value can be specified as a linear piece-wise function to emulate the wind variation or the power reference change. The simulation settings are listed in 4.5.

The simulation results of both Type 1A and Type 1B are illustrated in Fig. 4.11 and 4.12, respectively. The figures show first of all a very close agreement between PF RMS and PF EMT results. The waveforms of  $p_{\text{WTT}}$  and  $\omega_{\text{gen}}$  follow the wind variation. Due to the direct coupling between  $\omega_{\text{gen}}$  and system frequency, the normal slip is small whose range is between 1% and 1.3%. According to [125], there is a unique relation between active power, reactive power, terminal voltage and rotor speed. An increasing of the active power production will also cause the increasing reactive power consumption which leads to a relative low full-load power factor (about 0.8 in this case based on subplots (b) and (c)). In order to limit the reactive power absorption from the grid, the WTG is often equipped with capacitor banks [20]. Most reactive power required by induction generator was provided by the capacitor bank and



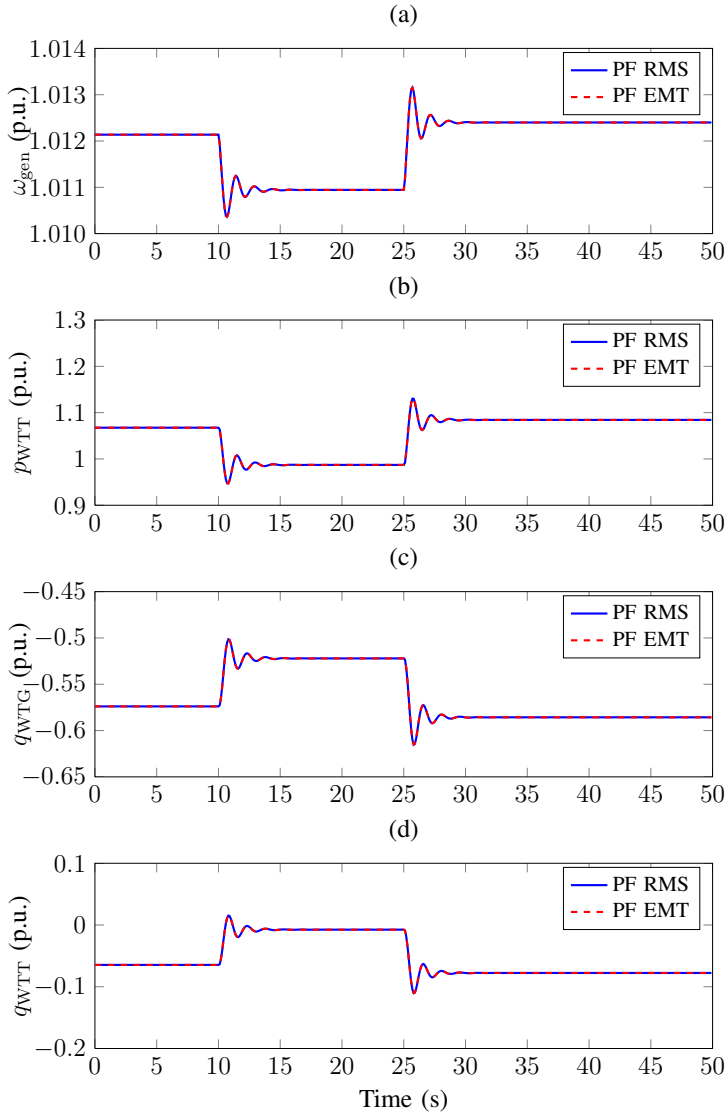
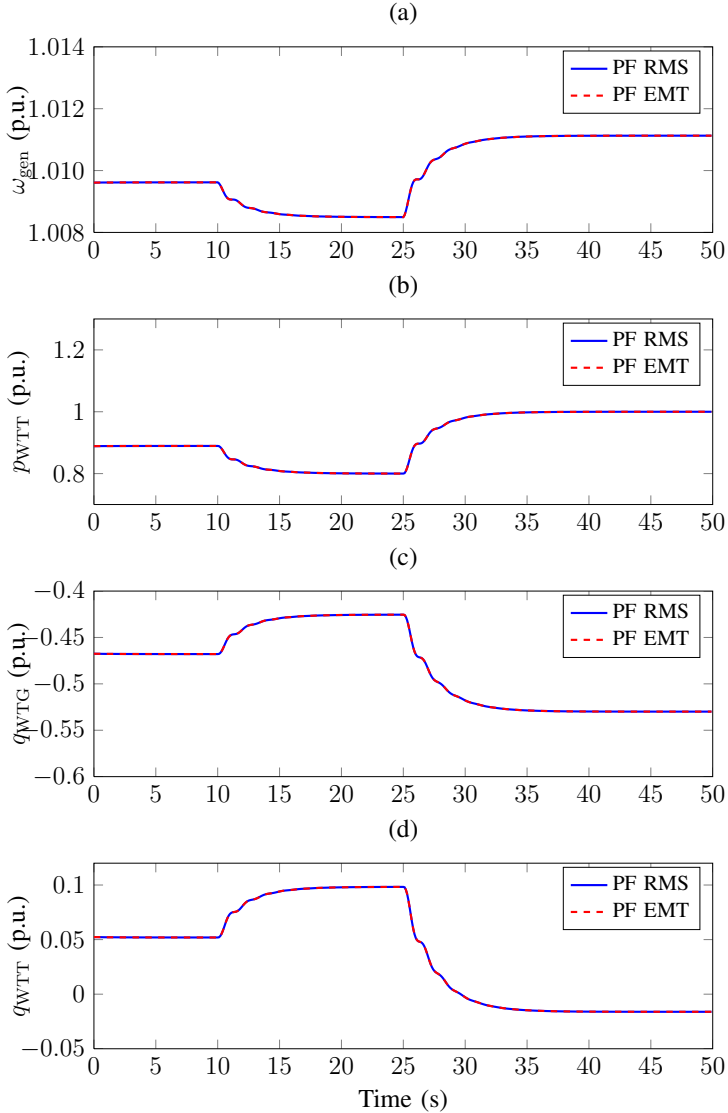


Figure 4.11: Simulation results in normal operation (Type 1A)

the power factor at WTT is almost 1 (according to subplots (b) and (d)).



**Figure 4.12:** Simulation results in normal operation (Type 1B)

#### 4.4.2 Fault condition

The three-phase short circuit event is used to represent the fault condition. During the short circuit, the dynamic responses of the models were captured

and tested. Two typical responses: low frequency oscillations (both Type 1A and Type 1B) and pitch regulation (FRT control of Type 1B) were described and analyzed. The simulation settings are listed in Table 4.5.

#### 4.4.2.1 Low frequency oscillation of the two-mass model

The torsional oscillations between different sections of the turbine-generator rotor are observed due to the perturbation in the short circuit, as illustrated in Fig. 4.13. The electrical torque decreases immediately and it results in the sudden increase of the generator rotation speed. This phenomenon lasts until the fault is cleared. Due to interaction of two masses, the generator rotation speed variation causes the torsional oscillation. As mentioned above, the torsional

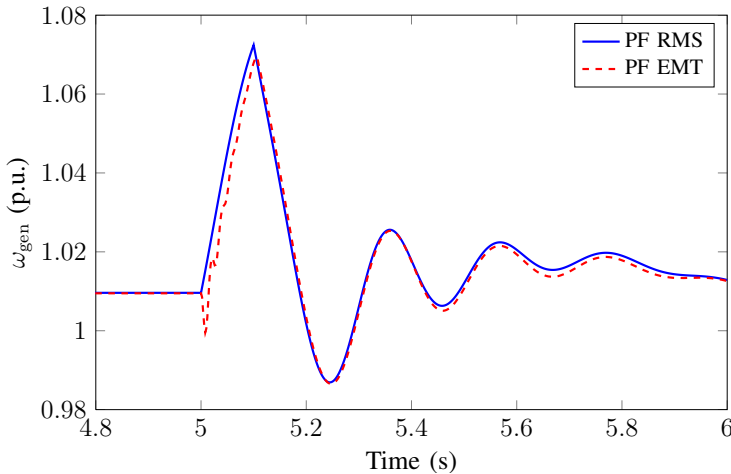


**Figure 4.13:** Generator speed  $\omega_{gen}$

oscillation is typically between 0.2 to 4 Hz. Here, according to the parameters listed in Appendix A.1 and equations by [122], the oscillation frequency modes are given by

$$f_1 = \frac{1}{2\pi} \sqrt{\frac{k_{sh}}{2H_{WTR}}} = 0.7368 \text{ Hz}, \quad (4.1)$$

$$f_2 = \frac{1}{2\pi} \sqrt{\frac{k_{sh}(H_{WTR} + H_{gen})}{2H_{WTR}H_{gen}}} = 2.0839 \text{ Hz}. \quad (4.2)$$

Through the comparison between RMS and EMT results, the main waveforms match except the short period after the fault. A rotor speed dip was detected

in EMT simulation due to the different induction generator models. The reason is explained in Section 4.4.2.3.

#### 4.4.2.2 FRT control of Type 1B

Type 1B model has FRT control block which can detect the low voltage level  $u_{\text{dip}}$  at wind turbine terminal and reduce the power reference  $p_{\text{WTTref}}$  to constraint the output power  $p_{\text{WTT}}$ . The short circuit fault will result in the voltage drop and trip the FRT control.

The voltage drop detection level  $u_{\text{dip}}$  is set 0.85 p.u.. In order to trip the FRT control block correctly, it is important to avoid the disturbance of high frequency harmonics. Therefore, the low-pass filter is used for the measured voltage. As illustrated in Fig.4.14, the voltage drop and recovery were detected through the filtered voltage  $u_{\text{WTT}}$ . The curves of RMS and EMT simulations are very close and the trip time and recovery time are almost the same.

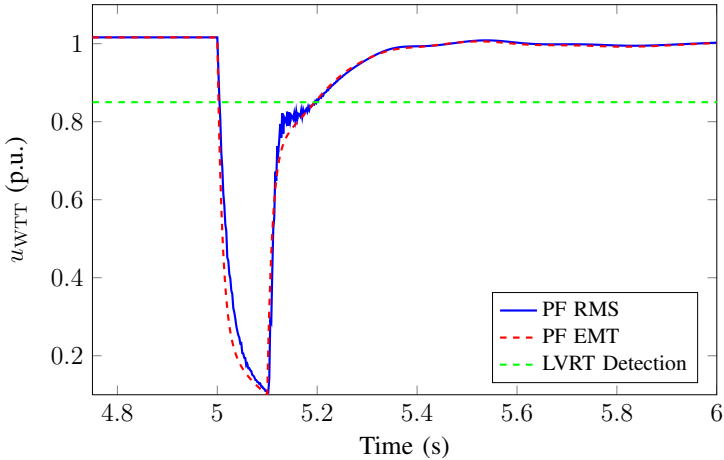


**Figure 4.14:** Filtered voltage of WTT  $u_{\text{WTT}}$  during FRT

The aerodynamic power  $p_{\text{aero}}$  is controlled by the blade angle regulation. In the real operation, the blade angle is adjusted slowly because of the mechanical movement. The adjustment range is limited as well. Therefore, there are magnitude and ramp limitations in the controller (Fig. 4.6). As shown in Fig. 4.15, the regulated  $p_{\text{aero}}$  decreased slowly during the fault condition to limit the output power  $p_{\text{WTT}}$ . After the fault was cleared,  $p_{\text{aero}}$  varies in order to smooth the oscillations of  $p_{\text{WTT}}$  of caused by the two-mass mechanical model.

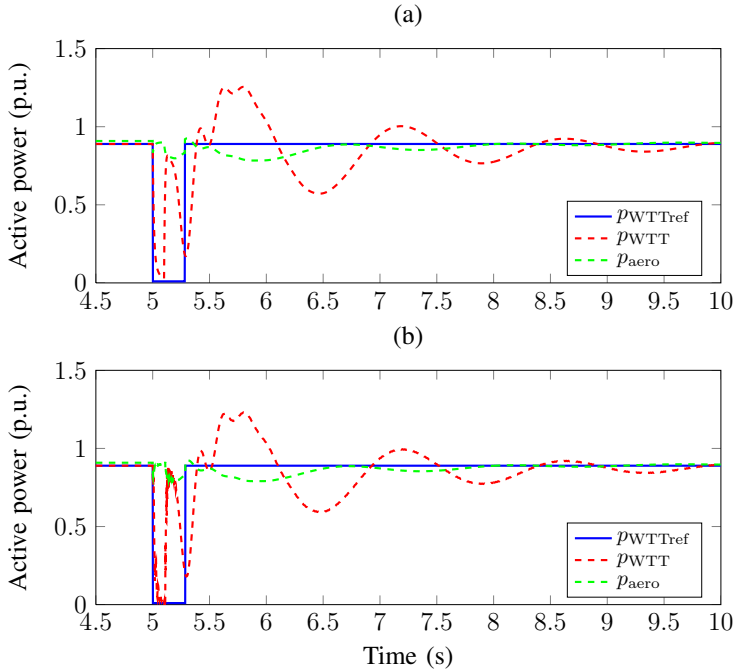


**Figure 4.15:** Power outputs during FRT. Above: PF RMS results; Below: PF EMT results

The waveforms between  $p_{aero}$  and  $p_{WTT}$  were opposite. After several seconds, the system got into steady state. It is observed that there were no difference between EMT and RMS results.

#### 4.4.2.3 Comparison of EMT and RMS models

This part compares the EMT and RMS models and evaluates to what extent this difference influences the simulation results. As mentioned in Section 4.2.1.4, the main difference between EMT and RMS WTG models is the built-in induction generator model. The RMS model neglects the stator transients and is based on the positive sequence simulation of the fundamental frequency (50 Hz). This simplification reduces the simulation time significantly compared to the EMT model and makes it possible to simulate much longer event and more complex system. The simulation results illustrated in the normal operation reach a very close agreement.

During the fault condition, due to the higher frequency variation of stator current  $i_s$ , this simplification resulted in larger error than steady state. Fig. 4.16 shows the simulated  $\omega_{\text{gen}}$ ,  $i_s$  and generator torque  $T_{\text{gen}}$  during the short circuit with EMT and RMS options respectively.

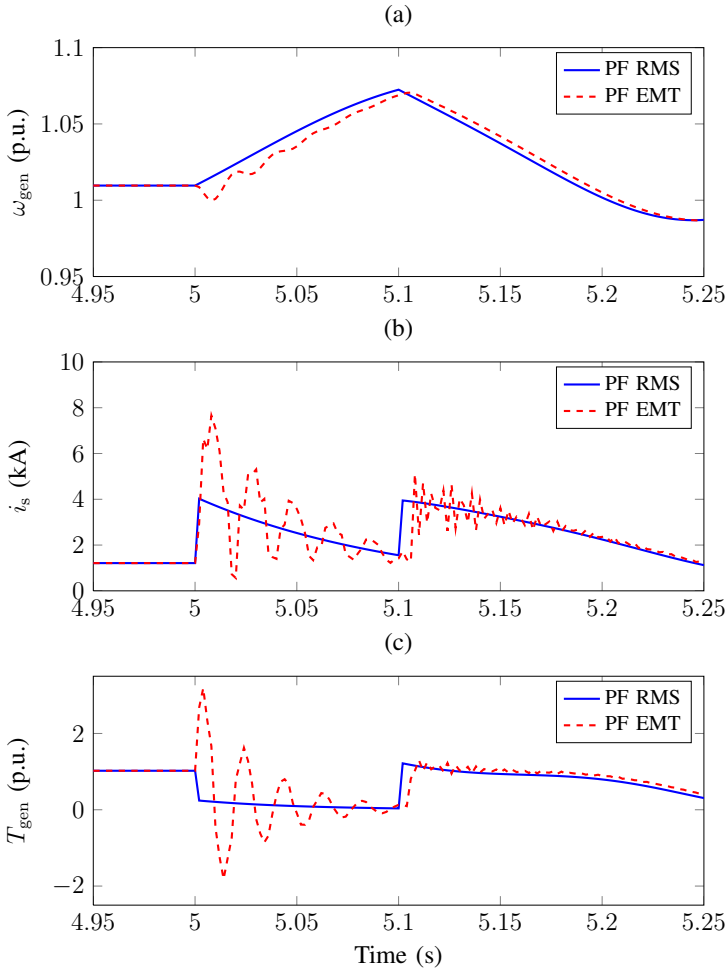


**Figure 4.16:** Dynamic responses of the  $\omega_{\text{gen}}$ ,  $i_s$  and  $T_{\text{gen}}$  during the fault

It is clearly seen that the RMS simulations strongly underestimate the variations in the generator torque by excluding the fundamental frequency oscillations. The oscillations are due to the stator flux transients. Instead of decreasing, the generator torque increases in the first circle. It can explain the rotation speed

dip detected in Section 4.4.2.1. The discrepancy is relevant when fast protection equipment is considered in the simulations [126]. For the power system stability analysis, it is commonly neglected [127].

## 4.5 Model validation against the field measurement

This generic model is a measurement-based model. Its accuracy and to what extent it reflects the practical operation are decided by the comparison between the simulation results and measurements data provided by manufacturers.

As concluded in [128], the measurement-based model validation is the most fruitful exercise. Therefore, the model validation against the field measurement was carried out. In order to validate the dynamic performance of the IEC generic Type 1A WTG model, the WTG parameters and measurement data under balanced fault conditions of a Siemens Wind Power Type 1 WTG were obtained. The rated power of the WTG is 2 MW, and the rated voltage of the WTT is 0.69 kV. The test was carried out with a test container with series and parallel impedance. For the test, the prefault active power is 0.6 pu, and a three-phase fault was applied at the medium voltage (MV) side of the WTG step-up TR. The measurement data at both the MV side and LV side of the WTG step-up TR were obtained and consist of positive sequence data of voltage, current, and power.

For the model validation against the field measurements, the “play-back” approach was used to carry out the case studies. Since the play-back approach was used and the transformer model was not of the interest of the model validation, the measurement data at the WTT were used to carry out the model validation studies. The WTG under study is connected to a voltage source through a CB and the voltage source gets measured positive sequence voltage during the play-back simulation.

The active and reactive power, and active and reactive currents at the WTT were obtained according to the played-back voltage at the WTT and compared to the measurements. In order to compare the simulation results against measurements and calculate the characteristic quantities, the voltage dip windows were determined according to the voltage measurements at the WTT and the window definitions specified in [19]. The voltage dip windows were determined according to the voltage dip in the field test and are shown in Fig. 4.17.

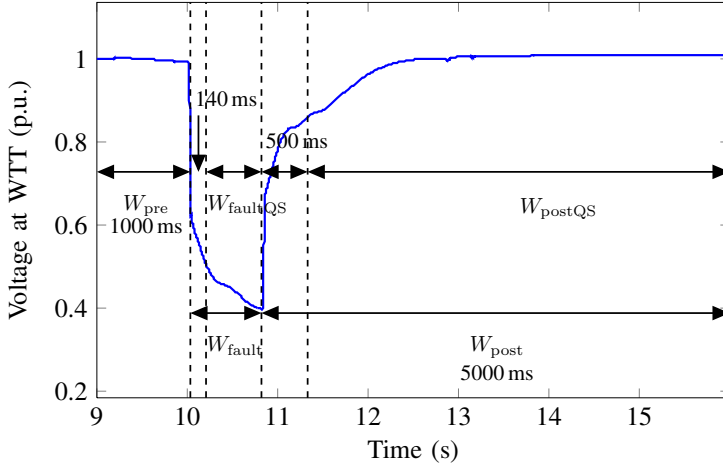


**Figure 4.17:** Voltage dip windows

The measurement data were divided into three adjacent windows – the pre-fault window  $W_{pre}$ , the fault window  $W_{fault}$  and the post-fault window  $W_{post}$ . On top of the three windows, two more windows are defined in [19] for calculating the characteristic quantities—the quasi steady state part of the fault window  $W_{faultQS}$  and the quasi steady state part of the post-fault window  $W_{postQS}$ .

The comparison of active power and active current against measurements is shown in Fig. 4.18 to Fig. 4.19. It is shown that there is a good match of the simulated active power and active currents against the measurements during the fault and after the fault. However, it is shown that there is a big difference between the simulation results and the measurements before the fault. The reason for that is that the active power right before the fault is used for initialization. It can be observed that the active power is fluctuating before the fault which could be caused by wind speed change or due to the opening of the bypass switch across the series impedance.



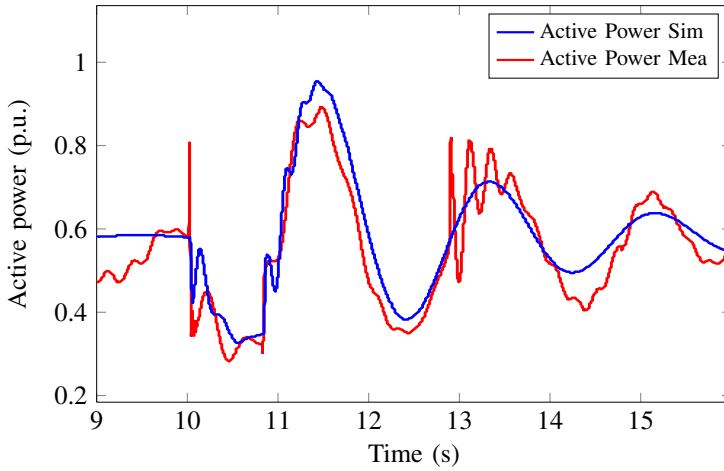


Figure 4.18: Comparison of simulated active power against measurements

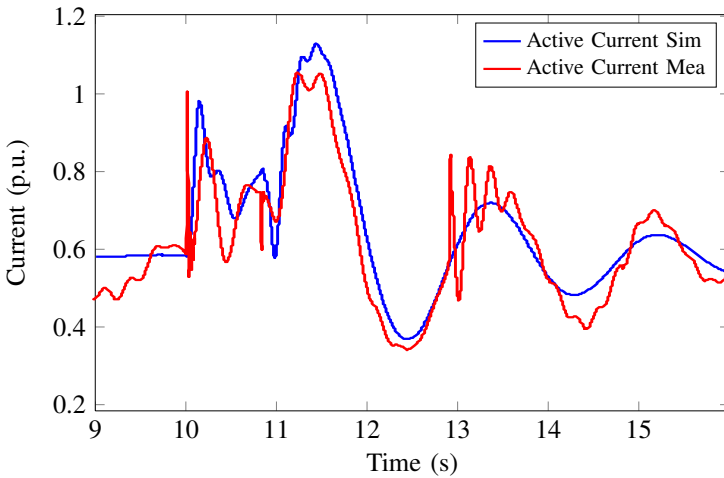
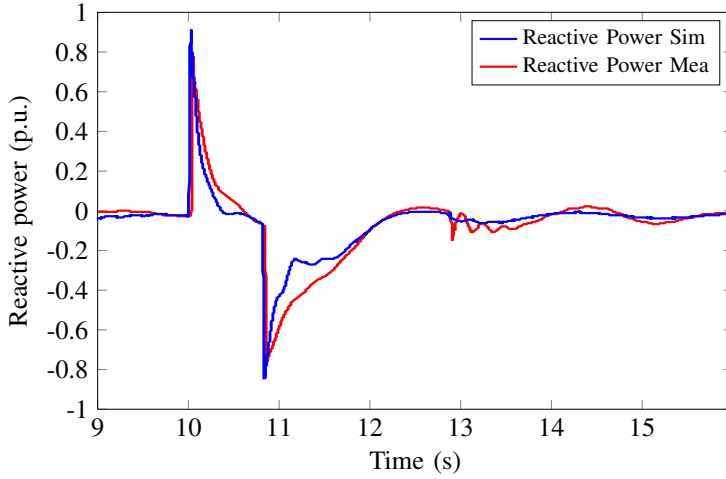
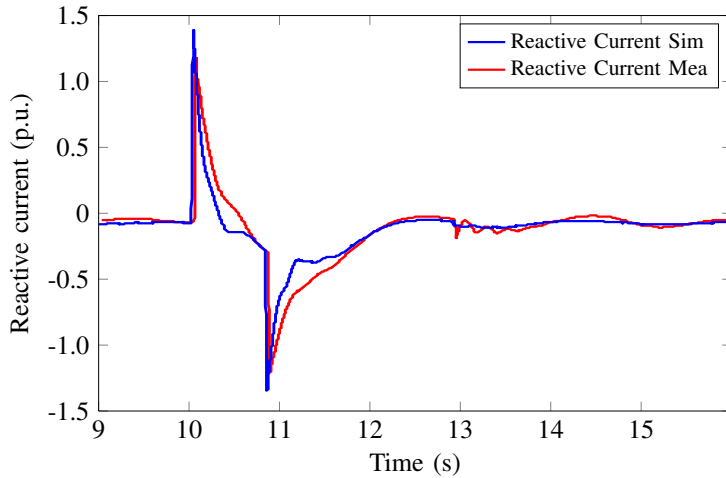


Figure 4.19: Comparison of simulated active current against measurements

The comparison of reactive power and reactive current against measurement is shown in Fig. 4.20 to Fig. 4.21. According to the waveforms, it is shown that the simulated reactive power and reactive currents are quite close to the measurements during the fault and after the fault.



**Figure 4.20:** Comparison of simulated reactive power against measurements



**Figure 4.21:** Comparison of simulated reactive current against measurements

In order to quantify the difference between the simulation results and the measurements, three characteristic quantities are defined in [19] which are the maximum error  $X_{MA}$ , the mean absolute error  $X_{MAE}$ , and the mean error  $X_{ME}$ .  $X$  is the variable to be validated against measurements. The three characteristic quantities were calculated for active and reactive currents and are listed in Table 4.6 and Table 4.7.

**Table 4.6:** Characteristic quantities of active current

Period	$I_{pMA}$ (p.u.)	$I_{pMAE}$ (p.u.)	$I_{pME}$ (p.u.)
Prefault	0.387	0.061	0.044
Fault	0.198	0.069	0.082
Postfault	0.251	0.055	0.029

**Table 4.7:** Characteristic quantities of reactive current

Period	$I_{qMA}$ (p.u.)	$I_{qMAE}$ (p.u.)	$I_{qME}$ (p.u.)
Prefault	0.037	0.018	-0.016
Fault	0.0218	0.110	-0.076
Postfault	0.141	0.026	0.024

It is shown that the characteristic quantities have the highest value in the fault window. It is also shown that the characteristic quantities of active current in the fault window are smaller than the ones of reactive current.

## 4.6 Discussion and conclusion

The details of implementing the IEC generic Type 1A in PF are presented in this chapter. In order to comply with the IEC generic model structure and use the PF built-in generator model, the data exchange between the mechanical and generator system blocks are adjusted, and the two mass mechanical model is adjusted in order to accommodate the change. Through several simulation case studies, it has been illustrated that the implemented IEC generic Type 1 models in PF can represent the relevant dynamics during normal operation and fault conditions. In normal operation, the wind power variation is simulated by changing the aerodynamic torque (Type 1A) or power output reference set point (Type 1B). The results response correctly and match the real operation. In fault case, the torsional oscillations of the two-mass mechanical model due to the disturbance are captured. The FRT capability of Type 1B with means of blade angle adjustment is tested. The practical limitations of the WTG behavior in real life are taken into consideration. The EMT and RMS models of induction generator are compared and the influences for the simulation results are evaluated as well. Since the generic models are to be used primarily for power stability studies, positive sequence are sufficient for bulk system and stator transient are generally neglected.

---

In order to verify the implemented IEC Type 1A WTG model, the model against measurements validation was carried out. The “play-back” model validation approach has been employed to verify the IEC generic Type 1A WTG model against measurements. The comparison of the waveforms of the simulated power and currents and the measurements show that there is a good match between the simulation results and the measurements. In order to give an indication of the errors between the simulation results and the measurements, the characteristic quantities have been obtained for active current and reactive current. The results show that the characteristic quantities of active current in the fault window are smaller than the ones of reactive current.



# Advanced Wind Turbine Control: $\mathcal{L}_1$ Adaptive Control Approach

---

According to different environmental conditions and control purposes, the control objectives of the variable speed wind turbine normally include limiting the captured wind power in the full load regime and maximizing the harvested wind power in the partial load regime. This chapter gives a brief introduction of control system for variable-speed WECS and focuses on the Maximum Power Point Tracking (MPPT) control. A novel  $\mathcal{L}_1$  adaptive controller for MPPT of a small variable speed WECS is designed. It has a generic structure and can be used for different generator types. This controller has also the potential to be extended for the application in the full load regime.

## 5.1 Background and basic knowledge

For variable-speed WECS control system, there are generally three main sub-controllers—pitch control, generator control and power transfer control. Their control targets correspond to the subsystems of WECS, as illustrated in Fig. 5.1.

## 76 Advanced Wind Turbine Control: $\mathcal{L}_1$ Adaptive Control Approach

The specific control objectives of each controller differ according to the operating regime. The Optimal Regimes Characteristic (ORC) curve is depicted in Fig. 5.2. According to the wind speed, the operating regime is divided into two parts:

- Partial load regime, when the wind speed is between the cut-in and the rated speed.
- Full load regime, when the wind speed exceeds the rated wind speed.

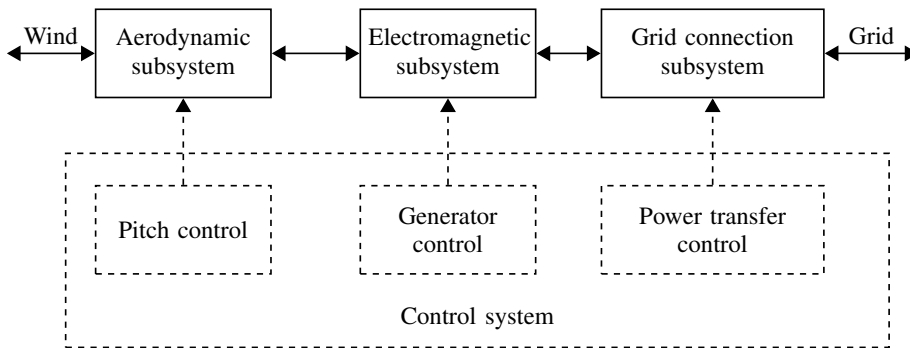


**Figure 5.1:** Control system for variable speed WECS

### Pitch control

During the partial load regime, the pitch control system is typically inactive. There are two exceptions:

- Assistance for start-up process, as the starting torque of wind turbines is relatively low.
- Limitation of the rotation speed, as the wind speed approaches the rated value.

During the full load regime, the pitch control system is active. Its objective is to limit the aerodynamic power to the rated power. When the wind speed reaches the cut-out value, the pitch control is used to stop the wind turbine. Thus, the pitch control system deals mainly with alleviating the mechanical loads on the wind turbine structure [20].

### Generator control

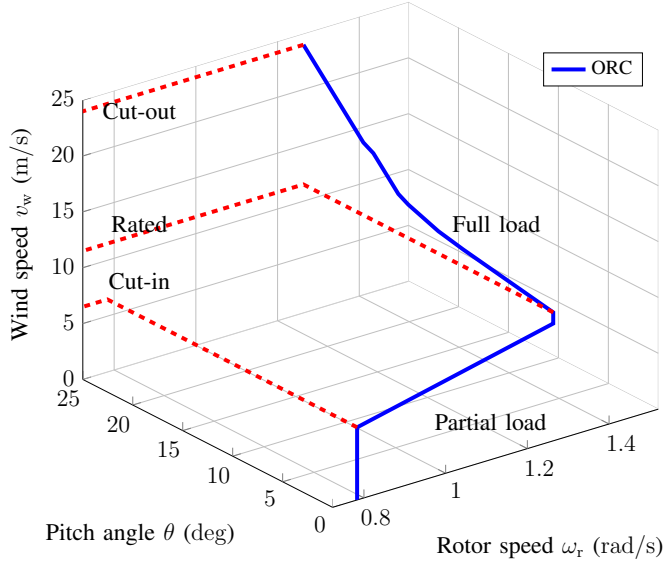


**Figure 5.2:** ORC of variable speed WECS

During the partial load regime, the generator control aims at maximizing the energy captured from the wind and/or at limiting the rotational speed at rated. By generator torque regulation, the generator speed can be controlled to track the optimum tip speed ratio. At the rated wind speed, the generator control limits the generator speed. Thus, the generator control deals mainly with the optimization of power conversion efficiency .

### Power transfer control

The power transfer control is used to ensure that the strict power quality standards are met (frequency, power factor, harmonics, flicker, etc). Besides, the WECS are required to provide more grid supports. In the grid fault case, the WECS should be remained connected, cope with sudden and important loads, and even assist the grid in voltage or frequency control. Thus, the power electronics converter control deals mainly with power quality standards [20].

This chapter focuses on the generator control of wind turbines in the partial load regime. It generally aims at MPPT algorithm by adjusting the electrical generator speed [129]. The MPPT control methods proposed in the literature can be classified into three control concepts [130], [131]:

- Hill-Climbing Search (HCS) control: It normally requires the rotor speed



and the turbine power variation for the MPPT. Recently, other variables, like the DC-link voltage and the duty cycle are used as the control inputs [132], [133]. The control algorithm is simple, robust and has the advantage of employing very few parameter and feedback information [134]. However, it is more feasible to use the HCS control in the slow varying system such as PV systems, and not for WECS with fast wind speed changes [135].

- Power Signal Feedback (PSF) control: It is based on the maximum power curve of the wind turbine and requires the rotor speed information for calculating the power reference [136]. However, the tracking speed is dependent on the rotor inertia of wind turbine [137]. Larger rotor inertia leads to the slow tracking speed which further affects the efficiency, especially in the low wind speed condition.
- Tip Speed Ratio (TSR) control: It directly regulates the rotational speed to keep the optimal TSR. Differently from the two control methods above, an additional wind speed information is required. One solution is the application of anemometer. However, the external anemometer will increase the system cost [136], [138]. Moreover, the measurement accuracy is limited due to the location constraints. To get rid of complexity and cost of external anemometer, the effective wind speed could also be estimated [139].

A series of control techniques are designed based on TSR control. Normally it generates the optimum torque for the torque control loop of the vector controlled generator side converter. The Proportional Integration (PI) controller is simplest and robust [20]. It is designed based on a linearized WECS model at a steady-state operating point. However, its dynamic performance is expected to vary with the move of operation point. The Sliding Mode Controller (SMC) is effective and intrinsically robust, requiring few information and being insensitive to parameter variation [140], [141]. However, the main drawback of the SMC controller is the chattering. It might result in unmodeled dynamics and produce destructive oscillations [20]. The feedback linearization is appropriate and effective for nonlinear WECS [142]. However, its formulation is based on the specific system modeling which may not be available.

Recently, the  $\mathcal{L}_1$  adaptive control is developed by N. Hovakimyan and C. Cao. Compared with the conventional Model Reference Adaptive Control (MRAC), it has guaranteed transient performance and robustness in the presence of fast adaption to uncertainties [143], [144], [145]. [146], [147]. Due to the nonlinearity, uncertainty and disturbances of WECS, it is very suitable to apply the  $\mathcal{L}_1$  adaptive control to design the MPPT controller for WECSs.

In this chapter, a novel MPPT algorithm based on  $\mathcal{L}_1$  control is proposed. The developed  $\mathcal{L}_1$  adaptive controller is generic generator controller and thus can be used for most generator types.

## 5.2 Generator control system of WECSs

The full converter wind turbine with SCIG is used to illustrate the generator control system for variable speed WECS. The generator control system based on TSR concept is depicted in Fig. 5.3. With the knowledge of the generator speed  $\omega_g$  and power  $P_{gen}$ , the optimal reference speed  $\omega_g^{ref}$  can be calculated and given to the speed control block. Compared with the measured generator speed  $\omega_g$ , speed controller generates the torque reference  $T_{gen}^{ref}$  as the input for the torque controller. A vector control is employed for the torque controller to generate the control signal  $u_{(a,b,c)}$  for the grid-side converter.

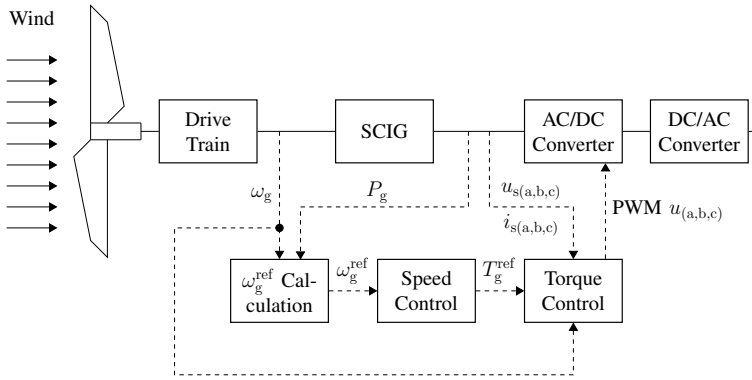


**Figure 5.3:** Generator control system based on TSR concept.

### 5.2.1 Speed Reference Calculation

The captured power by a wind turbine  $P_{wt}$  can be expressed as follows:

$$P_{wt} = \frac{1}{2} \cdot \rho \pi R^2 v_w^3 C_p(\lambda, \theta) = \frac{1}{2} \cdot \frac{C_p(\lambda)}{\lambda^3} \rho \pi R^5 \omega_r^3, \lambda = \frac{\omega_r R}{v_w}, \quad (5.1)$$

where  $\rho$  is the air density,  $R$  is the blade length,  $v_w$  is the wind speed,  $\omega_r$  is the rotor speed,  $C_p$  represents the power extraction efficiency and it is a function

## 80 Advanced Wind Turbine Control: $\mathcal{L}_1$ Adaptive Control Approach

of tip speed ratio  $\lambda$  and pitch angle  $\theta$  in pitch-controlled wind turbine. In the partial load operation, the pitch control system is inactive:  $\theta = 0$  [148]. Normally,  $C_p$  can be expressed as a polynomial in  $\lambda$ ,  $\alpha_0 \sim \alpha_6$  are polynomial coefficients.

$$C_p = \alpha_6 \lambda^6 + \alpha_5 \lambda^5 + \alpha_4 \lambda^4 + \alpha_3 \lambda^3 + \alpha_2 \lambda^2 + \alpha_1 \lambda + \alpha_0. \quad (5.2)$$

There exists an optimal tip speed ratio  $\lambda_{\text{opt}}$  by which the power efficiency  $C_p$  has a maximum value:  $C_p^{\text{max}} = C_p(\lambda_{\text{opt}})$ . Accordingly, the maximum power can be captured. In order to drive the system working at  $\lambda_{\text{opt}}$ ,  $\omega_r$  needs be regulated following the wind variation. Assumed that the drive train is infinitely stiff, there is a fixed multiplier ratio of gear box  $\eta$  between  $\omega_r$  and  $\omega_g$ . The generator speed reference  $\omega_g^{\text{ref}}$  can be decided by,

$$\omega_g^{\text{ref}} = \eta \frac{\lambda_{\text{opt}} v_w}{R}. \quad (5.3)$$

### Wind speed estimation

So far, wind speed  $v_w$  is considered as a measurable disturbance. Instead of anemometer, the effective wind speed is estimated in this study. The power balance estimator is used which is widely applied in the wind turbine industry as well as wind research community for wind speed estimation [149]. In this study, the estimated variable is noted with hat symbol  $\hat{\cdot}$ . The calculation procedure can be divided into three steps:

**Step 1:** the smoothed aerodynamic torque  $\hat{T}_a$  and rotor speed  $\hat{\omega}_r$  are estimated and calculated by,

$$\hat{T}_a(s) = \frac{1}{1 + s\tau} (J_{\text{eq}} s \hat{\omega}_r + T_g(s) + T_{\text{loss}}(s)), \quad (5.4)$$

where  $J_{\text{eq}}$  is the equivalent inertia:  $J_{\text{eq}} = J_{\text{wt}} + \eta^2 J_{\text{gen}}$ .  $J_{\text{wt}}$  and  $J_{\text{gen}}$  represent wind turbine rotor inertia and generator inertia, respectively.  $\hat{\omega}_r$  is considered equivalent to  $\omega_g$  with the notch filter which is used to remove the drive train eigen-frequency component. The low pass filter is applied to smooth out  $\hat{T}_a$ . The loss term  $T_{\text{loss}}$  is represented by viscous friction:  $T_{\text{loss}} = b_r \omega_r$ , where  $b_r$  is the viscous coefficient. The estimator implementation is illustrated in Fig. 5.4.

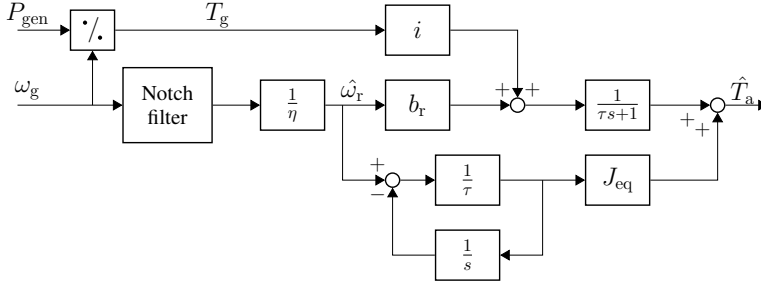


**Figure 5.4:** Block diagram of differentiation based estimator.

**Step 2:** Eqn. 5.1 can be transformed into:

$$C_p(\lambda)\lambda^{-3} = \frac{2T_a}{\rho\pi R^5\omega_r^2}. \quad (5.5)$$

By replacing  $\omega_r$  and  $T_a$  with the derived estimation values  $\hat{\omega}_r$  and  $\hat{T}_a$  from Step 1,  $C_p(\lambda)\lambda^{-3}$  as a whole can be calculated,

$$C_p(\hat{\lambda})\hat{\lambda}^{-3} = \frac{2\hat{T}_a}{\rho\pi R^5\hat{\omega}_r^2}. \quad (5.6)$$

By substituting Eqn. 5.2 into 5.6,  $C_p(\hat{\lambda})\hat{\lambda}^{-3}$  is transformed into a polynomial equation and  $\hat{\lambda}$  is the root. For real-time control, the calculation of the polynomial equation will be quite time-consuming. The practical implementation would be look-up table.

**Step 3:** The estimated wind speed  $\hat{v}$  is decided by,

$$\hat{v} = \frac{\hat{\omega}_r R}{\lambda}. \quad (5.7)$$

By eliminating the speed error between reference  $\omega_g^{\text{ref}}$  and  $\omega_g$ , the operating point moves to the maximum power point following the Optimal Regimes Characteristic (ORC). The ORC curve for 6 kW WECS is depicted in Fig. 5.5.

## 5.2.2 Generator Torque Control

The wind turbine rotor is coupled to the electrical generator via gearbox. To drive the rotor following the speed reference  $\omega_r^{\text{ref}}$ , the generator torque  $T_g$  should

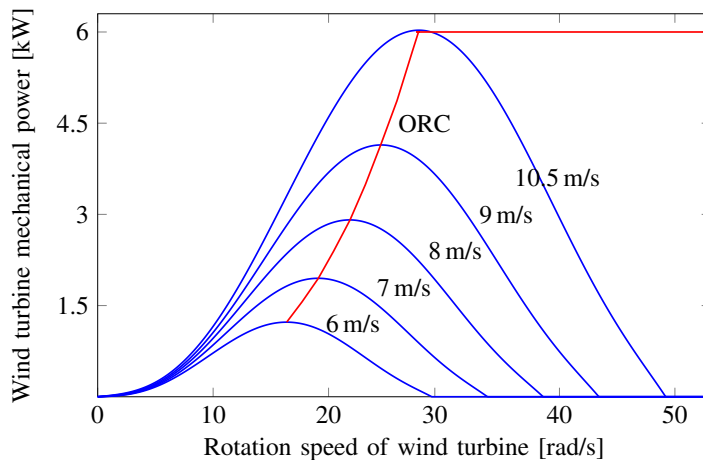


**Figure 5.5:** ORC curve for 6kW WECS.

be regulated by torque control.

There are two inputs of the torque controller. One is the torque reference  $T_{\text{gen}}^{\text{ref}}$  which is derived by speed controller described in Section 5.2.3. Another is the measurement of  $\omega_g$ . As the outputs the torque controller, the reference signals of generator electrical voltages ( $u_{\text{sa}}^{\text{ref}}$ ,  $u_{\text{sb}}^{\text{ref}}$ ,  $u_{\text{sc}}^{\text{ref}}$ ) are given to the AC-DC converter in order to generate the switching signals through Pulse-Width Modulation (PWM). The switching signals are generated and sent to the AC/DC converter at the turbine side [20].

The widely used vector control structure for SCIG is illustrated in Fig. 5.6 based on the rotor flux orientation. It is basically composed of two decoupled loops. The first is rotor flux loop ensuring the field orientation of the induction machine in order to control  $i_{\text{sd}}$ . The second is a torque control loop which imposes the electromagnetic torque in order to control  $i_{\text{sq}}$ .

The mathematical deviation has been demonstrated in many references [150], [151] and are, therefore, not repeated. The vector control used for DFIG is similar. However, there are some slight differences in conceiving the controller [151], like DFIG is based on stator flux orientation.

This vector control structure allows quite fast and accurate response under this control method. The torque controlled SCIG can be represented by a first-order

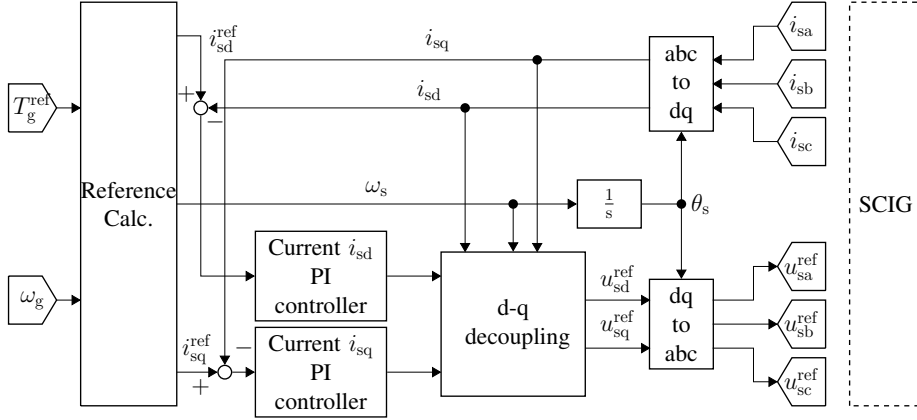


**Figure 5.6:** SCIG Vector Control.

element with quite fast dynamic. Its time constant  $\tau_g$  is normally in milliseconds,

$$T_g = \frac{1}{1 + s\tau_g} T_g^{\text{ref}}. \quad (5.8)$$

### 5.2.3 Speed Control

The object of this controller is to generate the torque reference  $T_g^{\text{ref}}$  in order to regulate  $\omega_g$  tracking the reference  $\omega_g^{\text{ref}}$ .

The controlled wind turbine can be represented by the four-order state space model (Eqn. 5.9) which includes both flexible drive train and generator dynamics (Eqn. 5.8). The state variables are defined as:  $x = [\omega_r, \omega_g, T_s, T_g]^t$ . The input  $u$  is  $T_g^{\text{ref}}$ ,  $u_d$  is friction torque,  $\xi$  indicates the aerodynamic torque  $T_a$  and the output  $y$  is  $\omega_g$ .

$$\begin{aligned} \dot{x}(t) &= Ax(t) + B(u(t) + u_d(t)) + E\xi(t) \\ y(t) &= Cx(t) \end{aligned} \quad (5.9)$$

with

$$\begin{aligned}
 A &= \begin{bmatrix} -\frac{b_r}{J_{wt}} & 0 & -\frac{\eta}{J_{wt}} & 0 \\ 0 & -\frac{b_g}{J_{gen}} & \frac{1}{J_{gen}} & -\frac{1}{J_{gen}} \\ \eta k_s & -k_s & \frac{b_s \eta^2}{\eta J_{wt}} + \frac{b_s}{J_{gen}} & \frac{b_s}{J_{gen}} \\ 0 & 0 & 0 & -\frac{1}{\tau_g} \end{bmatrix}, B = \begin{bmatrix} 0 \\ 0 \\ 0 \\ \frac{1}{\tau_g} \end{bmatrix}, \\
 C &= [0 \quad 1 \quad 0 \quad 0], E = \begin{bmatrix} \frac{1}{J_{wt}} \\ 0 \\ i b_s \\ \frac{1}{J_{wt}} \\ 0 \end{bmatrix}. \tag{5.10}
 \end{aligned}$$

where  $k_s$  and  $b_s$  are the stiffness and the damping coefficients of the drive train, respectively.  $b_r$  and  $b_g$  indicate the viscous friction coefficients for wind turbine rotor and generator, which are time-varying with known upper and lower bounds.  $T_s$  represents shaft torque for the input. The transfer function in  $s$  domain is expressed as,

$$y(s) = C(sI - A)^{-1}B(u(s) + u_d(s) + B^{-1}E\xi(s)). \tag{5.11}$$

Consider  $u_d$  and  $\xi$  as unmodeled disturbances, the transfer function is changed into the following form:

$$y(s) = C(sI - A)^{-1}B(u(s) + d(s)) \tag{5.12}$$

with  $d(s) = u_d(s) + B^{-1}E\xi(s)$ .

It is a Single Input and Single Output (SISO) system with unmodeled disturbances and parameter uncertainties. For control purpose, a PI controller can be designed considering the closed-loop stability and dynamic performance around the operating point. However, with the nonlinear uncertainty due to the movement of the operation point and disturbance, the transient performance cannot be guaranteed. To handle this problem, an  $\mathcal{L}_1$  adaptive controller is designed in Section 5.3.

## 5.3 Design of $\mathcal{L}_1$ adaptive controller

### 5.3.1 Problem formulation

In this section, the  $\mathcal{L}_1$  adaptive output feedback controller is designed for the SISO WECS described in Section 5.2.3. It has the property that ensures uniformly bounded transient response for both input and output. The control object is to enable the system output  $\omega_g$  following the reference  $\omega_g^{\text{ref}}$ . As the reference system, since first-order system has good dynamic performance, the following reference transfer function model  $M(s)$  with time constant  $\tau_m$  is used in this study,

$$M(s) = \frac{1}{\tau_m s + 1} = \frac{m}{s + m}, \tau_m = \frac{1}{m}, m > 0. \quad (5.13)$$

Consider the following class of system,

$$y(s) = A(s)(u(s) + d(s)), \quad (5.14)$$

where  $u(s)$  and  $y(s)$  are the Laplace transform of the system input  $T_g^{\text{ref}}(s)$  and  $\omega_g(s)$ , respectively.  $A(s)$  represents the strictly proper unknown transfer function of WECS,  $d(s)$  is the Laplace transform of the time-varying nonlinear uncertainties and disturbance, denoted by  $d(t) = f(t, y(t))$  in time domain. Two assumptions are made for  $f(t, y(t))$ :

**Assumption 1:** (Lipschitz continuity) There exist constants  $L > 0$  (Lipschitz gain) and  $L_0 > 0$ , possibly arbitrarily large, such that the following inequalities hold uniform:

$$\begin{cases} |f(t, y_1) - f(t, y_2)| \leq L |y_1 - y_2| \\ |f(t, y)| \leq L |y| + L_0, \quad L > 0, L_0 > 0. \end{cases} \quad (5.15)$$

**Assumption 2:** (Uniform boundedness of the variation rate of uncertainties) The variation rate of uncertainties is uniform bounded: there exist constants  $L_1, L_2, L_3 > 0$ , such that, for any  $t \geq 0$ ,

$$\left| \dot{d}(t) \right| \leq L |y_1 - y_2| \leq L_1 |\dot{y}(t)| + L_2 |y(t)| + L_3. \quad (5.16)$$

Based on Eqn. 5.13 and 5.14, the system can be rewritten in terms of the reference model as,

$$y(s) = M(s)(u(s) + \sigma(s)), \quad (5.17)$$



where uncertainties due to  $A(s)$  and  $d(s)$  are lumped into the signal  $\sigma(s)$ ,

$$\sigma(s) = \frac{(A(s) - M(s))u(s) + A(s)d(s)}{M(s)}.$$

### 5.3.2 Architecture of the $\mathcal{L}_1$ adaptive controller

The closed loop  $\mathcal{L}_1$  adaptive controller is illustrated in Fig. 5.7, which consists of state predictor, adaption law and control law.

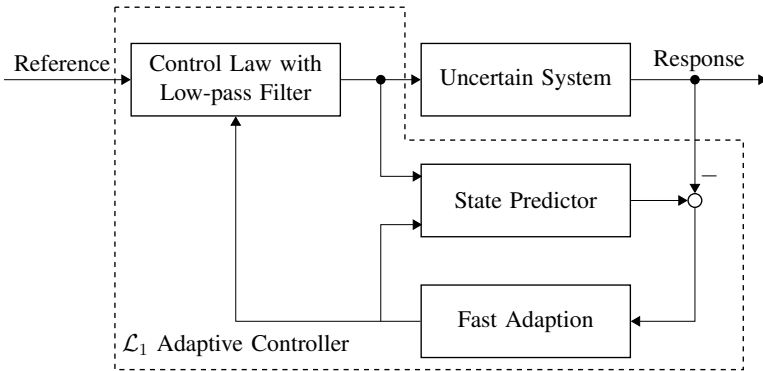


Figure 5.7: The closed loop  $\mathcal{L}_1$  Adaptive Controller.

#### State (Output) predictor

$$\dot{\hat{y}}(t) = -m\hat{y}(t) + m(u(t) + \hat{\sigma}(t)), \quad \hat{y}(0) = 0, \quad (5.18)$$

where  $\hat{\sigma}(t)$  is the adaptive estimate.

#### Adaption law

The adaption of  $\hat{\sigma}(t)$  is defined as

$$\dot{\hat{\sigma}}(t) = \Gamma \text{Proj}(\hat{\sigma}(t), -\tilde{y}(t)), \quad \hat{\sigma}(0) = 0, \quad (5.19)$$

where  $\tilde{y}(t) \triangleq \hat{y}(t) - y(t)$  is the error signal between the output and the predictor,  $\Gamma$  is the adaptive gain. Projection methods are introduced to ensure the boundary of the parameter estimates. More details about projection operator are described in Appendix B.1. The projection is bounded as following,

$$\hat{\sigma}(t) \leq \Delta, \quad (5.20)$$

where  $\Delta$  is the boundary.

The adaptive system tracks the state predictor, while the state predictor matches the expected closed loop reference system output very closely, the tracking errors of these signals go to zero as adaptive gain  $\Gamma \rightarrow \infty$ .

### Control law with low-pass filter

It is used to limit the compensation of the uncertainties within the bandwidth,

$$u(s) = C(s)(r(s) - \hat{\sigma}(s)), \quad (5.21)$$

where  $r(s)$  is the reference signal that  $y(s)$  should follow,  $C(s)$  is the low pass filter with cutoff frequency  $f_{\text{cut}} = \frac{w}{2\pi}$ , with  $C(0) = 1$ . The dc gain of one ensures reference tracking. Because of the approximation of  $\hat{\sigma}$ , the low pass filter  $C(s)$  is used to remove any high frequency chatter from passing into the system,

$$C(s) = \frac{w}{s + w}. \quad (5.22)$$

### 5.3.3 Closed loop reference system

Assume the adaptive variable  $\hat{\sigma}$  is exactly estimated, e.g.  $\hat{\sigma} = \sigma$ , the closed loop reference system is given by,

$$y_{\text{ref}}(s) = M(s)(u_{\text{ref}}(s) + \sigma_{\text{ref}}(s)), \quad (5.23)$$

$$u_{\text{ref}}(s) = C(s)(r(s) - \sigma_{\text{ref}}(s)), \quad (5.24)$$

$$\sigma_{\text{ref}}(s) = \frac{(A(s) - M(s))u_{\text{ref}}(s) + A(s)d_{\text{ref}}(s)}{M(s)}. \quad (5.25)$$

where  $d_{\text{ref}}(s)$  is the Laplace transform of  $d_{\text{ref}}(t)$  in time-domain,  $d_{\text{ref}}(t) \triangleq f(t, y_{\text{ref}}(t))$ . It is noticed that there is no algebraic loop involved in the definition of  $\sigma(s)$ ,  $u(s)$  and  $\sigma_{\text{ref}}(s)$ ,  $u_{\text{ref}}(s)$ .

By definition of  $H(s)$ ,

$$H(s) \triangleq \frac{A(s)M(s)}{C(s)A(s) + (1 - C(s))M(s)}. \quad (5.26)$$

For the proof of stability of the reference system (Eqn. 5.23-5.25), the selection of  $C(s)$  and  $M(s)$  must ensure that  $H(s)$  is stable and

$$\|G(s)\|_{\mathcal{L}_1} L < 1, \tag{5.27}$$

where

$$G(s) \triangleq H(s)(1 - C(s)). \tag{5.28}$$

The stability of the closed-loop reference system (Eqn. 5.23-Eqn. 5.25) is established in Lemma below. The proof of this lemma is described in [143].

**Lemma (Cao and Hovakimyan):** Let  $C(s)$  and  $M(s)$  verify the  $\mathcal{L}_1$ -norm condition (Eqn. 5.27), then the closed loop reference function (Eqn. 5.23, 5.24 and 5.25) is Bounded Input and Bounded Output (BIBO) stable.

### 5.3.4 Design of $\mathcal{L}_1$ adaptive controller parameters

It is expected that small variations in  $A(s)$  will not change the derived properties of the control method. As the approximation of the system,  $A(s)$  can be defined as the following transfer function of a 6 kW variable speed WECS [20] in this study based on matrices  $A$ ,  $B$ ,  $C$  derived in Eqn. 5.10. The parameters of 6 kW variable speed WECS are listed in Appendix A.2.

$$A(s) = \frac{A_n(s)}{A_d(s)} = C(sI - A)^{-1}B, \tag{5.29}$$

where  $A_n(s)$  and  $A_d(s)$  represent numerator and denominator of  $A(s)$ , respectively.

The closed loop reference transfer function can be expressed as,

$$H(s) = \frac{H_n(s)}{H_d(s)} = \frac{m(s+w)A_n(s)}{w(s+m)A_n(s) + msA_d(s)}. \tag{5.30}$$

where  $H_n(s)$  and  $H_d(s)$  are numerator and denominator of  $H(s)$ , respectively.

#### Determination of $w$

In order to get faster response, let close loop reference time constant  $\tau_m = 0.1$  s, e.g.  $m = \frac{1}{\tau_m} = 10$ . To ensure the stability of  $H(s)$ , its poles must be in the

left half side of the complex plane which restricts the choices of  $M(s)$  and  $C(s)$ . Instead of solving polynomial equation ( $H_n(s) = 0$ ), an alternative method for checking the stability of  $H(s)$  is by means of root locus method via loop transfer function  $L(s)$  (Eqn. 5.31), depicted in Fig. 5.8(a). The poles are always located in the left half complex plain if  $w > 0$ .

$$L(s) = \frac{\omega(s+m)}{ms}A(s). \quad (5.31)$$

If the cutoff frequency  $f_{\text{cut}}$  of the lowpass filter  $C(s)$  is very high,  $C(s)$  is like an all-pass filter and  $C(s) \approx 1$  (Eqn. 5.22). From Eqn. 5.26, it draws  $H(s) \approx M(s)$ , which means the system responses as the reference model. Therefore, increasing the cutoff frequency of the low-pass filter can lead to a better match. However, low-pass filter with high cutoff frequency may result in high gain feedback and thus lead to closed-loop systems with small robustness margins and susceptible to measurement noise. To keep the balance,  $w = 30$  in this study.

Assuming that the estimator  $\hat{\sigma}(s)$  in Eqn. 5.19 does not reach the boundary, then we can obtain

$$\dot{\hat{\sigma}}(t) = \Gamma(y(t) - \hat{y}(t)), \quad (5.32)$$

leading to the following closed-loop system:

$$\hat{\sigma}(s) = \frac{C(s)(A(s) - M(s))r(s) + A(s)d(s)}{\frac{1}{\Gamma}s + C(s)A(s) + (1 - C(s))M(s)}. \quad (5.33)$$

Obviously, the stability of estimator  $\hat{\sigma}(s)$  depends on  $\Gamma$  and its value range can be got by performing a root locus via loop function  $L(s)$ , where

$$L(s) = \frac{\Gamma C(s)A(s) + (1 - C(s))M(s)}{s}. \quad (5.34)$$

According to the root locus method, the adaptive gain can be limited. As depicted in Fig. 5.8 (b),  $\Gamma$  should be fulfill  $\Gamma < 160$  or  $\Gamma > 1.64 \cdot 10^4$ . To get more stability margin,  $\Gamma = 115$  in this study.

## 5.4 Simulation and results

In this section, several case studies have been carried out to verify the developed  $\mathcal{L}_1$  adaptive controller for WECSs. The optimal values of tip speed ratio and

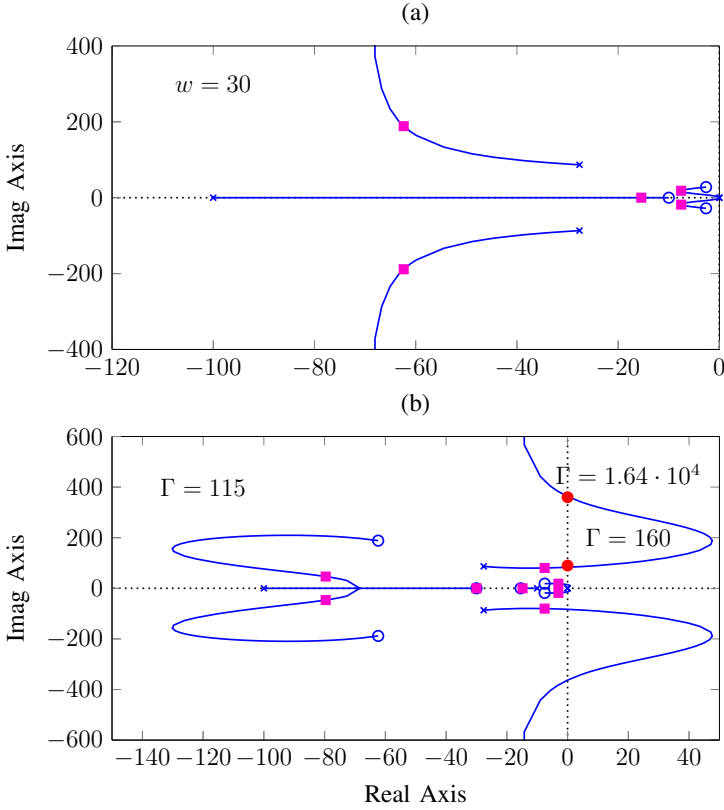


**Figure 5.8:** Root locus, (a) for decision of  $w$ ; (b) for decision of  $\Gamma$ .

power coefficient are:  $\lambda_{\text{opt}} = 7, C_p^{\text{max}} = 0.4763$ .

### 5.4.1 Step response

The  $\mathcal{L}_1$  adaptive controller under different step changes of wind speed is tested. It can be used to simulate the sudden change of aerodynamic torque  $T_a$  due to wind shear and tower shadow effects. The step responses of  $\lambda$  and  $C_p$  are shown in Fig. 5.9.

The step change of wind speed leads to a sudden change of  $\lambda$  and  $C_p$  drops. Then  $\lambda$  is regulated to go back to its optimal value  $\lambda_{\text{opt}}$  quite fast at different wind speed level (within 0.5s), even for the large step changes (from 7 m/s to 10 m/s). The wind turbine recovers to track the maximum power point.

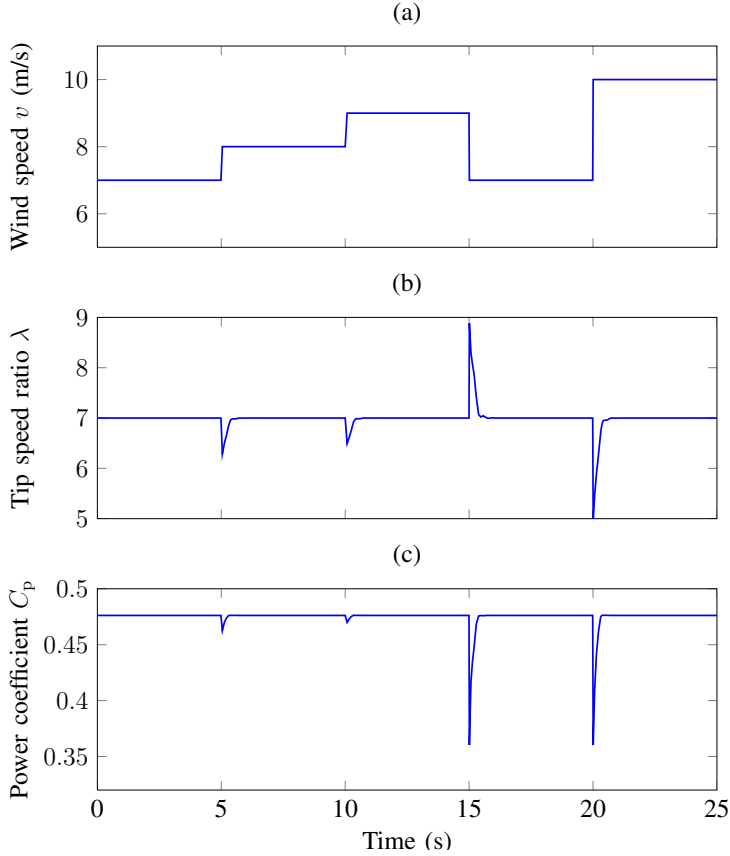


**Figure 5.9:** Step responses of  $\lambda$  and  $C_p$ .

### 5.4.2 Wind speed estimation

In this part, the estimation accuracy of wind speed is tested. The wind profile applied has average wind speed of 7 m/s and turbulence intensity is 0.15, derived by using the Von Karman spectrum in the IEC standard. The variation covers the most range of partial load regime—between 5 m/s and 11 m/s. The wind speed is estimated by means of the method described in Section 5.2.1. The comparison between actual and estimated wind speed is depicted in Fig. 5.10. It can be observed that there is a good match between both curves. The standard deviation is 0.0657 m/s.

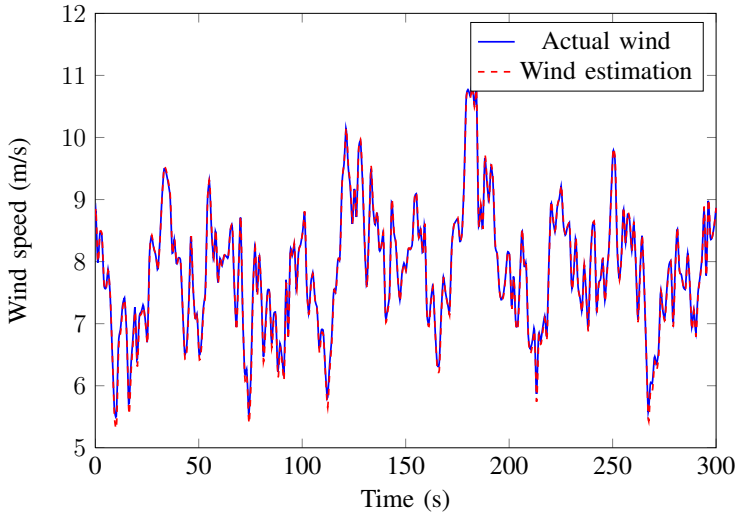


**Figure 5.10:** Comparison of actual wind and wind estimation.

### 5.4.3 Tracking performance with wind speed variation

Based on the estimated wind speed, the tracking performance of the speed reference  $\omega_g^{\text{ref}}$  is the key factor which determines the power efficiency and production. This case study is divided into two scenarios based on the different turbulence intensities of wind profiles: Scenario 1 and Scenario 2, depicted in Fig. 5.11 (a). The time-varying viscous coefficients ( $b_r$ ,  $b_g$ ) and the other disturbances except viscous friction are randomly generated with bounds, as shown in Fig. 5.11 (b) and (c). The simulation time is 300 s.

The tracking performances of  $\mathcal{L}_1$  adaptive controller and PI controller are illustrated in Fig. 5.12-5.15. A PI controller is normally designed based on the same SISO WECS considering the closed-loop stability and transient performances. To some extent, PI controller can also stabilize the system in presence of the unmodeled dynamics and disturbances  $d(t)$ . However, the transient performance by tracking the reference signal will be sacrificed.

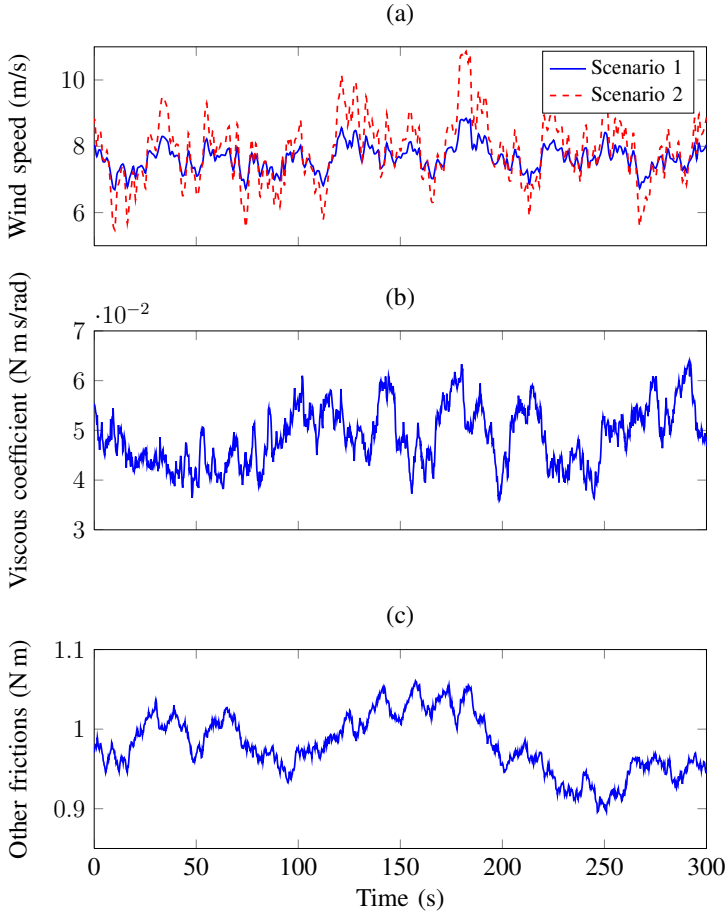


**Figure 5.11:** Friction disturbances.

For Scenario 1, since the turbulence intensity is small, the wind speed is limited between 7 m/s and 8.5 m/s. Both controllers show good capability in keeping the wind turbine operating around its optimal value  $\lambda_{\text{opt}}$  during simulation, between 6.85 and 7.15. From the density point of view (Fig. 5.12 (b)), it is much clearer that both controllers have the similar tracking performances in the presence of disturbance and parameter uncertainties.

Accordingly, the energy efficiency is maintained at a high level ( $0.4755 \sim 0.4763$ ) (Fig. 5.13). The power production is almost the same for both controllers and listed in Table 5.1. It can be observed that these values of Scenario 1 are almost the same. The energy captured with  $\mathcal{L}_1$  controller has 0.02% more.



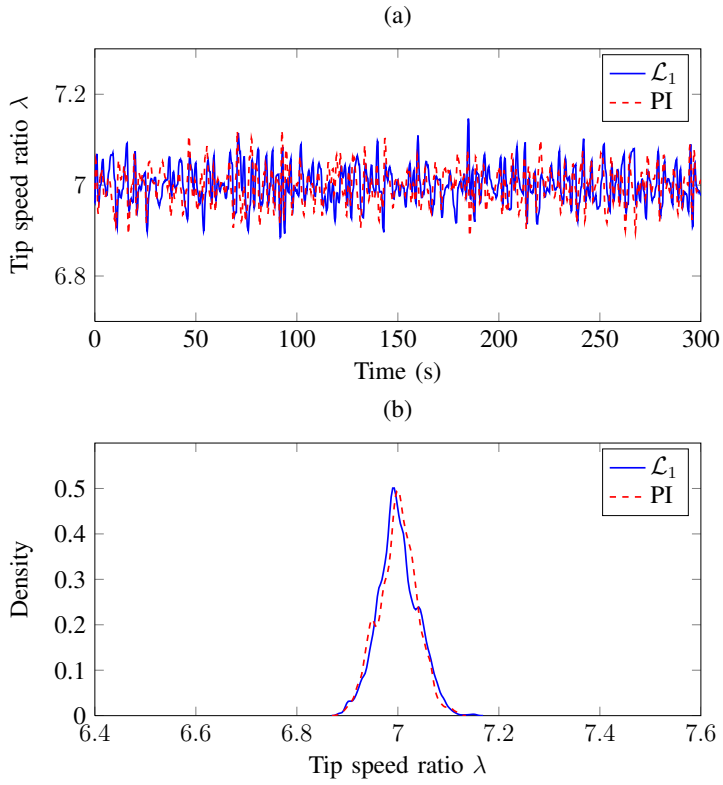


**Figure 5.12:** Comparison of  $\lambda$  variation during the operation in Scenario 1: (a) in time series format; (b)  $\lambda$  in density format.

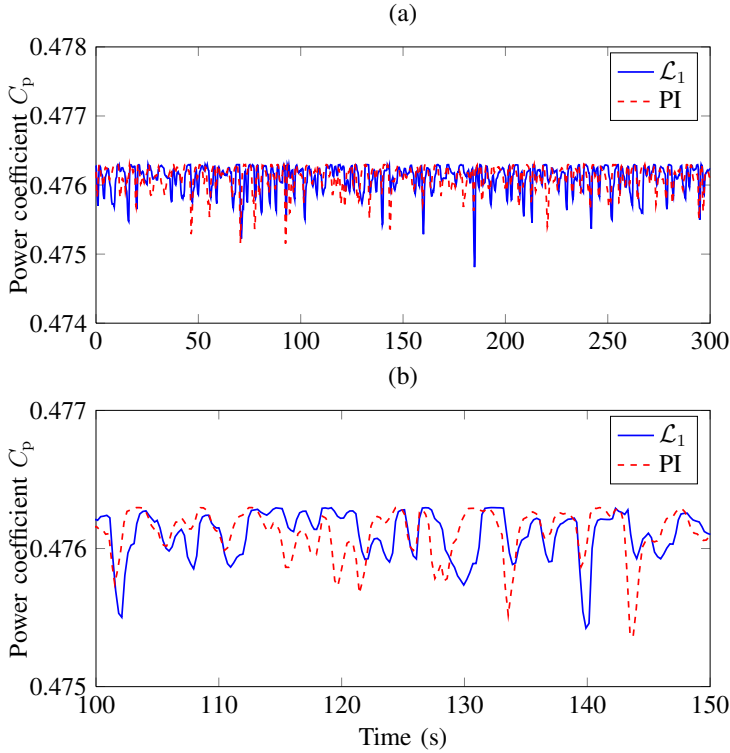


**Figure 5.13:** Efficiency comparison during the operation in Scenario 1. (a) Full time frame; (b) Zoomed in time frame (100 s ~ 150 s).

For Scenario 2, since the turbulence intensity is large, the wind speed variation is expanded between 5.5 m/s and 10.5 m/s, covering all the partial load regime. The tracking performances of both controllers are influenced and become worse compared with Scenario 1. As illustrated in Fig. 5.14,  $\mathcal{L}_1$  adaptive controller shows higher capability of keeping the wind turbine operating at its optimal value  $\lambda_{opt}$  than PI controller. The tip speed ratios with  $\mathcal{L}_1$  controller are distributed between 6.8 and 7.2 while these with PI controller are distributed between 6.6 and 7.4. Without precise tracking, the energy efficiency of the wind turbine by PI control is lower, as depicted in Fig. 5.15.

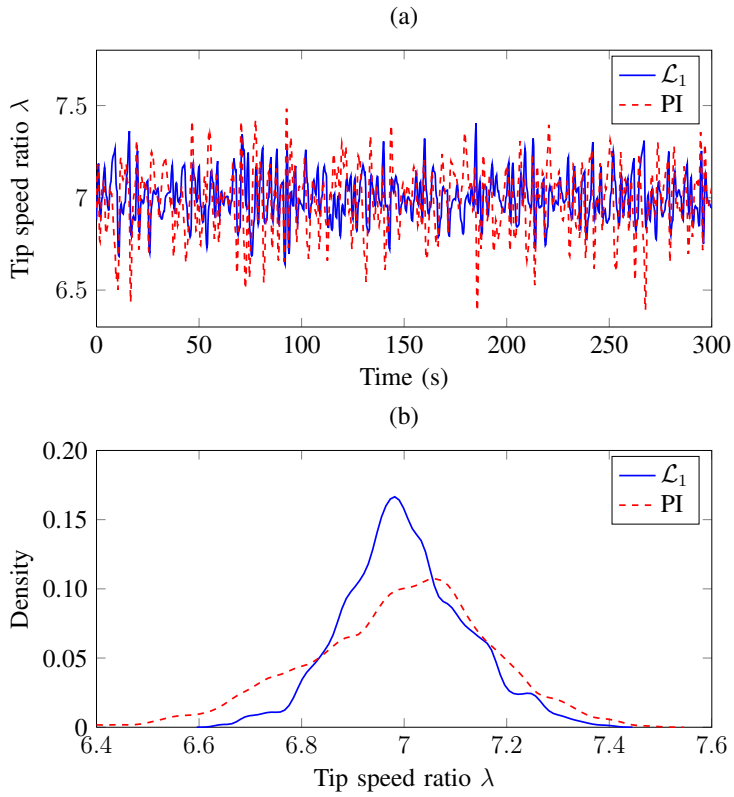


**Figure 5.14:** Comparison of  $\lambda$  variation during the operation in Scenario 2: (a) in time series format; (b)  $\lambda$  in density format.

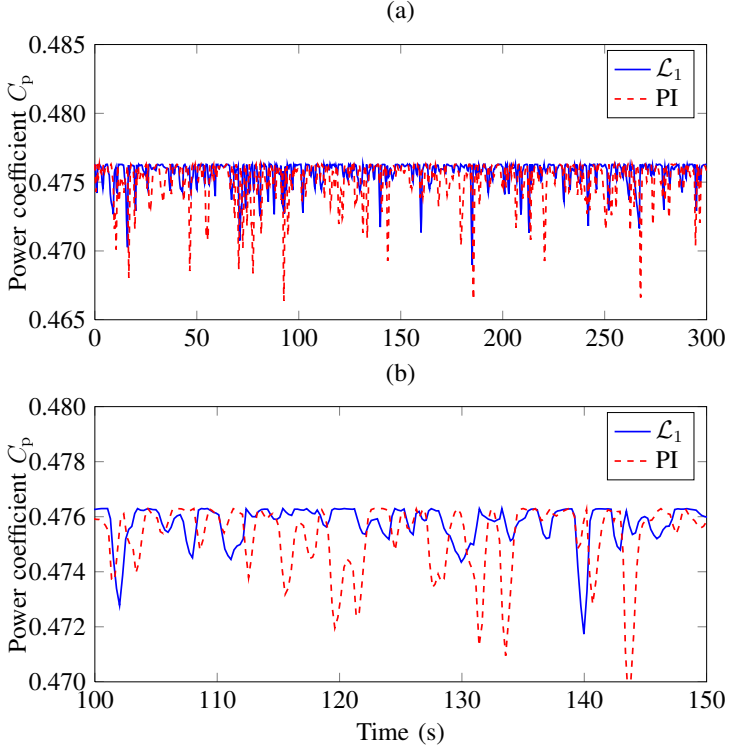


**Figure 5.15:** Efficiency comparison during the operation in Scenario 2. (a) Full time frame; (b) Zoomed in time frame (100 s ~ 150 s).

The power productions by means of both controller are listed in Table 5.1. The energy captured with  $\mathcal{L}_1$  controller has 0.59% more in Scenario 2, obviously larger than that of Scenario 1.

**Table 5.1:** Energy production comparison

Controller	Energy production (Scenario 1)	Energy production (Scenario 2)
PI	432409.50 J	526661.51 J
$\mathcal{L}_1$	432510.05 J	529787.99 J
Benefit of $\mathcal{L}_1$ (absolute)	100.55 J	3126.48 J
Benefit of $\mathcal{L}_1$ (percent)	0.02%	0.59%

## 5.5 Discussion and conclusion

With WECSs being nonlinear systems with parameter uncertainties and subject to disturbances, in the form of nonlinear and unmodeled aerodynamics, the  $\mathcal{L}_1$  adaptive speed control proposed in this chapter avoided the accurate WECS modeling. Instead, the WECS was modeled as a transfer function with the generator torque as the input and the generation speed as the output. Based on this simplified model, an  $\mathcal{L}_1$  adaptive speed controller was designed in order to achieve a trade-off between the transient performance and the stability of the MPPT under disturbances.

The  $\mathcal{L}_1$  adaptive speed controller showed good tracking performance towards the optimum TSR and robustness with fast adaptation to uncertainties and disturbances as shown in detailed simulation cases that included wind shear, shadow effects, and wind speed variations. Compared with the conventional optimized PI controller, the proposed  $\mathcal{L}_1$  adaptive speed control for MPPT captures more energy during operation, especially in highly turbulent wind conditions. Therefore, the proposed  $\mathcal{L}_1$  adaptive control is a reasonable alternative to the PI control and may present some advantages for MPPT in highly turbulent wind conditions.

### Potential application for the control in the full load regime

This chapter mainly focuses on the development of  $\mathcal{L}_1$  adaptive controller for generator control of WECS in partial load regime. It is also possible to extend the proposed controller in the full load regime. There are two possible realization ways.

For the case without stall or pitch control, the rotor speed will be regulated to decrease the power coefficient in order to limit the power production. The wind turbine system model in this region can be derived by system identification or linearization at operating point. The input is generator torque and output is power production. Since the power can be measured, the  $\mathcal{L}_1$  adaptive output feedback controller can be designed based on this model. The rated power is used as the reference. For the case with pitch control, the design procedure of  $\mathcal{L}_1$  adaptive controller is almost the same. The only difference is that the input for the identified WECS model is pitch angle.

# Advanced Wind Power Plant Control: D-MPC Approach

---

In this chapter, the optimal active power control of wind power plant based on Distributed Model Predictive Control (D-MPC) is presented. Through the D-MPC controller equipped in each actuation unit (wind turbine or ESS), the power references are dynamically coordinated and distributed to each unit. The control objective is twofold: tracking the power reference derived from the system operator and minimizing the mechanic loads of wind turbines. The D-MPC algorithm is implemented by using the fast dual gradient method.

## 6.1 Background and basic knowledge

As the wind penetration level in power systems grows, wind power plants are required to meet more stringent technical requirements for controllability specified by system operators. To fulfill these requirements, a wind power plant shall be capable of tracking the specific power references. In other words, the modern wind power plant is required to operate much more like a conventional power plant. The active power control scheme of a wind power plant can be implemented either by utilization of a separate energy storage device or through derated operation of wind turbines [152].

A typical wind field in the offshore wind power plant in Denmark - Horn Rev 1 is illustrated in Fig. 6.1. The wind field dynamics can be decoupled into two time scales:

- Slow dynamic. It represents the propagation of wind stream traveling through the wind power plant, which is related to the mean wind speed. Due to the wakes, wind turbines are coupled. According to the wind field model and measurements of the wind power plant, the mean wind speed of individual wind turbine can be estimated.
- Fast dynamic. It is related to the wind turbulence and gusts. The turbulence of different wind turbines is regarded as uncoupled, which leads to the increase of mechanical load, e.g. tower deflection and the mechanical load on the gearbox due to the torsion of the shaft.



**Figure 6.1:** Wind field in the offshore wind power plant Horn Rev 1

Conventionally, the power reference derived by the system operator is spread over all the turbines proportionally to their output power [152] or available power [153], which are estimated based on the slow dynamics. The wind turbine mechanical load, referring to the forces and moments experienced by the turbulence, is not considered. This will significantly shorten the service lifetime of wind turbines.

Recently, the wind power plant control with the mechanical load optimization has attracted more and more attentions and have been studied by several references [154], [155], [156], [157]. The control objective is to dynamically redistribute power in order to minimize the mechanical loads experienced by the turbines while maintaining the desired power production at all times. A Linear

Quadratic Gaussian (LQG) controller was introduced in [154], [155]. The computation burden is distributed via gradient descent method which relies only on few measurements.

The Model Predictive Control (MPC) scheme based on multi-objective performance optimization is another effective solution to handle this problem. It makes use of the receding horizon principle such that a finite-horizon optimal control problem is solved over a fixed interval of time [158]. The main advantage of MPC towards LQG is the control in presence of input and output constraints. A centralized MPC (C-MPC) algorithm has been developed in [156], [157]. The optimal power set points for the wind turbines are computed explicitly offline by multi-parametric programming. These set points are based on other auxiliary power variables that are then used for online coordination of the turbines in order to meet the total power demand. However, the wind power plant model is described as a coupled, constrained multiple-input and multiple output (MIMO) system whose order grows very fast with the increasing number of wind turbines. As an example, the largest onshore wind power plant under construction, the Gansu wind power plant in China, has a capacity of over 5,000 MW involving the installation of over 3,500 wind turbines. The computation of C-MPC is impractical for real-time application.

The Distributed MPC (D-MPC) concept is developed to solve the same optimization problems as C-MPC with reduced computation work. Each wind turbine can be considered as a single distributed unit, which are coupled by the shared wind field and by the power demand to the wind power plant. Some distributed algorithms are based on the property that the (sub)gradient to the dual of optimization problems can be handled in distributed fashion [159]. This approach is referred to as dual decomposition. The fast gradient method used in dual decomposition was originally proposed in early 1980s and has been applied for D-MPC in the past few years [160], [161]. In this study, the parallel generalized fast dual gradient method proposed in [162], [163] is adopted to design the wind power plant D-MPC controller. Compared with the standard gradient methods, the convergence rate can be largely improved.

A key issue for D-MPC implementation is the prediction model of wind turbine. The role that individual wind turbine plays is an actuator which operates in the derated condition, e.g. power production is less than the maximum available power. The wind turbine control is considered fixed and known, which aims to generate power according to the reference value derived from wind power plant control. As the appropriate prediction model, the inputs and outputs should fulfill the following requirements:

- The inputs should include the power reference  $P_{\text{ref}}^{\text{WT}}$  and wind speed  $v_w$ .



- The outputs should include the output power  $P_g$ , shaft torque  $T_s$  and thrust force  $F_t$  which are used to evaluate the mechanical load of wind turbine.

$F_t$  and  $T_s$  act on the tower structure and gearbox, respectively. The oscillatory transient of  $T_s$  leads to an undesired nodding of the tower, producing fatigue to the wind turbine. The torsional torque  $T_s$  is transferred through gearbox, which is the vulnerable part. Its oscillatory transient of  $T_s$  tends to create micro cracks in the material which can further lead to the component failure. A power controlled wind turbine model, proposed in [156], is adopted as the prediction model and shown in Fig. 6.2.

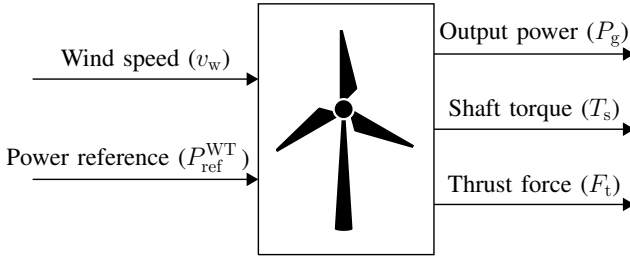


**Figure 6.2:** Power controlled wind turbine [156]

The aforementioned power controlled wind turbine model is a nonlinear system. It needs to be converted into a discrete-time model for MPC application [164]. The conventional identification method to approximate the nonlinearities is using first-order Taylor at various operating points [156], [165]. Due to the multiple state variables, the operating points are multidimensional and it is difficult to classify the multidimensional operating points and assign these points to the sub-models. To overcome this problem, a novel identification method is exploited in [166] which combines the clustering, pattern recognition and linear identification. The details of identification procedure are presented in the following section.

## 6.2 Linearization of wind turbine model

### 6.2.1 Operation areas of power controlled wind turbine

The popular variable speed pitch-controlled wind turbine model developed by National Renewable Energy Laboratory (NREL) [167] is illustrated in Fig. 6.3.

It consists of several subsystems, including aerodynamics, drive train, tower, generator, pitch actuator and the wind turbine controller. According to the power reference  $P_{\text{ref}}^{\text{WT}}$  generated from wind power plant controller, a pitch reference  $\theta_{\text{ref}}$  and a generator torque reference  $T_{\text{g}}^{\text{ref}}$  are computed and passed to the pitch controller and the generator torque controller, respectively.

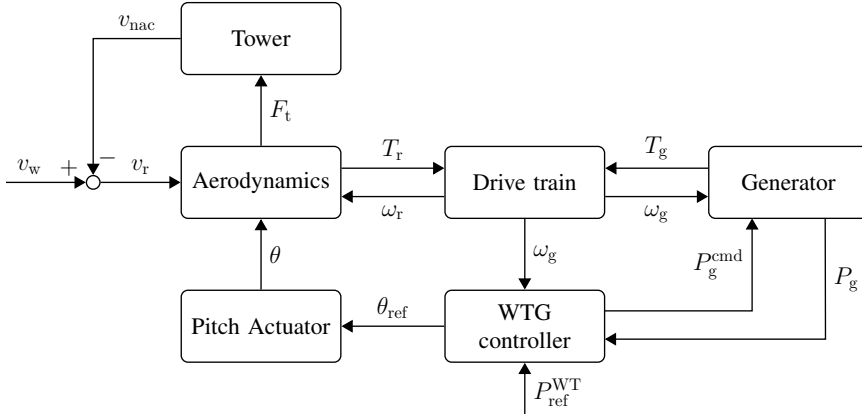


**Figure 6.3:** Wind turbine model by NREL.

As described in Chapter 2, normally the wind turbine control objective varies according to different wind conditions [168]. In the full load regime, the controller aims to limit the captured wind power to the rated power ( $P_{\text{ref}}^{\text{WT}} = P_{\text{rated}}$ ) by regulating the pitch angle to avoid the generator speed  $\omega_{\text{g}}$  from over-speeding. In the partial load regime, the controller aims to extract maximum available wind power ( $P_{\text{ref}}^{\text{WT}} = P_{\text{avi}} \leq P_{\text{rated}}$ ) by fixing the pitch angle ( $\theta = 0$ ) and adjust the generator torque to track the optimal rotor speed. The Optimal Regimes Characteristic (ORC), inherited in each wind turbine, is plotted in the  $\omega_{\text{r}} - \theta - v_{\text{w}}$  space, as illustrated in Fig. 6.4. The polyhedron marked in the figure is the area where the power efficiency  $C_{\text{p}} > 0$ .

When the wind turbine operates in the derated mode, e.g.  $P_{\text{ref}}^{\text{WT}} \leq P_{\text{avi}} \leq P_{\text{rated}}$ , the operation areas in stationary conditions should be below the ORC. According to activation status of pitch angle, two areas are divided, as labeled in Fig. 6.4:

- Area I, in which pitch angle is activated ( $\theta > 0$ ).
- Area II, in which pitch angle is deactivated ( $\theta = 0$ ).

Compared with the sampling time  $t_{\text{s}}$  for the wind power plant controller (normally in several seconds, e.g.  $t_{\text{s}} = 1$  s in [157]), the fast dynamics including

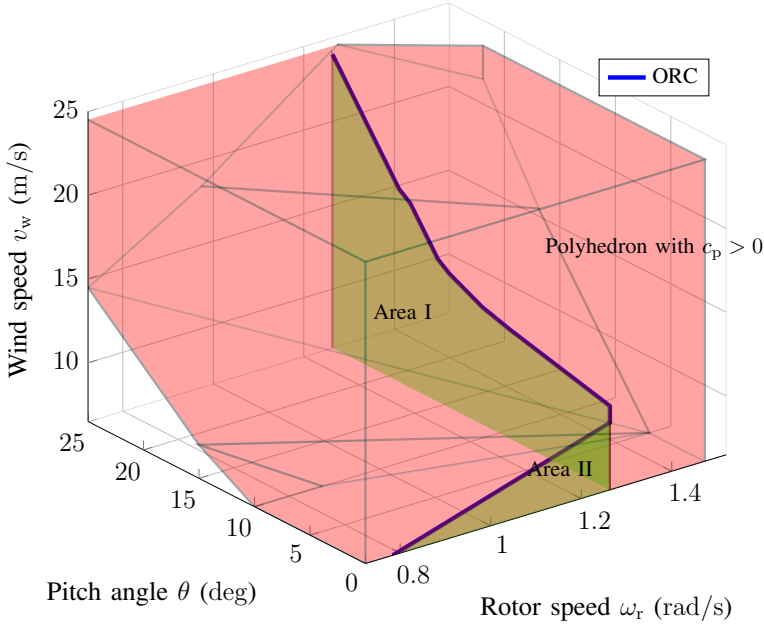


**Figure 6.4:** Operation areas in  $\omega_r - \theta - v_w$  space

electromagnetic transients are disregarded. Moreover, the oscillations presented in the shaft torsion and tower nodding are also ignored to reduce the complexity [156]. The model equations of this simplified nonlinear model of NREL wind turbine are listed in the following parts.

## 6.2.2 Simplified NREL wind turbine model

### Aerodynamics

The aerodynamic rotor  $T_a$  and thrust force  $F_t$  are expressed in Eqn. 6.1 and 6.2, respectively. They are the main source of nonlinearities.

$$T_a = \frac{0.5\pi\rho R^2 v_r^3 C_p(v_r, \omega_r, \theta)}{\omega_r} \quad (6.1)$$

$$F_t = 0.5\rho R^2 v_r^2 C_t(v_r, \omega_r, \theta) \quad (6.2)$$

where  $\rho$  is the air density,  $R$  is the blade length,  $v_r$  is the effective wind speed

on the rotor,  $C_p$  and  $C_t$  represent the power coefficient and thrust coefficient, respectively.

### Drive train

The drive train is considered to be rigidly coupled. The rotor inertia  $J_r$  and generator inertia  $J_g$  are lumped into one equivalent mass  $J_t$ . The single-mass model represented by the low-speed shaft motion equation is employed [20]:

$$J_t = J_r + \eta^2 J_g \quad (6.3)$$

$$\dot{\omega}_r = \frac{1}{J_t} (T_a - \eta T_g) \quad (6.4)$$

$$\omega_g = \eta \omega_r \quad (6.5)$$

where  $\eta$  is the multiplier ratio of the gear box,  $\omega_r$  and  $\omega_g$  indicate the speed of the rotor and generator,  $J_r$  and  $J_g$  are the inertias of the rotor and generator, respectively.

The shaft torque  $T_s$ , twisting the low-speed shaft is introduced. According to the definition,

$$\frac{1}{J_r} (T_a - T_s) = \dot{\omega}_r = \frac{1}{J_t} (T_s - \eta T_g). \quad (6.6)$$

By substituting Eqn. 6.3 into Eqn. 6.6,  $T_s$  can be calculated by

$$T_s = \frac{\eta^2 J_g}{J_t} T_a + \frac{\eta J_r}{J_t} T_g. \quad (6.7)$$

### Generator

Based on the torque control, the electrical torque  $T_g$  is regulated to follow the torque reference  $T_g^{\text{ref}}$ , obtained by the following nonlinear equation

$$T_g^{\text{ref}} = \frac{P_g^{\text{cmd}}}{\omega_g}. \quad (6.8)$$

where  $P_g^{\text{cmd}}$  indicates the power command for generator.

As described in Chapter 4, the vector control is often applied in the local torque control loop, which ensures a fast and accurate response. The time range of the dynamic is normally in the milliseconds and therefore can be disregarded, then

$$T_g \approx T_g^{\text{ref}}. \quad (6.9)$$

The output power  $P_g$  can be derived by

$$P_g = \mu T_g \omega_g, \quad (6.10)$$

where  $\mu$  denotes the generator efficiency.

Assumed that  $\mu$  is well compensated by setting  $P_g^{\text{cmd}} = \frac{P_{\text{ref}}^{\text{WT}}}{\mu}$ , we can get

$$P_g = P_{\text{ref}}^{\text{WT}}. \quad (6.11)$$

### Tower

The swaying movement of the nacelle changes the relative wind speed on the rotor. When the tower deflection is denoted as  $x_t$ , and the effective wind speed on the rotor is computed by  $v_r = v_w - \dot{x}_t$ . Since the dynamics are disregarded,

$$v_r \approx v_w. \quad (6.12)$$

### Pitch actuator

The dynamics and the nonlinearities of the pitch actuator are disregarded, as proposed in [156]. The inertia of the pitch system is considered in the wind turbine controller design. The pitch angle  $\theta$  is regulated by the gain-scheduled PI controller based on the deviation of filtered generator speed  $\omega_f$  to the rated speed  $\omega_{\text{rated}}$ ,

$$\theta = -\frac{K_P}{K_c} \dot{\omega}_f - \frac{K_I}{K_c} (\omega_f - \omega_{\text{rated}}), \quad (6.13)$$

$$\dot{\omega}_f = \frac{1}{\tau_g} \cdot \omega_g - \frac{1}{\tau_g} \cdot \omega_f, \quad (6.14)$$

$$K_c = f_{\text{corr}}(P_{\text{ref}}^{\text{WT}}(k-1), \theta(k-1)), \quad (6.15)$$

where  $K_P$  and  $K_I$  represent proportional and integral gain of PI controller,  $K_c$  indicates the correction factor which is a time-variant function of  $P_{\text{ref}}^{\text{WT}}$  and  $\theta$  of the last time step ( $P_{\text{ref}}^{\text{WT}}(k-1)$ ,  $\theta(k-1)$ ),  $\tau_g$  denotes the time constant of the measurement filter for generator speed  $\omega_g$ .

## 6.2.3 Linearization based on Taylor approximation

The conventional linearization method is based on the Taylor approximation at different operating points. Based on the equations 6.1–6.15, the state-space

wind turbine model around an operating point is expressed as follows,

$$\begin{aligned} \dot{x} &= Ax + Bu + Ed \\ y &= Cx + Du + Fd. \end{aligned} \quad (6.16)$$

where  $x$ ,  $u$ ,  $d$  and  $y$  indicate state, input, disturbance and output vectors,  $x = [\theta, \omega_r, \omega_f]'$ ,  $u = P_{\text{ref}}^{\text{WT}}$ ,  $d = v_w$ ,  $y = [T_s, F_t]'$ .

The state space matrices are

$$\begin{aligned} A &= \begin{bmatrix} 0 & -\frac{K_P^0 \eta}{\tau_g} & \frac{K_P^0 - K_I^0 \tau_g}{\tau_g} \\ \frac{K_{\theta T_r}}{J_t} & \frac{K_{\omega_r T_r}}{J_t} + \frac{1}{J_t} \frac{P_{\text{ref}}^0 \eta}{\mu \omega_g^0} & 0 \\ 0 & \frac{\eta}{\tau_g} & -\frac{1}{\tau_g} \end{bmatrix}, \\ B &= \begin{bmatrix} 0 \\ -\frac{\eta}{J_t \mu \omega_g^0} \\ 0 \end{bmatrix}, E = \begin{bmatrix} 0 \\ \frac{K_{v_w T_r}}{J_t} \\ 0 \end{bmatrix}, \\ C &= \begin{bmatrix} \frac{\eta^2 J_g K_{\theta T_r}}{J_t} & \frac{\eta^2 J_g K_{\omega_r T_r}}{J_t} - \frac{\eta^2 J_r P_{\text{ref}}^0}{J_t \mu \omega_g^0} & 0 \\ K_{\theta F_t} & K_{\omega_r F_t} & 0 \end{bmatrix}, \\ D &= \begin{bmatrix} \frac{1}{\mu \omega_g^0} \\ 0 \end{bmatrix}, F = \begin{bmatrix} \frac{\eta^2 J_g K_{v_w T_r}}{J_t} \\ K_{v_w F_t} \end{bmatrix}. \end{aligned}$$

where  $K_{\theta T_r}$ ,  $K_{\omega_r T_r}$ ,  $K_{v_w T_r}$ ,  $K_{\theta F_t}$ ,  $K_{\omega_r F_t}$  and  $K_{v_w F_t}$  are the coefficients derived from the Taylor approximation of  $T_r$  and  $F_t$  at the operating point  $[\omega_r^0, v_w^0, \theta^0, P_{\text{ref}}^0]$ , given by

$$\begin{aligned} K_{\theta T_r} &= \left. \frac{\partial T_r}{\partial \theta} \right|_{\omega_r^0, v_w^0, \theta^0, P_{\text{ref}}^0}, K_{\omega_r T_r} = \left. \frac{\partial T_r}{\partial \omega_r} \right|_{\omega_r^0, v_w^0, \theta^0, P_{\text{ref}}^0}, \\ K_{v_w T_r} &= \left. \frac{\partial T_r}{\partial v_w} \right|_{\omega_r^0, v_w^0, \theta^0, P_{\text{ref}}^0}, K_{\theta F_t} = \left. \frac{\partial F_t}{\partial \theta} \right|_{\omega_r^0, v_w^0, \theta^0, P_{\text{ref}}^0}, \\ K_{\omega_r F_t} &= \left. \frac{\partial F_t}{\partial \omega_r} \right|_{\omega_r^0, v_w^0, \theta^0, P_{\text{ref}}^0}, K_{v_w F_t} = \left. \frac{\partial F_t}{\partial v_w} \right|_{\omega_r^0, v_w^0, \theta^0, P_{\text{ref}}^0}. \end{aligned}$$

$K_P^0, K_I^0$  denote the proportional and integral gains of pitch controller at operating point. According to Eqn. 6.13–Eqn. 6.15, we get

$$K_P^0 = \frac{K_P}{K_C}, K_I^0 = \frac{K_I}{K_C}, K_C^0 = f_{\text{corr}}(P_{\text{ref}}^0, \theta^0).$$

By means of the discretization method introduced in [169], the wind turbine dynamic is described by the following linear, discrete, time-invariant system.

The formulation of  $A_d$ ,  $B_d$ ,  $C_d$ ,  $D_d$ ,  $E_d$  and  $F_d$  depending on the sampling time is elaborated in [169].

$$\begin{aligned} x(k+1) &= A_d x(k) + B_d u(k) + E_d d(k) \\ y_i(k) &= C_d x(k) + D_d u(k) + F_d d(k). \end{aligned} \quad (6.17)$$

Obviously, the operating points are multi-dimensional dependent on  $[\omega_r, v_w, \theta, P_{\text{ref}}]$ . It is difficult to classify the multi-dimensional points and assign these points to the sub-models. In the next section, the clustering-based identification method is presented to overcome this problem.

## 6.2.4 Clustering-based identification method

In this section, the procedure of the clustering based method is briefly introduced. A nonlinear static function  $f(x)$  can be approximated with a PWA map,

$$f(x) = \begin{cases} [x, 1] \alpha^1, & \text{if } x \in \chi^1 \\ [x, 1] \alpha^2, & \text{if } x \in \chi^2 \\ \vdots & \\ [x, 1] \alpha^s, & \text{if } x \in \chi^s \end{cases} \quad (6.18)$$

where  $x$  is the input for the static function,  $f(x)$  is the output,  $\chi$  represents a bounded polyhedron, termed as the regressor set. It is partitioned into  $s$  regions.  $\alpha^i$  indicates the affine function Parameter Vectors (PVs). The task of the identification is to reconstruct the map  $f$  based on the dataset  $(f(x_k), x_k)_{k=1}^n$ . The clustering-based method mainly consists of the following steps.

### Step 1: Build local datasets.

A Local Dataset (LD)  $C_k$  collects a point  $(f(x_k), x_k)$  and its nearest  $c-1$  points. The distance is measured in Euclidean metric [164]. A pure  $C_k$  is referred to a LD whose outputs are generated by only one model. Otherwise, the LD is termed mixed. The cardinality  $c$  is a tuning parameter. In order to achieve good approximation results, the ratio between pure and mixed LD should be high. On one side, a smaller  $c$  leads to a small number of mixed points. On the other side, a bigger  $c$  is required to counteract the effect of noise on the accuracy of local model. Therefore,  $c$  should be properly tuned.

The local parameter vector  $\alpha^{LS_k}$  is computed for each  $C_k$  through least squares. Parameter values  $\alpha^{LS_k}$  together and the mean value of the inputs  $m_k$  form the

feature vector  $\xi_k = [(\alpha^{LS_k})', m'_k]'$ .  $\xi_k$  holds both information about localization of  $C_k$  and about its corresponding affine model parameters. Furthermore, the variance  $R_k$  of the feature vectors is computed as a diagonal block matrix consisting of the co-variance  $V_k$  of  $\alpha^{LS_k}$  and the scatter matrix  $Q_k$  of  $m_k$ . The variance  $R_k$  is used to compute confidence measure of  $\xi_k$ .

**Step 2: Partition the feature vectors into clusters.**

It aims to partition the derived feature vectors into  $s$  clusters  $\{F_i\}_{i=1}^s$ . The partition could be performed either using a supervised clustering method (K-means) or unsupervised clustering method (single-linkage). In this study, the K-means method is adopted to reduce the complexity of the problem, where  $s$  should be pre-fixed. It exploits pre-computed confidence measures on feature vectors, which is used to reduce negative effects of LDs suspected to be mixed.

**Step 3: Estimate submodel parameters.**

As the local models with similar features are collected to each cluster, the data points are classified into one of the data subsets  $D_i$  using the mapping,

$$(f(u_k), u_k) \in D_i, \text{ if } \xi_k \in F_i. \quad (6.19)$$

The submodel parameter vector  $\alpha_i$  is estimated using weighted least squares over the data subset  $D_i$ .

**Step 4: Estimate the region.**

This step aims to find the complete polyhedral partitions of the regressor set. Polyhedrons  $\chi_i$  with  $(i = 1, \dots, s)$  are decided by solving multicategory classification problem. Different classification methods, such as Multi-category Robust Linear Programming (MRLP), Support Vector Classification (SVC) and Proximal SVC (PSVC) are introduced and compared in [170]. In this study, MRLP is used due to its high precision.

## 6.2.5 Discrete-time PWA modeling

As described in Section 6.2.2, the nonlinearities of simplified NREL wind turbine model are  $T_a$ ,  $T_g$ ,  $F_t$  and  $K_c$ . In this section, the discrete-time PWA model of wind turbine is identified following the procedure of the clustering-based method described in Section 6.2.4.



### 6.2.5.1 Identification of aerodynamic torque $T_a$

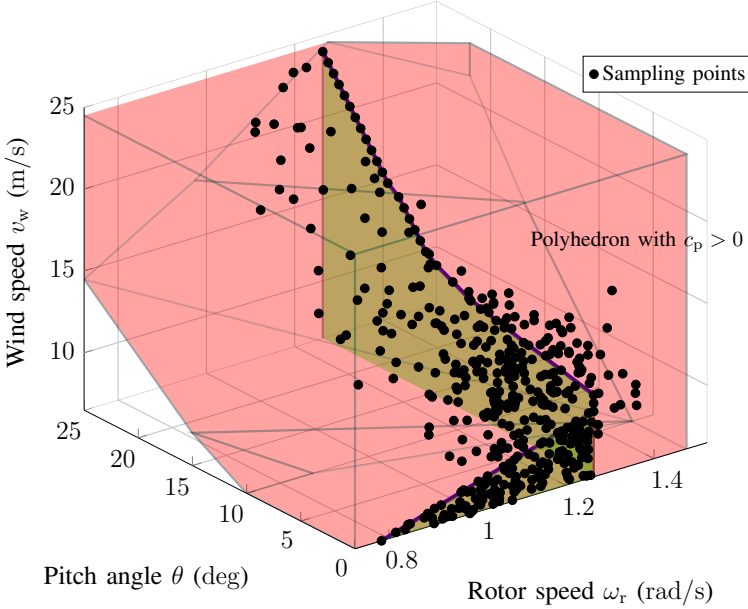


**Figure 6.5:** Regressors for identification of  $T_a$

According to Eqn. 6.1,  $T_a$  is a static nonlinear function of  $\omega_r$ ,  $v_w$ ,  $\theta$ . The regressors should be located close to the operation areas (Area I and Area II in Fig. 6.1) in the three-dimensional space  $[\omega_r, v_w, \theta]'$ . The ranges of  $\omega_r$ ,  $v_w$ ,  $\theta$  are limited by the practical constraints. Besides, sufficient regressors should be generated to have a good approximation of the nonlinear function. In this study, 1000 regressors are randomly generated with Gaussian distribution characterized with the mean value on the both operation areas and dispersion  $\sigma^2$  around them, as illustrated in Fig. 6.5.

For each regressor,  $C_p$  is obtained by interpolation of the look-up table in [167]. The corresponding aerodynamic torque  $T_a$  is computed according to  $C_p$  (Eqn. 6.1). As described in Section 6.2.4, the region number  $s$  and the number of the points in LD  $c$  should be pre-defined. A larger  $s$  can have better approximation. However, it leads to the increase of computation complexity for searching and more spaces requirements for storage. To achieve the trade-off,  $s = 5$  and  $c = 20$ . The clustering-based identification is carried out based on these output-input pairs  $(T_a, [\omega_r, v_w, \theta]')$ .

The partitioned regions for identified  $T_a$  is depicted in Fig. 6.6. With the

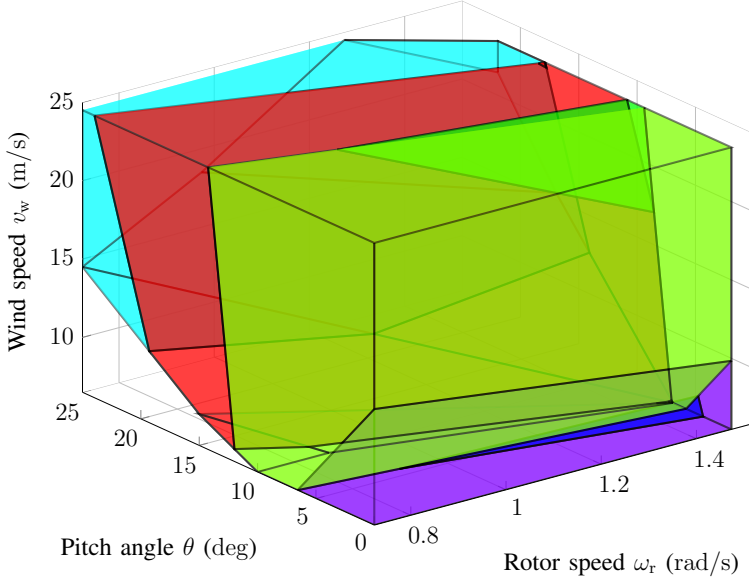


**Figure 6.6:** Regions  $\chi_{T_a}^i$  of  $T_a$  identification

parameter vector  $\alpha_{T_a}^i = [\alpha_1^i, \alpha_2^i, \alpha_3^i, \alpha_4^i]'$  and  $[\omega_r(k), \theta(k), v_w(k)] \in \chi_{T_a}^i$  ( $k$  and  $i$  are region index and time step index, respectively),  $T_a$  at time step  $k$  is expressed as

$$T_a(k) = \alpha_1^i \omega_r(k) + \alpha_2^i \theta(k) + \alpha_3^i v_w(k) + \alpha_4^i. \quad (6.20)$$

### 6.2.5.2 Identification of generator torque $T_g$

The static nonlinear function for computation of  $T_g$  is related to  $P_{\text{ref}}^{\text{WT}}$  and  $\omega_r$ . The regressors should be distributed in the two-dimensional space  $[\omega_r, P_{\text{ref}}^{\text{WT}}]'$  limited by the practical constraints. In this study, 500 regressors are generated uniformly. With  $s = 4$  and  $c = 10$ , the clustering-based identification is executed and the regions for identified  $T_g$  is shown in Fig. 6.7.

With the parameter vector  $\alpha_{T_g}^i = [\alpha_5^i, \alpha_6^i, \alpha_7^i]'$  and  $[\omega_r(k), P_{\text{ref}}^{\text{WT}}(k)] \in \chi_{T_g}^i$ ,  $T_g$  can be derived at time step  $k$

$$T_g(k) = \alpha_5^i \omega_r(k) + \alpha_6^i P_{\text{ref}}^{\text{WT}}(k) + \alpha_7^i. \quad (6.21)$$

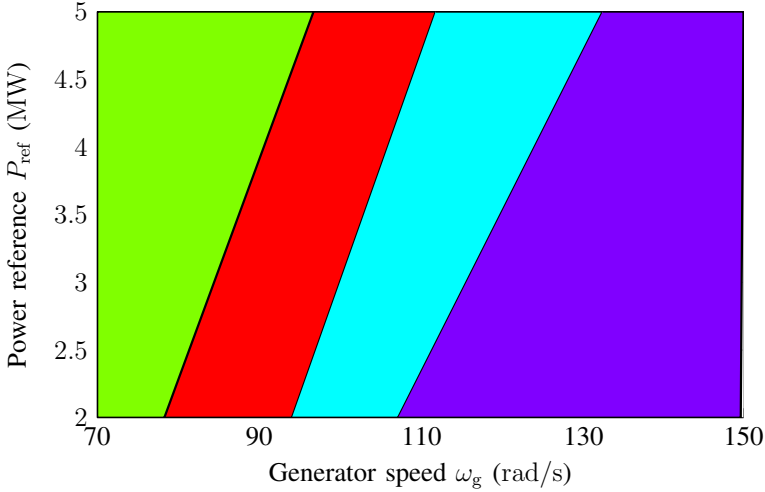


Figure 6.7: Regions  $\chi_{T_g}^i$  of  $T_g$  identification

### 6.2.5.3 Identification of thrust force $F_t$

The identification of  $F_t$  is similar to that of  $T_a$ . With the same regressor generation, the thrust force  $F_t$  to each regressor can be calculated according to Eqn. 6.2 where  $C_t$  is obtained by interpolation of the look-up table in [167]. In this study,  $s$  is set  $s = 4$  while  $c$  is set  $c = 20$ . The corresponding regions for identified  $F_t$  are illustrated in Fig. 6.8.

With the parameter vector  $\alpha_{F_t}^i = [\alpha_8^i, \alpha_9^i, \alpha_{10}^i, \alpha_{11}^i]'$  and  $[\omega_r(k), \theta(k), v_w(k)] \in \chi_{F_t}^i$ ,  $F_t$  can be derived at time step  $k$ ,

$$F_t(k) = \alpha_8^i \omega_r(k) + \alpha_9^i \theta(k) + \alpha_{10}^i v_w(k) + \alpha_{11}^i. \quad (6.22)$$

### 6.2.5.4 Identification of correction factor $K_c$

In the pitch control,  $K_c$  is a function of  $P_{\text{ref}}$  and  $\theta$ . Instead of the identification of the static nonlinear function,  $K_c$  is regarded as a fixed value with each region. It avoids from creating new nonlinearities.

The parameter vector  $\alpha_{K_c}^i = \alpha_{12}^i$ , if  $[P_{\text{ref}}(k), \theta(k)] \in \chi_{K_c}^i$ . Accordingly,

$$K_c = \alpha_{12}^i. \quad (6.23)$$

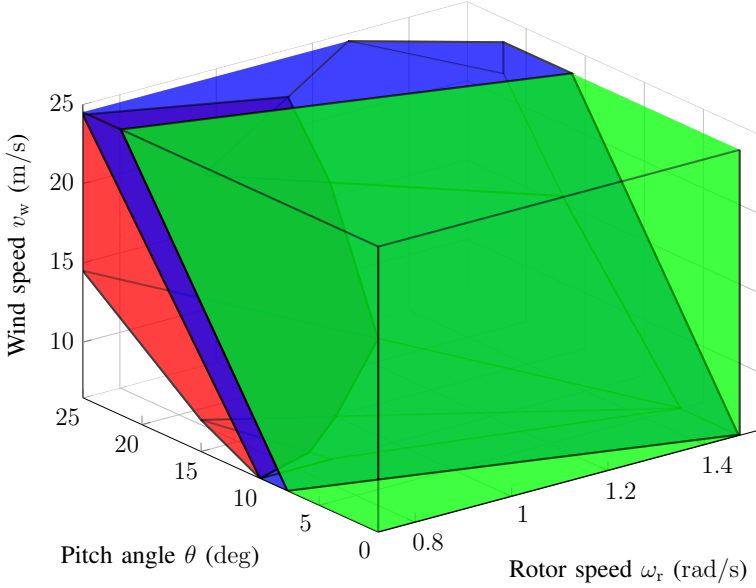


**Figure 6.8:** Regions  $\chi_{F_t}^i$  of  $F_t$  identification

In the NREL model [167],  $K_c$  applied in the gain-scheduling is only related to  $\theta$ . By selecting  $s = 4$ , the range  $[\theta_{\min}, \theta_{\max}]$  is equally divided into 4 segments.

### 6.2.5.5 Region construction through intersection

To include all the polytope regions identified above, a four dimensional space  $[\omega_r, v_w, \theta, P_{\text{ref}}^{\text{WT}}]'$  is introduced. According to the operation areas, when the wind turbine operates in Area I, pitch angle control is considered deactivated:  $\theta = 0$ . Therefore, the judgment is only three-dimensional space  $[\omega_r, v_w, P_{\text{ref}}^{\text{WT}}]'$ . Each polyhedron regions constructed by the identification has to be intersected with others. In this case, the total number of all the intersected regions  $\{\chi_i\}_{i=1}^{s_{\text{total}}}$  is  $s_{\text{total}} = 40$ .

### 6.2.5.6 PWA model of a wind turbine

The procedure to derive the PWA model of a wind turbine can be divided into the following two steps.

### Step 1: Formulate the initial form of state-space model

Based on the equations above (Eqn. 6.1–Eqn. 6.15), the nonlinear dynamics of the wind turbine model can be described by the following state-space model:

$$\begin{aligned}\dot{x} &= Ax + Bg \\ y &= Cx + Dg\end{aligned}\quad (6.24)$$

with  $x = [\omega_r, \omega_f, \theta]'$ ,  $g = [T_a, T_g, F_t, \omega_{\text{rated}}]'$ ,  $y = [T_s, F_t]'$ .

The state space matrices are

$$\begin{aligned}A &= \begin{bmatrix} 0 & 0 & 0 \\ \frac{\eta}{\tau_g} & -\frac{1}{\tau_g} & 0 \\ -\frac{K_P \eta}{K_c \tau_g} & \frac{K_P - K_I \tau_g}{K_c \tau_g} & 0 \end{bmatrix}, \\ B &= \begin{bmatrix} \frac{1}{J_t} & -\frac{\eta}{J_t} & 0 & 0 \\ 0 & 0 & 0 & 0 \\ 0 & 0 & 0 & \frac{K_i}{K_c} \end{bmatrix}, \\ C &= \begin{bmatrix} 0 & 0 & 0 \\ 0 & 0 & 0 \end{bmatrix}, D = \begin{bmatrix} \frac{\eta^2 J_g}{J_t} & \frac{\eta J_r}{J_t} & 0 & 0 \\ 0 & 0 & 1 & 0 \end{bmatrix}.\end{aligned}\quad (6.25)$$

where  $\omega_{\text{rated}}$  is considered fixed. For each region  $\chi_i$ , the constant  $K_c$  is firstly determined and then brought into  $A$  in Eqn. 6.25. The corresponding discrete-time form of the system in Eqn. 6.24 with sampling time  $t_s$  can be obtained:

$$\begin{aligned}x(k+1) &= A_d' x(k) + B_d' g(k), \\ y(k) &= C_d' x(k) + D_d' g(k),\end{aligned}\quad (6.26)$$

where  $A_d'$ ,  $B_d'$ ,  $C_d'$ ,  $D_d'$  are the discrete form of  $A$ ,  $B$ ,  $C$ ,  $D$  in Eqn. 6.24, respectively.

### Step 2: Substitute $g(k)$ into Eqn. 6.24 and derive PWA model.

According to the equations 6.20-6.23,  $g(k)$  can be expressed with the identified parameters,

$$g(k) = A_p x(k) + B_p u(k) + E_p d(k) + F_p, \quad (6.27)$$

where  $u = P_{\text{ref}}^{\text{WT}}$ ,  $d = v_w$ . The matrices are

$$A_p = \begin{bmatrix} \alpha_1^i & 0 & \alpha_2 \\ \alpha_5^i & 0 & 0 \\ \alpha_8^i & 0 & \alpha_9^i \\ 0 & 0 & 0 \end{bmatrix}, B_p = \begin{bmatrix} \alpha_3^i \\ 0 \\ \alpha_{10}^i \\ 0 \end{bmatrix}, E_p = \begin{bmatrix} 0 \\ \alpha_6^i \\ 0 \\ 0 \end{bmatrix}, F_p = \begin{bmatrix} \alpha_4^i \\ \alpha_7^i \\ \alpha_{11}^i \\ \omega_{\text{rated}} \end{bmatrix}.$$

Substituting Eqn. 6.27 into Eqn. 6.26, the standard PWA format can be obtained,

$$\begin{aligned} x(k+1) &= A_d x(k) + B_d u(k) + E_d d(k) + F_d, \\ y(k) &= C_d x(k) + D_d u(k) + G_d d(k) + H_d, \\ \text{if } \begin{bmatrix} x(k) \\ u(k) \\ d(k) \end{bmatrix} &\in \chi_i. \end{aligned} \quad (6.28)$$

with

$$\begin{aligned} A_d &= A'_d + B'_d A_p, \quad B_d = B'_d B_p, \quad E_d = B'_d E_p, \quad F_d = B'_d F_p, \\ C_d &= C'_d + D'_d A_p, \quad D_d = D'_d B_p, \quad G_d = D'_d E_p, \quad H_d = D'_d F_p. \end{aligned}$$

## 6.3 D-MPC without energy storage

### 6.3.1 Control structure

The hierarchical wind power plant active power control setup is illustrated in Fig. 6.9.

#### High level control

The high level control deals with the slower time scale. To be specific, the wind power plant power reference  $P_{\text{ref}}^{\text{wfc}}$  is generated according to the requirements by the system operator and available wind power plant power. With the wind field model and measurement data, the mean wind speed of a certain period (normally in several minutes) can be estimated. Several approaches have been developed to distribute the mean power references for individual wind turbines ( $\overline{P_{\text{ref}}^{\text{WT}_1}}, \overline{P_{\text{ref}}^{\text{WT}_2}}, \dots, \overline{P_{\text{ref}}^{\text{WT}_i}}$ ), which is reviewed in [157]. Since it is out of the scope of this study, the proportional distribution algorithm proposed in [153] is adopted.

#### Low level control

Conventionally, these mean power reference signals are directly assigned to the individual wind turbines without consideration of the turbulence. In this study, these references are given into the D-MPC controller locally equipped in each wind turbine. It is considered as the low level wind power plant control for fast time scale. By adjusting the power reference to each turbine, the wind turbine loads are alleviated.

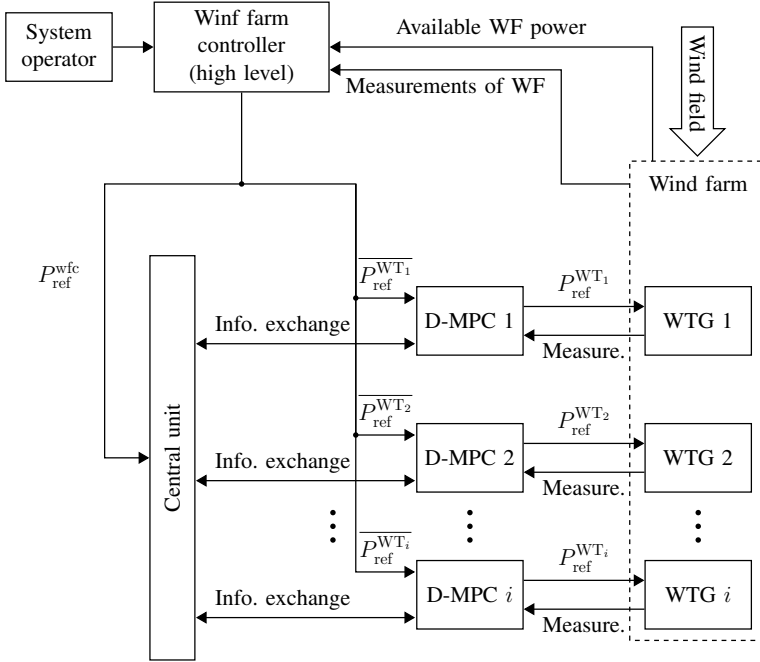


**Figure 6.9:** Control structure of wind power plant based on D-MPC

With the developed linearization turbine model proposed in Section 6.2 and measurement feedback, the D-MPC can determine the operation region in which the wind turbine is located. The corresponding prediction model and matrix for local optimization are formulated. With the mutual communication with the central unit, the iterations are executed to reach the global constraints. The central unit doesn't afford much computation task. Instead, it is used to update the dual variables by collecting the matrices from wind turbines which are computed off-line. More details are described in Section 6.3.4. As the outputs of D-MPC, the modified power references ( $P_{ref}^{WT_1}$ ,  $P_{ref}^{WT_2}$ ,  $\dots$ ,  $P_{ref}^{WT_i}$ ) are assigned to the individual wind turbine controller.

### 6.3.2 MPC problem formulation

The cost function of the D-MPC design considers both the tracking performance of the wind power plant power reference and the alleviation of the wind turbine load. During the wind power plant operation, it is assumed that the mean wind speed  $\bar{v}_w$  of a certain period (10 minutes in [156]) can be estimated and an

initial distribution of individual wind turbine power references for this period is known. Therefore, the mean power reference for the  $i$ th wind turbine  $\overline{P_{\text{ref}}^{\text{WT}_i}}$  can be calculated by simple proportional algorithm according to the available power.

$$\overline{P_{\text{ref}}^{\text{WT}_i}} = \alpha_i P_{\text{ref}}^{\text{wfc}}, \quad \text{with } \sum_{i=1}^{n_t} \alpha_i = 1, \quad (6.29)$$

where  $n_t$  is the number of wind turbine in the wind power plant,  $P_{\text{ref}}^{\text{wfc}}$  is the power reference for the wind power plant,  $\alpha_i$  indicates the distribution factor for the  $i$ th wind turbine. Accordingly, other steady state variables, e.g. the shaft torque  $\overline{T_s^{\text{WT}_i}}$ , can be decided.

The prediction horizon is  $n_p$ . By defining

$$\begin{aligned} P_g^{\text{WT}_i}(k) &= u_i(k), \\ T_s^{\text{WT}_i}(k) &= S_1 \cdot y_i(k), S_1 = [1, 0], \\ F_t^{\text{WT}_i}(k) &= S_2 \cdot y_i(k), S_2 = [0, 1], \\ u_i &= [u_i(0), \dots, u_i(n_p - 1)]', \\ u &= [u_1', \dots, u_{n_t}']', \end{aligned}$$

the MPC problem at time step  $k$  can be formulated as follows,

$$\begin{aligned} \min_u \sum_{i=1}^{n_t} \left( \underbrace{\sum_{k=0}^{n_p-1} \| u_i(k) - \overline{P_{\text{ref}}^{\text{WT}_i}} \|^2}_{\text{Term1}} \right) &+ \underbrace{\sum_{k=0}^{n_p-1} \| S_1 \cdot y_i(k) - \overline{T_s^{\text{WT}_i}} \|^2}_{\text{Term2}} \\ &+ \underbrace{\sum_{k=0}^{M-1} \| \Delta(S_2 \cdot y_i(k)) \|^2}_{\text{Term3}} \end{aligned} \quad (6.30)$$

subject to

$$x_i(k+1) = A_d x_i(k) + B_d u_i(k) + E_d d_i(k) + F_d \quad (6.31)$$

$$y_i(k) = C_d x_i(k) + D_d u_i(k) + G_d d_i(k) + H_d \quad (6.32)$$

$$x_i(0) = x_i(t) \quad (6.33)$$

$$\sum_{i=1}^{n_t} u_i(0) = P_{\text{ref}}^{\text{wfc}} \quad (6.34)$$

$$x_i \in \mathcal{X}_i, u_i \in \mathcal{U}_i, \quad (6.35)$$

where  $Q_P$ ,  $Q_T$  and  $Q_F$  are the weighting factors. The second and third terms in the cost function are used to penalize the deviation of the shaft torque from



the steady state and the derivative of the thrust force in order to reduce the wind turbine load,  $\mathcal{X}_i$  and  $\mathcal{U}_i$  are the local state and control input constraint sets, respectively. As the optimization variable  $u$ , the first values ( $u_i(0)$ ,  $i \in [1, \dots, n_t]$ ) are taken as the control inputs for each turbine. The control inputs are coupled whose summary equals to the power reference of the wind power plant  $P_{\text{ref}}^{\text{wfc}}$  (see Eqn. 6.34).

### 6.3.3 Transform into standard QP problem

The MPC problem described in Section 6.3.2 can be reformulated as a standard Quadratic Programming (QP) problem. In this section, the transform procedure is described.

#### 6.3.3.1 Preliminary and notation

Consider a single wind turbine disregarding the turbine index  $i$ , the discrete model is rewritten as

$$x(k+1) = A_d x(k) + B_d u(k) + E_d d(k) + F_d, \quad (6.36)$$

$$y(k) = C_d x(k) + D_d u(k) + G_d d(k) + H_d, \quad (6.37)$$

with

$$u = [u(0), \dots, u(n_p - 1)]',$$

$$d = [d(0), \dots, d(n_p - 1)]',$$

$$y = [y(0), \dots, y(n_p - 1)]'.$$

By substituting Eqn. 6.36 into Eqn. 6.37 recursively, we get

$$\begin{aligned}
 y = & \underbrace{\begin{bmatrix} C_d \\ C_d A_d \\ \vdots \\ C_d A_d^{n_p-1} \end{bmatrix}}_{\Phi} x_0 + \underbrace{\begin{bmatrix} D_d & 0 & \cdots & 0 \\ C_d B_d & D_d & \cdots & 0 \\ \vdots & \vdots & \ddots & \vdots \\ C_d A_d^{n_p-2} B_d & C_d A_d^{n_p-3} B_d & \cdots & D_d \end{bmatrix}}_{\Gamma_u} u \\
 & + \underbrace{\begin{bmatrix} G_d & 0 & \cdots & 0 \\ C_d E_d & G_d & \cdots & 0 \\ \vdots & \vdots & \ddots & \vdots \\ C_d A_d^{n_p-2} E_d & C_d A_d^{n_p-3} E_d & \cdots & G_d \end{bmatrix}}_{\Gamma_d} d \\
 & + \underbrace{\begin{bmatrix} H_d & 0 & \cdots & 0 \\ C_d F_d & H_d & \cdots & 0 \\ \vdots & \vdots & \ddots & 0 \\ C_d A_d^{n_p-2} F_d & C_d A_d^{n_p-3} F_d & \cdots & H_d \end{bmatrix}}_{\Gamma_f}, \quad (6.38)
 \end{aligned}$$

where  $\Phi$ ,  $\Gamma_u$ ,  $\Gamma_d$ ,  $\Gamma_f$  represent the coefficient matrices of  $u$ ,  $d$  and constant matrix, respectively. As  $y = [T_s^{\text{WT}}, F_t^{\text{WT}}]'$ , let  $y_1$ ,  $y_2$  indicate  $T_s^{\text{WT}}$  and  $F_t^{\text{WT}}$  for simplification. Accordingly, the coefficient matrices and constant matrix can be decomposed into two parts and we obtain the following equations,

$$y_1 = \Phi_1 x_0 + \Gamma_{1u} u + (\Gamma_{1d}) d + \Gamma_{1f}, \quad (6.39)$$

$$y_2 = \Phi_2 x_0 + \Gamma_{2u} u + (\Gamma_{2d}) d + \Gamma_{2f}. \quad (6.40)$$

### 6.3.3.2 Transformation

Similar with Eqn. 6.30, the cost function of MPC for single wind turbine can be separated into three terms, as shown in Eqn. 6.41

$$\underbrace{\sum_{k=0}^{n_p-1} \frac{1}{2} \| u(k) - r_0 \|_{Q_0}^2}_{\text{Part1}} + \underbrace{\sum_{k=0}^{n_p-1} \frac{1}{2} \| y_1(k) - r_1 \|_{Q_1}^2}_{\text{Part2}} + \underbrace{\sum_{k=1}^{n_p-1} \frac{1}{2} \| \Delta y_2(k) \|_{Q_3}^2}_{\text{Part3}}, \quad (6.41)$$

where  $r_0, r_1$  represent the reference values  $\overline{P_{\text{ref}}^{\text{WT}}}, \overline{T_s^{\text{WT}}}$ ,  $Q_0, Q_1, Q_2$  correspond to  $Q_P, Q_T, Q_F$ .

**Term 1**

By defining vector  $\Lambda = [1, \dots, 1]'$ ,  $\Lambda \in \mathbb{R}^{n_p \times 1}$  and identity matrix  $I \in \mathbb{R}^{n_p \times n_p}$ , Term 1 can be transformed into

$$\sum_{k=0}^{n_p-1} \frac{1}{2} \|u(k) - r_0\|_{Q_1}^2 = \frac{1}{2} u' H_0 u + g_0' u + \rho_0, \quad (6.42)$$

with

$$\begin{aligned} b_0 &= r_0 \Lambda, \\ H_0 &= I Q_0, \\ g_0 &= -I Q_0 b_0, \end{aligned}$$

where  $H_0 \in \mathbb{R}^{n_p \times n_p}$ ,  $g_0 \in \mathbb{R}^{n_p \times 1}$  represent Hessian and coefficient vector for Term 1, respectively. As the constant part  $\rho_0$  doesn't affect the solution of cost function, it is disregarded. It is the same case for Term 2 and Term 3.

**Term 2**

With the similar calculation procedure in Term 1, Term 2 can be transformed into

$$\sum_{k=0}^{n_p-1} \frac{1}{2} \|y_1(k) - r_1\|_{Q_1}^2 = \frac{1}{2} u' H_1 u + g_1' u + \rho_1, \quad (6.43)$$

with

$$\begin{aligned} b_1 &= r_1 \Lambda - \Phi_1 x_0 - \Gamma_{1d} d \Lambda - \Gamma_{1f}, \\ H_1 &= \Gamma_{1u}' I Q_1 \Gamma_{1u}, \\ g_1 &= -\Gamma_{1u}' I Q_1 b_1, \end{aligned}$$

where  $H_1 \in \mathbb{R}^{n_p \times n_p}$ ,  $g_1 \in \mathbb{R}^{n_p \times 1}$  represent Hessian and coefficient vector for Term 2, respectively.

**Term 3**

With  $\Delta y_2(k) = y_2(k) - y_2(k-1)$ , the value of  $y_2$  at previous time step is marked as  $y_2(-1)$ , Term 3 can be transformed into

$$\sum_{k=1}^{n_p-1} \frac{1}{2} \|\Delta y_2(k)\|_{Q_2}^2 = \frac{1}{2} u' H_2 u + g_2' u + \rho_2, \quad (6.44)$$

with

$$M_1 = \begin{bmatrix} 1 & 0 & 0 & \cdots & 0 \\ -1 & 1 & 0 & \cdots & 0 \\ 0 & -1 & 1 & \cdots & 0 \\ \vdots & \vdots & \vdots & \ddots & \vdots \\ 0 & 0 & 0 & \cdots & 1 \end{bmatrix}, M_2 = \begin{bmatrix} 1 \\ 0 \\ 0 \\ \vdots \\ 0 \end{bmatrix},$$

$$\begin{aligned} b_2 &= -\Phi_2 x_0 - \Gamma_{2d} d\Lambda - \Gamma_{2f}, \\ H_2 &= \Gamma'_{2u} (M'_1 I Q_3 M_1) \Gamma_{2u}, \\ g_2 &= -\Gamma'_{2u} (M'_1 I Q_3 M_1) b_2 + \Gamma'_{2u} (M_2 Q_2 y_2(-1)), \end{aligned}$$

where  $M_1, M_2 \in \mathbb{R}^{n_p \times n_p}$ ,  $H_2 \in \mathbb{R}^{n_p \times n_p}$ ,  $g(2) \in \mathbb{R}^{n_p \times 1}$  represent Hessian and coefficient vector for Term 3, respectively.

Based on Eqn. 6.42–Eqn. 6.44, the equivalent standard QP format of MPC problem for single wind turbine can be written as

$$\frac{1}{2} u' H u + g' u, \quad (6.45)$$

with  $H = H_0 + H_1 + H_2$ ,  $g = g_0 + g_1 + g_2$ .

For wind power plant with multiple wind turbines, the MPC problem in Eqn. 6.30 is derived

$$\min_u \Phi = \sum_{i=1}^{n_t} \Phi_i(u_i) = \sum_{i=1}^{n_t} \left( \frac{1}{2} u'_i H_i u_i + g'_i u_i \right), \quad (6.46)$$

subject to

$$G u = b, \quad (6.47)$$

$$u \in \mathcal{U}. \quad (6.48)$$

where  $u = [u'_1, \dots, u'_N]'$ ,  $\mathcal{U}$  indicates the feasible region of  $u$ , the equality constraint Eqn. 6.47 represents  $\sum_{i=1}^{n_t} (0) = P_{\text{ref}}^{\text{wfc}}$ . Accordingly,  $G$  and  $b$  can be derived as

$$\begin{aligned} G &= [G_1, \dots, G_{n_t}], G_i = [1, 0, \dots, 0], G_i \in \mathbb{R}^{1 \times n_p}, \\ b &= P_{\text{ref}}^{\text{wfc}}. \end{aligned}$$

### 6.3.4 Parallel generalized fast dual method

#### 6.3.4.1 Properties of dual problem

In this section, the key properties are described which is required for the implementation of fast dual gradient method in the following. From Eqn. 6.46, it is obvious that the cost functions  $\Phi$  and  $\Phi_i$  are strongly convex with matrices  $H$  and  $H_i$ , which is defined as  $H = \text{blkdiag}(H_1, \dots, H_{n_t})$ . By introducing the dual variable  $\lambda$ , the primal minimization problem is transformed into the following Lagrange dual problem,

$$\begin{aligned} & \sup_{\lambda} \inf_u \{ \Phi(u) + \lambda(Gu - b) \} \\ & = \sup_{\lambda} \sum_{i=1}^{n_t} [\inf_{u_i} \{ \Phi_i(u_i) + \lambda G_i u_i \} - \lambda \frac{b}{n_t}]. \end{aligned} \quad (6.49)$$

With the definition of conjugate functions for  $\Phi$  and  $\Phi_i$ ,

$$\begin{aligned} \Phi^*(-G'\lambda) &= \sup_u (-\lambda Gu - \Phi(u)), \\ \Phi_i^* &= \sup_{u_i} (-\lambda G_i u_i - \Phi_i(u_i)), \end{aligned}$$

the dual problem in Eqn. 6.49 can be rewritten as

$$\begin{aligned} & \sup_{\lambda} \{ -\Phi^*(-G'\lambda) - \lambda b \} \\ & = \sup_{\lambda} \sum_{i=1}^{n_t} \{ -\Phi_i^*(-G'_i \lambda) - \lambda \frac{b}{n_t} \}. \end{aligned} \quad (6.50)$$

For simplicity, the following equations are defined,

$$d_i(\lambda) = -\Phi_i^*(-G'_i \lambda) - \lambda \frac{b}{n_t}, \quad (6.51)$$

$$d(\lambda) = -\Phi^*(-G'\lambda) - \lambda' b, d = \sum_{i=1}^N d_i. \quad (6.52)$$

**Theorem 1:** Assume that  $\Phi$  is strongly convex with matrix  $H$ . The dual function  $d$  defined in (6.52) is concave, differentiable and satisfies

$$d(\lambda_1) \geq d(\lambda_2) + \nabla d(\lambda_2)(\lambda_1 - \lambda_2) - \frac{1}{2} \|\lambda_1 - \lambda_2\|_{\mathbf{L}}^2 \quad (6.53)$$

for every  $\lambda_1, \lambda_2$  and  $\mathbf{L}$  with  $\mathbf{L} \succeq GH^{-1}G'$ . The proof is presented in [162].

**Corollary 1:** According to Theorem 1, assume that  $\Phi_i$  is strongly convex with matrix  $H_i$ , the local dual function  $d_i$  defined in (6.51) is concave, differentiable and satisfies

$$d_i(\lambda_1) \geq d_i(\lambda_2) + \nabla d_i(\lambda_2)(\lambda_1 - \lambda_2) - \frac{1}{2} \|\lambda_1 - \lambda_2\|_{\mathbf{L}_i}^2 \quad (6.54)$$

for every  $\lambda_1, \lambda_2$  and  $\mathbf{L}_i$  with  $\mathbf{L}_i \succeq G_i H_i^{-1} G_i'$ . The proof is presented in [162].

Theorem 1 and Corollary 1 imply a tighter quadratic lower bound to the dual function. It can be further proved that the obtained bound is the best obtained bound. Therefore, the approximation of the dual function is more accurate, which improves the converge rate. A generalized parallel optimization algorithm proposed in [162] is presented in the following.

#### 6.3.4.2 Distributed optimization algorithm

The fast dual gradient method is implemented in parallel way for the wind power plant control. Dual variables  $\lambda$ ,  $\eta$  and  $\varphi$  are introduced. Generally, the iteration stops if the predefined tolerance is met. In this study, a fixed number of iteration  $k_{\max}$  is selected as the stopping criterion in order to limit the online computation time.

---

#### Parallel generalized fast dual gradient method

---

**Require:** Initial guesses  $\lambda^{[1]} = \eta^{[0]}$ ,  $\phi^{[1]} = 1$ .

**for:**  $k = 1, \dots, k_{\max}$ , **do**

1. Send  $\lambda^{[k]} = (\dots, \mu_j^k, \dots)$  to wind turbines through communication from Central Unit to D-MPC.
2. Update and solve the local optimization with augmented cost function in individual D-MPC:  

$$u_i^{[k]} = \arg \min_{u_i} \{\Phi_i + u_i' G' \lambda^{[k]}\}.$$
3. Receive  $u_i^{[k]}$  from D-MPC of each turbine and form  $u^{[k]} = (u_1^{[k]}, \dots, u_{n_t}^{[k]})$  in Central Unit.

4. Update the dual variables in Central Unit:

$$\begin{aligned}\eta^{[k]} &= \lambda^{[k]} + \mathbf{L}^{-1}(Gu^{[k]} - b) \\ \varphi^{[k+1]} &= \frac{1 + \sqrt{1 + 4(\varphi^{[k]})^2}}{2} \\ \lambda^{[k+1]} &= \eta^{[k]} + \left(\frac{\varphi^{[k]} - 1}{\varphi^{[k+1]}}\right)(\eta^{[k]} - \eta^{[k-1]})\end{aligned}$$

**end for**

---

**Proposition:** If the assumption in Theorem 1 holds and  $\mathbf{L} \succeq GH^{-1}G'$ , the algorithm converges with the rate,

$$d(\lambda^*) - d(\lambda^k) \leq \frac{2\|\lambda^* - \lambda_2\|_{\mathbf{L}}^2}{(k+1)^2}, \forall k \geq 1, \quad (6.55)$$

where  $k$  is the iteration number index. The details of the proof is described in [162].

As illustrated, the convergence rate is improved from  $\mathcal{O}(1/k)$  to  $\mathcal{O}(1/k^2)$  with negligible increase in iteration complexity, compared with the standard gradient method.  $\mathbf{L} = GH^{-1}G'$  has the tightest upper bounds and is adopted in this study.

Since all the turbines are related, the  $\mathbf{L}^{-1}$  could be calculated as follows,

$$\mathbf{L}^{-1} = \sum_{i=1}^{n_t} \mathbf{L}_i^{-1} = \sum_{i=1}^{n_t} (G_i H_i^{-1} G_i)^{-1}. \quad (6.56)$$

To be noticed, the linearized model of the individual turbine varies with the change of the operating region. According to Eqn. 6.42–6.44, the Hessian matrix  $H_i$  is dependent on the linearized model and time-variant. It further leads to the variation of  $\mathbf{L}_i^{-1}$ . In order to reduce the online computation complexity, the variables involved in the computation, including  $H_i$  and  $\mathbf{L}_i^{-1}$  can be pre-computed offline and stored according to the operation regions.

The calculation burden of Central Unit only consists of the calculation of  $\mathbf{L}^{-1}$  which is the simple addition of the individual  $\mathbf{L}_i^{-1}$  and the dual variable updates during iterations. Most computation tasks are distributed to the local D-MPCs.

Besides, due to the reduced iteration number, the communication burden between D-MPC and Central Unit has been largely reduced. In summary, this control structure is mostly independent on the scale of the wind power plant and suitable for modern wind power plant control application.

## 6.4 D-MPC with energy storage

The D-MPC control algorithm applied for coordination between wind turbines in Section 6.3 can be extended to the case with ESS integration.

As described in Chapter 3, a typical application of ESS with small energy density but large power density for wind power plant is smoothing the power output fluctuation to improve the power quality. Moreover, it has the potential to contribute to the mitigation of mechanical loads. To be specific, with the coordinate control strategy described in Section 6.3, the power references distributed to individual wind turbines ( $P_{\text{ref}}^{\text{WT}_i}, i \in [1, \dots, n_t]$ ) are limited by the constraint in Eqn. 6.34. With additional ESS, the constraint can be relaxed to some extent. Accordingly, the references can be regulated more flexibly which leads to a better performance of load alleviation.

### 6.4.1 Control structure

The control structure of wind power plant with ESS is illustrated in Fig. 6.10. Compared with the case without ESS (Fig. 6.9), an additional ESS part is marked with dashed rectangle. The power reference  $P_{\text{ref}}^{\text{ESS}}$  consists of two parts:  $P_{\text{ref1}}^{\text{ESS}}$  and  $P_{\text{ref2}}^{\text{ESS}}$  corresponding to different controllers.

- $P_{\text{ref1}}^{\text{ESS}}$ . This reference is derived by D-MPC controller which aims to minimize the mechanical loads of wind turbines. It is described in the following.
- $P_{\text{ref2}}^{\text{ESS}}$ . This reference is derived by smoothing controller which aims to smooth the wind power plant production. The functionality and control structure are introduced in Section 3.6.2.



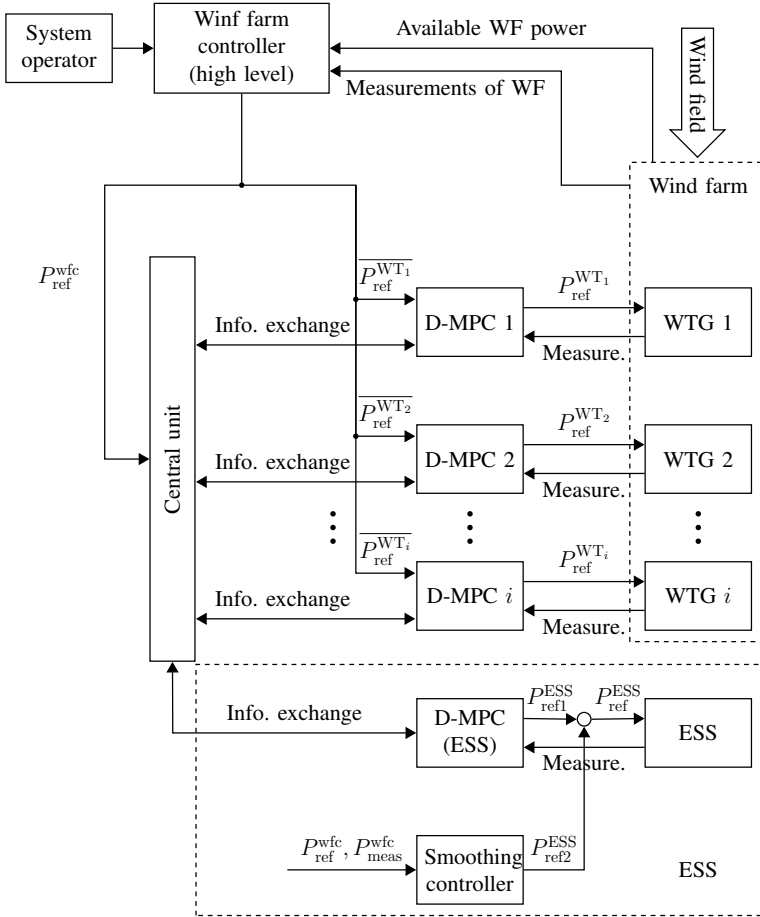


Figure 6.10: Control structure of wind power plant with ESS

### 6.4.2 MPC problem formulation

Similarly with the cost function described in Section 6.3.2, both the tracking performance of the wind power plant power reference and the alleviation of the wind turbine load. The additional variable related to ESS are introduced,  $c_{ess}$  indicates the State of Charge (SOC) of ESS,  $p_{ess}$  indicated the power of ESS which is the optimization variable. The technical constraints regarding power, capacity and power rate are considered.

The MPC problem at time step  $k$  can be formulated as follows

$$\begin{aligned} \min_{u, p_{\text{ess}}} \sum_{i=1}^{n_t} & \left( \sum_{k=0}^{n_p} \| u_i(k) - \overline{P_{\text{ref}}^{\text{WT}_i}} \|^2_{Q_P} + \sum_{k=0}^{n_p} \| S_1 \cdot y_i(k) - \overline{T_s^{\text{WT}_i}} \|^2_{Q_T} \right. \\ & \left. + \sum_{k=0}^{n_p-1} \| \Delta(S_2 \cdot y_i(k)) \|^2_{Q_F} \right) + \underbrace{\| c_{\text{ess}} - c_{\text{mid}} \|^2_{Q_C}}_{\text{Term for ESS}}. \end{aligned} \quad (6.57)$$

subject to

$$\begin{aligned} x_i(k+1) &= A_d x_i(k) + B_d u_k(t) + E_d d_i(k) + F_d \\ y_i(k) &= C_d x_i(k) + D_d u_i(k) + G_d d_i(k) + H_d \end{aligned} \quad (6.58)$$

$$x_i(0) = x_i(t) \quad (6.59)$$

$$x_i \in \mathcal{X}_i, u_i \in \mathcal{U}_i \quad (6.60)$$

$$c_{\text{ess}}(k+1) = c_{\text{ess}}(k) + p_{\text{ess}}(k) \cdot t_s \quad (6.61)$$

$$p_{\text{ess}}(0) + \sum_{i=1}^{n_t} u_i(0) = P_{\text{ref}}^{\text{wfc}} \quad (6.62)$$

$$p_{\text{ess}} \in \mathcal{P} = [-\overline{p_{\text{ess}}}, \overline{p_{\text{ess}}}] \quad (6.63)$$

$$c_{\text{ess}} \in \mathcal{C} = [\underline{c_{\text{ess}}}, \overline{c_{\text{ess}}}] \quad (6.64)$$

$$\Delta p_{\text{ess}} \in \mathcal{D}_i = [-\overline{\Delta p_{\text{ess}}}, \overline{\Delta p_{\text{ess}}}] \quad (6.65)$$

Compared with the cost function in Eqn. 6.30, the additional term for ESS is used to penalize that charging level of ESS is too low or high.  $Q_C$  is the weighting factor,  $c_{\text{mid}}$  is the middle charging level. Eqn. 6.63 represents the power constraint of ESS and  $\overline{p_{\text{ess}}}$  indicates the power limit. Eqn. 6.64 represents the capacity constraint of ESS,  $\overline{c_{\text{ess}}}$  and  $\underline{c_{\text{ess}}}$  indicate the capacity upper and lower limit, respectively. Eqn. 6.65 represents the power rate constraint of ESS and  $\overline{\Delta p_{\text{ess}}}$  indicates the power rate limit.

By combination of Eqn. 6.62 and Eqn. 6.63, we can get

$$P_{\text{ref}}^{\text{wfc}} - \overline{p_{\text{ess}}} \leq \sum_{i=1}^{n_t} u_i(0) \leq P_{\text{ref}}^{\text{wfc}} + \overline{p_{\text{ess}}}. \quad (6.66)$$

Compared with Eqn. 6.34, the control inputs are relaxed and have more regulation flexibility. Accordingly, a better load minimization performance can be expected. It will be verified in the simulation.

## 6.5 Simulation and results

### 6.5.1 Verification of PWA Model

In this section, the proposed PWA model is compared with 5 MW NREL non-linear wind turbine model. The PWA modeling and simulation are carried out by means of the Matlab toolbox–Multi-Parametric Toolbox (MPT) [171]. Two case scenarios including high and low wind conditions are designed to test the developed PWA model. Percentage Root Mean Square Error (%RMSE) is used for model mismatch evaluation. Lower %RMSE means less mode mismatch and better model estimation. The simulation time for both cases is 300 s. Besides, the power reference is also variable during simulation, as illustrated in Fig. 6.11, which has two step changes at  $t = 100$  s and  $t = 200$  s.

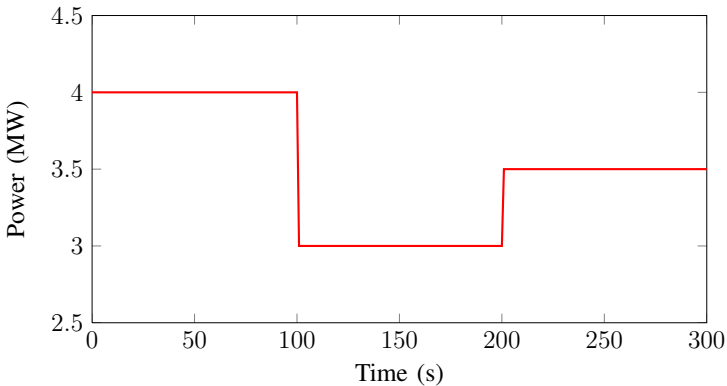


**Figure 6.11:** Power reference during simulation

#### 6.5.1.1 Low wind speed case

The wind speed profile of this case is shown in Fig. 6.12, which covers the range between 10 m/s and 15 m/s. The simulation results of both PWA model (PWA) and nonlinear NREL model (NL) are illustrated and compared in Fig. 6.13 and Fig. 6.14, including system states ( $\theta$  and  $\omega_r$ ) and outputs ( $T_s$ ,  $F_t$ ).

The pitch angle  $\theta$  varies following the wind variation to regulate the power production. When the pitch angle is reduced to  $\theta = 0$ , the pitch angle control is deactivated and the system gets into Area II. Otherwise rotor speed  $\omega_r$  is regulated to avoid the rotor from over-speeding. The rated rotor speed value

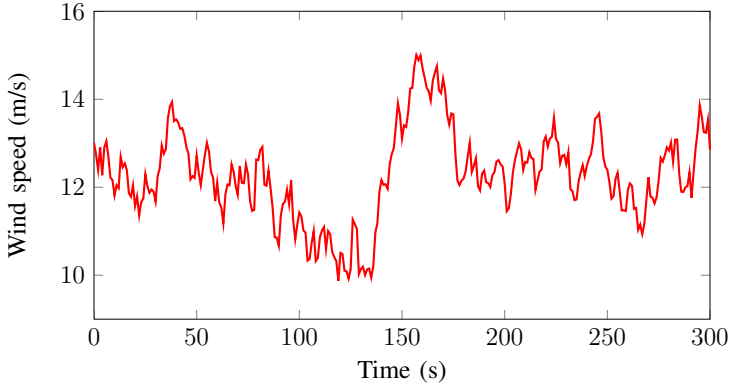


**Figure 6.12:** Wind speed variation in the low speed condition

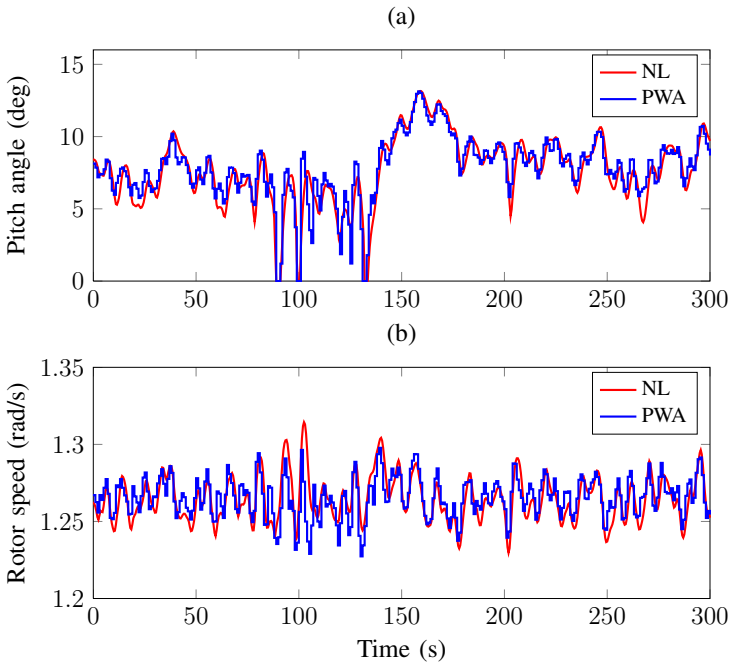


**Figure 6.13:** State variable comparison

$\omega_{\text{rated}} = 1.2671$  p.u.. The shaft torque basically follows the variation of the power reference. The %RMSE values of  $\theta$ ,  $\omega_r$ ,  $T_s$  and  $F_t$  are listed in Table 6.1. The maximum %RMSE value is 9.8916 which is lower than the commonly used threshold of 10. Thus, it shows a good agreement between these two models

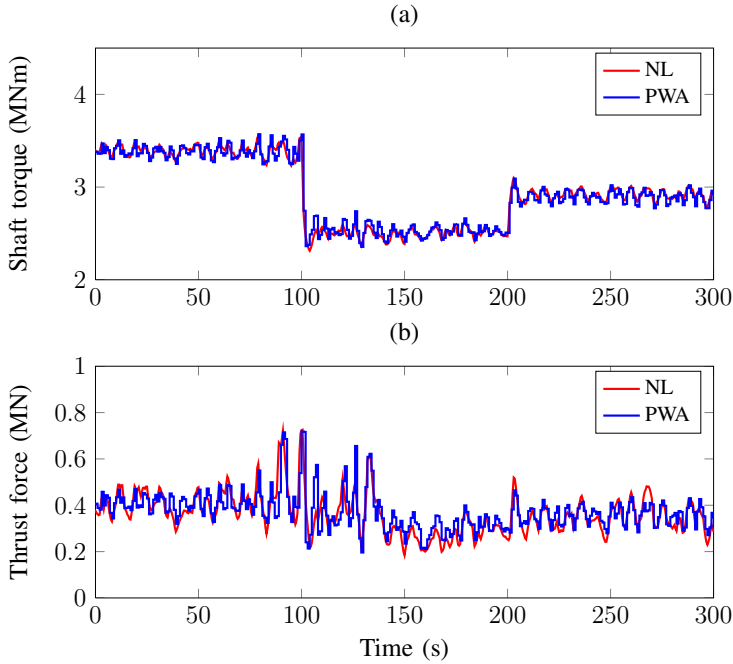


**Figure 6.14:** Output variable comparison

which verifies the developed PWA model in the low wind condition.

**Table 6.1:** Simulation statistics %RMSE

	$\theta$	$\omega_r$	$T_s$	$F_t$
Low Wind	5.5827	1.0283	2.1631	9.8316
High Wind	3.8706	0.8070	1.6585	7.7993

### 6.5.1.2 High wind speed case

The Similar procedure is carried out for the high wind speed case. By shifting the low speed wind profile upwards, the high wind speed ranges from 15 m/s to 20 m/s, as depicted in Fig. 6.15. The simulation results of both PWA model (PWA) and nonlinear NREL model (NL) are illustrated and compared in Fig. 6.16 and Fig. 6.17, including system states ( $\theta$  and  $\omega_r$ ) and outputs ( $T_s$ ,  $F_t$ ).

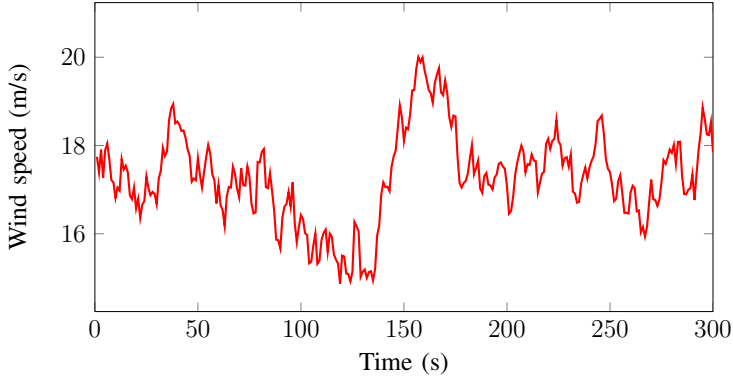


**Figure 6.15:** Wind speed variation in the high speed condition

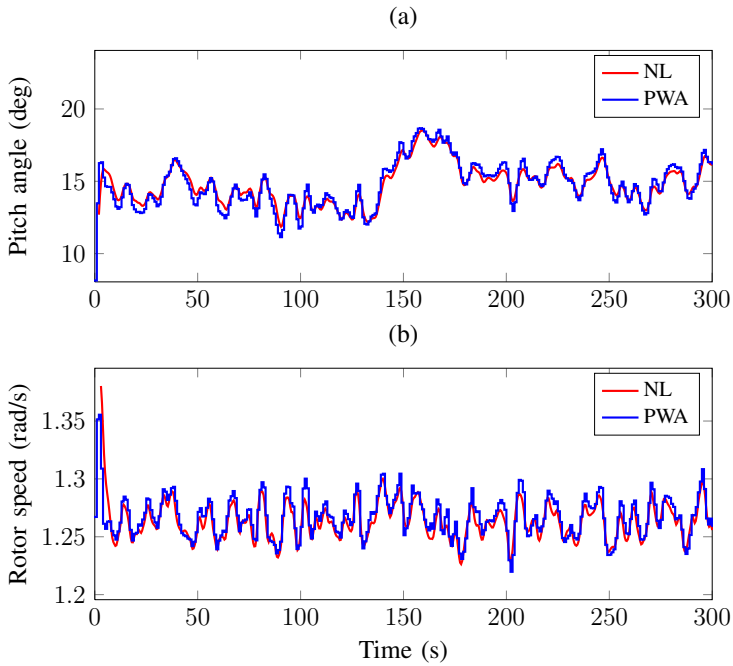


**Figure 6.16:** State variable comparison

The pitch angle  $\theta$  varies following the wind variation to regulate the power production. The pitch angle control is always in the active status (Area I). Rotor speed  $\omega_r$  is regulated around its rated value 1.2671. The shaft torque basically follows the variation of the power reference. The %RMSE values in the high wind case are listed in Table 6.1, which ranges from 0.8070 to 7.7993.

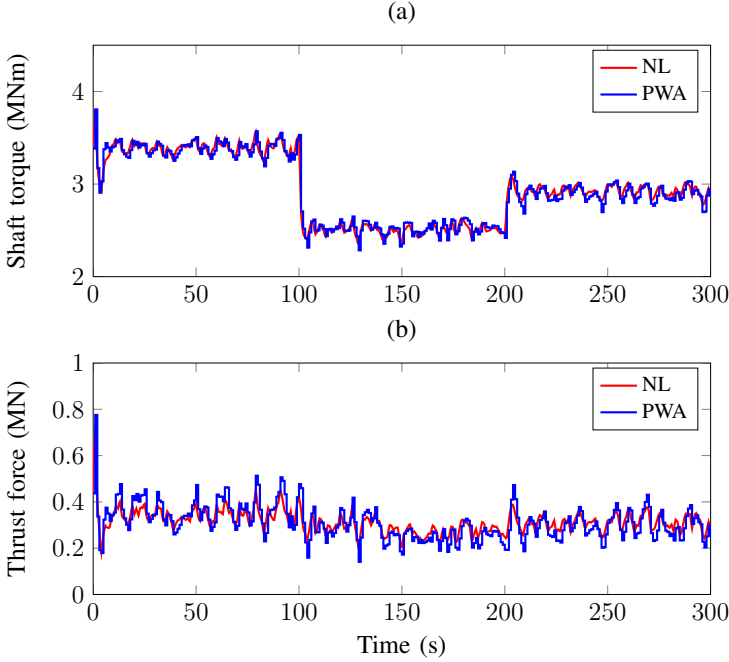


**Figure 6.17:** Output variable comparison

It shows a good agreement between these two models. The developed PWA model is verified in the high wind condition.

### 6.5.2 wind power plant control based on D-MPC without ESS

In this section, different case scenarios are designed to evaluate the control performance of the developed D-MPC. Firstly, the convergence of the adopted fast dual gradient method is shown. The suitable maximum iteration number  $k_{\max}$  can be determined which is used for the following simulation cases. Secondly, the operation of the wind power plant under both low and high wind conditions are tested and analyzed.

A wind power plant including  $10 \times 5$  MW wind turbines is used as the test system. The sampling time for wind power plant control  $t_s$  is set 1 s. The mean wind speed for each wind turbine is assumed to be known. All the wind turbines are in the derated operation. The wind field modeling for the wind power plant

is generated in SimWindFarm [172], which is a toolbox for dynamic wind power plant model, simulation and control. The prediction horizon for MPC is set  $N_p = 10$ . The wind speed is considered as a measurable disturbance and the value for the prediction horizon is based on persistence assumption, suitable for the short period prediction.

### 6.5.2.1 Convergence with the fast dual gradient method

The convergences of the fast dual gradient with different  $\mathbf{L}$  are compared in Fig. 6.18. The  $y$ -axis denotes the deviation to the constraints (see (7)). Apparently, the convergence rate with  $\mathbf{L} \succeq GH^{-1}G'$  is higher. Especially when  $\mathbf{L} = GH^{-1}G'$ , which has the tightest upper bounds, the convergence is fastest. Only 5 iterations can guarantee the good performance of D-MPC. Therefore, the maximum iteration number is selected  $k_{\max} = 5$  for the following.

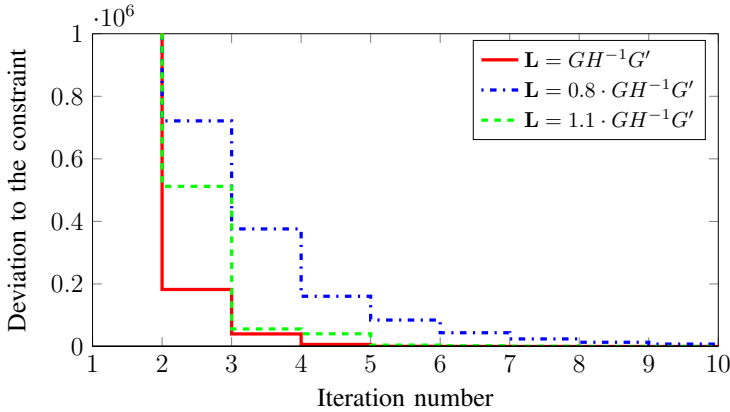


**Figure 6.18:** Convergence comparison with different  $\mathbf{L}$

### 6.5.2.2 Operation under high and low wind conditions

The operation of the wind power plant is simulated under both high and low wind conditions. Accordingly, the power references of the wind power plant  $P_{\text{ref}}^{\text{wfc}}$  are defined 40 MW and 30 MW and assumed to be invariable during the simulation. The wind profiles of the high speed case are derived by shifting low speed wind profile upwards by 4 m/s. The turbulence part is therefore regarded as the same.



WT 05 is taken as an example to illustrate the simulation results. Its wind speed profile for both wind conditions is shown in Fig. 6.19, which covers the range between 11 m/s and 20 m/s. The mean values of all the wind turbines for both conditions are listed in Table 6.3 and 6.5, respectively. The simulation time is 300 s.

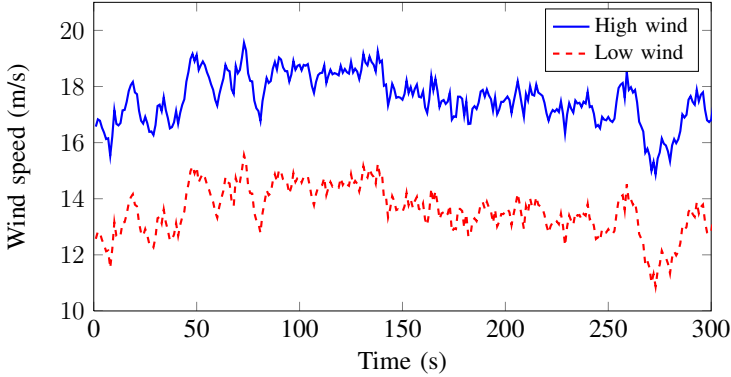


**Figure 6.19:** Wind speed variation of WT 05

The weighting factors are set,  $Q_P = 1$ ,  $Q_T = 20$ ,  $Q_F = 5$ . As explained in [156],  $Q_F$  should be kept small to avoid violent control and shaft load increase.

The control performances of three controllers are illustrated and compared, including: (1) Centralized Control, (2) C-MPC, (3) D-MPC. For the centralized wind power plant controller, the proportional distribution algorithm proposed in [153] is adopted. The power reference for all the wind turbines are considered the same. That means  $P_{\text{ref}}^{\text{WF}_i} = \frac{P_{\text{ref}}^{\text{wfc}}}{n_t}$ . For the high wind case,  $P_{\text{ref}}^{\text{WF}_i} = 4 \text{ MW}$  while  $P_{\text{ref}}^{\text{WF}_i} = 3 \text{ MW}$  for the low wind case.

### Power reference tracking

To evaluate the primary objective of the wind power plant controller, the comparison of  $P_{\text{gen}}^{\text{wfc}}$  for different controllers under both wind conditions is illustrated in Fig. 6.20. The standard deviation  $\sigma(P_{\text{gen}}^{\text{wfc}})$  is used to quantify the deviation to the references (40 MW in Fig. 6.20(a) and 30 MW in Fig. 6.20(b)), listed in Table 6.2. It can be observed that D-MPC shows almost identical control effect with the other two controllers. For the high wind condition, all the controllers have the same standard deviation value (0.0081 MW), only 0.020% of the reference (40 MW). For the low wind condition, the standard deviations of C-MPC and D-MPC are the same (0.0056 MW) and a little smaller than that of centralized controller (0.0057 MW). Compared with the reference value (30 MW), this tiny difference can be disregarded.

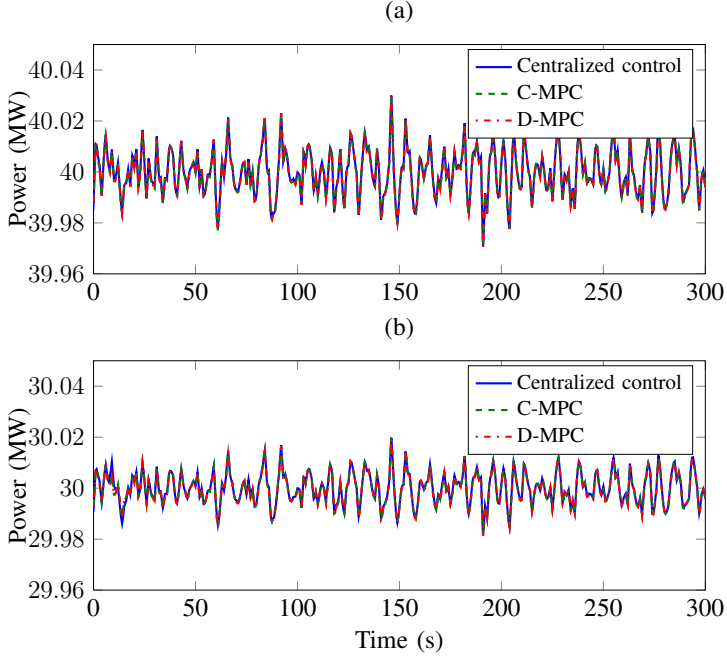


**Figure 6.20:** Active power of the wind power plant  $P_{gen}^{wfc}$ , (a) represents the high wind condition; (b) represents the low wind condition.

**Table 6.2:** Simulation Statistics  $\sigma(P_{gen}^{wfc})$  in MW

Turbine	Centralized Control	C-MPC	D-MPC
High Wind	0.0080	0.0080 (0.00%)	0.0080 (0.00%)
Low Wind	0.0057	0.0056 (-1.75%)	0.0056 (-1.75%)

### Mechanical load alleviation

There is no need to illustrate the waveforms of all the simulation results. As the example,  $T_s$  and  $F_t$  of a single wind turbine (WT 05) with different controllers are illustrated in Fig. 6.21 and Fig. 6.22. It can be observed that the power reference by the MPC (C-MPC and D-MPC) varies following the wind speed (Fig. 6.21(a) and Fig. 6.22(a)). Accordingly, the deviation of the shaft torque  $T_s$  is significantly reduced (Fig. 6.21(b) and Fig. 6.22(b)). The alleviation of the thrust force is not obvious (Fig. 6.21(c) and Fig. 6.22(c)). Moreover, the results show that the control inputs of both C-MPC and D-MPC are almost identical, which proves that the D-MPC has the same control performance as

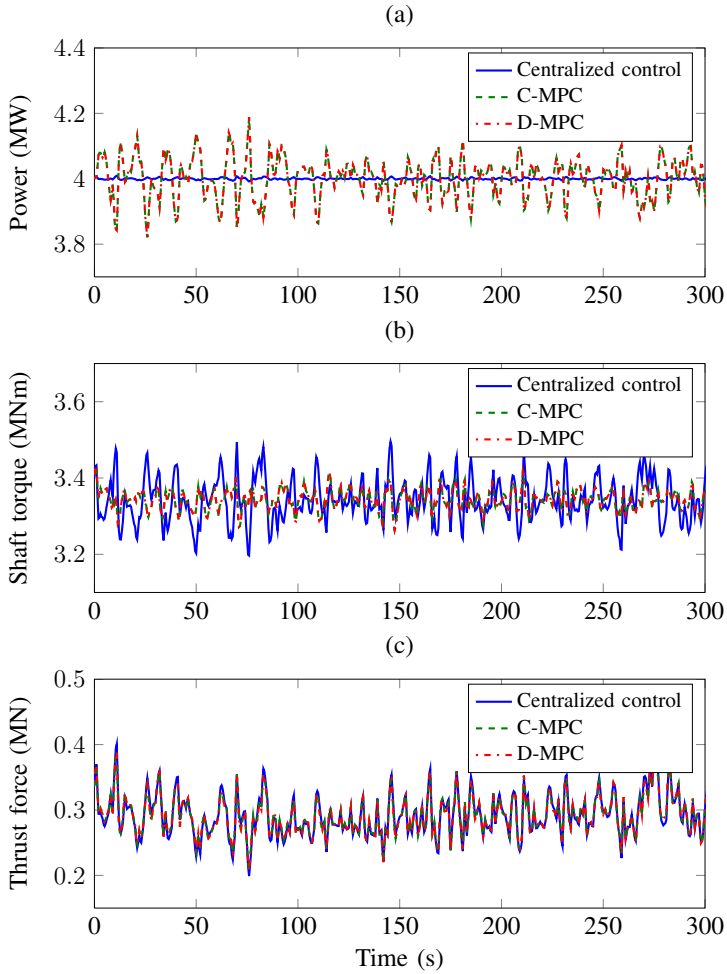


**Figure 6.21:** Simulation results of WT 05 under the high wind condition

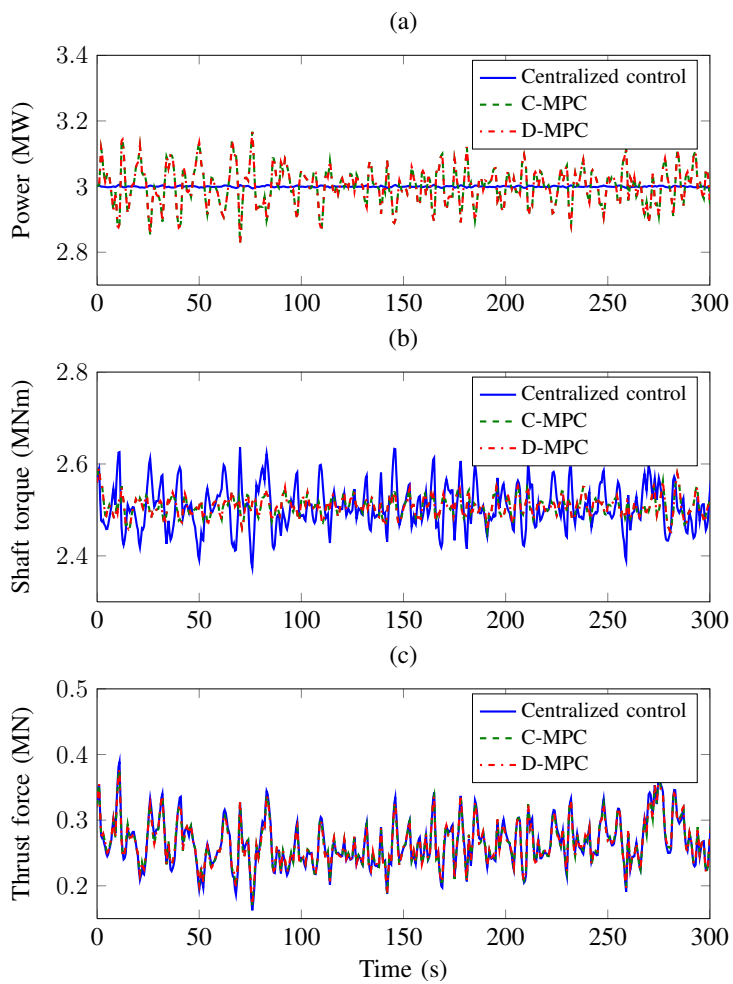


**Figure 6.22:** Simulation results of WT 05 under the low wind condition

**Table 6.3:** Simulation Statistics  $\sigma(T_s)$  in 0.01MNm

Turbine	$v_{avr}$ (m/s)	Centralized Control	C-MPC High Wind	D-MPC High Wind
WT 01	17.50	6.52	3.79 (-41.87%)	3.79 (-41.87%)
WT 02	17.02	6.99	3.33 (-52.36%)	3.33 (-52.36%)
WT 03	16.54	6.65	2.88 (-56.69%)	2.88 (-56.69%)
WT 04	16.64	6.48	3.22 (-50.31%)	3.22 (-50.31%)
WT 05	17.46	5.80	2.95 (-49.14%)	2.95 (-49.14%)
WT 06	17.00	5.70	3.10 (-45.61%)	3.10 (-45.61%)
WT 07	16.38	6.32	3.25 (-48.58%)	3.25 (-48.58%)
WT 08	17.14	6.11	2.84 (-53.52%)	2.84 (-53.52%)
WT 09	17.11	6.42	3.33 (-48.13%)	3.33 (-48.13%)
WT 10	16.45	7.26	3.70 (-49.04%)	3.70 (-49.04%)

**Table 6.4:** Simulation Statistics  $\sigma(\Delta F_t)$  in 0.01MN

Turbine	$v_{avr}$ (m/s)	Centralized Control	C-MPC High Wind	D-MPC High Wind
WT 01	17.50	1.76	1.76 (-0.00%)	1.76 (-0.00%)
WT 02	17.02	1.93	1.89 (-2.07%)	1.89 (-2.07%)
WT 03	16.54	1.77	1.74 (-1.69%)	1.74 (-1.69%)
WT 04	16.64	1.78	1.72 (-3.37%)	1.72 (-3.37%)
WT 05	17.46	1.56	1.53 (-1.92%)	1.53 (-1.92%)
WT 06	17.00	1.66	1.64 (-1.20%)	1.64 (-1.20%)
WT 07	16.38	1.82	1.77 (-2.75%)	1.77 (-2.75%)
WT 08	17.14	1.76	1.74 (-1.14%)	1.74 (-1.14%)
WT 09	17.11	1.57	1.52 (-3.18%)	1.52 (-3.18%)
WT 10	16.45	1.99	1.94 (-2.51%)	1.94 (-2.51%)

**Table 6.5:** Simulation Statistics  $\sigma(T_s)$  in 0.01MNm

Turbine	$v_{avr}$ (m/s)	Centralized Control	C-MPC Low Wind	D-MPC Low Wind
WT 01	13.50	5.48	2.85 (-47.99%)	2.85 (-47.99%)
WT 02	13.02	5.78	2.71 (-53.11%)	2.71 (-53.11%)
WT 03	12.54	5.60	2.99 (-46.61%)	2.99 (-46.61%)
WT 04	12.64	6.06	3.94 (-34.98%)	3.94 (-34.98%)
WT 05	13.46	4.85	2.24 (-53.81%)	2.24 (-53.81%)
WT 06	13.00	4.77	2.22 (-53.46%)	2.22 (-53.46%)
WT 07	12.38	5.99	3.10 (-48.25%)	3.10 (-48.25%)
WT 08	13.14	5.05	2.25 (-55.45%)	2.25 (-55.45%)
WT 09	13.11	5.31	3.19 (-39.92%)	3.19 (-39.92%)
WT 10	12.45	6.69	3.91 (-41.55%)	3.91 (-41.55%)

**Table 6.6:** Simulation Statistics  $\sigma(\Delta F_t)$  in 0.01MN

Turbine	$v_{avr}$ (m/s)	Centralized Control	C-MPC Low Wind	D-MPC Low Wind
WT 01	13.50	1.85	1.84 (-0.54%)	1.84 (-0.54%)
WT 02	13.02	2.03	1.99 (-2.01%)	1.99 (-2.01%)
WT 03	12.54	1.92	1.85 (-3.65%)	1.85 (-3.65%)
WT 04	12.64	2.59	2.55 (-1.54%)	2.55 (-1.54%)
WT 05	13.46	1.63	1.59 (-2.45%)	1.59 (-2.45%)
WT 06	13.00	1.75	1.72 (-1.71%)	1.72 (-1.71%)
WT 07	12.38	2.64	1.95 (-26.1%)	1.95 (-26.1%)
WT 08	13.14	1.84	1.81 (-1.63%)	1.81 (-1.63%)
WT 09	13.11	1.72	1.65 (-4.02%)	1.65 (-4.02%)
WT 10	12.45	2.63	2.62 (-0.38%)	2.62 (-0.38%)

the C-MPC.

The standard deviation  $\sigma(T_s)$  and  $\sigma(\Delta F_t)$  are used to quantify the variation of  $T_s$  and  $\Delta F_t$ . They can be used to evaluate the shaft and thrust-induced loads, respectively.

According to the statistics in Table 6.3 and 6.5, the shaft torque deviation is alleviated largely with MPC (C-MPC and D-MPC) for each wind turbine, compared with the centralized control.  $\sigma(T_s)$  in centralized control is taken as the reference. For the high wind case, the values range from 41.87% to 56.69% (Table 6.3). For the low wind case, the reduction percentages of the standard deviation are between 34.98% and 55.45% (Table 6.5).

The thrust force change is also damped to some extent in each wind turbine with D-MPC, according to Table 6.4 and 6.6. For the high wind case, the reduction percentages of standard deviation are between 0.00% and 3.18% (Table 6.4). For the low wind case, the values are between 0.38% and 26.1% (Table 6.6).

### 6.5.3 wind power plant control based on D-MPC with ESS

In order to illustrate the better control performance with ESS integration by D-MPC, the simulation results of three controllers are shown and compared, including: (1) Centralized Control, (2) D-MPC for the wind power plant without ESS, (3) D-MPC for the wind power plant with ESS. The simulation settings are the same as the case without ESS.

#### Power reference tracking

The fluctuation wind power plant production can be smoothed by ESS. The smooth effect is dependent on the time constant of the filter. This conclusion is obvious and there is no need to illustrate the results.

#### Mechanical load alleviation

The standard deviation  $\sigma(T_s)$  and  $\sigma(\Delta F_t)$  are used to evaluate the shaft and thrust-induced loads. According to the statistics in Table 6.7 and 6.9, compared with the wind power plant without ESS, the alleviation of shaft torque with ESS by D-MPC integration becomes larger. It matches the expectation in Section 6.4.2.  $\sigma(T_s)$  in centralized control is taken as the reference. For the high wind case, the the reduction percentages of the standard deviation range from 44.17% to 65.71% (Table 6.7). For the low wind case, the values are between 37.62% and 65.54% (Table 6.9).

**Table 6.7:** Simulation Statistics  $\sigma(T_s)$  in 0.01MNm

Turbine	$v_{avr}$ (m/s)	Centralized Control	D-MPC(No ESS) High Wind	D-MPC(With ESS) High Wind
WT 01	17.50	6.52	3.79 (-41.87%)	3.64 (-44.17%)
WT 02	17.02	6.99	3.33 (-52.36%)	3.00 (-57.08%)
WT 03	16.54	6.65	2.88 (-56.69%)	2.28 (-65.71%)
WT 04	16.64	6.48	3.22 (-50.31%)	3.08 (-52.47%)
WT 05	17.46	5.80	2.95 (-49.14%)	2.93 (-49.48%)
WT 06	17.00	5.70	3.10 (-45.61%)	2.94 (-48.42%)
WT 07	16.38	6.32	3.25 (-48.58%)	2.58 (-59.18%)
WT 08	17.14	6.11	2.84 (-53.52%)	2.24 (-63.34%)
WT 09	17.11	6.42	3.33 (-48.13%)	2.99 (-53.43%)
WT 10	16.45	7.26	3.70 (-49.04%)	3.77 (-48.07%)

Similarly, compared with the wind power plant without ESS, the thrust force change has more damping to some extent in each wind turbine with ESS integration by D-MPC, according to the statistics in Table 6.8 and 6.10. For the high wind case, the reduction percentages of standard deviation are between 0.00% and 3.32% (Table 6.8). For the low wind case, the values are between 0.54% and 26.5% (Table 6.10).



**Table 6.8:** Simulation Statistics  $\sigma(\Delta F_t)$  in 0.01MN

Turbine	$v_{avr}$ (m/s)	Centralized Control	D-MPC(No ESS) High Wind	D-MPC(With ESS) High Wind
WT 01	17.50	1.76	1.76 (-0.00%)	1.76 (-0.00%)
WT 02	17.02	1.93	1.89 (-2.07%)	1.88 (-2.59%)
WT 03	16.54	1.77	1.74 (-1.69%)	1.73 (-2.25%)
WT 04	16.64	1.78	1.72 (-3.37%)	1.72 (-3.37%)
WT 05	17.46	1.56	1.53 (-1.92%)	1.53 (-1.92%)
WT 06	17.00	1.66	1.64 (-1.20%)	1.63 (-1.81%)
WT 07	16.38	1.82	1.77 (-2.75%)	1.77 (-2.75%)
WT 08	17.14	1.76	1.74 (-1.14%)	1.73 (-1.70%)
WT 09	17.11	1.57	1.52 (-3.18%)	1.51 (-3.82%)
WT 10	16.45	1.99	1.94 (-2.51%)	1.94 (-2.51%)

**Table 6.9:** Simulation Statistics  $\sigma(T_s)$  in 0.01MNm

Turbine	$v_{avr}$ (m/s)	Centralized Control	D-MPC(No ESS) Low Wind	D-MPC(With ESS) Low Wind
WT 01	13.50	5.48	2.85 (-47.99%)	2.54 (-53.65%)
WT 02	13.02	5.78	2.71 (-53.11%)	2.44 (-61.25%)
WT 03	12.54	5.60	2.99 (-46.61%)	2.71 (-51.61%)
WT 04	12.64	6.06	3.94 (-34.98%)	3.78 (-37.62%)
WT 05	13.46	4.85	2.24 (-53.81%)	1.93 (-60.21%)
WT 06	13.00	4.77	2.22 (-53.46%)	1.93 (-59.54%)
WT 07	12.38	5.99	3.10 (-48.25%)	2.81 (-53.09%)
WT 08	13.14	5.05	2.25 (-55.45%)	1.74 (-65.54%)
WT 09	13.11	5.31	3.19 (-39.92%)	2.81 (-47.08%)
WT 10	12.45	6.69	3.91 (-41.55%)	3.79 (-43.35%)

**Table 6.10:** Simulation Statistics  $\sigma(\Delta F_t)$  in 0.01MN

Turbine	$v_{avr}$ (m/s)	Centralized Control	D-MPC(No ESS) Low Wind	D-MPC(With ESS) Low Wind
WT 01	13.50	1.85	1.84 (-0.54%)	1.84 (-0.54%)
WT 02	13.02	2.03	1.99 (-2.01%)	1.99 (-2.01%)
WT 03	12.54	1.92	1.85 (-3.65%)	1.85 (-3.65%)
WT 04	12.64	2.59	2.55 (-1.54%)	2.54 (-1.93%)
WT 05	13.46	1.63	1.59 (-2.45%)	1.59 (-2.45%)
WT 06	13.00	1.75	1.72 (-1.71%)	1.72 (-1.71%)
WT 07	12.38	2.64	1.95 (-26.1%)	1.94 (-26.5%)
WT 08	13.14	1.84	1.81 (-1.63%)	1.79 (-2.72%)
WT 09	13.11	1.72	1.65 (-4.02%)	1.64 (-4.65%)
WT 10	12.45	2.63	2.62 (-0.38%)	2.56 (-2.66%)

## 6.6 Discussion and conclusion

In this chapter, the D-MPC algorithm based on the fast dual gradient method is proposed for the active power control of a wind power plant.

As the prediction model for D-MPC, a dynamic discrete-time PWA model of a power controlled wind turbine is obtained by identification of the nonlinearities with clustering-based method. Compared with the linearization at some selected operating points, it has advantages to estimate the linear sub-models by classifying the multidimensional operating points and reconstructing the regions optimally. Moreover, all the state variables are measurable or easily estimated.

The developed PWA model is verified by comparison with the nonlinear wind turbine model under both high and low wind conditions. There exists small model mismatch whose reasons are twofold. Firstly, the model has been simplified and some dynamics are ignored. Secondly, in order to reduce the complexity of the PWA model, the number of sub-models is limited which reduces the approximation accuracy. However, this small mismatch will not significantly affect the wind power plant control performance. The simulation time in the study case is set 300s (5 min), while in the real-time MPC control, the prediction horizon is much shorter than this range, normally in several seconds. Besides, the prediction error can be compensated by the feedback mechanism.

Compared with the conventional wind power plant control, the D-MPC strikes a balance between the power reference tracking and the minimization of the

wind turbine loads. Different from C-MPC, in the developed D-MPC, most of computation tasks are distributed to the local D-MPCs equipped at each actuator (wind turbine or ESS). The computation burden of the central unit is significantly reduced. This control structure is independent of the scale of the wind power plant. Besides, with properly calculated Lipschitz constant  $\mathbf{L}$ , the adopted fast dual gradient method can significantly improve the convergence rate from  $\mathcal{O}(1/k)$  to  $\mathcal{O}(1/k^2)$ , which reduces the communication burden between local D-MPC and central unit. By means of the developed PWA model, the calculation work of  $\mathbf{L}$  dependent on the model parameter of the operation region can be done off-line and stored. Through different case studies, the power tracking control performances of the developed D-MPC are verified to be identical with these of C-MPC. The mechanical loads experienced by individual wind turbines have been largely alleviated without affecting tracking the power reference of the wind power plant. The D-MPC can be used for real-time control of modern wind power plants.

The proposed D-MPC is implemented for two wind power plant configurations: with and without ESS installation. It is expected that larger mechanical load alleviation can be obtained with additional ESS which is verified by simulation results. However, it also leads to the increase of capital and maintenance cost.

## CHAPTER 7

# Optimal Siting and Sizing of Energy Storage System

---

In this chapter, a heuristic algorithm for optimal sizing and siting of ESS is presented for the operation planning of power systems with large scale wind power integration. The ESS in this study aims to mitigate the wind power fluctuations in the time period between two rolling hourly Economic Dispatches (EDs), which also corresponds to the charging-discharging cycle of ESS. During each cycle, the optimal charging and discharging are scheduled by solving the optimization problem. In order to describe the spatial correlation of the wind power among the wind power plants distributed in large area, copula function is used to generate synthetic wind power data. The statistics from simulated system operations are then coupled to the planning process to determine the optimal siting and sizing of storage throughout the network.

## 7.1 Background and basic knowledge

### 7.1.1 Energy storage sizing

The ESS sizing problem includes the determination of both power rating and energy rating. Several methodologies have been developed for the sizing of Battery Energy Storage System (BESS) for daily wind power dispatch. In [173], through spectral analysis of wind and solar resources combined with daily load profiles, a mathematical model is applied to a stand-alone system where the storage is calculated for different levels of mean load. The ESS sizing is designed according to the worst case scenario (worst day of the year). A novel method was developed to obtain a probability density function of wind power forecast error in [174]. Based on the density function, the nominal power of ESS can be determined. As the following work, the ESS capacity estimation was completed in [175]. A probabilistic methodology was presented which considers the estimation of ESS as a function of unreserved energy. The ESS sizing aims to compensate forecast errors up to a certain extent.

The sizing problem can be modeled as an optimization problem. The factors related to the sizing of BESS, including wind power forecasting accuracy (error in range between 10% and 30% [113]), application purpose, control strategy and economical aspect, can be quantified and taken into the optimization equations.

In [158], the cost function was formed as the power deviation from the next hourly average. The forecasting error was considered to be within 10%. Based on State Of Charge (SOC), current constraints and charging-discharging rules, the reference power for next hour can be generated to minimize the cost function. The results indicate 15%-25% of the rated wind power plant capacity could have an effective hourly dispatch. The same cost function was used in [176]. The hour-long wind power production scenarios were firstly generated by a probabilistic forecast of the hourly average wind power and the inverse of the joint cumulative distribution. From these scenarios, the ESS characteristics were then determined as a function of the desired risk parameter.

The cost function can be formed as the economic benefit obtained from the dispatched power of wind power plant against the ESS cost. In [177], the optimal dispatched power level from wind power plant was obtained by solving the optimization problem based on given wind power profile. The DC voltage of converter is another constraints to be considered. The corresponding BESS power and energy ratings can be then determined. With the same procedure, [178] aims to minimize the cost of BESS. Additionally, ESS output is required to meet the forecast wind power plant output within 4%~90% of the time. Dif-

ferent intelligent control methodologies including simple and advanced methods (Fuzzy and ANN) are applied and compared. Besides economic benefits from wind power dispatch and ESS cost, new benefit component related to voltage stability was introduced into the cost function in [80]. Using the exhaustive search of all possible solution candidates, the method is capable of finding a unique optimum for the ESS sizing. A new planning tool for MV distribution networks was proposed in [91] based on Genetic Algorithm (GA) and Dynamic Programming (DP). It is able to locate the optimal rating of energy storage plants that minimizes the overall network cost.

The cost function can also be formed as the service life of energy storage system. In [101], the historical long-term wind speed data was assumed to be known. A new dispatch strategy is proposed to ensure the BESS goes through full charging-discharging cycle and thus maximizes the energy storage potential of BESS.

### 7.1.2 Energy storage siting

Some large-scale ESS such as PHS and CASE, are heavily dependent on topographical condition. Other ESS types have the installation flexibility. For wind power dispatch purpose, the potential siting is not only within a wind power plant, but also at other locations in the power system for additional benefits, like deferring or avoiding capacity and transmission upgrade, reduced transmission and distribution losses and more robust system stability [89].

For on-site installation of ESS within a wind power plant, ESS can be either placed at Point of Common Coupling (PCC) or equipped with WTGs. The former configuration is adopted by the most as hybrid wind power plant-ESS. The latter configuration was introduced in [87], each wind turbine is equipped with a supercapacitor-based ESS connected to the DC link of back to back converter. This scheme enhances the control flexibility of each wind turbine. However, due to the smoothing effect on power fluctuations of distributed wind power plants over large geographic areas, the requirement of power and energy rating is high and not cost-effective.

In [5] [179], a staged procedure was introduced to seek the minimum number of storage nodes and total network storage that can still mitigate the effects of renewable fluctuations on network constraints. An interesting result shows that instead of wind power injection nodes, the other nodes at the end or the middle of crucial transmission lines have higher degree of control over congestion. The optimal siting problem was also investigated in [180]. The optimal storage locations which allows highest wind power penetration are selected based on the

calculation of different location scenarios. The simulation results demonstrate that optimal storage distribution can effectively utilize transmission capacity and eliminate the need for transmission expansion.

## 7.2 Operation of ESS for wind power dispatch

The operation with wind power plant integration in the modern day-ahead and real-time power market is described in [181], [182]. The unit commitment problem is assumed to be resolved in the day-ahead scheduling. In the real-time market, the wind power production for next economic dispatch period is predicted and submitted to the grid operator by the wind power plant operator. Subsequently, the grid operator will adjust the system operating state to obtain the economic dispatch. The dispatchable conventional generators are scheduled by solving the optimal power flow (OPF) problem. During the interval between two OPFs, the wind power fluctuation results in the mismatch between power production and consumption and further makes the frequency unstable.

As described in Chapter 2, with low wind penetration level, the mismatch can be compensated through ancillary service (AGC) by regulating the committed conventional generators without increasing the operating reserves. The cost for AGC is also limited. However, as the penetration level grows, the ancillary service cost increases and more operating reserves are required. Besides, due to the ramp rate limitation of the conventional generators, the fast variation of wind power can not be well compensated within a short period. In this case, ESS (in particular BESS), due to its capabilities of flexible charging-discharging ability and fast response, can participate in AGC to mitigate the fluctuation.

## 7.3 Methodology for optimal siting and sizing

The flow chart of the proposed optimal siting and sizing algorithms is shown in Fig. 7.1. The implementation of these two algorithms are sequential. The optimal siting algorithm is firstly implemented, all the candidate buses for the ESS installation in the grid are sorted according to the power exchange activity. According to the specific requirements of the system operator, a certain number of buses are selected. Subsequently, the optimal sizing algorithm for the ESS installed on selected buses can be carried out.

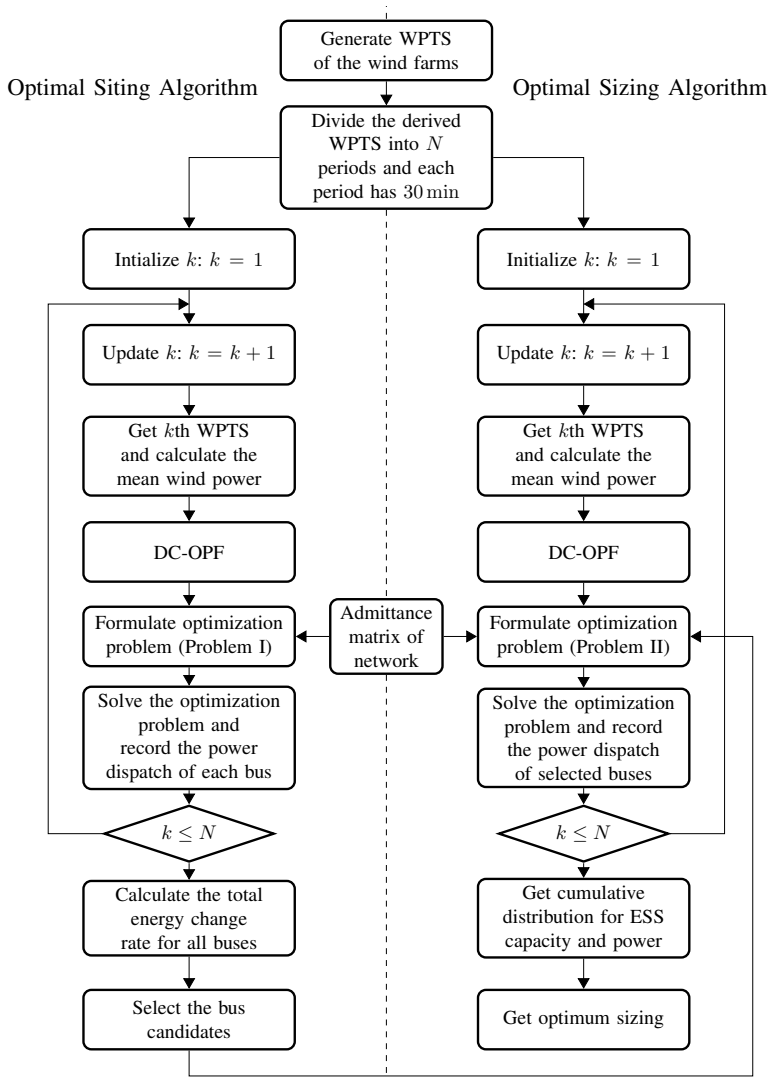


Figure 7.1: Flow chart of optimal siting and sizing algorithms

### 7.3.1 Optimal siting algorithm

As illustrated in Fig. 7.1, long-term WPTS are firstly generated and divided into  $N$  periods. More details of WPTS generation are described in Section 7.4. The wind power profile of each period can be considered as wind fluctuations. Accordingly, with a large number of realizations, each level of wind penetrations



can be represented. In this study, the length of a single period is 30 minutes which corresponds to the charging-discharging cycle of the ESS as well as the interval between two EDs.

For each period, the mean wind power is assumed to be perfectly predicted. Subsequently, the dispatch of conventional generators can be scheduled by solving a deterministic OPF. To reduce the computation complexity, DC-OPF is applied in this study. During the period, the wind power fluctuation leads to the mismatch between production and consumption. From the point of view of system operator, the participation of the ESS in AGC service can no doubt reduce the service cost and improve the regulation capability for the fast variation.

All the buses are assumed to have the ESS installation with unlimited amounts of power and energy. The control of the ESS for charging and discharging can be decided by solving an optimal problem, labeled as Problem I. The cost function consists of the penalty of deviation from the scheduled dispatch, the ESS cost and grid losses. The details regarding the formulation of the optimal problem are described in Section 7.5. Accordingly, a summary of the absolute ESS power at each bus can be calculated, which is used to evaluate the activity of “power exchange” for this period.

By gathering the results of  $N$  periods, the statistics on the activities of the ESS at all buses can be derived. Based on the power exchange activities, all buses can be sorted. A bus with larger power exchange indicates that grid can benefit more if this bus is equipped with the ESS. In this study, the total number of bus where the ESS will be installed and the power and energy constraints are decided by the system operator.

### 7.3.2 Optimal sizing algorithm

Similar to the optimal siting algorithm, the generated WPTS is divided into  $N$  periods which is considered as a realization of wind fluctuations.

For each period, the mean wind power is assumed to be perfectly predicted. The dispatch of conventional generators can be scheduled by solving the deterministic DC-OPF. The ESSs installed in the selected buses are involved in the AGC service in order to reduce the service cost and improve the regulation capability for the fast variation.

For the selected buses, the control of ESSs for charging and discharging can be decided by solving an optimal problem (labeled as Problem II), whose cost function is identical with that of the optimal siting problem. The additional

requirements by the system operator such as total power and energy capacity are included in the constraints. More details regarding the formulation of the optimal problem are described in Section 7.5.

By gathering the results of  $N$  periods, the Empirical Cumulative Distribution Functions (ECDFs) for power and capacity are generated, respectively. With a given probability value which is assumed to fulfill the requirements for sufficient time periods (95% in this study), the optimal sizing can be determined based on the derived ECDFs.

## 7.4 Generation of Wind Power Time Series

Due to the lack of or limited length of historical wind data records, a general approach for long-term planning of combined wind and storage is to use parameterized time series model. The recommended modeling of the WPTS is either directly from field records or indirectly from converted WSTS measurements. Since the wind speed data are usually easier to be obtained, the first approach which transforms the modeled WSTS to WPTS by applying a suitable wind turbine power curve is preferred by most of the literature.

So far, various techniques of the WSTS have been developed to model temporal dependence structure of univariate wind speed, including Markov Chain and Autoregressive Moving Average (ARMA) models [183]. For the case with multiple wind power plant integration, due to the locational relationship between different wind sites, there exists spatial dependence between WSTS. This dependence has a considerable impact on the stability and reliability of power system with wind power integration. As the wind power penetration grows, the impact will be more prominent. Therefore, it is necessary to model the multivariate WSTS.

The Linear Correlation Coefficient (LCC) is normally used to indicate the dependence between multi-variables. However, it can only represent the linear dependence and cannot provide a complete representation. As the most comprehensive method, the Multivariate Distribution Function (MDF) is used to describe the correlation of multiple random variables. It has the advantage of containing all statistical properties of random variables. However, it is only suitable for some specific marginal distributions such as normal, lognormal and etc. [184]. In order to overcome this problem, the Copula method is applied in this study. It separates multivariate WSTS into dependence structure and univariate time series which is represented by a ARMA model. In other words, the spatial dependence is modeled by Copula method while the temporal dependence is modeled by ARMA.

### 7.4.1 Copula-ARMA model

#### Sklar's Theorem

Let  $X = (X_1, \dots, X_n)$  be a random vector with distribution function  $F$  and with marginal distribution functions  $F_i$ ,  $X_i \sim F_i$ ,  $i \in [1, \dots, n]$ . A distribution function  $C$  with uniform marginals on  $[0, 1]$  is called a "Copula" of  $X$ . There exists a copula  $C \in \mathcal{F}(\mathcal{U}, \dots, \mathcal{U})$  with uniform marginals such that

$$F(x_1, \dots, x_n) = C(F_1(x_1), \dots, F_n(x_n)) \quad (7.1)$$

By means of Sklar's Theorem, the dependence structure of multivariate distributions can be analyzed.

#### ARMA model

Wind speeds for a specific wind power plant site can be simulated by the site-specific ARMA model, which reproduces the high-order auto-correlation, the seasonal and diurnal distribution of the actual wind speed [109], [185]. The approach proposed in [185] is introduced.

The mathematical expression of ARMA( $n, m$ ) model is

$$\begin{aligned} y_t &= \varphi_1 y_{t-1} + \varphi_2 y_{t-2} + \dots + \varphi_n y_{t-n} + \varepsilon_t - \theta_1 \varepsilon_{t-1} - \theta_2 \varepsilon_{t-2} - \dots - \theta_m \varepsilon_{t-m} \quad (7.2) \\ &= \sum_{i=1}^n \phi_i y_{t-i} + \varepsilon_t - \sum_{j=1}^m \theta_j \varepsilon_{t-j}, \end{aligned}$$

where  $y_t$  is the time series value at time  $t$ ,  $\phi_i$  ( $i \in 1, 2, \dots, n$ ) and  $\theta_j$  ( $j \in 1, 2, \dots, m$ ) are the auto-regressive and moving average parameters, respectively.  $\varepsilon_t$  is a normal white noise process with zero mean and a variance of  $\sigma_\varepsilon^2$ , i.e.  $\varepsilon_t \in \text{NID}(0, \sigma_\varepsilon^2)$ , NID represents Normal Independent Distribution.

Accordingly, the wind speed  $v_t$  at a given time  $t$  can be obtained according to the historical mean wind speed  $\mu_t$  and standard deviation  $\sigma_t$ ,

$$v_t = \mu_t + \sigma_t y_t. \quad (7.3)$$

#### Copula-ARMA model for multivariate WSTS

Copula-ARMA model proposed in [184] is used to describe the dependence of multivariate WSTS. Consider that  $y = (y_{1t}, y_{2t}, \dots, y_{Nt})$  is an  $N$ -dimensional

vector of time series and each marginal series can be described by ARMA( $n, m$ ), then the  $N$ -dimensional Copula-ARMA( $n, m$ ) model can be expressed as,

$$y_{kt} = \sum_{i=1}^n \varphi_{ki} y_{kt-i} + \varepsilon_{kt} - \sum_{j=1}^m \theta_{kj} \varepsilon_{kt-j}, k = 1, \dots, N,$$

$$(\varepsilon_{1t}, \varepsilon_{2t}, \dots, \varepsilon_{Nt}) \sim C_{\varepsilon} \left( \Phi \left( \frac{\varepsilon_{1t}}{\sigma_{\varepsilon 1}} \right), \Phi \left( \frac{\varepsilon_{2t}}{\sigma_{\varepsilon 2}} \right), \dots, \Phi \left( \frac{\varepsilon_{Nt}}{\sigma_{\varepsilon N}} \right) \right), \quad (7.4)$$

where  $\varepsilon = (\varepsilon_{1t}, \varepsilon_{2t}, \dots, \varepsilon_{Nt})$  indicates the white noise series of  $N$ -dimensional vector,  $(\sigma_{\varepsilon 1}, \sigma_{\varepsilon 2}, \dots, \sigma_{\varepsilon N})$  denote the corresponding standard deviations of  $\varepsilon$ ,  $\Phi$  is the standard normal distribution. The Copula function  $C_{\varepsilon}$  describes the dependence structure between white noise series. According to [184], the  $N$ -dimensional copula function describing dependence structure among time series  $y$  is identical to copula function  $C_{\varepsilon}$  in Eqn. 7.4,

$$(y_{1t}, y_{2t}, \dots, y_{Nt}) \sim C_{\varepsilon} \left( \Phi \left( \frac{\varepsilon_{1t}}{\sigma_{\varepsilon 1}} \right), \Phi \left( \frac{\varepsilon_{2t}}{\sigma_{\varepsilon 2}} \right), \dots, \Phi \left( \frac{\varepsilon_{Nt}}{\sigma_{\varepsilon N}} \right) \right). \quad (7.5)$$

## 7.4.2 Algorithm of generating WPTS

The algorithm of WPTS can be implemented in the following steps:

**Step 1:** Determine the ARMA model for WSTS at each wind power plant site.

**Step 2:** Select a copula function among the copula function family to describe the dependence structure among time series  $y_{it}$  ( $i \in (1, 2, \dots, N)$ ). More details of the commonly used copula types are listed in Appendix B.3.

**Step 3:** Construct the multivariate Copula-ARMA model of WSTS according to Eqn. 7.3–Eqn. 7.5.

**Step 4:** Transform the derived multivariate WSTS into WPTS based on a suitable power curve model of the wind power plants. As proposed in [186], [187], the relationship between wind speed and mechanical power extracted from the wind power plant  $P_{wf}$  can be described as,

$$P_{wf} = \begin{cases} 0 & (v_w < v_{ci} \text{ or } v_w \geq v_{co}) \\ \frac{(v_w^3 - v_{ci}^3)}{(v_r^3 - v_{ci}^3)} P_{wfr} & (v_{ci} \leq v_w \leq v_r) \\ P_{wfr} & (v_r < v_w < v_{co}) \end{cases} \quad (7.6)$$

where  $v_{ci}$  and  $v_{co}$  indicate the cut-in and cut-out wind speed, respectively,  $v_r$  denotes the rated wind speed,  $P_{wfr}$  represents the wind power plant capacity.

## 7.5 Periodical optimization problem

The optimization problems (Problem I and Problem II) are formulated in this section. As illustrated in Fig. 7.1, they are periodically solved for each cycle to obtain the optimal control of the ESSs.

### 7.5.1 Notation and system description

Consider a power network with  $n$  buses,  $l$  lines,  $m$  generators ( $m \leq n$ ) and  $s$  ESSs ( $s \leq n$ ). Define  $\mathcal{N} = \{1, 2, \dots, n\}$ ,  $\mathcal{L} = \{1, 2, \dots, l\}$ ,  $\mathcal{G} = \{1, 2, \dots, m\}$ ,  $\mathcal{S} = \{1, 2, \dots, s\}$  as the sets of all buses, generator buses and ESS buses, respectively.

The power injection at  $i$ th bus at time step  $k$  is denoted by  $P_i(k)$ . The voltage at  $i$ th bus at time step  $k$  is denoted by  $V_i(k)$  whose magnitude and phase angle are indicated by  $|V_i(k)|$  and  $\theta_i(k)$ , respectively.

According to the different generator types,  $\mathcal{G}$  are classified into two types:

- Conventional generator buses  $\mathcal{G}_g$ . These generators are considered dispatchable and committed for the AGC service.
- Renewable energy buses  $\mathcal{G}_r$ . In order to make full use of renewable energy, these renewable energy are considered nondispatchable. In this case, renewable energy only refers to wind energy.

Accordingly, the power of conventional generator and renewable energy of the  $i$ th bus at time step  $k$  are denoted by  $P_i^g(k)$  ( $i \in \mathcal{G}_g$ ) and  $P_i^r(k)$  ( $i \in \mathcal{G}_r$ ), respectively. The load demand of the  $i$ th bus is denoted by  $P_i^l(k)$  ( $i \in \mathcal{N}$ ). If there is no load connected at that bus,  $P_i^l(k) = 0$ .

The set of ESS buses  $\mathcal{S}$  is dependent on the optimal algorithms. For the optimal siting algorithm, the ESSs are assumed to be installed at all the buses, then  $\mathcal{S} = \mathcal{N}$ . For the optimal sizing algorithm, the ESSs are installed at selected buses, then  $\mathcal{S} \subset \mathcal{N}$ . The power of the ESS at the  $i$ th bus is  $P_i^s(k)$  ( $i \in \mathcal{S}$ ).

### 7.5.2 Network constraints

Power flow equations are used to represent the network constraints. Compared with the nonlinear AC power flow, DC power flow equations are considered as

a linearization of AC power flow with the following assumptions:

- Line resistance are negligible.
- Voltage angle difference  $\Delta\theta$  are assumed to be small, i.e.  $\sin(\Delta\theta) = \Delta\theta$ .
- Voltage magnitudes are set to 1.0 p.u., i.e.  $|V| = 1$ .

It can significantly reduce the computation complexity of optimization problems and thus be adopted in this study.

Based on the aforementioned assumptions, the power injection at bus  $i$  can be calculated by,

$$P_i = \sum_{j \in \mathcal{N}} B_{ij}(\theta_i - \theta_j), \quad (7.7)$$

where  $B_{ij}$  indicates the reciprocal of the reactance between bus  $i$  and  $j$ . Consequently, the DC power flow  $F_{ij}$  through the transmission line  $L_{ij}$  between bus  $i$  and  $j$  can be calculated by,

$$F_{ij} = \frac{\theta_j - \theta_i}{X_{ij}}, \quad (7.8)$$

where  $X_{ij}$  denotes the reactance of the line.

These DC power flow equations can be expressed in the matrix form,

$$\theta = B^{-1}P, \quad (7.9)$$

$$F = (bA)\theta = (bA)B^{-1}P, \quad (7.10)$$

where

$P \in \mathbb{R}^{n \times 1}$ : vector of active power injections for all the buses  $\mathcal{N}$ .

$B \in \mathbb{R}^{n \times n}$ : admittance matrix neglecting the resistance.

$\theta \in \mathbb{R}^{n \times 1}$ : vector of bus voltage angles for all the buses  $\mathcal{N}$ .

$F \in \mathbb{R}^{l \times 1}$ : vector of line flows for all the lines  $\mathcal{L}$ .

$b \in \mathbb{R}^{l \times l}$ : the diagonal elements  $b_{kk}$  equal to the susceptance of line  $k$  and the non-diagonal elements are zero.

$A \in \mathbb{R}^{l \times n}$ : bus-line incidence matrix. If the line exists from bus  $i$  to bus  $j$ , its element  $a_{ij} = 1$ . For the starting and ending buses, the elements are 1 and -1, respectively. Otherwise  $a_{ij} = 0$ .

### 7.5.3 Transmission losses calculation

According to the assumption of the bus voltage angle in Section 7.5.2, we get

$$\cos(\theta_i - \theta_j) \approx 1 - \frac{(\theta_i - \theta_j)^2}{2}, \quad (7.11)$$

where  $i$  and  $j$  indicate the starting and ending buses of line  $L_{ij}$ . According to the AC power flow, the transmission loss of the line  $P_{\text{loss},L_{ij}}$  is calculated by

$$P_{\text{loss},L_{ij}} = (|V_i|^2 + |V_j|^2 - 2|V_i||V_j|\cos(\theta_i - \theta_j))g_{ij}, \quad (7.12)$$

where  $g_{ij}$  is the conductance of the line  $L_{ij}$ .

With the assumption of the bus voltage magnitude in Section 7.5.2, substituting  $|V_i| = |V_j| = 1$  into Eqn. 7.12,

$$P_{\text{loss},L_{ij}} = (\theta_i - \theta_j)^2 g_{ij}. \quad (7.13)$$

With Eqn. 7.9, the transmission losses in the whole network can be calculated

$$P_{\text{loss}} = \frac{1}{2} \sum_i \sum_j (\theta_i - \theta_j)^2 g_{ij} = \theta' G \theta = (B^{-1} P)' G (B^{-1} P). \quad (7.14)$$

where  $G \in \mathcal{R}^{n \times n}$  with matrix element  $G_{ii} = \sum_{j,j \neq i} g_{ij}$ ,  $G_{ij} = G_{ji} = -g_{ij}$ .

## 7.5.4 Formulation of Problem I

### 7.5.4.1 Cost function

For the multi-objective optimization problem, three objects are considered in the cost function. Suppose the optimization period has  $M$  steps,

$$\min_{p_i^s, i \in \mathcal{S}} (\text{cost1} + \text{cost2} + \text{cost3}). \quad (7.15)$$

#### Object 1: Minimization of the ESS cost

Frequent charging and discharging will significantly reduce the life of ESS. Therefore, the absolute summary of power inflow and outflow during the optimization period are used to quantify the usage of the ESS. The ESS cost is calculated by

$$\text{cost1} = \sum_{k=1}^M (\alpha_1 \sum_{i \in \mathcal{S}} |P_i^s(k)|), \quad (7.16)$$

where  $\alpha_1$  denotes the weighting cost of total exchanged ESS power.

### Object 2: Minimization of transmission losses

The minimization of the transmission losses in the grid is considered. Based on Eqn. 7.14, the cost is represented by

$$\text{cost2} = \sum_{k=1}^M (\alpha_2 P_{\text{loss}}), \quad (7.17)$$

where  $\alpha_2$  denotes the weighting cost of transmission losses.

### Object 3: Minimization of the additional cost by adjusting the conventional generator

In the AGC market, committed generators offer a regulation band within an upper and a lower limit, which are capable of providing ancillary services, such as AGC dispatched by the system operator. It leads to an additional cost which is dependent on the generator dispatch power. Assumed that the dependence is proportional, the cost can be obtained,

$$\text{cost3} = \sum_{k=1}^M \left( \sum_{i \in \mathcal{G}_g} \alpha_{3i} \Delta P_i^g(k) \right), \quad (7.18)$$

where  $\alpha_{3i}$  denotes the weighting cost of  $i$ th generator,  $\Delta P_i^g$  indicates the power deviation from the value derived by the ED for this period.

#### 7.5.4.2 Constraints

##### Constraints of dispatchable generators

$\Delta P^r(k)$  denotes the deviation of the total wind power production at time  $k$  from the predicted mean value of wind power during the period.

$$\Delta P^r(k) = \sum_{i \in \mathcal{G}_r} P_i^r(k) - \frac{1}{M} \sum_{k=1}^M P_i^r(k). \quad (7.19)$$

In order to keep the balance between production and consumption, the deviation should be compensated by AGC through regulation of the ESS and committed dispatchable generators. The distribution algorithm between these generators



are assumed predefined and proportional to their power ratings. Let  $d_i^g(i \in \mathcal{G}_g)$  represent the distribution factor,  $P_i^g(k)$  can be derived,

$$P_i^g(k) = P_i^g(k-1) - d_i^g(\Delta P^r(k) + \sum_{i \in \mathcal{S}} P_i^s(k)), \forall i \in \mathcal{G}_g. \quad (7.20)$$

Accordingly, the power and ramp rate constraints are expressed by,

$$\underline{P}_i^g \leq P_i^g(k) \leq \overline{P}_i^g, \forall i \in \mathcal{G}_g, \quad (7.21)$$

$$\underline{\Delta P}_i^g \leq \Delta P_i^g(k) \leq \overline{\Delta P}_i^g, \forall i \in \mathcal{G}_g. \quad (7.22)$$

where  $\underline{P}_i^g, \overline{P}_i^g$  denote the lower and upper limitation of  $P_i^g(k)$ , respectively;  $\underline{\Delta P}_i^g, \overline{\Delta P}_i^g$  denote the lower and upper limitation of  $\Delta P_i^g(k)$ , respectively.

### Constraints of ESS

As described in Section 7.3.1, all the buses are assumed to have ESS installation with unlimited amounts of power and energy. The dispatch period of ESS is corresponding to the charging-discharging cycle of ESS, accordingly,

$$\sum_{k=1}^M P_i^s(k) = 0, \forall i \in \mathcal{S}. \quad (7.23)$$

### Constraints of transmission capacity

Firstly, the active power injections  $P_i(k)$  for all the buses  $\mathcal{N}$  are calculated.

For the dispatchable generator buses  $\mathcal{G}_g$ ,

$$P_i(k) = P_i^g + P_i^s - P_i^l, i \in \mathcal{G}_g. \quad (7.24)$$

For the renewable energy buses  $\mathcal{G}_r$ ,

$$P_i(k) = P_i^r + P_i^s - P_i^l, i \in \mathcal{G}_r. \quad (7.25)$$

For other buses (load with ESS),

$$P_i(k) = P_i^s - P_i^l, i \in \mathcal{L}. \quad (7.26)$$

Based on Eqn. 7.24–7.26 and Eqn. 7.10, the power flow constraint can be described in the matrix form,

$$\underline{F} \leq (bA)B^{-1}P \leq \overline{F}, \quad (7.27)$$

where  $\underline{F} \in \mathbb{R}^{l \times 1}$  is the vector of lower limits of line flows for all the lines  $\mathcal{L}$ ,  $\overline{F} \in \mathbb{R}^{l \times 1}$  is the vector of upper limits of line flows for all the lines  $\mathcal{L}$ .

## 7.5.5 Formulation of Problem II

### 7.5.5.1 Cost function

The cost function of Problem II is identical with that of Problem I.

### 7.5.5.2 Constraints

Most constraints of Problem II are the same as these of Problem I, including constraints of dispatchable generators, transmission capacity. The difference lies in the constraints of ESS. In Problem II, ESSs are installed at selected buses. The power and its ramp rate at specific bus are limited. Besides, the total power and energy capacity are limited. The additional constraints are listed as follows.

The power and ramp rate constraints are:

$$\underline{P}_i^s \leq P_i^s(k) \leq \overline{P}_i^s, \forall i \in \mathcal{S}, \quad (7.28)$$

$$\underline{\Delta P}_i^s \leq \Delta P_i^s(k) \leq \overline{\Delta P}_i^s, \forall i \in \mathcal{S}. \quad (7.29)$$

where  $\underline{P}_i^s, \overline{P}_i^s$  denote the lower and upper limitation of  $P_i^s(k)$ , respectively;  $\underline{\Delta P}_i^s, \overline{\Delta P}_i^s$  denote the lower and upper limitation of  $\Delta P_i^s(k)$ , respectively.

The total energy capacity constraint is,

$$\sum_{i \in \mathcal{S}} \left| \sum_{k=1}^M P_i^s(k) \Delta t \right| \leq E, \forall i \in \mathcal{S}, \quad (7.30)$$

where  $\Delta t$  indicates the interval between two steps,  $E$  is the total energy capacity limit.

## 7.6 Simulation and results

The IEEE 14 bus system was used as the test system to demonstrate the developed algorithms. As illustrated in Fig. 7.2, there are two wind power plants which are located at Bus 6 and Bus 8, termed as WF 1 and WF 2, respectively.

First of all, the Copula-ARMA model developed based on this historical wind speed measurements on both sites was verified. As the inputs, WPTS were

generated for both wind power plants. Then, the optimal siting and sizing algorithms were implemented and solved. In this study, the implementation tool is YALMIP [188] with the solver SeDuMi [189].

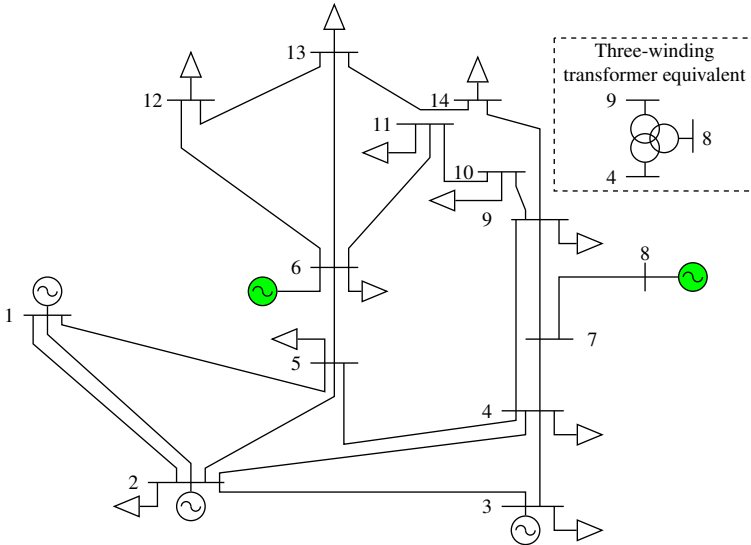


**Figure 7.2:** Single line diagram of IEEE 14 buses system

### 7.6.1 Verification of Copula-ARMA model

#### Selection of Copula type

Different Copula function types including Gaussian, Archimedean Copula, were used to capture the dependence structure between WSTS of the two wind power plant sites. In order to get the suitable Copula function among these types, the Euclidean distance between the empirical and theoretical copulas were used as the selection criteria. More details about empirical and theoretical copulas are described in Appendix B.3. According to the values listed in Table 7.1, Archimedean-Gumel has the shortest distance and it was adopted in this study.

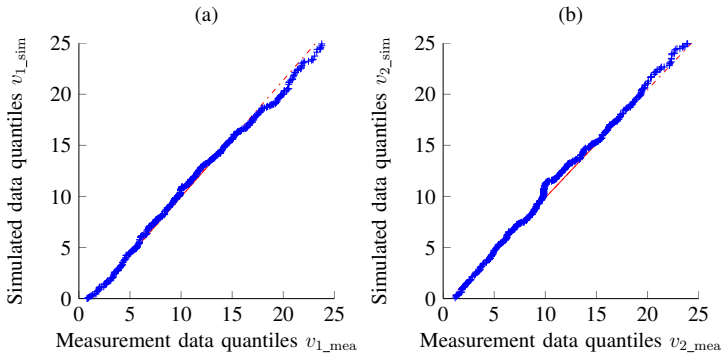
#### Evaluation of temporal and spatial dependencies

One year WSTS were generated for the two sites by means of the proposed Copula-ARMA model ( $v_{1\_sim}$  for WF 1 and  $v_{2\_sim}$  for WF 2).

**Table 7.1:** Euclidean distance between empirical and theoretical copulas

Copula type	Euclidean distance
Gaussian	0.0682
Archimedean-Gumel	0.0620
Archimedean-Clayton	0.0733
Archimedean-Frank	0.0678

To evaluate the temporal dependence between simulated WSTS and historical measurement data ( $v_{1\_meas}$  for WF 1 and  $v_{2\_meas}$  for WF 2), the Quantile-Quantile (Q-Q) plot was used which compares two probability distributions by plotting their quantiles against each other. As illustrated in Fig. 7.3, the Q-Q plots follow approximately a straight line with a unit slope for both sites ((a) and (b)). It verifies that the simulated WSTS and the historical measurements are from the same distribution.

**Figure 7.3:** P-P plot for the WSTS: (a) WF 1, (b) WF 2

To evaluate the spatial dependence, several correlation coefficients were compared between simulated WSTS and historical data. Pearson's  $r$  is a measure of the linear correlation between two variables. Rank correlation coefficients, such as Kendall's  $\tau$  and Spearman's  $\rho$  measure the extent to which, as one variable increases, the other variable tends to increase, without requiring that increase to be represented by a linear relationship. As shown in Table 7.2, the coefficients are similar which verifies the obtained Copula-ARMA model.

**Table 7.2:** Comparison of the correlation coefficients

Data	Pearson's $r$	Kendall's $\tau$	Spearman's $\rho$
Simulated WSTS	0.2153	0.0618	0.0928
Historical Meas.	0.2106	0.0654	0.0945

## 7.6.2 Optimal siting

The optimal siting of ESS is dependent on many factors, including the wind power fluctuation, transmission capacity and etc. In order to illustrate the effect of each factor, a single period (30 minutes in this case) was used as an example. The wind power productions of both sites are depicted in Fig. 7.4. The optimization Problem I is implemented in this period to derive the optimal control of ESSs installed at all the buses. Three different case scenarios are defined in Table 7.3.

**Table 7.3:** Case scenario definition

Scenario	Description	
	Wind power production	Transmission capacity
Scenario 1	Bus 6: $P_{wf1}$ in MW	Line 13-14: 10 MW
	Bus 8: $P_{wf2}$ in MW	
Scenario 2	Bus 6: $P_{wf1}$ in MW	Line 13-14: 10 MW
	Bus 8: $P_{wf2} + 20$ in MW	
Scenario 3	Bus 6: $P_{wf1}$ in MW	Line 13-14: 6.5 MW
	Bus 8: $P_{wf2}$ in MW	

### 7.6.2.1 Influence of wind power fluctuation

The influence of wind power fluctuation on the ESS siting is analyzed in this part.

For Scenario 1, by solving the optimization problem, the power exchanges for all the buses ( $\sum_{k=1}^M |P_i^s|, i \in \mathcal{N}$ ) are illustrated in Fig. 7.5. Obviously, Bus 6, where WF 1 is located, is the most active bus. In other words, if the ESS is installed at Bus 6, the minimum cost can be achieved. It can be observed that compared with WF 2, the power fluctuation and mean power of WF 1 are larger.

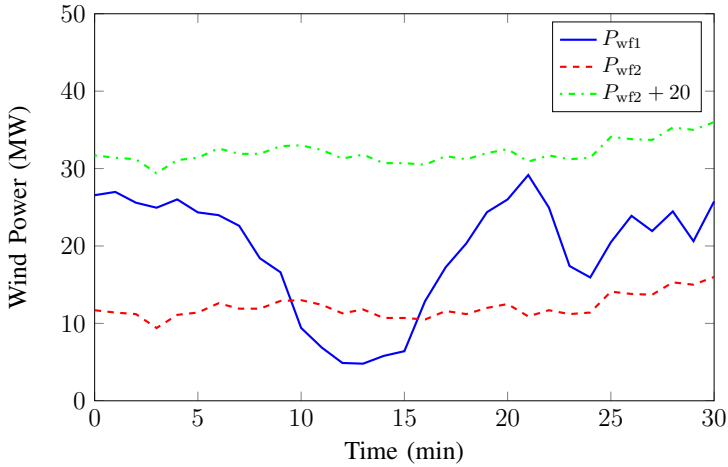


**Figure 7.4:** Wind power productions

For Scenario 2, the power production of WF 2 is shifted by introducing an additional 20 MW. In this case, WF 2 has a larger mean power value. However, the result depicted in Fig. 7.5 shows that it is almost identical with Scenario 1.

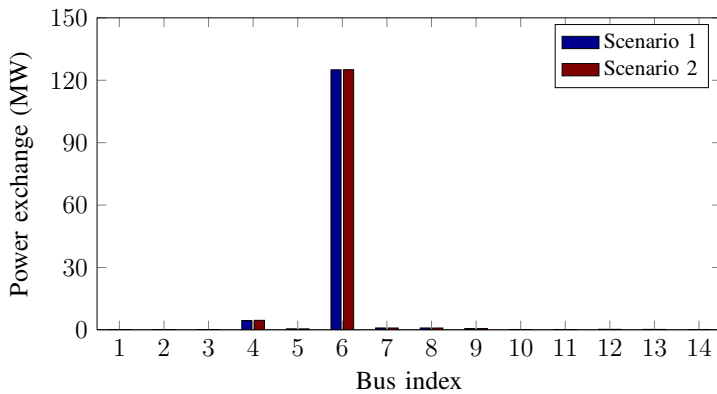


**Figure 7.5:** Power exchange comparison between Scenario 1 and 2

Consequently, following conclusions can be drawn:

- The results indicate that optimal storage siting in the absence of transmission limits is fairly robust to the position of wind power plant site in the network.

- If more wind power plants are present, the ESS is preferred to be installed at the wind power plant bus with larger power fluctuation, instead of larger capacity.

It can be understood that if most wind power fluctuations are compensated on site, the transmission losses will be reduced.

### 7.6.2.2 Influence of transmission capacity

The influence of transmission capacity on the ESS siting is analyzed in this part.

Compared with Scenario 1, the transmission line between bus 13 and bus 14 has a tighter limitation (6.5 MW). By solving the optimization problem, the power exchanges for all the buses ( $\sum_{k=1}^M |P_i^s|, i \in \mathcal{N}$ ) are illustrated in Fig. 7.6. It can be observed that almost half of the power exchange has been transferred from Bus 6 to bus 13 which is the terminal bus of the line with limited transmission capacity. Bus 6 and Bus 13 are the most active buses.

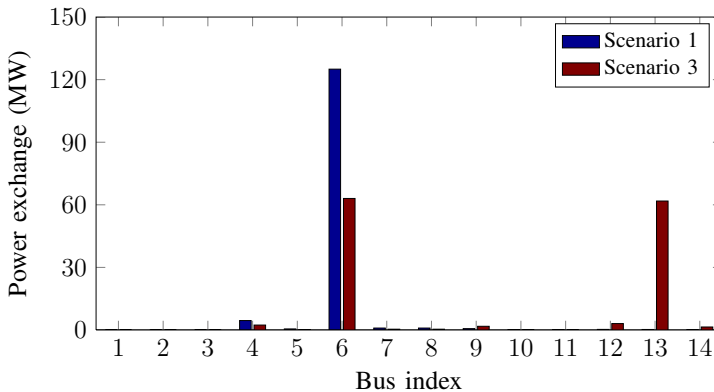


**Figure 7.6:** Power exchange comparison between Scenario 1 and 3

We can conclude that

- In order to avoid overloading of the line with limited transmission capacity, the ESS is preferred to be installed at terminal bus of the line.

### 7.6.2.3 Bus selection

By taking into account these factors for a large number of wind profile realizations, the power exchanges for all the buses ( $\sum^N \sum_{k=1}^M |P_i^s|, i \in \mathcal{N}$ ) are illustrated in Fig. 7.7. Subsequently, all the buses can be sorted according to the power exchange activity. The ranking can be considered as the reference for the bus selection. In this case, Buses 6, 9, 13 are selected for ESS installation.

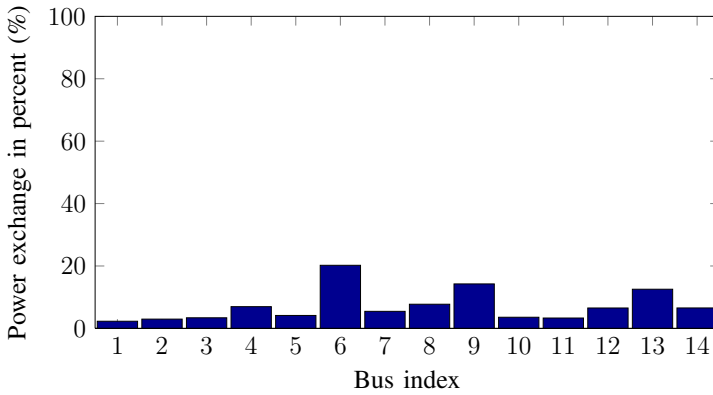


Figure 7.7: Power exchange in percent

### 7.6.3 Optimal sizing

As described in Section 7.4, for the case with multiple wind power plant integration, the spatial correlation between wind power plants has a considerable impact on the power system. In order to study to which extent the correlation affects the power and capacity ratings, two case scenarios are defined in Table 7.4.

Table 7.4: Case scenario definition

Scenario	Description	
	Wind power profile	Pearson's $r$
Scenario 1	Bus 6: $P_{wf1}$ in MW	$r = 0.2153$
	Bus 8: $P_{wf2}$ in MW	
Scenario 2	Bus 6: $P_{wf1}$ in MW	$r = 1$
	Bus 8: $P_{wf1}$ in MW	



Pearson's  $r$  is used to represent the linear correlation between WF 1 and WF 2. With smaller Pearson's  $r$ , the smoothing effect of the multiple wind power plants becomes more obvious, which leads to reduced power fluctuation to the network.

Cumulative Distribution Function (CDF)  $F$  describes the probability that a real-valued random variable  $X$  with a given probability distribution  $P$  will be found to have a value less than or equal to  $x$ , i.e.  $F_X(x) = P(X \leq x)$ .

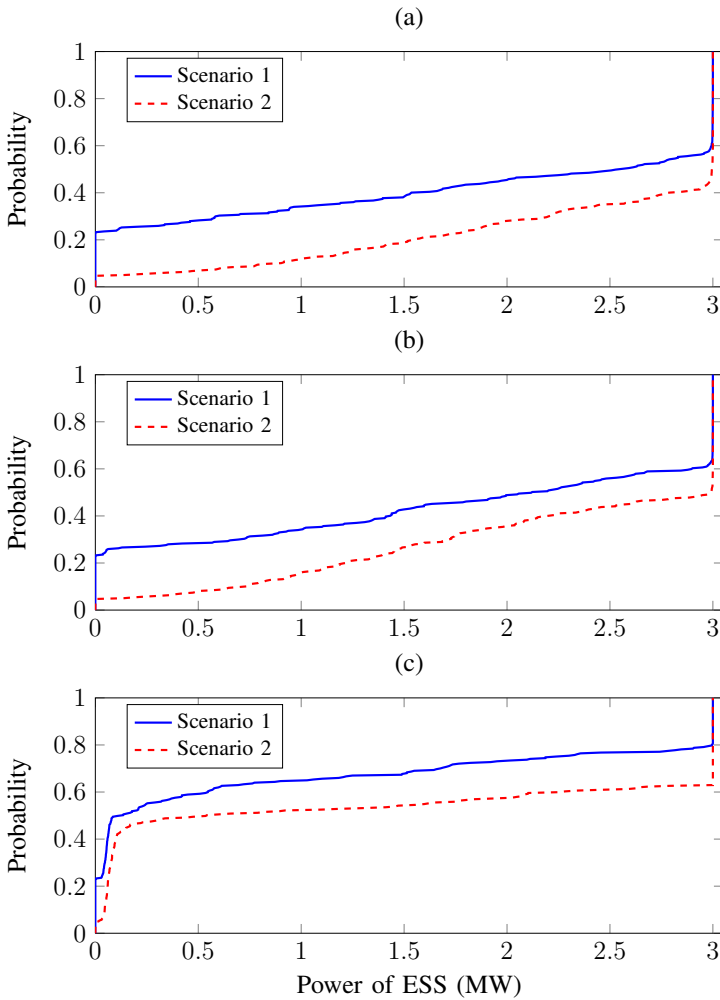


**Figure 7.8:** ECDF for power rating at different buses, (a) Bus 6, (b) Bus 9, (c) Bus 13

For the power rating, considering the technical limitation, the upper limit of all ESSs are set  $\bar{P}_i^s = 3 \text{ MW}$ ,  $\forall i \in \mathcal{S}$ . The Empirical CDF (ECDF)  $F_{\text{pow}}$  is shown in Fig. 7.8.  $F_{\text{pow}}^{-1}$  is the inverse of  $F_{\text{pow}}$ .  $F_{\text{pow}}^{-1}(0.95)$  represents the guaranteed power rating requirement for 95% of the time and adopted as the selection criterion. The values of all the selected buses (Buses 6, 9, 13) for both scenarios are listed in Table 7.5.

As illustrated in Fig. 7.8, at lower probability level ( $0 \sim 0.7$ ), the power rating of Scenario 2 is obviously larger than that of Scenario 1. It shows that a larger power capability is required to compensate larger fluctuations in Scenario 2. At the high probability level  $0.7 \sim 1.0$ , due to the upper power limits, the difference between two scenarios is not obvious. When the probability is 0.95, the power ratings for all the buses are almost the upper limits: 3 MW.

**Table 7.5:** Power comparison

Bus index	$F_{\text{pow}}^{-1}(0.95)$ (Scenario 1)	$F_{\text{pow}}^{-1}(0.95)$ (Scenario 2)
Bus 6	2.9978 MWh	2.9990 MWh
Bus 9	2.9988 MWh	2.9990 MWh
Bus 13	2.9808 MWh	2.9990 MWh

For the energy capacity rating, the Empirical CDF (ECDF)  $F_{\text{cap}}$  is shown in Fig. 7.9. During the most probability range, the energy rating of Scenario 2 is obviously larger than that of Scenario 1. It shows that larger energy capacity is required to compensate the larger power fluctuations in Scenario 2.  $F_{\text{cap}}^{-1}(0.95)$  represents the guaranteed energy capacity rating requirement for 95% of the time and adopted as the selection criterion. The values of all the selected buses (Buses 6, 9, 13) for both scenarios are listed in Table 7.6.

**Table 7.6:** Energy comparison

Bus index	$F_{\text{cap}}^{-1}(0.95)$ (Scenario 1)	$F_{\text{cap}}^{-1}(0.95)$ (Scenario 2)
Bus 6	0.5193 MWh	0.6140 MWh
Bus 9	0.5420 MWh	0.5938 MWh
Bus 13	0.3320 MWh	0.4349 MWh
Summary	1.3933 MWh	1.6427 MWh

The total energy capacity required for Scenario 2 is 1.6427 MWh, which is 17.9%

less than that of Scenario 1 (1.3933 MWh). Consequently, the correlation between wind power plants has considerable impact on the optimal sizing of ESS.

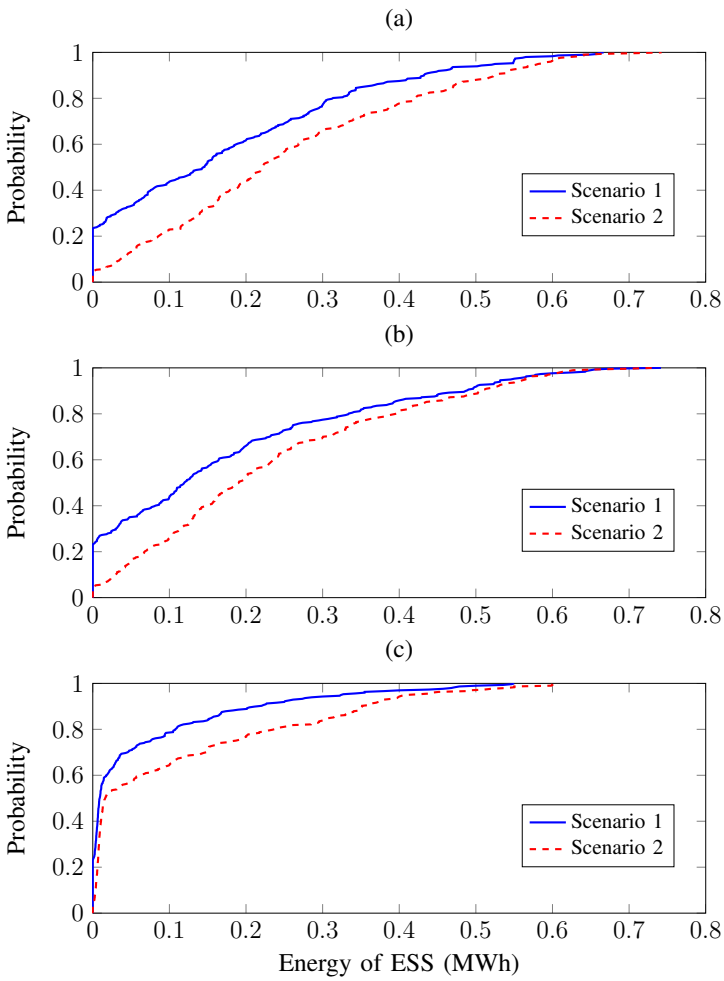


**Figure 7.9:** ECDF for energy rating at different buses, (a) Bus 6, (b) Bus 9, (c) Bus 13

## 7.7 Discussion and conclusion

In this study, the algorithms for optimal siting and sizing of ESS in the grid with a significant penetration of wind power are presented.

As the inputs for both algorithms, the long-term synthetic WPTS was generated. Since the wind speed data are usually easier to be obtained, the modeled WSTS is transformed to WPTS by applying the wind turbine power curve. For the case with multiple wind power plant integration, there exists spatial dependence between WSTSs. The multivariate WSTSs are separated into dependence structure represented by Copula function and univariate time series represented by ARMA model. According to the simulation results, the Copula-ARMA model can correctly represent the spatial and temporal correlations between two wind power plants.

For optimal siting algorithm, all the buses are assumed to have ESS installation with unlimited amounts of power and energy. The absolute power exchange of ESS at each bus is used to evaluate its activity. The activity ranking of all the buses can be used as the reference for the optimal siting of ESS. As illustrated in the simulation results, the placement of ESS at the wind power plant site is not always the best option, although this choice can reduce the transmission losses to some extent. From the point of view of improving system performance, installation of ESS at other buses, such as terminal bus of critical transmission line, can enhance the controllability.

For optimal sizing algorithm, the additional power and energy constraints are incorporated in the optimization problem. By solving a large number of the periodical optimization problems, the CDF of charging and discharging control of ESS for different realizations of wind power fluctuations can be derived. Accordingly, the optimal power and energy rating can be determined by setting the probability level (95% in this study). It shows that the correlation between wind power plants has a significant impact on the derived power and energy rating.



# Coordinated Control Strategies for Microgrid Application

---

In this Chapter, two coordinate control strategies are developed for islanded operation of the microgrid with wind power integration. These two strategies aim to handle different study cases which are dependent on the roles that ESSs and wind turbines play.

For the first case (Case 1), the wind power production is not dominant for the load consumption. In order to maximally utilize the wind power, wind turbines are controlled in the MPPT mode during the partial load regime and power limiting mode during the full load regime. Based on the Fuzzy control strategy, the ESS is coordinated with other dispatchable Distributed Generation (DG) units to keep the frequency and voltage stable.

For the second case (Case 2), the wind power penetration level is high which can cover most load consumption. The full converter wind turbine (DD-PMSG in this study) is regulated following the loads. Its Voltage Source Inverter (VSI), is controlled to provide voltage and frequency references. According to the operation statuses of the wind turbine, when and how much power should be compensated by the ESS (BESS in this study) can be determined. In such way,

the ESS is not always online and activated only if necessary.

## 8.1 Background and basic knowledge

DG types and technologies applied in the microgrid are illustrated in Fig. 8.1. Conventional generators have direct coupling between rotational machines and microgrid, such as synchronous generators or induction generators. Besides, the majority of distributed resources are interfaced to the utility grid or to the customer load via DC-AC Pulse-Width Modulated (PWM) Voltage Source Inverter (VSI) systems including variable frequency sources (such as wind energy sources), high frequency sources (such as micro-turbines), and direct energy conversion sources producing DC voltages or currents (such as fuel cells and photovoltaic sources).

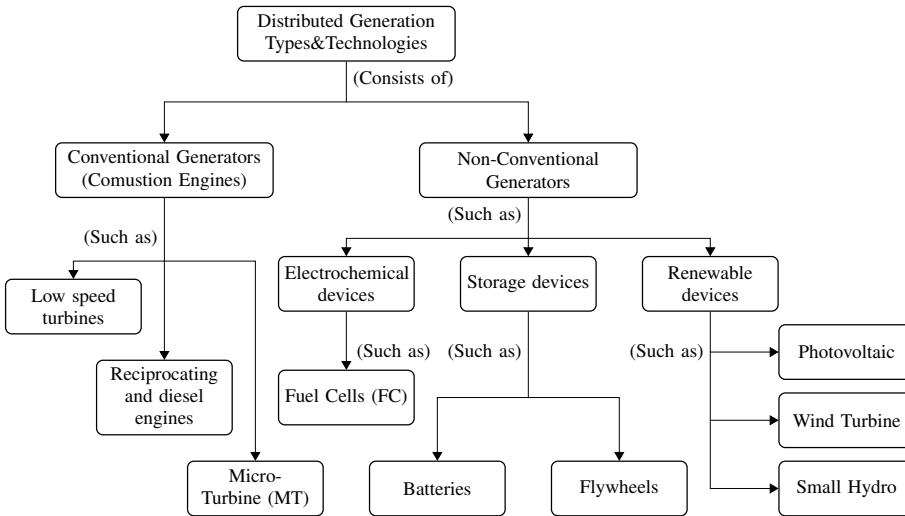


**Figure 8.1:** DG types and technologies [16]

The performance of DG units in the microgrid is largely dependent on the interfacing scheme. Compared with the conventional rotary generators, inverter interfaces make the energy sources more flexible in their operation and control. However, new issues are introduced, such as the absence of physical inertia, wide-band of dynamics, limited overload capability, susceptibility to parameters variation, and switching harmonics generation [16].

## 8.2 Modeling of DG units

The modeling of several DG units used for the case studies are presented in this section.

### 8.2.1 BESS modeling

#### 8.2.1.1 Battery model

Different modeling approaches of battery have been developed in [190], [191]. The battery model should include the terminal DC voltage  $u_{DC}$  and the internal resistance  $Z$  which is a function of several internal variables such as State of Charge (SOC), the age and temperature of the battery [192]. A simplified electric equivalent battery model and a complex equivalent with parasitic path are shown in Fig 8.2 (a) and Fig. 8.2 (b), respectively. In this study, the simplified battery model is adopted under the following additional assumptions.

- The internal resistance is assumed as constant because it has to be very small to the high current application  $Z(s, SOC) = Z$ .
- The Controlled Voltage Source (CVS) is dependent on  $SOC$  and calculated by  $E(s, SOC) = u_{max} \cdot SOC + u_{min} \cdot (1 - SOC)$ , where  $u_{max}$  and  $u_{min}$  indicate the voltage of fully loaded cell and voltage of discharged cell, respectively.
- The battery capacity is assumed as constant ignoring the aging problem.

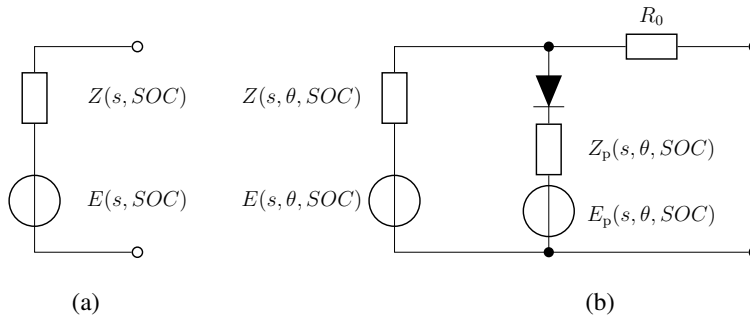


**Figure 8.2:** Battery Electric Equivalent: (a) simple (b) with parasitic reaction



The SOC is calculated with an integrator, counting the current  $i_{DC}$  of the battery,

$$SOC(t) = SOC_0 - \int_{t_0}^t i_{DC}(t)dt, \quad (8.1)$$

where  $SOC_0$  indicates the initial charging level.

Accordingly, the equation for the terminal voltage  $u_{DC}$  is,

$$u_{DC} = u_{max} \cdot SOC + u_{min} \cdot (1 - SOC) - i_{DC} \cdot Z. \quad (8.2)$$

### 8.2.1.2 BESS Controller

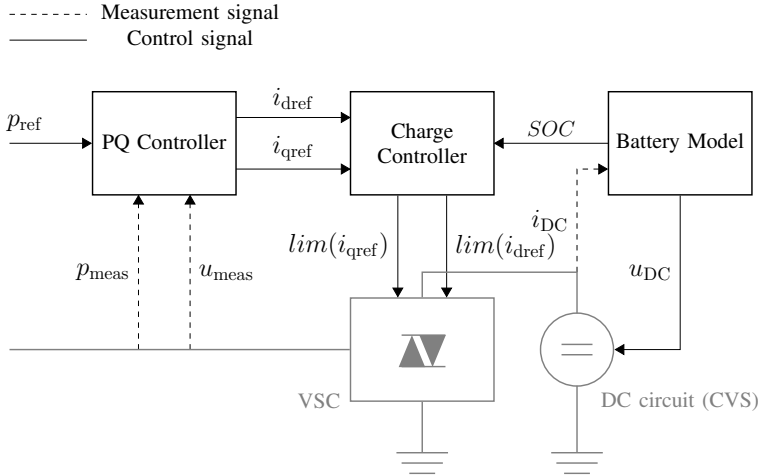


**Figure 8.3:** BESS Configuration

The BESS configuration is illustrated in Fig. 8.3. The battery model is interfaced with the microgrid by the Voltage Source Converter (VSC). More details about VSC control with different control strategies are described in Section 8.3. In this study, the VSC of BESS is always controlled to operate in the  $P/Q$  mode. In other words, the VSC can be considered as a Controlled Current Source (CCS).

The BESS controller can be divided into two parts: PQ controller, charge controller. Based on the power reference  $p_{ref}$ , PQ controller generates the current references  $i_{dref}$  ( $d$ -axis) and  $i_{qref}$  ( $q$ -axis). These references are limited by the charge controller according to the measured SOC. The derived currents  $lim(i_{dref})$  and  $lim(i_{qref})$  are fed into VSC [192].

### 8.2.2 Modeling of dispatchable DG units

In this study, dispatchable DG units such as diesel generators are considered to be conventional synchronous generators directly coupled with the microgrid. It can be modeled as a typical synchronous generator system, depicted in Fig. 8.4. Automatic voltage regulator (AVR) is used for the excitation system control, while Governor (GOV) is used to control the prime mover according to the load reference value. The classical models defined by IEEE (1981) are used in this study and listed in Table 8.1.

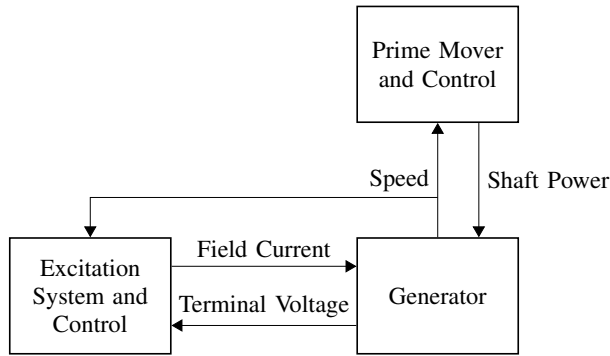


**Figure 8.4:** Generation System

**Table 8.1:** Model

Component	Model type
Generator	Built-in synchronous generator model
GOV	IEEEG1
AVR	EXST1

### 8.2.3 Modeling of wind power resource

The modeling of wind power resource is dependent on the roles that wind turbine plays.

- If the wind turbine is controlled to maximally extract the wind power, the wind power production is largely dependent on the wind speed and can be simplified modeled by a non-dispatchable “negative load”.

- If the wind turbine is controlled coordinately with other devices (ESS), a detailed model is required. In this study, the modeling of Direct Drive PMSG (DD-PMSG) wind turbine is described.

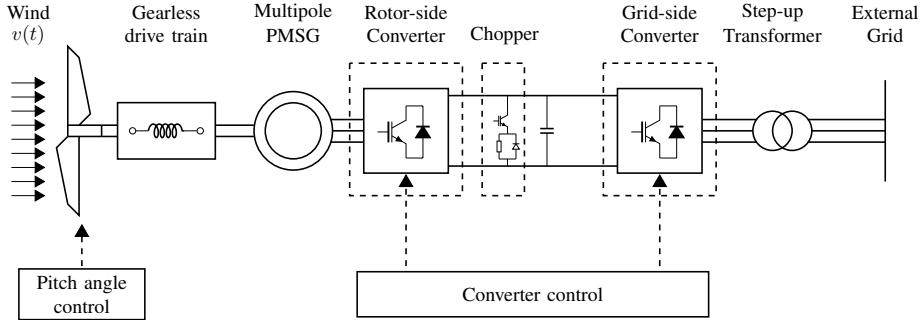


**Figure 8.5:** Configuration of a PMSG wind turbine

DD-PMSG wind turbine has several advantages compared with other WTG types, including gearless construction, self excitation capacity, high efficiency operation and ease in accomplishing fault-ride through and grid support [76], [193]. Currently, commercial DD-PMSG wind turbine primarily makes use of passive rectifier followed by an Insulated Gate Bipolar Transistor (IGBT) inverter [194], [195]. However, a DD-PMSG wind turbine with two back-to-back VSCs is considered more efficient and becomes more and more favored by the wind power industry [193], [196].

The general configuration of a DD-PMSG wind turbine is depicted in Fig. 8.5. The aerodynamic power is captured by the rotor blades and then transferred to the PMSG where mechanical energy is converted into electrical energy. The stator windings of the PMSG is connected to the grid through a back-to-back converter which is built by two Pulse Width Modulation (PWM) based VSCs: a Rotor-Side Converter (RSC) and a Grid-Side Converter (GSC) with a DC voltage link in between. A chopper is equipped to dissipate the surplus of DC energy through an unloading resistance. GSC (equivalent to VSI) is connected to a filter for elimination of harmonics in order to improve the power quality. Through a step-up transformer, the converted electrical energy is transferred to the external grid.

### 8.2.3.1 Generator

A detailed treatment of the synchronous generator is beyond the scope of this paper. The differential equations of a synchronous machine have been described

by many references. The equation of PMSG can be expressed from the equation of a DC excited synchronous generator with the simplification that PMSG does not have damper winding. The steady-state voltage equation of the generator, expressed in the rotor-oriented  $dq$  reference, can be expressed as follows,

$$\begin{aligned} v_{sd} &= R_s i_{sd} + \frac{d}{dt} \psi_{sd} - p \omega_g \psi_{sq}, \\ v_{sq} &= R_s i_{sq} + \frac{d}{dt} \psi_{sq} + p \omega_g \psi_{sd}, \end{aligned} \quad (8.3)$$

with the stator flux linkage,

$$\begin{aligned} \psi_{sd} &= (L_{ls} + L_{dm}) i_{sd} + \psi_{PM}, \\ \psi_{sq} &= (L_{ls} + L_{qm}) i_{sq}, \end{aligned} \quad (8.4)$$

where  $R_s$  is the resistance of the stator winding,  $p$  is the number of pole-pairs.  $v_{sd}$ ,  $v_{sq}$ ,  $i_{sd}$ ,  $i_{sq}$ ,  $\psi_{sd}$  and  $\psi_{sq}$  are the  $d$  and  $q$  components of instant stator voltage, current and flux.  $L_{ls}$  is the leakage inductance of the stator winding,  $L_{dm}$  and  $L_{qm}$  are the mutual inductances,  $\psi_{PM}$  is the flux linkage by permanent magnet.

The electrical torque  $T_g$ , active and reactive power of generator can be derived by,

$$\begin{aligned} T_g &= 1.5p\psi_{PM}i_{sq}, \\ P_{gen} &= 1.5(u_{sd}i_{sd} + u_{sq}i_{sq}), \\ Q_{gen} &= 1.5(u_{sq}i_{sd} - u_{sd}i_{sq}). \end{aligned} \quad (8.5)$$

### 8.2.3.2 Back-to-back VSCs

A detailed VSC model consists of valves with turn-off capability and anti-parallel diodes. Due to the high switching frequencies (several kHz), such a detailed model requires very small simulation time steps. The calculation task becomes very time-consuming.

Since this study focuses on the power system stability, the major interest is the control behavior of PWM-converter instead of switching frequencies, or high frequency phenomenon. A fundamental frequency model in a stator-voltage oriented reference frame is applied. By assumption of ideal PWM modulation (infinite modulation frequency), the fundamental frequency line to line AC voltage  $U_{AC}$  and DC voltage  $U_{DC}$  are related by,

$$\begin{aligned}
 U_{AC} &= U_{AC,d} + jU_{AC,q}, \\
 U_{AC,d} &= \frac{\sqrt{3}}{2\sqrt{2}}P_{md}U_{DC}, \\
 U_{AC,q} &= \frac{\sqrt{3}}{2\sqrt{2}}P_{mq}U_{DC},
 \end{aligned} \tag{8.6}$$

where  $P_{md}$  and  $P_{mq}$  represent the PWM modulation indices of the  $d$  and  $q$  components, respectively. The control scheme of back-to-back VSCs for microgrid application will be elaborated in Section 8.6.

### 8.2.3.3 Chopper

As depicted in Fig. 8.5, the chopper consists of a valve (e.g. IGBT) in series with an up-latching resistance and anti-parallel diode [20], [197]. An hysteresis loop is included in the controller (see Fig. 8.6),

- When the DC-link voltage  $U_{DC}$  increases over a critical high threshold  $U_{th\_high}$ , the chopper is triggered.
- When  $U_{DC}$  is below a critical low threshold  $U_{th\_low}$ , the chopper is blocked.

The hysteresis is to prevent the chopper from repeated acting.

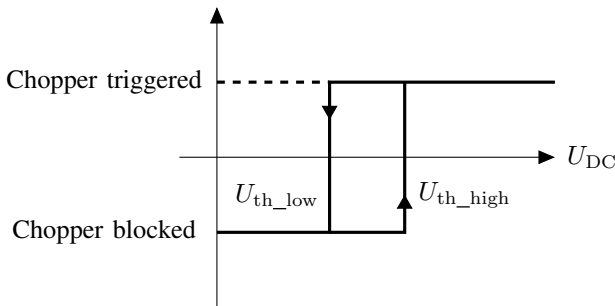


**Figure 8.6:** Control strategy of chopper

### 8.2.3.4 Pitch angle control

The pitch actuator is a nonlinear servo that generally rotates all the blades-or part of them in unison. It can be simply modeled as a first-order dynamic servo with saturation in the amplitude and derivative of the output signal [198]. The pitch angle controller and pitch actuator are shown in Fig. 8.7. The control objectives for different operation modes in micro-grid are different. The details are explained in Section 8.6.

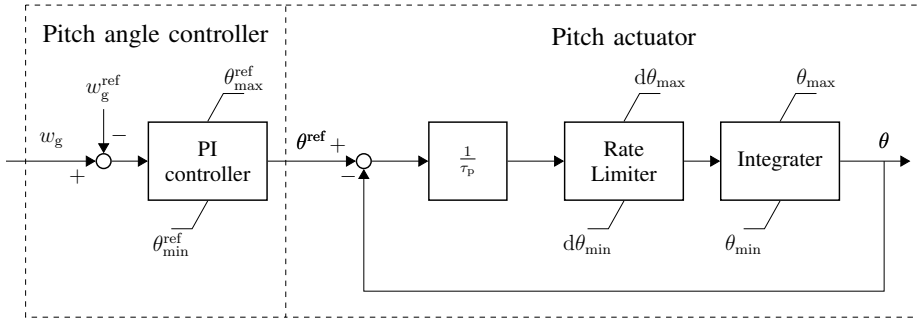


Figure 8.7: Pitch angle control

## 8.3 Control strategies of VSI-interfaced DG units

There are two main strategies proposed in literatures for controlling VSI-interfaced DG (DG for short in this section) units in a microgrid, including the master/slave approach and the droop control approach [199].

In the master/slave approach, one DG (master) operates as a voltage source. It is responsible for controlling the microgrid voltage and frequency by  $U/f$  control. The other DG units (as slaves) operate as current sources, which are responsible for supplying active power to meet the load demand by  $P/Q$  control. The DG units communicate with each other for load sharing. Therefore, the master/slave approach can be realized by implementing  $U/f$  control for the master DG unit and  $P/Q$  for the slave DG unit.

In the droop control approach, the DG units are equipped with a  $P-f$  and  $Q-V$  droop controllers. Based on the droop values, the amount of load is shared by the DG units. The main advantage of this technique is that no communication links are required.

The aforementioned three controllers ( $P/Q$ ,  $U/f$  and droop control) are briefly introduced in this section.

### 8.3.1 $P/Q$ Control

The control objective is to enforce the active and reactive power ( $P, Q$ ) following the given references ( $P_{\text{ref}}, Q_{\text{ref}}$ ). The control structure is illustrated in Fig. 8.8. The working principle is shortly described.

Considering the filter impedance, the equivalent mathematical model of the filter in three phases can be expressed by,

$$\begin{aligned} U_{ia} &= U_{ga} + (R_f I_{ga} + L_f \frac{dI_{ga}}{dt}), \\ U_{ib} &= U_{gb} + (R_f I_{gb} + L_f \frac{dI_{gb}}{dt}), \\ U_{ic} &= U_{gc} + (R_f I_{gc} + L_f \frac{dI_{gc}}{dt}), \end{aligned} \quad (8.7)$$

where  $U_{i(a,b,c)}$  indicate the three phase voltages at the VSI terminal,  $U_{g(a,b,c)}$  indicate the three phase voltages at the grid terminal,  $R_f$  and  $L_f$  represent the resistance and inductance of the filter, respectively.

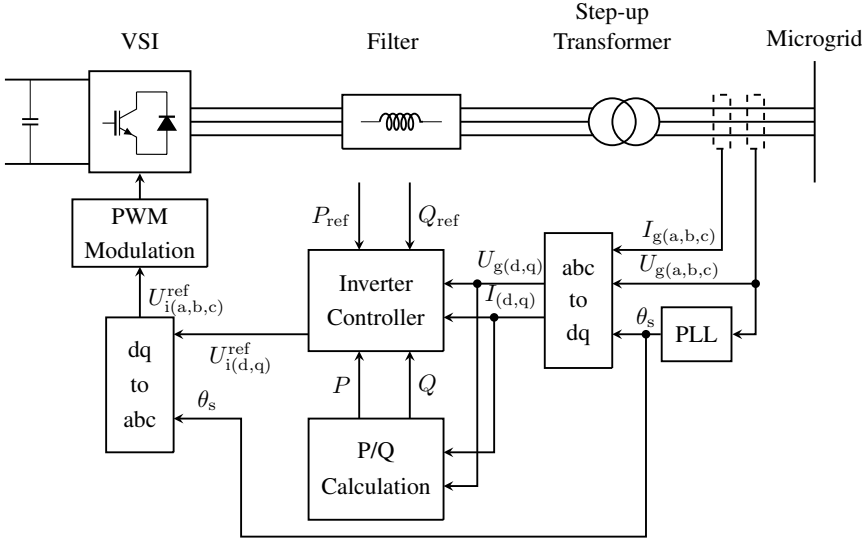


Figure 8.8: Structure of  $P/Q$  control

Accordingly, Eqn. 8.7 can be transformed into  $dq$  coordinates,

$$U_{id} = U_{gd} + (R_f I_{gd} + L_f \frac{dI_d}{dt} - \omega L_f I_q) \quad (8.8)$$

$$, U_{iq} = U_{gq} + (R_f I_{gq} + L_f \frac{dI_q}{dt} + \omega L_f I_d), \quad (8.9)$$

where  $\omega$  indicates the frequency of voltage and current. In the grid-connected operation, it equals to the network frequency. In the islanded operation, it is dependent on the DG unit which provide  $U/f$  or droop control.

It is observed that there exist coupling terms  $-\omega L_f I_q$  and  $\omega L_f I_d$  in Eqn. 8.8 and Eqn. 8.9, respectively. By introducing the feedforward decoupling, the control system for the grid-connected inverter can be designed consisting of two cascaded loops, as shown in Fig. 8.9. The inner loop regulates the  $d$ - and  $q$ -axis currents ( $I_d, I_q$ ), while the outer loop regulates the real and reactive power injections ( $P, Q$ ) to the grid.

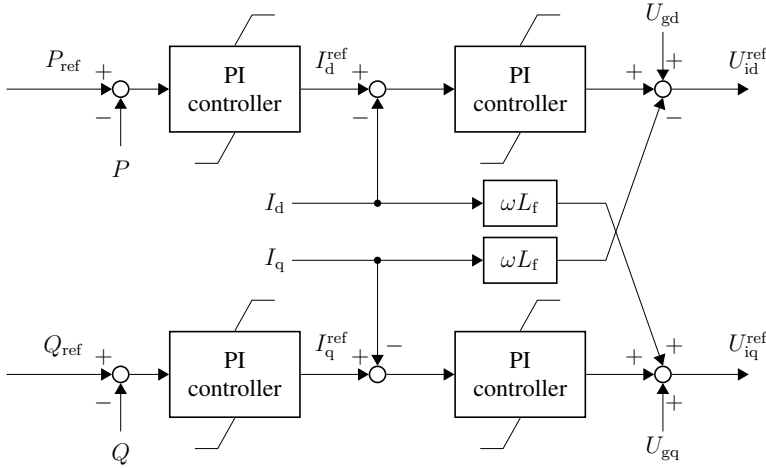


**Figure 8.9:** Dual-loop control block of inverter controller ( $P/Q$ )

As the inputs of the inverter controller,  $U_{g(d,q)}, I_{g(d,q)}$  can be calculated by the measured three-phase voltage and current  $U_{g(a,b,c)}$  and  $I_{g(a,b,c)}$  through Park transformation. The required phase reference  $\theta_s$  is calculated by Phase Locked Loop (PLL). The active and reactive power injections ( $P, Q$ ) can be calculated based on  $U_{g(d,q)}, I_{g(d,q)}$ .

The  $d - q$  decoupling terms are omitted following engineering practices since their effect is neglectable. In the modulation,  $U_{id}^{ref}, U_{iq}^{ref}$  are limited. As the outputs, instead of using  $U_{id}^{ref}, U_{iq}^{ref}$ , the PWM modulation indices  $P_{md}$  and  $P_{mq}$



are applied,  $P_{\text{md}}, P_{\text{mq}} \in [0, 1]$ . The modified dual-loop control block is depicted in Fig. 8.10.

$$\begin{aligned} U_{\text{id}}^{\text{ref}} &= \frac{\sqrt{3}}{2\sqrt{2}} P_{\text{md}} U_{\text{DC}} \\ U_{\text{iq}}^{\text{ref}} &= \frac{\sqrt{3}}{2\sqrt{2}} P_{\text{mq}} U_{\text{DC}} \end{aligned} \quad (8.10)$$

To be noticed, the active and reactive power control in the outer loop can be replaced by DC voltage and AC voltage control, respectively.

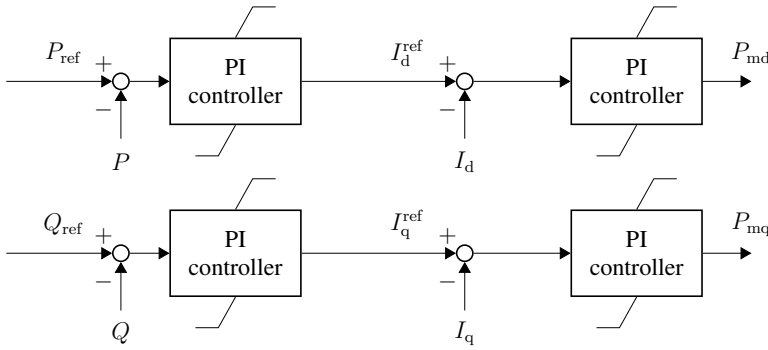


**Figure 8.10:** Dual-loop control block of inverter controller ( $P/Q$ )

### 8.3.2 $U/f$ Control

Due to the fault or power quality problem, the microgrid will be disconnected from the external grid, which leads to the mismatch between power generation and consumption. By means of  $U/f$  control strategy which aims to provide solid frequency and voltage support, one DG unit can act as a master to response to the sudden change. The  $U/f$  control structure is shown in Fig. 8.11.

The dual-loop control block of inverter controller is depicted in Fig. 8.12. Different from  $P/Q$  control, the voltage phase reference  $\theta_s$  should be decided instead of measured by the PLL.  $\theta_s$  is based on the pre-islanding phase condition. The  $d$  and  $q$  components of grid voltage are controlled by the  $d$  and  $q$  components of the AC grid current, respectively. The inner current loop determines the PWM modulation indices.

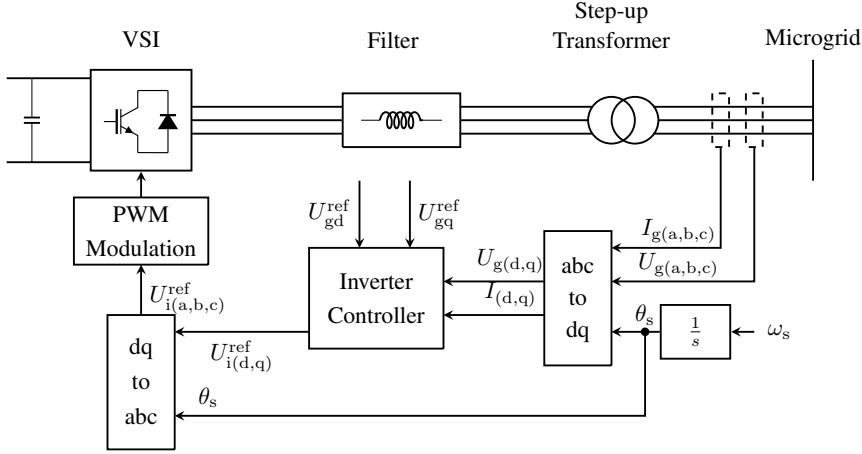


Figure 8.11: Structure of  $U/f$  control

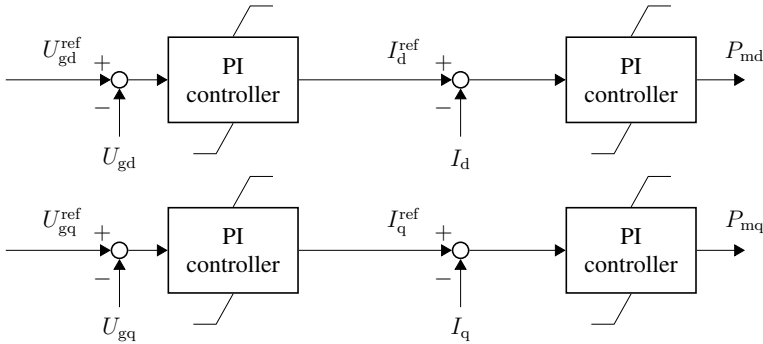


Figure 8.12: Dual-loop control block of inverter controller  $U/f$

### 8.3.3 Droop Control

Under this control, the VSI acts as a voltage source, with the magnitude and frequency of the output voltage controlled through droops which emulates the behavior of a synchronous machine, as described in the following equations,

$$\omega_s = \omega_{s0} - k_P P, \tag{8.11}$$

$$|U_i^{\text{ref}}| = |U_{i0}^{\text{ref}}| - k_Q Q. \tag{8.12}$$

where  $P$  and  $Q$  are the active and reactive power outputs of the inverter,  $k_P$  and  $k_Q$  are the droop slopes,  $\omega_{s0}$  and  $|U_{i0}^{\text{ref}}|$  are the idle values of the angular frequency and voltage (values of the inverter angular frequency and terminal

voltage at no load conditions).

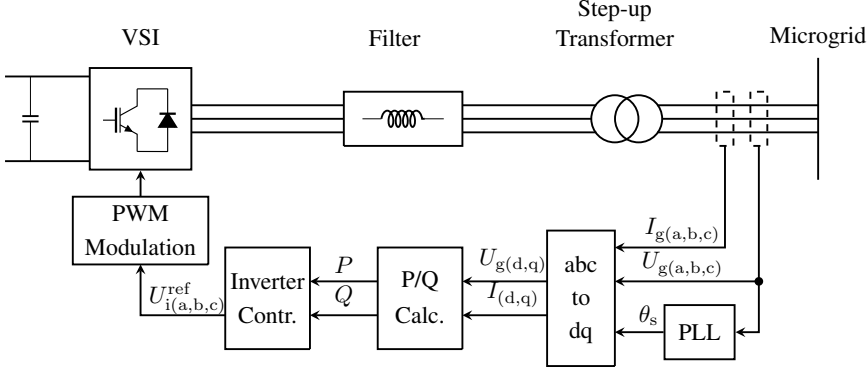


**Figure 8.13:** Structure of droop control

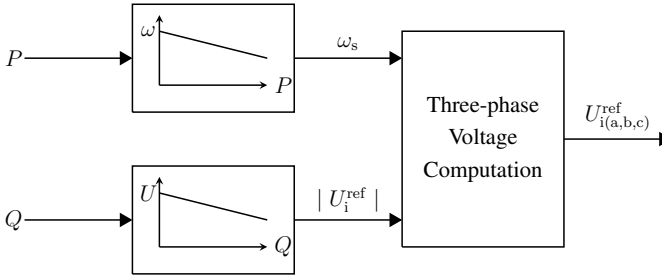


**Figure 8.14:** Droop control

When a VSI is interconnected with a stiff AC system, characterized by an angular frequency  $\omega_{\text{grid}}$  and terminal voltage  $U_{\text{grid}}$ , the voltage and frequency references are externally imposed. In this case, the desired output powers  $P_1$  and  $Q_1$  can be obtained in the VSI output by adjusting the idle values of the angular frequency and voltage as follows,

$$\omega_{s0} = \omega_{\text{grid}} + k_P P_1, \quad (8.13)$$

$$|U_{i0}^{\text{ref}}| = |U_g| + k_Q Q_1. \quad (8.14)$$

When a cluster of VSIs operates in a standalone AC system, frequency variation leads to an automatic power sharing, such that for a system with VSIs, the following equality stands,

$$\Delta P = \sum_{i=1}^n \Delta P_i, \quad (8.15)$$

with  $\Delta P_i$  being the power variation in the  $i$ th VSI. The frequency variation can be computed as,

$$\Delta\omega = k_{P_i} \Delta P_i. \quad (8.16)$$

## 8.4 Control topology of microgrid

The microgrid is composed of several DG units which can be located at some distance from one another. It is required to maintain coordinated operation and control of all DGs in the microgrid to maintain stability in the system and accomplish the goals of the microgrid.

According to [17], [200], the control topology has two levels: MicroGrid Central Controller (MGCC) and Local Controller (LC). The MGCC is a supervisory centralized controller which coordinates all the LCs of DG units through a communication network. MGCC can receive status information from all the local controllers and monitoring systems in the microgrid and make decisions from a system point of view. Some of the key objectives based on a literature review are listed below [200]:

- To provide power references for the DG units.
- Economic scheduling.
- Supervise demand side bidding.
- To control peak load during peak load hours.
- To control non critical loads during islanding.
- To minimize system losses.
- To detect islanding conditions based on the PCC measurements.
- To initiate resynchronization with the LCs when the grid is restored.
- To monitor power flows through local generating units and the PCC.

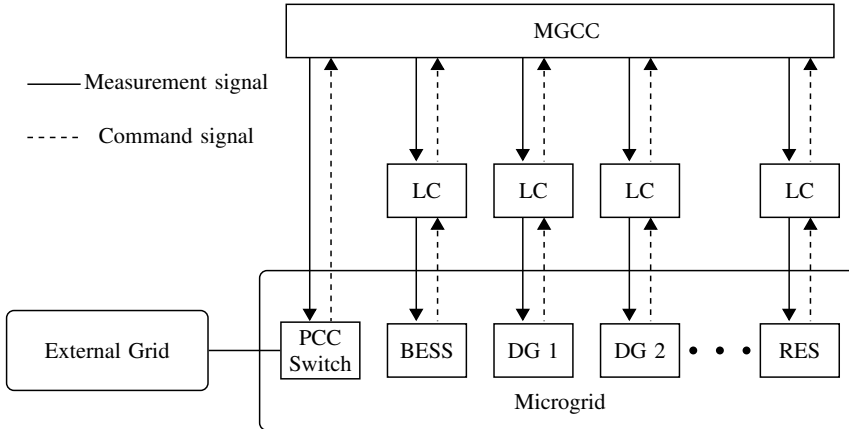


**Figure 8.15:** The hierarchical control topology of microgrid

## 8.5 Coordinated control strategy (Case 1)

In this section, a fuzzy logic based coordinate control strategy between a BESS and dispatchable DG units for frequency support is proposed. Compared with other conventional controllers, the fuzzy logic controller is not sensitive to the variations of system structure, parameters and operation points and can be easily implemented in a large scale nonlinear system. Due to the large energy capacity and good capability of power regulation, BESS can be not only involved in the primary control but also in the secondary control. Besides, state of charge (SOC) of the BESS is taken into account, which affects the control performances of BESS.

### 8.5.1 Islanded Mode

In this mode, synchronous generator based DG units will support frequency and voltage by GOV and AVR, respectively. BESS has the advantages of large capacity, flexibility of charging and discharging and fast-response capability and can be considered as a complementary component. We mainly concentrate on the frequency control. Similar to the conventional large power system, the main reason of the frequency deviation is the imbalance between generation and consumption. When the deviation exceeds a predefined threshold, the primary control responses by the locally equipped droop controllers. The time scale is in the order of seconds. The secondary control restores frequency to its nominal value. It adjusts the load reference set point of the governor of dispatchable DG

units. The time scale is in the order of minutes.

The coordinated controller is illustrated in Fig. 8.16. The BESS participates in both primary and secondary control together with the dispatchable DG units. The participation rate is dependent on the SOC and power command ( $p_{\text{cmd}}$ ), which is derived from the frequency controller.  $p_{\text{cmd}}$  is partly compensated by the BESS. The rest part  $p_{\text{total}}^{\text{ref}}$  would be further allocated by the dispatch function block to generate the load reference set points for the dispatchable DG units  $p_{\text{DG}}^{\text{ref}}$ , as shown in Eqn. 8.17.

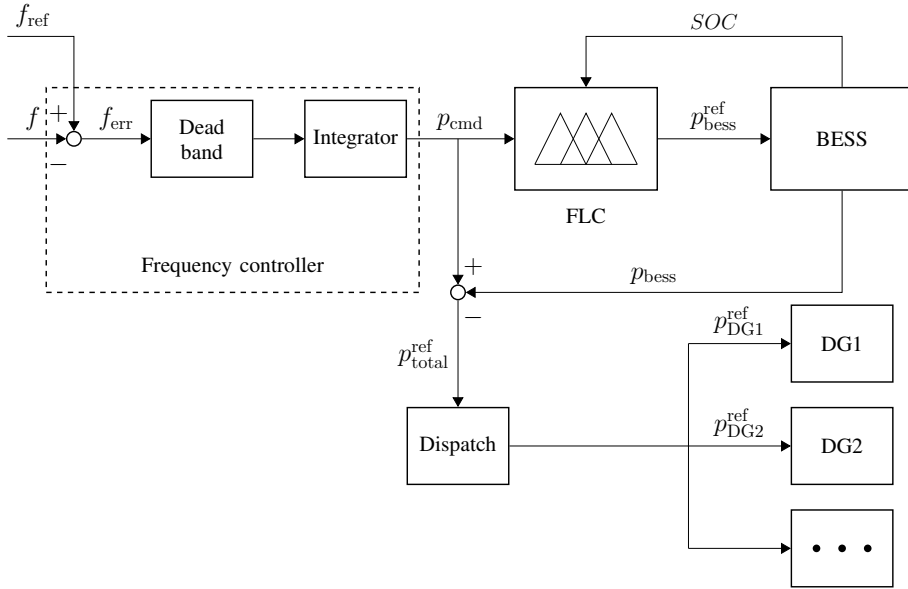


**Figure 8.16:** Islanded control

$$p_{\text{DG}i}^{\text{ref}} = d_i \cdot p_{\text{total}}^{\text{ref}}, \quad (8.17)$$

where  $d_i$  indicates the distribution factor for the  $i$ th dispatchable DG unit. It is predefined and fixed which can be either based on the nominal power or available power of dispatchable DG units. In this study, it is proportional to the nominal power  $p_{\text{nom}i}$ ,

$$d_i = \frac{p_{\text{nom}i}}{p_{\text{total\_nom}i}}, \quad \text{with } p_{\text{total\_nom}i} = \sum_{i=1}^n p_{\text{nom}i}. \quad (8.18)$$

## 8.5.2 Design of fuzzy logic controller

As illustrated in Fig. 8.16, the fuzzy-logic controller adjusts  $p_{\text{bess}}^{\text{ref}}$  based on the charging level of BESS (SOC) and target power  $p_{\text{bess}}^{\text{tar}} = p_{\text{cmd}}$  to secure its operation range. The proposed control strategy can be formulated in the following equations Eqn. 8.19-8.21. Fuzzy rules for  $p_{\text{bess}}^{\text{ref}}$  is listed in Table 8.2, the relevant fuzzy surface is shown in Fig. 8.17.

$$p_{\text{bess}}^{\min} \leq p_{\text{bess}} \leq p_{\text{bess}}^{\max} \quad (8.19)$$

$$SOC_{\min} \leq SOC \leq SOC_{\max} \quad (8.20)$$

$$p_{\text{bess}}^{\text{ref}} = f_{\text{fuzzy}}(p_{\text{bess}}^{\text{tar}}, SOC) \quad (8.21)$$

**Table 8.2:** Fuzzy rules

SOC	$p_{\text{bess}}^{\text{tar}}$	NB	NM	NS	ZO	PS	PM	PB
VS		NB	NB	NB	NM	NM	NS	ZO
S		NB	NB	NM	NM	NS	ZO	PS
M		NM	NM	NS	ZO	PS	PM	PM
B		NS	ZO	PS	PM	PM	PB	PB
VB		ZO	PS	PM	PM	PB	PB	PB

## 8.6 Coordinated control strategy (Case 2)

The WECS-based DG unit is one of the fastest growing sources of power generation for microgrid. In the grid-connected mode, since voltage and frequency are provided by the external grid, wind turbine is expected to work under  $P/Q$  control, normally Maximum Power Point Tracking (MPPT) from the efficiency point of view.

In the islanded mode, if conventional synchronous generators are present (diesel or gas generators), the equipped excitation and governor are used to regulate voltage and frequency at a reference value. Otherwise, one VSI will act as the master VSI to provide a primary voltage and frequency regulation ( $U/f$  control)

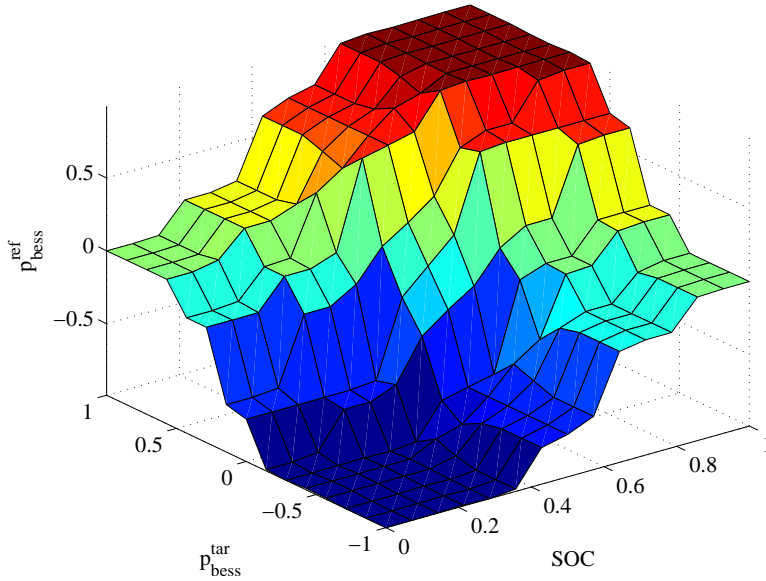


**Figure 8.17:** Fuzzy rule surface plot

[201]. The other inverters are controlled as slaves in  $P/Q$  mode. Generally, the master VSI is coupled to an ESS which can continuously supply power for load following. In that way, the ESS needs continuous online operation under this condition.

Previously, the application of WECSs for isolated power system was limited due to the intermittent nature of wind. Currently, the application has been expanded due to the improvement of controllability of WECSs. A simple control strategy of a PMSG wind turbine for stand-alone operation was proposed in [202]. A BESS was equipped at DC link and coordinated with the PMSG to achieve maximum power extraction from wind. In this way, the surplus of wind energy can be stored in the BESS and fed back to the load during a wind power shortage. However, the required BESS capacity will be large if the surplus or shortage is large. This problem occurs for the island application with wealthy wind resources and low load demand. BESS is still an expensive solution. The cost increases depending on the power and energy capacity [158]. Besides, the BESS is always required to be in online operation and activated frequently which are harmful to its lifetime. In [203], a load-following mode of operation control scheme was presented. Since there is no additional energy storage and could only operate when the available wind power is larger than the load consumption. In [195], the main generation role was assigned to the wind module by supervisory controller. The sliding mode controller (SMC) was designed for integration of



PMSG wind turbine into a islanded hybrid system in two different operational modes: optimum power conversion and power regulation. However, pitch angle control is assumed to be fixed which constraints the load following capability of the PMSG wind turbine.

This study has the following aspects. Firstly, it aims to design the converter controller of the PMSG wind turbine for the microgrid application in areas with wealthy wind regimes. By means of the developed controller, the PMSG could operate both in grid-connected mode and islanded mode for different control purposes. The smooth transition between two modes by means of a chopper and the elimination of torsional oscillations are taken into account as well. Secondly, in the case with insufficient wind power during the islanded operation, the BESS is considered as complementary generation unit. The coordinated control strategy is developed to fulfill the load demand with less capacity of BESS.

### 8.6.1 Converter control scheme design

The control objective of the back-to-back VSCs is dependent on the operation modes. In the grid-connected operation, VSCs are required to operate coordinately to transfer the reference power into the grid. So far, there have been two main control structures [204], [205]:

1. RSC is utilized for the power control while GSC controls the DC voltage to balance the input and output power [206].
2. The functions of RSC and GSC are swapped.

The islanded operation could be due to either a planned (intentional) or an unplanned (unintentional) switching event [207]. In the islanded operation, GSC is considered as the master VSI and  $U/f$  control is applied to establish the stable voltage and frequency for the microgrid [208]. Accordingly, the voltage of the DC link should be kept constant by the RSC.

Obviously, the operation mode transition leads to a controller switch, which results in voltage or frequency transients. The smooth transition between the modes is of the main interest. First of all, structure 2 is selected for grid-connected controller. As such, the RSC control can be kept in both operation modes. Secondly, the chopper is applied to unload the excess energy gathered in DC link. Thirdly, the torsional oscillation due to transition can be eliminated by the damping controller.

## 8.6.1.1 RSC control

The RSC is similar to the one described in [204], [197], which is to control the DC link voltage and to maintain the stator voltage  $U_s$ .

As shown in Fig. 8.18, the controller has a two-loop structure, using the stator voltage oriented reference frame. The outer loop is to control the DC voltage  $U_{DC}$  by the  $d$ -component of the stator current, while the stator voltage  $U_s$  is controlled by the  $q$ -component of the stator current. The inner loop is a current loop which decides modulation indices of  $d$  and  $q$  axis. The reference of DC voltage  $U_{DC}^{\text{ref}}$  is derived from a damping controller which generates additional damping torque to handle the torsional oscillation between rotor and generator masses. According to [197], the rated reference value of stator voltage  $U_s^{\text{ref}}$  provides a robust control of the generator to avoid the risk of over-voltage and saturation of the converter.

As mentioned above, this control structure can be maintained in both grid-connected and islanded operation modes to eliminate the potential transients during the controller switch.

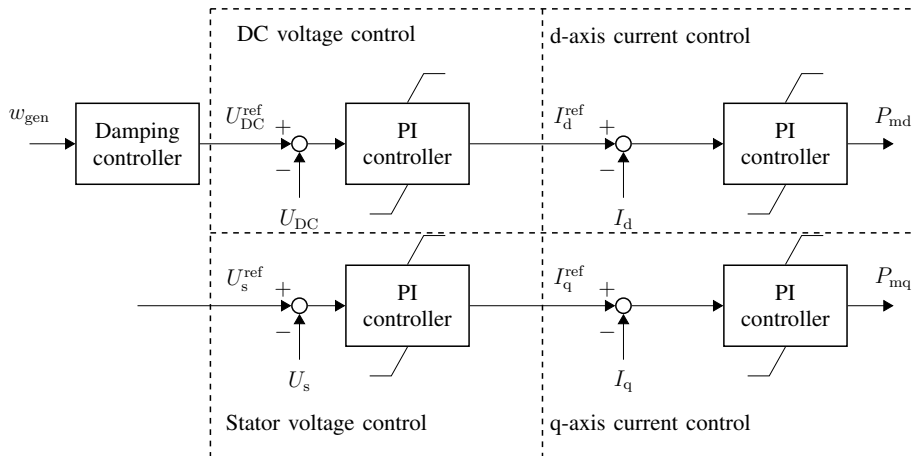
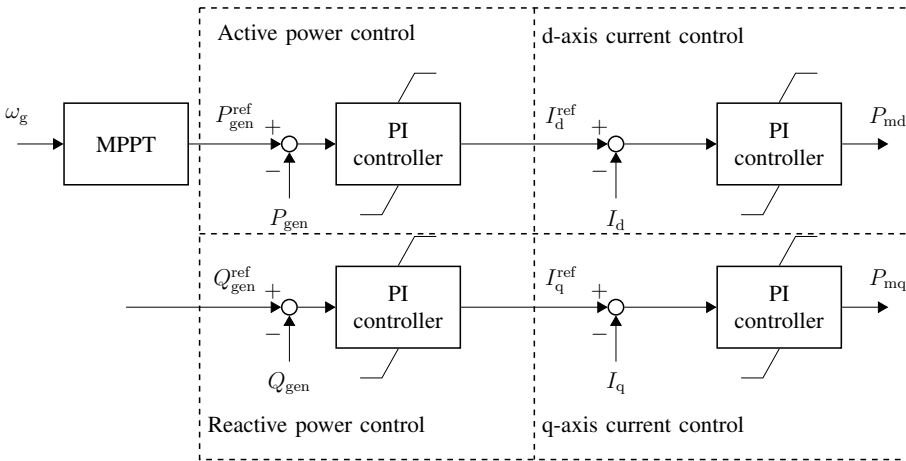


Figure 8.18: Rotor side converter control

### 8.6.1.2 GSC control

The GSC control is equivalent to the VSI control described in Section 8.3. Its structure depends on different operation modes.

In the grid-connected mode, the GSC operates in  $P/Q$  mode: the active and reactive power transferred to the grid are controlled separately by the  $d$  and  $q$  current components. The controller in the grid-connected mode is illustrated in Fig. 8.19. The active power reference  $P_{\text{gen}}^{\text{ref}}$  can be decided by the grid operator. Normally, it is determined by the MPPT controller from the efficiency point of view, which is adopted in this study. More details about the MPPT control methods are reviewed in Chapter 5.



**Figure 8.19:** Grid side converter control for grid-connected mode

In the islanded mode, the GSC aims to provide fixed grid voltage and frequency level. The classic  $U/f$  mode is applied, as illustrated in Fig. 8.12.

### 8.6.1.3 Damping controller

Wind turbines have relatively soft shafts [21]. The drive train of a wind turbine behaves as a torsional spring characteristic. The torsional oscillation between different sections of wind turbine can be observed whenever the system exited by mechanical or electrical load changes. The eigen-frequency of the drive train is rather low and within the bandwidth that is normally taken into account in power system dynamic simulations. The frequency of these oscillations can be

calculated by equations in [209] (see Eqn. 8.22). The frequency rang is normally between 0.1 Hz and 10 Hz [204].

$$f_{\text{osc1}} = \frac{1}{2\pi} \sqrt{\frac{k_{\text{tg}}}{J_{\text{t}}}}, f_{\text{osc2}} = \frac{1}{2\pi} \sqrt{\frac{k_{\text{tg}}}{J_{\text{eq}}}} \quad (8.22)$$

where  $J_{\text{eq}}$  is the equivalent inertia of the drive-train model, determined by:

$$J_{\text{eq}} = \frac{J_{\text{t}} J_{\text{g}}}{J_{\text{t}} + J_{\text{g}}} \quad (8.23)$$

Due to the fact that the PMSG wind turbine with full-scale converter has no inherent damping, any small speed perturbation may be amplified causing self-excitation, high mechanical stress of the drive train [197]. The idea of the present damping controller is that the DC capacitor is considered as a short-term energy storage, the speed oscillations are buffered and reflected in an oscillating defined DC voltage reference. It has been fully studied in [204]. The controller configuration is depicted in Fig. 8.20. The band pass filter with transfer function

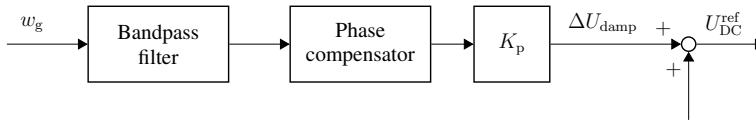


**Figure 8.20:** Damping controller

can be designed based on the calculated frequency [205],

$$G_{\text{filter}}(s) = \frac{2\xi_n \omega_n s}{s^2 + 2\xi_n \omega_n s + \omega_n^2}, \quad (8.24)$$

where  $\xi_n$  and  $\omega_n$  are the damping factor and the band pass frequency respectively. The bode diagram is shown in Fig. 8.21. The phase compensator can be modeled as a low-pass filter by introducing 90 deg phase lag.

### 8.6.2 Coordinated control during the islanded operation

Due to the wind fluctuation, the available energy ( $P_{\text{max}}$ ) from the wind may not be sufficient to the load demand ( $P_{\text{load}}$ ) even in areas with wealthy wind resource during the islanded operation. In this case, voltage and frequency will be sensitive to load variations. An additional BESS with fast-response capability

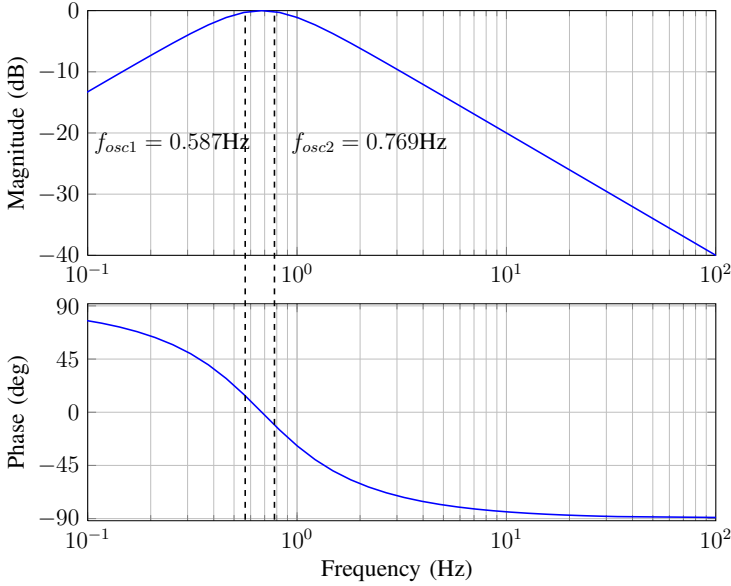


**Figure 8.21:** Bode diagram for band-pass filter design

for active power compensation is an effective solution. In this study, the wind turbine rotor is used as the additional ESS. A coordinated control of the PMSG wind turbine and the BESS has been developed.

### 8.6.2.1 Stability area

As illustrated in Fig. 8.22, the maximum available power can be captured following the MPPT curve. When  $P_{\max} > P_{\text{load}}$ , the excess power will be stored in the turbine rotor as the kinetic energy. Consequently, it results in the rotor speed increase. The wind turbine operates in the overspeeding area. When the generator speed  $\omega_g$  exceeds reference  $\omega_g^{\text{ref}}$ , pitch angle control will be activated to constraint the wind power capture. The relation between pitch angle  $\theta$  and deloading coefficient is illustrated in Fig. 2.8. The captured wind power can be regulated significantly by the pitch angle adjustment. The wind turbine operation will moves towards to a new equilibrium through rotor increase or pitch regulation during the wind variation. It is stable to operate in this area.

When  $P_{\max} < P_{\text{load}}$ , the stored energy in the rotor blade would be released temporarily which will result in the decrease of the rotation speed. The status can last for several seconds depending on the rotor inertial. However, continuous ex-

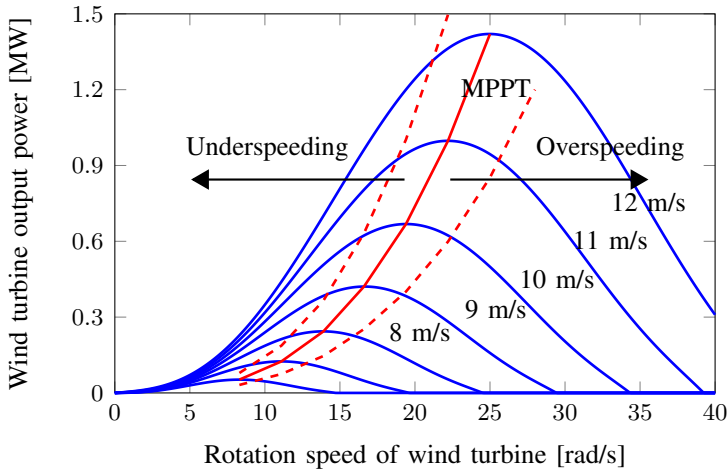


**Figure 8.22:** Comparison between overspeeding and underspeeding operations

traction from rotor will make the wind turbine operation move to underspeeding area, shown in Fig 8.22. The underspeeding condition is detrimental since the reaction during the first period goes in the direction opposite to the target [41]. For example, if  $P_{load}$  becomes larger, rotation speed will continue decreasing. That will further leads to the decrease of power coefficient  $C_p$ , which conversely results in continuous rotor speed decrease until it stops. In that case, the BESS should be activated for the power compensation.

### 8.6.2.2 Coordinated control of BESS

When and how much energy should be compensated by the BESS are two main problems to solve for the coordinated control strategy design.

If synchronous generators as DG units are included in a microgrid, the activation time of the BESS can be determined by local indicators, either voltage or frequency. The situation is different without synchronous generators. That is because the energy stored in the rotor inertia can be released and support the microgrid operation temporarily (normally several seconds). However, wind turbine has been operated in the underspeeding area which results in the sudden collapse of voltage and frequency. It would be too late for the BESS to compensate. This phenomenon is described together with simulation results in Section 8.7.2. The criterion of activation time of the BESS could be determined by comparison between measured generator speed  $\omega_g$  and optimal speed  $\omega_{opt}$

based on the wind speed  $v_w$  (measured or estimated), which is also the dividing line between overspeeding area (stable) and underspeeding area (unstable). The schematic diagram of the developed coordinated control strategy is depicted in Fig. 8.23.

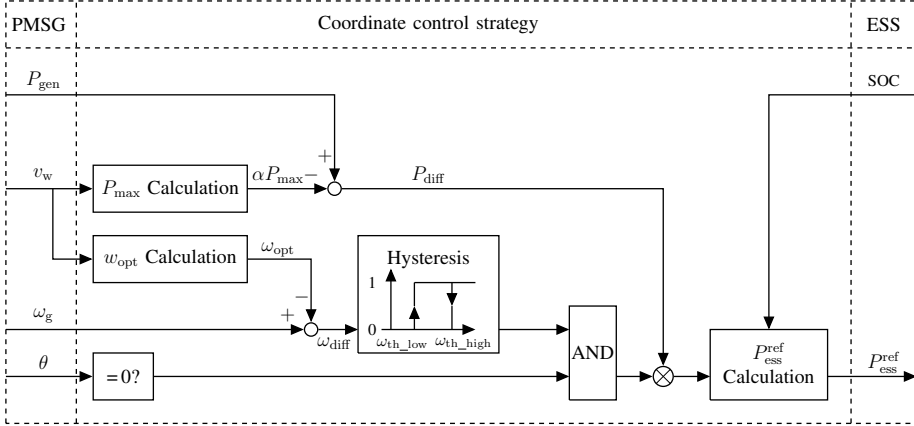


**Figure 8.23:** Coordinated control strategy

The maximum available wind power  $P_{\max}$  can be easily calculated by  $P_{\max} = \frac{1}{2} \rho \pi R^2 v_w^3$ . In order to avoid frequent start-up of the BESS, a hysteresis is included.  $\omega_{th\_low}$  and  $\omega_{th\_high}$  are the thresholds.  $\omega_{diff}$  represents how close the wind turbine operates to the dividing line. If  $\omega_{diff} < \omega_{th\_low}$ , the BESS is triggered and start power compensation until  $\omega_{diff} > \omega_{th\_high}$ . Considering power losses and operation reliability, the maximum available wind power can be scaled with coefficient  $\alpha$  to have safety margin ( $\alpha \in [0, 1]$ ). The reference power command of BESS  $P_{ess}^{ref}$  can be determined considering  $P_{diff} = P_{gen} - \alpha P_{\max}$  and charging level SOC during the activation. The proposed coordination and communication between the PMSG wind turbine and the BESS are implemented by MGCC.

## 8.7 Simulation and results

### 8.7.1 Simulation for Case 1

A typical microgrid introduced in [17] is used as the test case. It is composed of two dispatchable DG units (DG 1 and DG 2), a RES, a BESS, a distribution line

and three loads, as depicted in Fig. 8.24. The parameters of these components are listed in Appendix A.4. The normal operation range of the BESS is set between 20% and 80%. In order to be better viewed, both grid-connected and islanded operation modes are included in the same simulation process. In order to test the control performances of the BESS at different charging levels, two case scenarios with different initial SOC are defined (Scenario 1:  $SOC = 50\%$ ; Scenario 2:  $SOC = 70\%$ ). The case study specifications are listed in Table 8.3.

**Table 8.3:** Case study specification

Operation mode	Event	Duration/Time
Grid-connected operation	N/A	$t = 0 \sim 1000$ s
Transition	PCC Switch is open	$t = 1000$ s
Islanded operation	N/A	$t = 1000 \sim 2500$ s

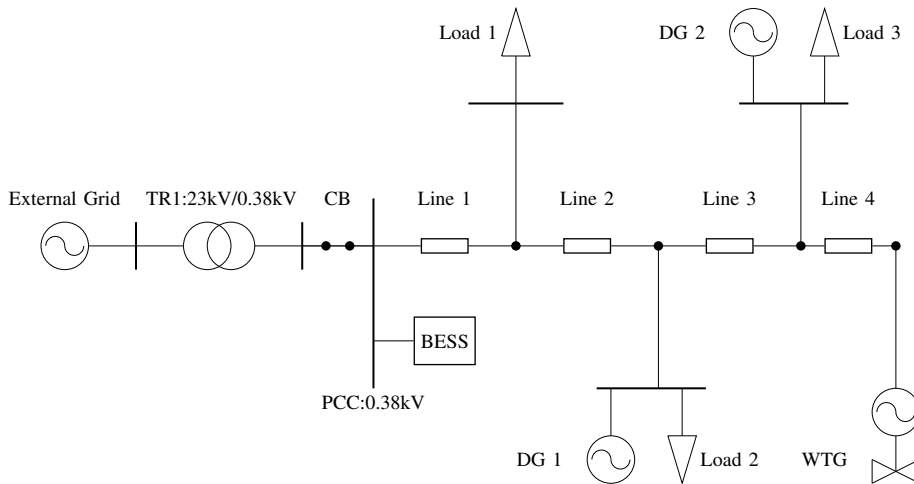


**Figure 8.24:** Test case configuration

The wind and load profiles are plotted in Fig. 8.25. The total load consumption varies from 100 kW to 110 kW and the total wind power varies from 5 kW to 35 kW. The wind penetration level is about 25%.

During  $t = 1000 \sim 2500$  s, the system operates in the islanded mode. The main objective of the coordinated control strategy of the BESS is to stabilize frequency. The voltage and frequency during the transition between two modes



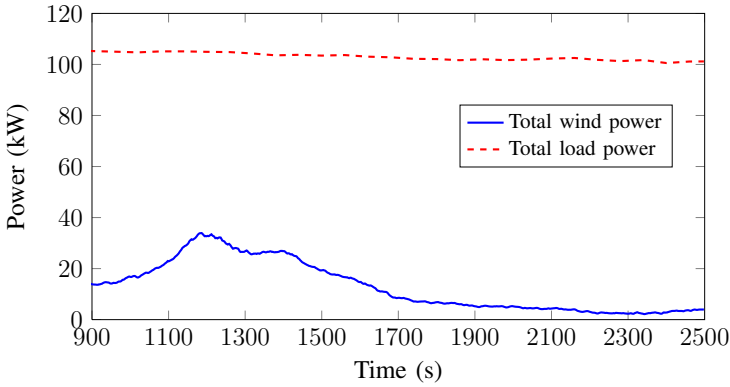


**Figure 8.25:** Wind and load power profile

are illustrated in Fig. 8.26 and Fig. 8.27, respectively. The voltage fluctuates during a very short period and is quickly damped after several cycles. After about 0.5s, the voltage gets into a steady state.

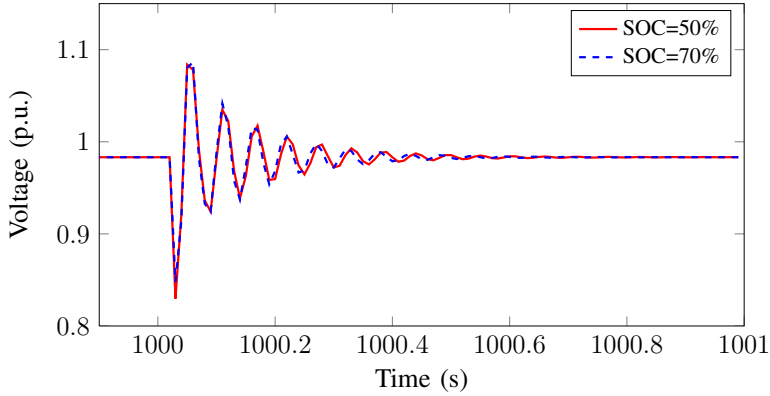


**Figure 8.26:** Voltage at PCC

The frequency recovery can be divided into two parts. Within a very short period (several seconds) after the PCC switch is open, the frequency stops decreasing and reaches to its nadir (50-0.05 Hz). As illustrated in Fig. 8.28, most dispatched power is from the BESS due to its fast response capability. The contributions of DGs are limited (Fig. 8.29). This time frame belongs to the primary frequency control.

Since the charging level is still high, the BESS is still involved in this part.

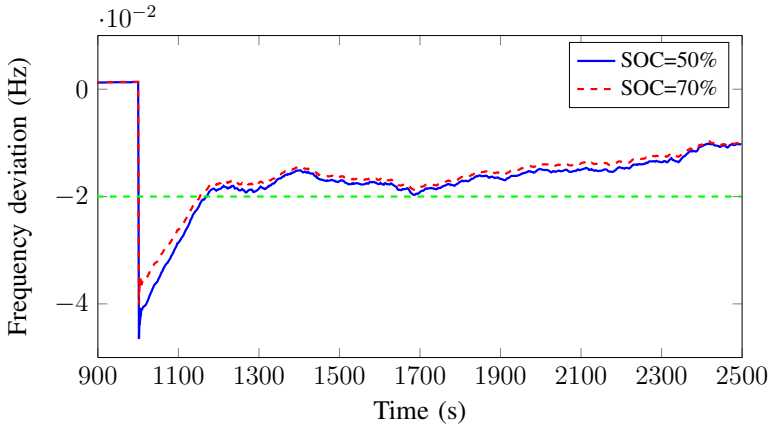


Figure 8.27: Frequency at PCC

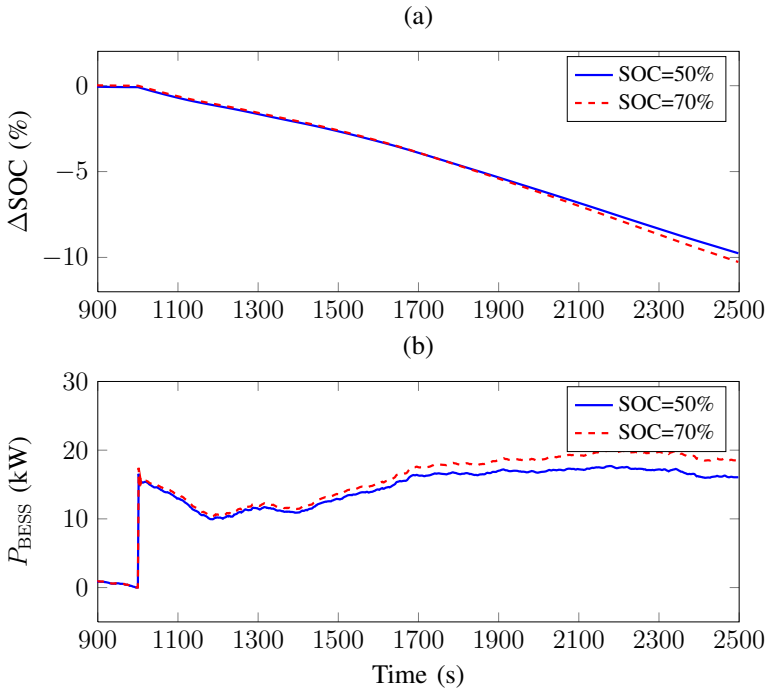
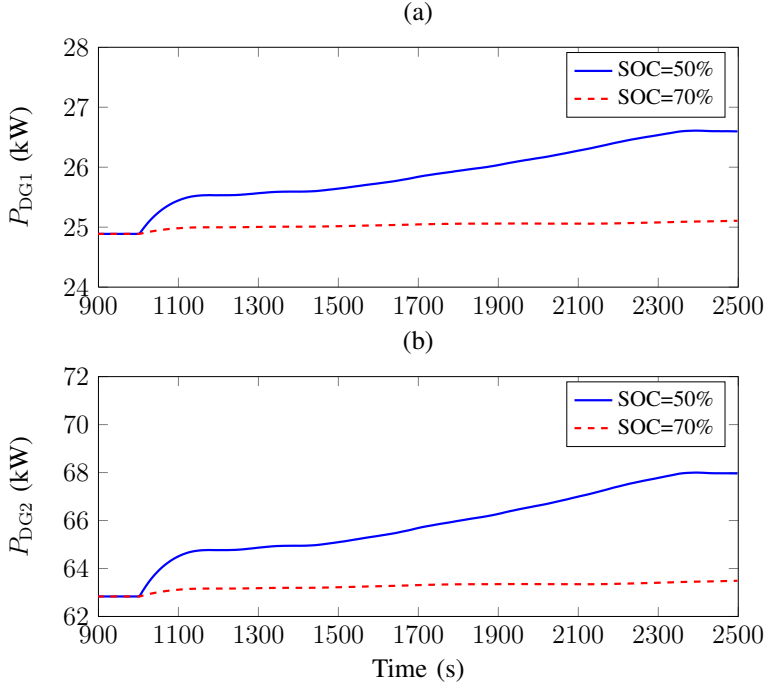


Figure 8.28: Results of BESS in islanded operation

The time span is dependent on the target input power and the SOC level. As the charging level decreases (Fig. 8.28 (b)), more power is distributed to the



**Figure 8.29:** Results of dispatchable DGs in islanded operation

dispatchable DG units, as shown in Fig. 8.29. Obviously, the BESS with lower charging level (50%) decreases earlier. The gap is filled by the DG units. The power distribution factors between DG units are predefined and fixed:  $d_{DG1} : d_{DG2} = 1 : 3$ . At about  $t = 1200$  s, the frequency recovers to its normal range (49.98 Hz–50.02 Hz, dead band is set to  $\pm 0.02$  Hz). This time frame belongs to the secondary frequency control.

### 8.7.2 Simulation for Case 2

The microgrid for the case study is illustrated in Fig 8.30, which consists of a 1.5 MW PMSG, a 0.5 MW BESS, a 0.2 MW PV and 0.7 MW load. The wind profile has an average wind speed of 10 m/s and the turbulence intensity is 0.15 derived by using the Von Karman spectrum in the IEC standard. The simulation time is 300 s, including grid-connected, islanded operation and transition in between. The case studies are specified in Table 8.4, which focus on the islanded operation and transition parts.

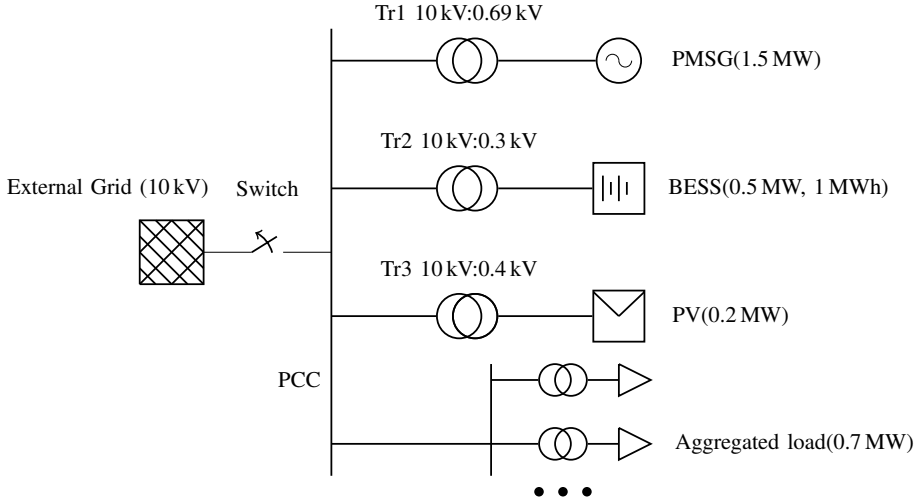


**Figure 8.30:** Microgrid test system

**Table 8.4:** Case study specification

Study scenario	Event	Duration/Time
Grid-connected operation	N/A	$t = 0 \sim 100$ s
Transition	PCC Switch is open	$t = 100$ s
Islanded operation	N/A	$t = 100 \sim 300$ s
	Step change of load 0.5 MW to 1 MW	$t = 200$ s
	Step change of load 1 MW to 0.6 MW	$t = 250$ s

The PCC switch opens at  $t = 100$  s which makes the microgrid transit from the grid-connected operation to the islanded operation. The islanding detection is assumed instantaneous without any time delay. As explained in Section 8.6.1, the RSC controller is kept unchanged and the GSC controller is switched. At the last moment of pre-landing,  $P_{\text{gen}} = 1.2$  MW. The load is assumed to be 0.7 MW, which is partly satisfied by the PV generation – 0.2 MW. The net generation demand is 0.5 MW.

Due to the sudden decrease of generation  $P_{\text{gen}}$ , the excess power is gathered in the DC link and results in the increase of DC voltage  $U_{\text{DC}}$ . A chopper is equipped to unload the excess power to avoid over-voltage of the DC link and eliminate the transients. The high and low thresholds are defined as:  $U_{\text{th\_high}} =$

1.06 p.u. and  $U_{th\_low} = 1.02$  p.u.. The transients with and without the chopper during the transition are compared in Fig. 8.31. Without the chopper, the

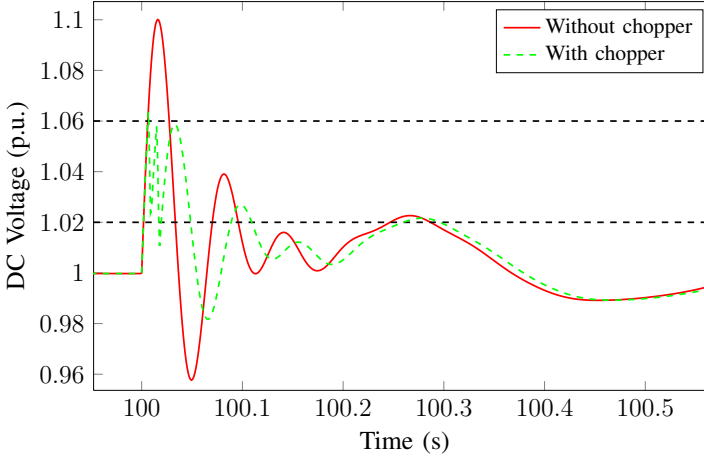


**Figure 8.31:**  $U_{DC}$  during transition

voltage overshoot can reach 1.1 p.u.. With the chopper, the overshoot of  $U_{DC}$  is greatly limited according to the pre-defined threshold.

The active power transferred into grid drops from 1.2 MW to 0.5 MW. The response is quite fast and the transition is quite smooth (Fig. 8.32 (a)). The sudden increase of grid voltage  $U_{PCC}$  and decrease of frequency  $f_{PCC}$  are observed. The maximum variation magnitudes are small: 3% for  $U_{PCC}$  and  $-0.4\%$  for  $f_{PCC}$  (Fig. 8.32 (b) and (c)). The system recovers within 0.05 s.

In the following 200 seconds, the microgrid operates in the islanded mode. As illustrated in Fig. 8.33, there are two step changes of load which occur at  $t = 200$  s and  $t = 250$  s, respectively. The simulation results between with and without the BESS are compared in Fig. 8.34 and 8.35.

During  $100 \sim 200$  s,  $P_{max} > P_{load}$  (Fig. 8.33). The rotor is accelerated and generator operates in a high speed: 1.2 p.u. (Fig. 8.34 (b)). Subsequently, the pitch angle is activated to limit the generator speed (Fig. 8.34 (c)). The wind generation  $P_{gen}$  is regulated following the load.

During  $200 \sim 250$  s,  $P_{max} < P_{load}$  (Fig. 8.33). In the case without storage support, the kinetic energy stored in the rotor will be released. Accordingly,  $\omega_{gen}$  starts decreasing. The pitch angle is also regulated for more generation. Before  $t = 234$  s, the wind turbine still operates in the overspeeding area. It is

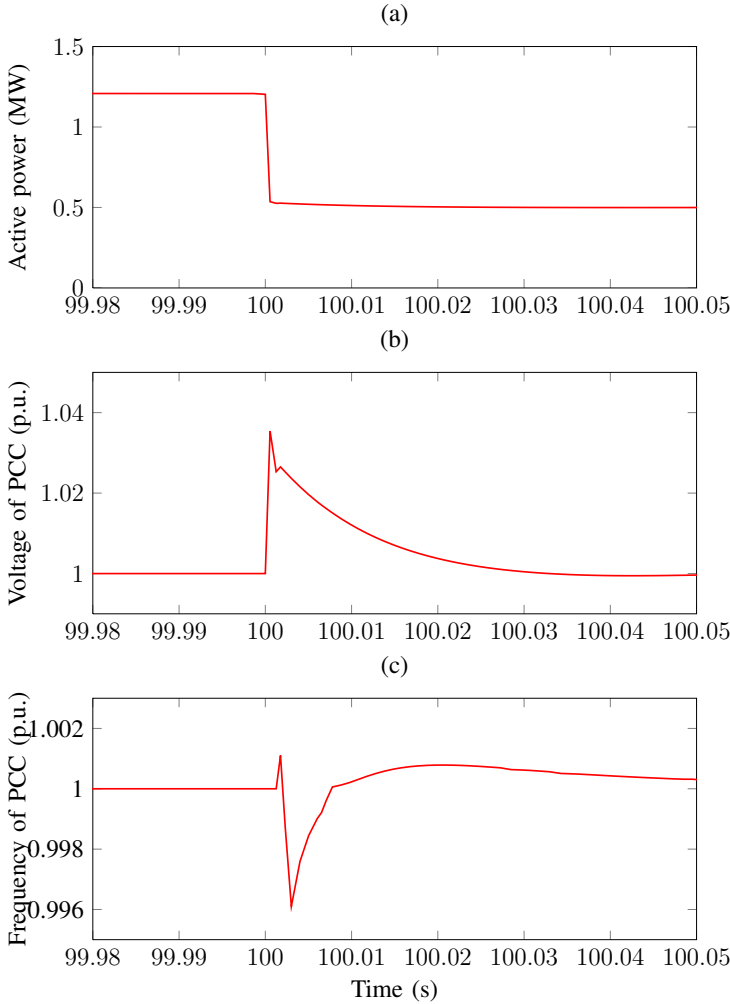


**Figure 8.32:** Transients during the transition between grid-connected mode and islanded mode

the cut-off point. Without external generation support, the rotor speed would continue decreasing and then results in the sudden collapse (Fig. 8.34 (b)). From the voltage and frequency point of view, these variables are still kept stable until collapse occurs at  $t = 260$  s (Fig. 8.35). It verifies the discussion described in Section 8.6.2.2. Instead of these local indicators, the operation variables of wind turbine are communicated with the BESS as an activation criterion. With the BESS and the developed control strategy, the stored kinetic energy will be extracted. When the generation speed gets closer to the dividing

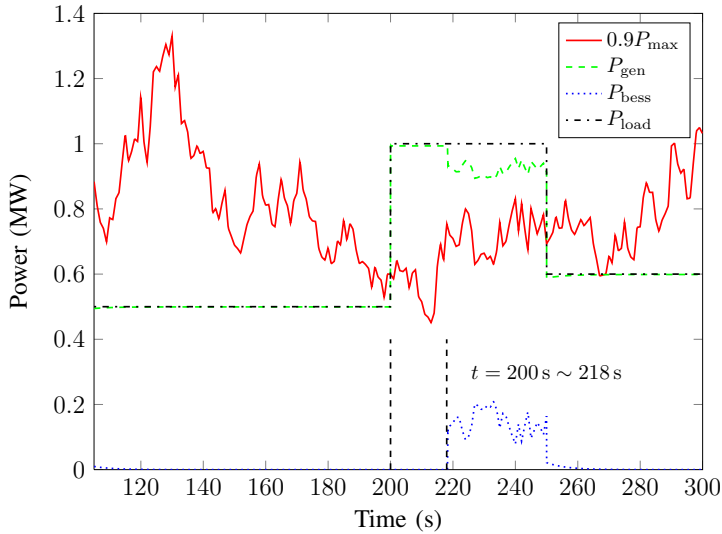


**Figure 8.33:** Active power comparison during islanded operation

line, BESS is activated. The load requirements are fulfilled and the rotor is "charged" until it returns to the stable area (Fig. 8.34 (b)). The voltage and frequency are kept stable during the islanded operation.

During  $250 \sim 300$  s,  $P_{\max} > P_{\text{load}}$  (Fig. 8.33), the wind turbine recovers and continues working in the deloading operation. The pitch angle is activated to limit the power generation. The wind generation  $P_{\text{gen}}$  is regulated following the demand.

## 8.8 Discussion and conclusion

In this chapter, two coordinated control strategies are developed for the islanded operation of microgrid according to the different cases.

For Case 1, the wind power penetration level is relatively low and wind power production is not dominate compared with the other power productions. Wind power production is dependent on the wind speed and considered nondispatchable. With the proposed fuzzy logic based coordinated control strategy between the BESS and the dispatchable DG units,

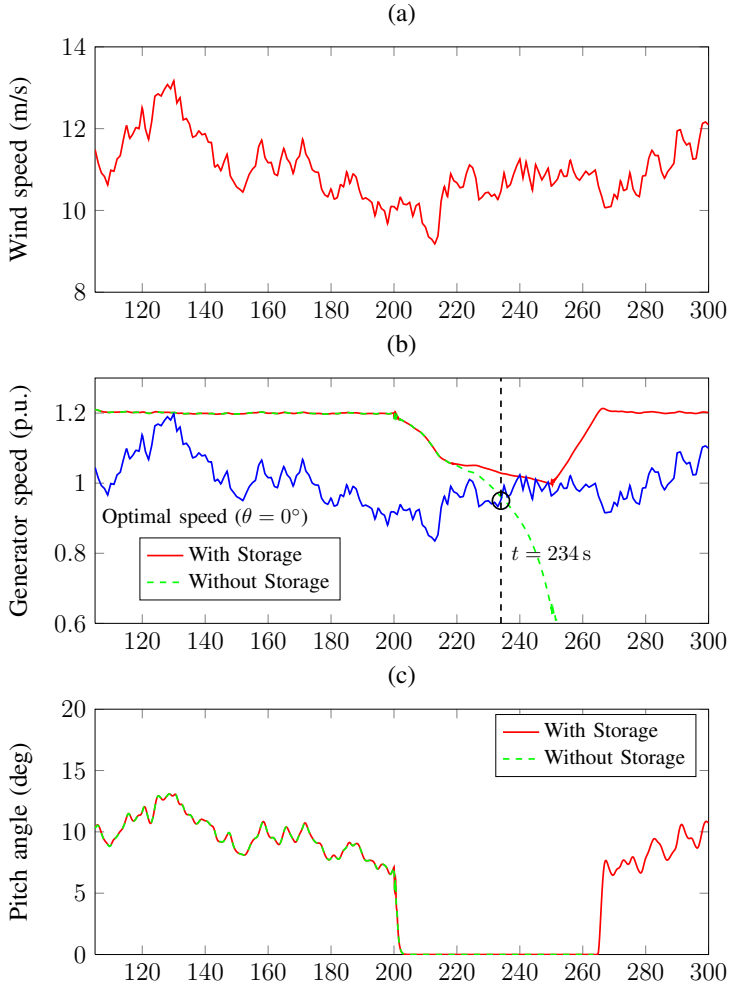


**Figure 8.34:** Simulation results of PMSG in islanded operation

- The fast fluctuation caused by the wind power can be compensated due to the fast response capability of BESS, which improve the frequency stability.
- The BESS can adjust the charging and discharging according to the charging level and power command through fuzzy controller to avoid overcharging and discharging.

For Case 2, the coordinated control strategy aims to solve a series of control



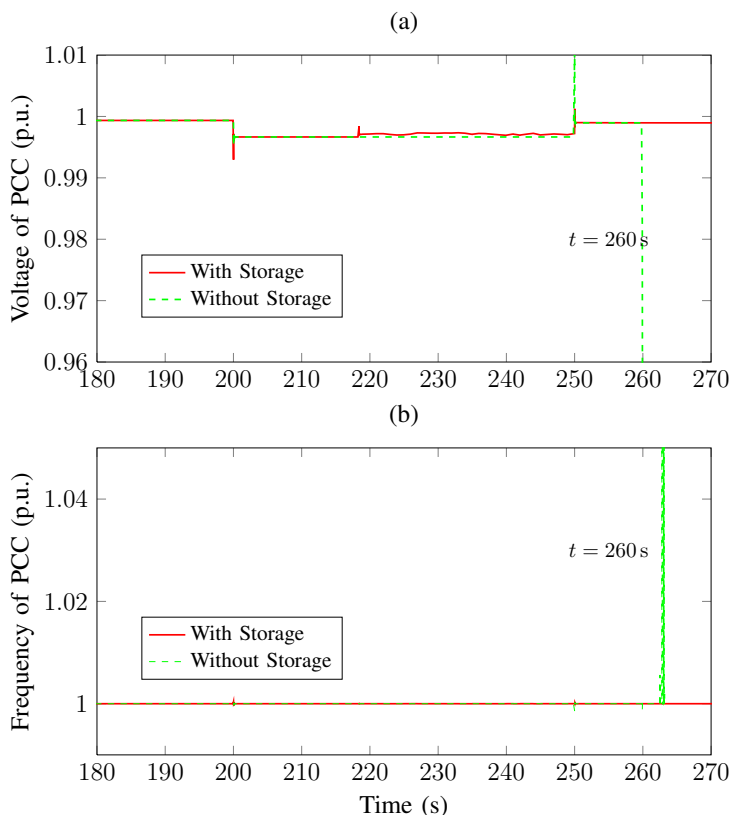


**Figure 8.35:** Simulation results of PMSG in islanded operation

problems of WTG with full-scale converter for microgrid application in geographical areas with wealthy wind regimes without conventional synchronous generators. These problems consist of the converter controller design in local level and coordinated control strategy in supervisory level. The wind module is used as the main generation component and supply stiff voltage and frequency during the islanded operation.

A switchable converter control scheme is proposed. RSC is applied to keep DC voltage and AC voltage of stator while GSC is employed to switch between  $P/Q$  controller and  $U/f$  controller based on the operation modes. In this way, the configuration changes during transition can be largely reduced since RSC controller is kept independently. The excess power collected in DC load can be unloaded very fast to keep DC voltage stable. The operation of wind turbine in the mode transition is validated by the simulation results.

---

As the complementary generation component, the ESS is not needed to operate always online and only be activated when the available wind power is insufficient. A comprehensive supervisory control algorithm for efficiently managing the operation of microgrid is presented. The optimal generator speed is adopted as the criterion of ESS activation while the power reference command is determined considering the available wind power, actual wind generation and charging level. The developed control strategy is proved to be effective. Large rotor inertial of wind turbine is regulated as an energy storage medium and the requirement of power and capacity of ESS is reduced.



# Conclusion and scope for future work

---

This thesis has studied coordinated control between wind power and ESS as well as its realizations in different cases according to the role that ESS plays. Around the main thread, the relevant research fields including the wind turbine modeling and control, wind power plant modeling and control, optimal sizing and siting of ESS are also included.

## 9.1 Conclusions

- The implementation and validation of the IEC generic Type 1A in PF are presented in this thesis. Several places were adjusted in order to comply with the IEC generic model structure and use the PF built-in generator model. The simulation illustrated that the implemented IEC generic Type 1 models in PF can represent the relevant dynamics during normal operation and fault conditions. The model against measurements validation was carried out to verify the implemented WTG model. The comparison of the simulated power and currents with the measurements shows that there is a good match between the simulation results and the measurements. Through the comparison of the characteristic quantities by IEC

committee draft, the quantities of active current in the fault window are smaller than the ones of reactive current.

- The design of  $\mathcal{L}_1$  adaptive controller for MPPT of a small variable speed WECS is presented in this thesis. The developed controller showed good tracking performance towards the optimum TSR and robustness with fast adaptation to uncertainties and disturbances as shown in detailed simulation cases that included wind shear, shadow effects, and wind speed variations. Compared with the conventional optimized PI controller, the proposed  $\mathcal{L}_1$  adaptive speed control for MPPT captures more energy during operation, especially in highly turbulent wind conditions. It is a reasonable alternative to the PI control and may present some advantages for MPPT in highly turbulent wind conditions.
- The optimal active power control of wind power plant based on D-MPC is proposed in this thesis. As the prediction model for D-MPC, a dynamic discrete-time PWA model of a power controlled wind turbine was obtained by identification of the nonlinearities with clustering-based method. The developed model was verified by comparison with the nonlinear wind turbine model under both high and low wind conditions. With the developed D-MPC, most of computation tasks are distributed to the local D-MPCs equipped at each actuator (wind turbine or ESS). The computation burden of the central unit is significantly reduced. This control structure is independent of the scale of the wind power plant. The proposed D-MPC is implemented for two wind power plant configurations: with and without ESS installation. The simulation results show that larger mechanical load alleviation can be obtained with additional ESS. However, it also leads to the increase of capital and maintenance cost.
- The algorithms for optimal siting and sizing of ESS in the grid with a significant penetration of wind power are proposed and implemented in a test network. For the optimal siting algorithm, as illustrated in the simulation results, the placement of ESS at the wind power plant site is not always the best option, although this choice can reduce the transmission losses to some extent. From the system performance point of view, installation of ESS at other buses, such as terminal bus of critical transmission line, can enhance the controllability. For optimal sizing algorithm, by solving a large number of the periodical optimization problems, the CDF of charging and discharging control of ESS for different realizations of wind power fluctuations can be derived. The optimal power and energy rating can be determined by setting the probability level. It shows that the correlation between wind power plants has a significant impact on the derived power and energy rating.
- Two coordinated control strategies are developed for the islanded operation of microgrid according to the different cases in this thesis. For Case

1, with the proposed fuzzy logic based coordinated control strategy between BESS and dispatchable DG units, the fast fluctuation caused by the wind power can be compensated due to the fast response capability of BESS, which improve the frequency stability. Besides, BESS can adjust the charging and discharging according to the charging level and power command through fuzzy controller to avoid over-charging and discharging. For Case 2, wind turbine was considered as the master DG unit and responsible for load following. As the complementary generation component, ESS is not needed to operate always online and only be activated when the available wind power is insufficient. Large rotor inertial of wind turbine is regulated as an energy storage medium. Consequently, the requirement of power and capacity of the ESS is reduced.

## 9.2 Future work

Some questions have been answered and some others have been created. Much work still remains to be done, particularly in the area of advanced control strategies of wind turbine and wind power plant, coordinated control of dispersed wind power plants and ESSs, operation based planning of ESS and etc. These are some suggestions for the future work:

- It is necessary to extend the proposed  $\mathcal{L}_1$  adaptive controller in the full load regime of the wind turbine operation. There are two possible implementation ways. For the case without stall or pitch control, the rotor speed will be regulated to decrease the power coefficient in order to limit the power production. The wind turbine system model in this region can be derived by system identification or linearization at the operating point. The input is the generator torque and the output is the power production. Since the power can be measured, the  $\mathcal{L}_1$  adaptive output feedback controller can be designed based on this model. The rated power is used as the reference. For the case with pitch control, the design procedure of  $\mathcal{L}_1$  adaptive controller is almost the same. The only difference is that the input for the identified WECS model is pitch angle.
- In this thesis, the implemented D-MPC algorithm for the wind power plant control is based on the fast dual method. Other popular distribution algorithms, such as Alternating Direction Method of Multipliers (ADMM), can also be implemented for D-MPC and compared with the one proposed in the thesis.
- It is promising that the D-MPC algorithm is used for the AGC by coordinated control between wind power plants and ESSs dispersed in a large

power system.

- The network constraints and power losses applied in the optimal sizing and siting algorithms in this thesis are based on DC load flow. Consequently, the voltage constraints can not be considered and the power loss calculation is inaccurate. AC-OPF, due to its non-convex, is generally difficult to solve. Recently, Semi-Definite Programming (SDP) has been proposed for solving AC-OPF problem. A global optimum solution can be retrieved if a sufficient zero-duality gap is derived. Therefore, SDP could be used for the optimal sizing and siting studies.

# Parameter for case studies

---

## A.1 Test case for IEC Generic WTG model

### A.1.1 External grid

The 50 kV external grid is modeled by a Thevenin equivalent circuit. The corresponding parameters are listed in Table A.1.

**Table A.1:** Parameter for external grid

Symbol	Description	value
$U_{Th}$	Equivalent voltage	50 kV
$R_{Th}$	Equivalent resistance	2.1156 $\Omega$
$X_{Th}$	Equivalent reactance	8.2998 $\Omega$



### A.1.2 50/10 kV Transformer Tr1

It is modeled by the T-equivalent. All the reactances are without saturation. No-load losses are excluded. The phase connection is YNd5. The transformer is directly grounded. The corresponding parameters are listed in Table A.2.

**Table A.2:** Parameter for 50/10 kV transformer Tr1

Symbol	Description	value
$S_n$	Rated power	16 MVA
$U_p$	Rated voltage on primary side	50 kV
$U_s$	Rated voltage on secondary side	10.5 kV
$R_p$	Resistance on primary side	0.4052 $\Omega$
$X_p$	Leakage reactance on primary side	7.655 $\Omega$
$X_m$	Magnetizing impedance	19530 $\Omega$
$R_s$	Resistance on secondary side	0.4052 $\Omega$
$X_s$	Leakage reactance on secondary side	7.655 $\Omega$

### A.1.3 Short Circuit

The three-phase short circuit fault lasts 0.1 s. The error impedance before the fault is 1 M $\Omega$  (star impedance). The short circuit impedance is 0.00011  $\Omega$  (star impedance).

### A.1.4 10 kV Collection Cable

The wind power plant 10 kV collection cable is modeled by the  $\pi$ -equivalent with the parameters given in Table A.3.

### A.1.5 10/0.96 kV Transformer Tr2

It is modeled by the T-equivalent. All the reactances are without saturation. No-load losses are excluded. The phase connection is Dyn5. The transformer is directly grounded. The corresponding parameters are listed in Table A.4.

**Table A.3:** Parameter for 10 kV collection cable

Symbol	Description	value
$C_1$	Equivalent capacitance	$1.58 \mu\text{F}$
$R$	Equivalent resistance	$0.7568 \Omega$
$X$	Equivalent reactance	$0.4473 \Omega$
$C_2$	Equivalent capacitance	$1.58 \mu\text{F}$

**Table A.4:** Parameter for 10/0.96 kV transformer Tr2

Symbol	Description	value
$S_n$	Rated power	2 MVA
$U_p$	Rated voltage on primary side	10.5 kV
$U_s$	Rated voltage on secondary side	0.96 kV
$R_p$	Resistance on primary side	$0.2756 \Omega$
$X_p$	Leakage reactance on primary side	$1.654 \Omega$
$X_m$	Magnetizing impedance	$6890 \Omega$
$R_s$	Resistance on secondary side	$0.2756 \Omega$
$X_s$	Leakage reactance on secondary side	$1.654 \Omega$

### A.1.6 Capacitor bank

The capacitor bank in the wind turbine is delta connected, with the capacity  $C_\Delta = 1333 \mu\text{F}$  in series with  $R_\Delta = 0.003 \Omega$ .

### A.1.7 Wind Turbine Generator (WTG)

The induction generator (SCIG) in the wind turbine is modeled by the T-equivalent with the parameters given in Table A.5.

### A.1.8 Mechanical system

The parameters of the mechanical part are listed in Table A.6

**Table A.5:** Parameter for SCIG

Symbol	Description	value
$S_n$	Rated power	2.3 MVA
$U_n$	Rated voltage	0.96 kV
$N_0$	Rated speed	1500 rpm
$R_s$	Stator resistance	0.004 $\Omega$
$X_s$	Stator reactance	0.05 $\Omega$
$X_m$	Magnetizing reactance	1.6 $\Omega$
$R_r$	Rotor resistance	0.004 $\Omega$
$X_r$	Rotor reactance	0.05 $\Omega$

**Table A.6:** Parameter for mechanical part

Symbol	Description	value
$I_{wtr}$	Inertia of wind turbine rotor	$4.176 \times 10^6 \text{ kg} \cdot \text{m}^2$
$I_{gen}$	Inertia of generator	$93.22 \text{ kg} \cdot \text{m}^2$
$k_{sh}$	Stiffness coefficient	$8.949 \times 10^7 \text{ N} \cdot \text{m/rad}$
$\eta$	Multiplier ratio	80

## A.2 Parameter for 6 kW WECS

6 kW variable speed WECS, introduced in [20] is used as the test case. The parameters are listed in Table A.7 and Table A.8.

**Table A.7:** Parameter for mechanical part

Symbol	Description	value
$R$	Blade length	2.5 m
$\eta$	Multiplier ratio	6.25
$J_{wt}$	Rotor inertia	$3.6 \text{ kg} \cdot \text{m}^2$
$J_g$	Generator inertia	$0.01 \text{ kg} \cdot \text{m}^2$
$\eta$	Efficiency	0.95
$k_{sh}$	Shaft stiffness	$75 \text{ N} \cdot \text{m/rad}$
$c_{sh}$	Shaft damping	$0.5 \text{ kg} \cdot \text{m}^2/\text{s}$

**Table A.8:** Parameter for SCIG

Symbol	Description	value
$p$	Pole pair	2
$R_s$	Stator resistance	1.265 $\Omega$
$R_r$	Rotor resistance	1.43 m $\Omega$
$L_m$	Mutual reactance	0.1397 H
$L_s$	Stator reactance	0.1452 H
$L_r$	Rotor reactance	0.1452 H
$w_s$	Synchronous speed	100 $\pi$ rad/s
$U_s$	Voltage level	220 V

### A.3 NREL 5 MW wind turbine model

The parameters of NREL wind turbine model are listed in Table A.9 and Table A.10.

**Table A.9:** Parameter for mechanical part

Symbol	Description	value
$\theta_{\max}$	Max. pitch angle	25 deg
$\theta_{\min}$	Min. pitch angle	-5 deg
$\dot{\theta}_{\max}$	Max. pitch angular velocity	8 deg/s
$\dot{\theta}_{\min}$	Min. pitch angular velocity	-8 deg/s
$\ddot{\theta}_{\max}$	Max. pitch angular acceleration	15 deg/s <sup>2</sup>
$\ddot{\theta}_{\min}$	Min. pitch angular acceleration	-15 deg/s <sup>2</sup>
$\eta$	Multiplier ratio	97
$R$	Rotor blade length	63 m
$H$	Height of the rotor center	90 m
$J_r$	Moment of inertia of rotor	5.9154 $\times 10^7$ kg·m <sup>2</sup>
$J_g$	Moment of inertia of rotor	500 kg·m <sup>2</sup>
$k_{\text{sh}}$	Drive shaft spring constant	8.7354 $\times 10^8$ N·m/rad
$c_{\text{sh}}$	Drive shaft damping constant	8.3478 $\times 10^7$ N·m·s/rad
$M_t$	Mass of floating tower and nacelle	4.4642 $\times 10^5$ kg
$\omega_n$	Natural frequency of pitch actuator	0.88 rad/s
$\varsigma$	Damping of pitch actuator	0.9

**Table A.10:** Parameter for generator

Symbol	Description	value
$P_{\text{nom}}$	Nominal generator power	$5 \times 10^6$ W
$\omega_{\text{gmax}}$	Max. generator speed	122.91 rad/s
$\omega_{\text{gmin}}$	Min. generator speed	70.16 rad/s
$\tau_{\text{g}}$	Time constant of generator torque actuator	0.1 s

## A.4 Parameter for Microgrid

Parameters for the test case are listed in Table A.11.

**Table A.11:** Model parameter

Item	Description and Parameters
Disp. DG units	DG1: 30 kW DG2: 90 kW
RES (Wind power)	Rated power 40 kW
Battery	Capacity per cell: 100 Ah Voltage when the cell is empty ( $u_{\text{min}}$ ): 12 V Voltage when the cell is full ( $u_{\text{max}}$ ): 13.85 V Amount of cells in parallel: 10 Amount of cells in row: 5 Internal Resistance per cell: 0.001 $\Omega$
Load	Load 1: 50 kW, Load 2: 50 kW, Load 3: 10 kW
Transformer	3-phase 22.9/0.38 kV, 200 kVA
Line impedance	$R$ : 0.1878 $\Omega$ /km, $X$ : 0.0968 $\Omega$ /km

The parameters of 1.5 MW DD-PMSG are listed in Table A.12– Table A.14 [210].

**Table A.12:** Parameter for mechanical part

Symbol	Description	value
$\omega_r_{\min}$	Minimal rotor speed	9 rpm
$\omega_r_{\text{rate}}$	Rated speed	18 rpm
$R$	Rotor blade length	30 m
$v_r$	Rated wind speed	14 m/s
$H_{\text{WTR}}$	Inertia constant	0.72 s
$P_{\text{shaft}}$	Rated power	1.5 MW
$c_{\text{sh}}$	Turbine damping	$14 \times 10^6 \text{ N}\cdot\text{m}\cdot\text{s}/\text{rad}$
$J_r$	Rotor inertia	$6.1 \times 10^6 \text{ kg}\cdot\text{m}^2$
$k_{\text{sh}}$	Shaft stiffness	$83 \times 10^6 \text{ N}\cdot\text{m}/\text{rad}$

**Table A.13:** Parameter for pitch controller and actuator

Symbol	Description	value
$K_p$	Blade angle controller gain	100 deg/p.u.
$\omega_g^{\text{ref}}$	Speed reference	1.25 p.u.
$\tau_p$	Servo time constant	0.5 s
$d\theta_{\max}$	Max. pitch rate	-15 deg/s
$d\theta_{\min}$	Min. pitch rate	15 deg/s
$\theta_{\min}^{\text{ref}}$	Min. reference pitch	0 deg
$\theta_{\max}^{\text{ref}}$	Max. reference pitch	70 deg
$\theta_{\min}$	Min. pitch limit	0 deg
$\theta_{\max}$	Max. pitch limit	70 deg

**Table A.14:** Parameter for PMSG

Symbol	Description	value
$P_{\text{rate}}$	Rated power	1.5 MW
$\omega_{\text{g\_rate}}$	Rated speed	1.8 rpm
$p$	Pole pair	80
$U_{\text{DC}}$	Rated DC voltage	3300 V
$R_{\text{s}}$	Stator resistance	1.7850 $\Omega$
$L_{\text{d}}$	$d$ -axis inductance	8.5 mH
$L_{\text{q}}$	$q$ -axis inductance	8.5 mH
$\phi_{\text{PM}}$	Magnet flux linkage	0.57 Vs
$J_{\text{g}}$	Generator inertia	$8.5 \times 10^6 \text{ kg} \cdot \text{m}^2$
$X''_{\text{d}}$	$d$ -axis subtransient reactance	0.17 p.u.
$X''_{\text{q}}$	$q$ -axis subtransient reactance	0.17 p.u.
$T''_{\text{d0}}$	$d$ -axis subtransient time constant	0.02 s
$T''_{\text{q0}}$	$q$ -axis subtransient time constant	0.05 s

## APPENDIX B

# Theoretical background

---

## B.1 Projection operator for adaptation laws

Projection-based adaptation laws are used to prevent parameter drift in adaptation schemes. In this appendix, the relevant definitions and properties of the projection operator are introduced ([143]).

**Definition 1**  $\Omega \subseteq \mathbb{R}^n$  is a convex set, if for all  $x, y \in \Omega$  the following holds:

$$\lambda x + (1 - \lambda)y \in \Omega, \quad \forall \lambda \in [0, 1]. \quad (\text{B.1})$$

**Definition 2**  $f : \mathbb{R}^n \rightarrow \mathbb{R}$  is a convex function, if for all  $x, y \in \mathbb{R}^n$  the following holds:

$$f(\lambda x + (1 - \lambda)y) \leq \lambda f(x) + (1 - \lambda)f(y), \quad \forall \lambda \in [0, 1]. \quad (\text{B.2})$$

**Lemma 1** Let  $f : \mathbb{R}^n \rightarrow \mathbb{R}$  be a convex function. Then for arbitrary constant  $\delta$ , the set  $\Omega_\delta \triangleq \{\theta \in \mathbb{R}^n \mid f(\theta) \leq \delta\}$  is convex. The set  $\Omega_\delta$  is called a sublevel set. The proof of this lemma can be found in [143].

**Lemma 2** Let  $f : \mathbb{R}^n \rightarrow \mathbb{R}$  be a continuously differentiable convex function. Choose a constant  $\delta$  and consider the convex set  $\Omega_\delta \triangleq \{\theta \in \mathbb{R}^n \mid f(\theta) \leq \delta\}$ . Let



$\theta, \theta^* \in \Omega_\delta$  and  $f(\theta^*) < \delta$  and  $f(\theta) = \delta$  (i.e.,  $\theta^*$  is not on the boundary of  $\Omega_\delta$ , while  $\theta$  is on the boundary of  $\Omega_\delta$ ). Then the following inequality takes place:

$$(\theta^* - \theta)' \nabla f(\theta) \leq 0, \quad (\text{B.3})$$

where  $\nabla f(\theta)$  is the gradient vector of  $f(\cdot)$  evaluated at  $\theta$ .

**Definition 3** Consider a convex compact set with a smooth boundary given by

$$\Omega_c \triangleq \{\theta \in \mathbb{R}^n \mid f(\theta) \leq c\}, \quad 0 \leq c \leq 1, \quad (\text{B.4})$$

where  $f : \mathbb{R}^n \rightarrow \mathbb{R}$  is the following smooth convex function:

$$f(\theta) \triangleq \frac{(\varepsilon_\theta + 1)\theta' \theta - \theta_{\max}^2}{\varepsilon_\theta \theta_{\max}^2}, \quad (\text{B.5})$$

with  $\theta_{\max}$  being the norm bound imposed on the vector  $\theta$ , and  $\varepsilon_\theta > 0$  is the projection tolerance bound of our choice. The projection operator is defined as

$$\text{Proj}(\theta, y) \triangleq \begin{cases} y & \text{if } f(\theta) < 0, \\ y & \text{if } f(\theta) \geq 0 \text{ and } \nabla f' y \leq 0, \\ y - \frac{\nabla f}{\|\nabla f\|} \left\langle \frac{\nabla f}{\|\nabla f\|}, y \right\rangle f(\theta) & \text{if } f(\theta) \geq 0 \text{ and } \nabla f' y > 0. \end{cases} \quad (\text{B.6})$$

**Property 1:** The projection operator  $\text{Proj}(\theta, y)$  does not alter  $y$  if  $\theta$  belongs to the set  $\Omega_0 \triangleq \{\theta \in \mathbb{R}^n \mid f(\theta) \leq 0\}$ . In the set  $\{\theta \in \mathbb{R}^n \mid 0 \leq f(\theta) \leq 1\}$ , if  $\nabla f' y > 0$ , the  $\text{Proj}(\theta, y)$  operator subtracts a vector normal to the boundary  $\bar{\Omega}_{f(\theta)} = \{\bar{\theta} \in \mathbb{R}^n \mid f(\bar{\theta}) = f(\theta)\}$ , so that we get a smooth transformation from the original vector field  $y$  to an inward or tangent vector field for  $\Omega_1$ .

**Property 2:** Given the vectors  $y \in \mathbb{R}^n$ ,  $\theta^* \in \Omega_0 \subset \Omega_1 \subset \mathbb{R}^n$ , and  $\theta \in \Omega_1$ , we have

$$(\theta - \theta^*)' (\text{Proj}(\theta, y) - y) \leq 0. \quad (\text{B.7})$$

Indeed,

$$(\theta^* - \theta)'(y - \text{Proj}(\theta, y)) = \begin{cases} 0 & \text{if } f(\theta) < 0, \\ 0 & \text{if } f(\theta) \geq 0 \text{ and } \nabla f' y \leq 0, \\ \frac{(\theta^* - \theta)' \nabla f \nabla f' y f(\theta)}{\|\nabla f\|^2} & \text{if } f(\theta) \geq 0 \text{ and } \nabla f' y > 0. \end{cases} \quad (\text{B.8})$$

Changing the signs on the left side, one gets (B.1). An illustration of the projection operator is shown in Fig. B.1.

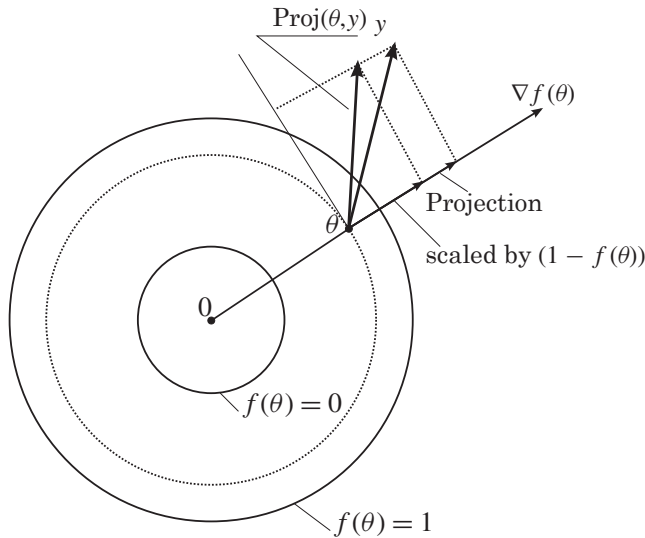


Figure B.1: Projection operator

## B.2 Model discretization

The discretization procedure of SISO system is described in the section. This procedure is equally applicable to MIMO system which gives essentially the same results. The ones in the shift part of the matrices are exchanges by identity matrices of appropriate dimension.

Consider the continuous-time Linear Time Invariant (LTI) state space system:

$$\dot{x}(t) = A_c x(t) + B_c u(t) \quad (\text{B.9})$$

$$y(t) = C_c x(t) + D_c u(t) \quad (\text{B.10})$$

where  $x(t_0) = x_0$ . The solution of Eqn. B.9 is

$$x(t) = e^{A_c(t-t_0)} x_0 + \int_{t_0}^t e^{A_c(t-\tau)} B_c u(\tau) d\tau. \quad (\text{B.11})$$

Assume that the inputs are sampled with Zero-Order-Hold (ZOH):

$$u(t) = u_k \quad t_k \leq t \leq t_{k+1} = t_k + T_s, \quad (\text{B.12})$$

where  $T_s$  is the sampling time. Let  $x(t_k) = x_k$ , then the solution  $x(t_{k+1})$  at time  $t_{k+1}$  can be expressed as

$$\begin{aligned} x_{k+1} = x(t_{k+1}) &= e^{A_c(t_{k+1}-t_k)} x_k + \int_{t_k}^{t_{k+1}} e^{A_c(t_{k+1}-\tau)} B_c u(\tau) d\tau \\ &= [e^{A_c T_s}] x_k + \left[ \int_0^{T_s} e^{A_c s} B_c ds \right] u_k \end{aligned} \quad (\text{B.13})$$

Accordingly, the continuous system (Eqn. B.9–B.10) can be transformed into the following discrete form

$$\begin{aligned} x_{k+1} &= A_d x_k + B_d u_k \\ y_k &= C_d x_k + D_d u_k \end{aligned} \quad (\text{B.14})$$

with

$$\begin{aligned} A_d &= e^{A_c T_s}, \\ B_d &= \int_0^{T_s} e^{A_c s} B_c ds, \\ C_d &= C_c, \\ D_d &= D_c. \end{aligned} \quad (\text{B.15})$$

## B.3 Empirical copulas and families of copulas

### B.3.1 Empirical copulas

Suppose  $(X_1^i, X_2^i, \dots, X_d^i)$ ,  $i = 1, \dots, n$  from a random vector  $(X_1, X_2, \dots, X_d)$  with continuous margins. The corresponding “true” copula observations would be  $:(U_1^i, U_2^i, \dots, U_d^i) = (F_1(X_1^i), F_2(X_2^i), \dots, F_d(X_d^i))$ ,  $i = 1, \dots, n$ .

As the marginal distribution functions  $F_i$  are usually not known, a pseudo copula observations by using the empirical distribution functions is constructed:  $F_k^n(x) = \frac{1}{n} \sum_{i=1}^n \mathbf{1}(X_k^i \leq x)$ . Then, the pseudo copula observations are defined as:  $(\tilde{U}_1^i, \tilde{U}_2^i, \dots, \tilde{U}_d^i) = (F_1^n(X_1^i), F_2^n(X_2^i), \dots, F_d^n(X_d^i))$ ,  $i = 1, \dots, n$ .

The corresponding empirical copula is then defined as :

$$C_n(u_1, \dots, u_d) = \frac{1}{n} \sum_{i=1}^n \mathbf{1}(\tilde{U}_1^i \leq u_1, \dots, \tilde{U}_d^i \leq u_d), \tag{B.16}$$

where  $\mathbf{1}$  denotes the indicator function. The components of the pseudo copula samples can also be written as

$$\tilde{U}_k^i = \frac{R_k^i}{n} \tag{B.17}$$

where  $R_k^i$  is the rank of the observation  $X_k^i$ :

$$R_k^i = \sum_{j=1}^n \mathbf{1}(X_k^j \leq X_k^i) \tag{B.18}$$

Therefore, the empirical copula can be seen as the empirical distribution of the rank transformed data.

### B.3.2 Families of copulas

The commonly-used families of copulas are described in this section, including Gaussian copula and Archimedean copulas.

#### B.3.2.1 Gaussian copula

The Gaussian copula is a distribution over the unit cube  $[0, 1]^d$ . It is constructed from a multivariate normal distribution over  $\mathbb{R}^d$  by using the probability integral transform. An  $d$ -dimensional Gaussian copula with correlation matrix  $\rho$  can be written as

$$C(u_1, \dots, u_d; \rho) = \Phi_\rho(\Phi^{-1}(u_1), \dots, \Phi^{-1}(u_d)), \tag{B.19}$$

where  $\Phi^{-1}$  is the inverse cumulative distribution function of a standard normal and  $\Phi_\rho$  is the joint cumulative distribution function of a multivariate normal distribution with mean vector zero and co-variance matrix equal to the correlation matrix  $\rho$ .

### B.3.2.2 Archimedean copulas

Archimedean copulas are popular because they allow modeling dependence in arbitrarily high dimensions with only one parameter, governing the strength of dependence. A  $d$ -dimensional Archimedean copula can be expressed as

$$C(u_1, \dots, u_d; \theta) = \psi^{-1}(\psi(u_1; \theta) + \dots + \psi(u_d; \theta); \theta) \quad (\text{B.20})$$

where  $\psi : [0, 1] \times \Theta \rightarrow [0, \infty)$  is a continuous, strictly decreasing and convex function such that  $\psi(1; \theta) = 0$ .  $\theta$  is a parameter within some parameter space  $\Theta$ .  $\psi$  is the so-called generator function. Commonly used Archimedean copulas include Gumbel copula, Clayton copula and Frank copula, whose generator functions are listed in Table B.1.

**Table B.1:** Generators of Archimedean copulas

Copula	Generator	Range of parameter
Gumbel	$(-\ln u)^\theta$	$[1, +\infty)$
Clayton	$(u^\theta - 1)/\theta$	$[-1, 0) \cup (0, +\infty)$
Frank	$\ln(e^{-\theta} - 1) - \ln(e^{-\theta u} - 1)$	$(-\infty, 0) \cup (0, +\infty)$

# Bibliography

---

- [1] V. Fthenakis, H. C. Kim, “Land use and electricity generation: A life-cycle analysis,” *Renewable and Sustainable Energy Reviews*, 13(6):1465–1474, 2009.
- [2] International Energy Agency, “World Energy Outlook 2011,” 2011.
- [3] Global Wind Energy Council, “Global wind report—annual market update,” 2014.
- [4] P. Wang, Z. Gao, and L. Bertling, “Operational Adequacy Studies of Power Systems With Wind Farms and Energy Storages,” 27(4):2377–2384, 2012.
- [5] S. Backhaus, M. Chertkov, and K. Dvijotham, “Operations-based planning for placement and sizing of energy storage in a grid with a high penetration of renewables,” arXiv preprint arXiv:1107.1382, 2011.
- [6] A. G. Abo-Khalil, “Impacts of wind farms on power system stability,” 2013.
- [7] Y. Sun, Z. Zhang, G. Li, and J. Lin, “Review on frequency control of power systems with wind power penetration,” *International Conference on Power System Technology (POWERCON)*, 1-8, 2010.
- [8] International Energy Agency, “Grid integration of large-capacity renewable energy sources and use of large-capacity electrical energy storage,” *Tech. Rep.*, Oct. 2012.
- [9] Eltra and Elkraft, “Wind turbines connected to grids with voltages above 100 kV - Technical regulation for the properties and the regulation of wind turbines,” *Tech. Rep.*, May. 2004.

- [10] National Grid PLC, "The grid code," Tech. Rep., 2006.
- [11] Hydro-Québec, "Technical requirements for the connection of generation facilities to the Hydro-Québec transmission system: supplementary requirements for wind generation," Tech. rep., 2005.
- [12] E. ON. GmbH, "Grid connection regulations of high and extra high voltage," Tech. Rep., 2006.
- [13] Spain, "Separata del Borrador del P.O. 12.2 Restringida a los Requisitos Técnicos de las Instalaciones Eólicas y Fotovoltaicas," Tech. Rep., Oct. 2008.
- [14] State Grid Corporation of China, "Technical rule for connecting wind farm to power network," Tech. Rep., 2011.
- [15] State Grid Corporation of China, "Technical rule for connecting wind farm to grid," Tech. Rep., 2009.
- [16] Y. A.-R. I. Mohamed, "New control algorithms for the distributed generation interface in grid-connected and micro-grid systems," PhD thesis, University of Waterloo, 2008.
- [17] J. Y. Kim , H. M. Kim , S. K. Kim, et al, "Designing an energy storage system fuzzy pid controller for microgrid islanded operation," *Energies*, 4(9):1443–1460, 2011.
- [18] A. Saha, S. Chowdhury, S. Chowdhury, and P. Crossley, "Modeling and performance analysis of a microturbine as a distributed energy resource," *IEEE Transactions on Energy Conversion*, 24(2):529 –538, Jun. 2009.
- [19] International Electrotechnical Commission, "IEC 61400-27 committee draft, wind turbines part 27-1: Electrical simulation models for wind power generation – wind turbines," Committee Draft (CD) 88/424/CD, Jan. 2012.
- [20] I. Munteanu, A. I. Bratcu, N. A. Cutululis, et al. "Optimal control of wind energy systems: towards a global approach," Springer, 2008.
- [21] V. Akhmatov, "Analysis of dynamic behaviour of electric power systems with large amount of wind power," PhD thesis, Technical University of Denmark, 2003.
- [22] G. Lalor, A. Mullane, and M. O'Malley, "Frequency control and wind turbine technologies," *IEEE Transactions on Power Systems*, 20(4):1905–1913, 2005.

- [23] J. Conroy and R. Watson, "Frequency response capability of full converter wind turbine generators in comparison to conventional generation," *IEEE Transactions on Power Systems*, 23(2):649–656, 2008.
- [24] B. M. G. Lauby, M. Ahlstrom, D. L. Brooks, S. Beuning, J. Caspary, W. Grant, B. Kirby, M. Milligan, M. O. Malley, M. Patel, R. Piwko, and P. Pourbeik, "Balancing Act: NERC Integration of Variable Generation Task Force Plans for a Less Predictable Future," *IEEE Journal and Magazines*, 75–85, 2011.
- [25] P. Sørensen, A. Hansen, and F. Iov, "Wind farm models and control strategies," *Tech. Rep.*, Risø-R-1464, 2005.
- [26] P. Bousseau and R. Belhomme, "Contribution of wind farms to ancillary services," *CIGRÉ General Meeting*, Paris, 2006.
- [27] Y. Rebours and D. Kirschen, "A survey of frequency and voltage control ancillary services—Part I: Technical features," *IEEE Transactions on Power Systems*, 22(1):350–357, 2007.
- [28] P. Kundur, "Power system stability and control," New York: McGraw-hill, 1994.
- [29] Y. Xue and N. Tai, "Review of contribution to frequency control through variable speed wind turbine," *Renewable Energy*, 36:1671–1677, Jun. 2011.
- [30] J. Ekanayake and N. Jenkins, "Comparison of the Response of Doubly Fed and Fixed-Speed Induction Generator Wind Turbines to Changes in Network Frequency," *IEEE Transactions on Energy Conversion*, 19(4):800–802, Dec. 2004.
- [31] M. Kayikçi and J. Milanovic, "Dynamic contribution of DFIG-based wind plants to system frequency disturbances," *IEEE Transactions Power Systems*, 24(2):859–867, 2009.
- [32] L. Holdsworth, J. B. Ekanayake, and N. Jenkins, "Power system frequency response from fixed speed and doubly fed induction generator-based wind turbines," *Wind Energy*, 7(1):21–35, 2004.
- [33] A. Causebrook, D. Atkinson, and A. Jack, "Fault ride-through of large wind farms using series dynamic braking resistors," *IEEE Transactions on Power Systems*, 22(3):966–975, 2007.
- [34] J. Morren and S. de Haan, "Wind turbines emulating inertia and supporting primary frequency control," *IEEE Transactions on Power Systems*, 21(1):2005–2006, 2006.



- 
- [35] P.-K. Keung, P. Li, H. Banakar, and B. T. Ooi, "Kinetic energy of wind-turbine generators for system frequency support," *IEEE Transactions on Power Systems*, 24(1):279–287, 2009.
- [36] N. W. Miller, K. Clark, and M. Shao, "Frequency responsive wind plant controls: Impacts on grid performance," *IEEE Power and Energy Society General Meeting*, 1–8, Jul. 2011.
- [37] N. Ullah, T. Thiringer, and D. Karlsson, "Temporary primary frequency control support by variable speed wind turbines — Potential and applications," *IEEE Transactions on Power Systems*, 23(2):601–612, 2008.
- [38] G. Tarnowski and P. Kjar, "Variable speed wind turbines capability for temporary over-production," *IEEE Power and Energy Society General Meeting*, 1–7, 2009.
- [39] J. M. Mauricio, A. Marano, and A. Gómez-Expósito, "Frequency regulation contribution through variable-speed wind energy conversion systems," *IEEE Transactions on Power Systems*, 24(1):173–180, 2009.
- [40] C. Hung and Y. Yin, "Dynamic Reserve Allocation for System Contingency by DFIG Wind Farms," *IEEE Transactions on Power Systems*, 23(2):729–736, May. 2008.
- [41] E. Loukarakis, I. Margaris, and P. Moutis, "Frequency control support and participation methods provided by wind generation," *IEEE Electrical Power Energy Conference (EPEC)*, 1–6, 2009.
- [42] P. Moutis, "Primary load-frequency control from pitch-controlled wind turbines," *IEEE PowerTech*, 1–7, 2009.
- [43] N. Janssens, G. Lambin, and N. Bragard, "Active power control strategies of dfig wind turbines," *IEEE PowerTech*, 516–521, 2007.
- [44] R. de Almeida, "Optimum generation control in wind parks when carrying out system operator requests," *IEEE Transactions on Power Systems*, 21(2):718–725, 2006.
- [45] R. de Almeida and J. Lopes, "Participation of doubly fed induction wind generators in system frequency regulation," *IEEE Transactions on Power Systems*, 22(3):944–950, 2007.
- [46] G. Ramtharan, N. Jenkins, and J. Ekanayake, "Frequency support from doubly fed induction generator wind turbines," *IET Renewable Power Generation*, 1(1):3–9, 2007.
- [47] A. D. Hansen, P. Sørensen, F. Iov, and F. Blaabjerg, "Centralised power control of wind farm with doubly fed induction generators," *Renewable Energy*, 31:935–951, Jun. 2006.

- [48] Z. Lubosny and J. W. Bialek, "Supervisory Control of a Wind Farm," *IEEE Transactions on Power Systems*, 22(3):985–994, Aug. 2007.
- [49] J. Rodriguez-Amenedo, "Automatic generation control of a wind farm with variable speed wind turbines," *IEEE Transactions on Energy Conversion*, 17(2):279–284, 2002.
- [50] T. HIYAMA, H. ESAKI, and T. FUNABASHI, "Experimental studies on multi-agent based AGC for isolated power system with dispersed power sources," *Engineering intelligent systems for electrical engineering and communications*, 13(2):135–140, 2005.
- [51] North American Electric Reliability Corporation, "Accommodating High Levels of Variable Generation," Tech. Rep., 2009.
- [52] Union for the Co-ordination of Transmission of Electricity, "Operation Handbook 2004-2010," Tech. Rep., 2010.
- [53] A. J. Wood and B. F. Wollenberg, "Power Generation, Operation, and Control", Wiley, 1996.
- [54] N. Atic, S. Membel, D. Rerkpreedapong, S. M. Ieee, A. Hasanovic, S. Membe, A. Feliachi, and S. Member, "NERC Compliant Decentralized Load Frequency Control Design Using Model Predictive Control," *IEEE Power Engineering Society General Meeting*, 554–559, 1997.
- [55] L. K. Kirchmayer, "Economic Control of Interconnected Systems," New York, NY: Wiley, 1959.
- [56] H. Bevrani, "Robust power system frequency control," Springer, 2009.
- [57] Q. Liu and M. Ilic, "Enhanced Automatic Generation Control (E-AGC) for future electric energy systems," *IEEE Power and Energy Society General Meeting*, 1-8, 2012.
- [58] H. Bevrani, F. Daneshfar, and T. Hiyama, "A New Intelligent Agent-Based AGC Design With Real-Time Application," 42(6):994–1002, 2011.
- [59] P. Kumar and D. Kothari, "Recent philosophies of automatic generation control strategies in power systems," *IEEE Transactions on Power Systems*, 20(1):346–357, 2005.
- [60] C. Fosha and O. Elgerd, "The megawatt-frequency control problem: a new approach via optimal control theory," *IEEE Transactions on Power Apparatus and Systems*, 1970(4):563–577, 1970.
- [61] M. D. Ili, "Control and Optimization Methods for Electric Smart Grids," New York, NY: Springer New York, 2012.

- [62] N. Jaleeli and L. Vanslyck, "Nerc's new control performance standards," *IEEE Transactions on Power Systems*, 14(3):1092–1099, 1999.
- [63] A. N. Venkat, I. Hiskens, J. Rawlings, and S. Wright, "Distributed MPC Strategies With Application to Power System Automatic Generation Control," *IEEE Transactions on Control Systems Technology*, 16:1192–1206, Nov. 2008.
- [64] H. Zeynelgil, a. Demiroren, and N. Sengor, "The application of ANN technique to automatic generation control for multi-area power system," *International Journal of Electrical Power & Energy Systems*, 24:345–354, June 2002.
- [65] C. Indulkar and B. Raj, "Application of fuzzy controller to automatic generation control," *Electric machines and power systems*, 37–41, 1995.
- [66] J. Talaq and F. Al-Basri, "Adaptive fuzzy gain scheduling for load frequency control," *IEEE Transactions on Power Systems*, 14(1):145–150, 1999.
- [67] D. Rerkpreedapong, A. Hasanovic, and A. Feliachi, "Robust load frequency control using genetic algorithms and linear matrix inequalities," *IEEE Transactions on Power Systems*, 18(2):855–861, 2003.
- [68] H. Bevrani, F. Daneshfar, and R. Daneshmand, "Intelligent Power System Frequency Regulations Concerning the Integration of Wind Power Units," *Wind Power Systems*, 2010.
- [69] F. Daneshfar and H. Bevrani, "Load–frequency control: a GA-based multi-agent reinforcement learning," *IET Generation, Transmission & Distribution*, 4(1):13, 2010.
- [70] D. Connolly, "An Investigation into the Energy Storage Technologies Available, for the Integration of Alternative Generation Techniques," *Tech. Rep.*, 2013.
- [71] International Electrotechnical Commission, "Electrical Energy Storage White paper," *Tech. Rep.*, 2011.
- [72] D. Zafirakis, K. J. Chalvatzis, G. Baiocchi, and G. Daskalakis, "Modeling of financial incentives for investments in energy storage systems that promote the large-scale integration of wind energy," *Applied Energy*, 105:138–154, 2013.
- [73] Electric Power Research Institute, "Energy Storage for Grid Connected Wind Generation Applications: EPRI-DOE Handbook Supplement," *Tech. Rep.*, 2004.

- [74] R. Madlener and J. Latz, "Economics of centralized and decentralized compressed air energy storage for enhanced grid integration of wind power," *Applied Energy*, 101:299–309, 2013.
- [75] S. van der Linden, "The Commercial World of Energy Storage: A Review of Operating Facilities," Conference of the Energy Storage Council, 2003.
- [76] Z. Chen, J. Guerrero, and F. Blaabjerg, "A review of the state of the art of power electronics for wind turbines," *IEEE Transactions on Power Electronics*, 24(8):1859–1875, 2009.
- [77] L. Wang, J. Y. Yu, and Y. T. Chen, "Dynamic stability improvement of an integrated offshore wind and marine-current farm using a flywheel energy-storage system," *IET Renewable Power Generation*, 5(5):387, 2011.
- [78] P. Ribeiro and B. Johnson, "Energy storage systems for advanced power applications," *Proceedings of the IEEE*, 89(12):1744–1756, 2001.
- [79] K. Yoshimoto, "New control method for regulating state-of-charge of a battery in hybrid wind power/battery energy storage system," *Power Systems Conference and Exposition, 2006. PSCE'06.*, 1244–1251, 2006.
- [80] H. Le, S. Santoso, and T. Nguyen, "Augmenting wind power penetration and grid voltage stability limits using ESS: application design, sizing, and a case study," *IEEE Transactions on Power Systems*, 27(1):161–171, 2012.
- [81] S. Nomura, Y. Ohata, T. Hagita, H. Tsutsui, S. Tsuji-Iio, and R. Shimada, "Wind Farms Linked by SMES Systems," *IEEE Transactions on Applied Superconductivity*, 15:1951–1954, Jun. 2005.
- [82] K. Tam and P. Kumar, "Application of superconductive magnetic energy storage in an asynchronous link between power systems," *IEEE Transactions on Energy Conversion*, 5(3):436–444, 1990.
- [83] S. Chen and L. Wang, "Power flow control and damping enhancement of a large wind farm using a superconducting magnetic energy storage unit," *Renewable Power*, 3(1):23–38, 2009.
- [84] Z. Wang, B. Yuwen, and M. Cheng, "Improvement of operating performance for the wind farm with a novel CSC type wind turbine-SMES hybrid system," *IEEE Transactions on Power Delivery*, 28(2):693–703, Apr. 2012.
- [85] L. Liang, J. Li, "An optimal energy storage capacity calculation method for 100 MW wind farm," *International Conference on Power System Technology (POWERCON)*, 1–4, Oct. 2010.

- [86] L. Wang, S. Chen, W. Lee, and Z. Chen, "Dynamic Stability Enhancement and Power Flow Control of a Hybrid Wind and Marine-Current Farm Using SMES," *IEEE Transactions on Energy Conversion*, 24(3):626–639, 2009.
- [87] L. Qu and W. Qiao, "Constant power control of DFIG wind turbines with supercapacitor energy storage," *IEEE Transactions on Industry Applications*, 47(1):359–367, 2011.
- [88] G. Joos and J. Belanger, "Real-Time Simulation of a Wind Turbine Generator Coupled With a Battery Supercapacitor Energy Storage System," *IEEE Transactions on Industrial Electronics*, 57(4):1137–1145, Apr. 2010.
- [89] S. Tewari and N. Mohan, "Value of NAS Energy Storage Toward Integrating Wind: Results From the Wind to Battery Project," *IEEE Transactions on Power Systems*, 28(1):532–541, Feb. 2012.
- [90] M. Korpås, "Distributed energy systems with wind power and energy storage," PhD thesis, Norwegian University of Science and Technology, 2004.
- [91] G. Celli, S. Mocci, F. Pilo, and M. Loddo, "Optimal integration of energy storage in distribution networks," *IEEE PowerTech*, 1–7, Jun. 2007.
- [92] D. D. Banham-Hall, G. A. Taylor, C. A. Smith, and M. R. Irving, "Flow Batteries for Enhancing Wind Power Integration," *IEEE Transactions on Power Systems*, 27(3):1690–1697, Aug. 2012.
- [93] C. Carrillo and A. Feijoo, "Power fluctuations in an isolated wind plant," *IEEE Transactions on Energy Conversion*, 19(1):217–221, 2004.
- [94] M. Swierczynski, R. Teodorescu R, C. N. Rasmussen, et al, "Overview of the energy storage systems for wind power integration enhancement," *IEEE International Symposium on Industrial Electronics (ISIE)*, 3749–3756, 2010.
- [95] P. S. Moura and A. T. De Almeida, "The role of demand-side management in the grid integration of wind power," *Applied Energy*, 87(8), 2581–2588, 2010.
- [96] W. Liu, W. Hu, H. Lund, and Z. Chen, "Electric vehicles and large-scale integration of wind power—the case of inner mongolia in china," *Applied Energy*, 104:445–456, 2013.
- [97] C. Quinn, D. Zimmerle, and T. H. Bradley, "The effect of communication architecture on the availability, reliability, and economics of plug-in hybrid electric vehicle-to-grid ancillary services," *Journal of Power Sources*, 195:1500–1509, Mar. 2010.

- [98] C. Binding and D. Gantenbein, "Electric vehicle fleet integration in the Danish EDISON project-a virtual power plant on the island of Bornholm," IEEE Power and Energy Society General Meeting, 1–8, 2010.
- [99] Q. Jiang and H. Wang, "Two-Time-Scale Coordination Control for a Battery Energy Storage System to Mitigate Wind Power Fluctuations," IEEE Transactions on Energy Conversion, 28:52–61, Mar. 2013.
- [100] J. Barton and D. Infield, "Energy storage and its use with intermittent renewable energy," IEEE Transactions on Energy Conversion, 19(2):441–448, 2004.
- [101] Q. Li, S. Choi, Y. Yuan, and D. Yao, "On the determination of battery energy storage capacity and short-term power dispatch of a wind farm," IEEE Transactions on Sustainable Energy, 2(2):148–158, 2011.
- [102] W. Li, G. Joos, and C. Abbey, "Wind power impact on system frequency deviation and an ESS based power filtering algorithm solution," Power Systems Conference and Exposition, 2006. PSCE'06, 2077–2084, 2006.
- [103] D. Yao and S. Choi, "Determination of short-term power dispatch schedule for a wind farm incorporated with dual-battery energy storage scheme," IEEE Transactions on Sustainable Energy, 3(1):74–84, 2012.
- [104] G. Salgi and H. Lund, "System behaviour of compressed-air energy-storage in denmark with a high penetration of renewable energy sources," Applied Energy, 85(4):182–189, 2008.
- [105] F. Baalbergen, P. Bauer, and J. Ferreira, "Energy storage and power management for typical 4Q-load," IEEE Transactions on Industrial Electronics, 56:1485–1498, May. 2009.
- [106] C. Abbey, K. Strunz, and G. Joós, "A knowledge-based approach for control of two-level energy storage for wind energy systems," IEEE Transactions on Energy Conversion, 24:539–547, Jun. 2009.
- [107] H. Lee, B. Y. Shin, S. Han, S. Jung, B. Park, and G. Jang, "Compensation for the Power Fluctuation of the Large Scale Wind Farm Using Hybrid Energy Storage Applications," IEEE Transactions on Applied Superconductivity, 22(3): 5701904–5701904, 2012.
- [108] T. Ise, M. Kita, and A. Taguchi, "A hybrid energy storage with a SMES and secondary battery," IEEE Transactions on Applied Superconductivity, 15(2):1915–1918, 2005.
- [109] P. Hu, R. Karki, and R. Billinton, "Reliability evaluation of generating systems containing wind power and energy storage," IET Generation, Transmission & Distribution, 3(8):783, 2009.

- 
- [110] S. Teleke, M. Baran, A. Huang, S. Bhattacharya, and L. Anderson, "Control strategies for battery energy storage for wind farm dispatching," *IEEE Transactions on Energy Conversion*, 24(3):725–732, 2009.
- [111] M. Korpaas, A. T. Holen, and R. Hildrum, "Operation and sizing of energy storage for wind power plants in a market system," *International Journal of Electrical Power & Energy Systems*, 25:599–606, Oct. 2003.
- [112] G. Bathurst and G. Strbac, "Value of combining energy storage and wind in short-term energy and balancing markets," *Electric Power Systems Research*, 67:1–8, Oct. 2003.
- [113] Y. Yuan, Q. Li, and W. Wang, "Optimal operation strategy of energy storage unit in wind power integration based on stochastic programming," *IET Renewable Power Generation*, 5(2):194, 2011.
- [114] E. D. Castronuovo, J. A. P. Lopes, "On the optimization of the daily Operation of a wind-hydro power plant," 19(3):1599–1606, 2004.
- [115] D. Yao and S. Choi, "A statistical approach to the design of a dispatchable wind power-battery energy storage system," *IEEE Transactions on Energy Conversion*, 24(4):916–925, 2009.
- [116] F. Díaz-González, A. Sumper, O. Gomis-Bellmunt, and F. D. Bianchi, "Energy management of flywheel-based energy storage device for wind power smoothing," *Applied Energy*, 110:207–219, 2013.
- [117] A. Ellis, Y. Kazachkov, E. Muljadi, P. Pourbeik, and J. Sanchez-Gasca, "Description and technical specifications for generic WTG models—a status report," *Power Systems Conference and Exposition (PSCE)*, 2011 IEEE/PES, 1–8, Mar. 2011.
- [118] P. Sørensen, B. Andresen, J. Fortmann, K. Johansen, and P. Pourbeik, "Overview, status and outline of the new IEC 61400 -27 – electrical simulation models for wind power generation," *International Workshop on Large-Scale Integration of Wind Power into Power Systems*, Oct. 2011.
- [119] International Electrotechnical Commission, "IEC 61400-21 Ed. 2, wind turbine generator system—part 21: Measurement and assessment of power quality characteristics of grid connected wind turbines," 2008.
- [120] T. Thiringer and J. Luomi, "Comparison of reduced-order dynamic models of induction machines," *IEEE Transactions on Power Systems*, 16:119 – 126, Feb. 2001.
- [121] DIgSILENT GmbH, "PowerFactory User's Manual - Version 14.1.," May. 2011.

- [122] W. Qiao, "Dynamic modeling and control of doubly fed induction generators driven by wind turbines," Power Systems Conference and Exposition, 2009. PSCE '09. IEEE/PES, 1–8, Mar. 2009.
- [123] A. D. Hansen, F. Iov, P. Sørensen, N. Cutululis, C. Jaush, and F. Blaabjerg, "Dynamic wind turbine models in power system simulation tool DIgSILENT," Tech. Rep. Risø-R-1400, Risø National Laboratory, Roskilde, Denmark, Aug. 2007.
- [124] P. Sørensen, A. D. Hansen, P. Christensen, M. Mieritz, J. Bech, B. B. Jensen, and H. Nielsen, "Simulation and verification of transient events in large wind power installations," Tech. Rep. Risø-R-1331, Risø National Laboratory, Roskilde, Denmark, Oct. 2003.
- [125] T. Ackermann, "Wind power in power systems," John Wiley & Sons, 2005.
- [126] V. Akhmatov, "Modelling of variable-speed wind turbines with doubly-fed induction generators in short-term stability analysis," Proceedings of the 3rd International Workshop on Transmission Networks for Off-shore Wind Farms, Apr. 2002.
- [127] P. Kundur, "Power System Stability and Control," McGraw-Hill, 1994.
- [128] M. Asmine, J. Brochu, J. Fortmann, R. Gagnon, Y. Kazachkov, C.-E. Langlois, C. Larose, E. Muljadi, J. MacDowell, P. Pourbeik, et al., "Model validation for wind turbine generator models," IEEE Transactions on Power Systems, 26(3):1769–1782, 2011.
- [129] P. Sørensen, A. D. Hansen and M. H. Donovan, "Operation and control of large wind turbines and wind farms," Tech. Rep. Risø-R-1532, Risø National Laboratory, Roskilde, Denmark, Sep. 2005.
- [130] R. Carriveau, "Fundamental and Advanced Topics in Wind Power," In-Tech, 2011.
- [131] Z. Chen, J. Guerrero, and F. Blaabjerg, "A review of the state of the art of power electronics for wind turbines," IEEE Transactions on Power Electronics, 24(8):1859–1875, 2009.
- [132] E. Koutroulis and K. Kalaitzakis, "Design of a maximum power tracking system for wind-energy-conversion applications," IEEE Transactions on Industrial Electronics, 53:486–494, Apr. 2006.
- [133] Z. M. Dalala, Z. U. Zahid, and J. S. Lai, "New overall control strategy for small-scale wecs in mppt and stall regions with mode transfer control," 2013.



- 
- [134] R. Datta and V. Ranganathan, "A method of tracking the peak power points for a variable speed wind energy conversion system," *IEEE Transactions on Energy conversion*, 18(1):163–168, 2003.
- [135] Z. M. Dalala, Z. U. Zahid, W. Yu, Y. Cho, and J.-S. Lai, "Design and analysis of an MPPT technique for small-scale wind energy conversion systems," *IEEE Transactions on Energy Conversion*, 28(3):756–767, 2013.
- [136] S. M. Barakati, M. Kazerani, and J. D. Aplevich, "Maximum power tracking control for a wind turbine system including a matrix converter," *IEEE Transactions on Energy Conversion*, 24(3):705–713, 2009.
- [137] K. H. Kim, T. L. Van, D. C. Lee, S. H. Song, and E. H. Kim, "Maximum output power tracking control in variable-speed wind turbine systems considering rotor inertial power," *IEEE Transactions on Industrial Electronics*, 60(8):3207–3217, 2013.
- [138] C. T. Pan and Y. L. Juan, "A novel sensorless mppt controller for a high-efficiency microscale wind power generation system," *IEEE Transactions on Energy Conversion*, 25(1):207–216, 2010.
- [139] A. Abo-Khalil and D.-C. Lee, "MPPT control of wind generation systems based on estimated wind speed using SVR," *IEEE Transactions on Industrial Electronics*, 55(3):1489–1490, 2008.
- [140] I. Munteanu, S. Bacha, A. Bratcu, J. Guiraud, and D. Roze, "Energy-reliability optimization of wind energy conversion systems by sliding mode control," *IEEE Transactions on Energy Conversion*, 23:975–985, Sep. 2008.
- [141] B. Beltran, M. El Hachemi Benbouzid, and T. Ahmed-Ali, "Second-order sliding mode control of a doubly fed induction generator driven wind turbine," *IEEE Transactions on Energy Conversion*, 27(2):261–269, 2012.
- [142] J. Mauricio, A. Leon, A. Gomez-Exposito, and J. Solsona, "An adaptive nonlinear controller for dfim-based wind energy conversion systems," *IEEE Transactions on Energy Conversion*, 23:1025–1035, Dec. 2008.
- [143] C. Cao, N. Hovakimyan, *L1 Adaptive Control Theory, Guaranteed Robustness with Fast Adaptation*. SIAM, 2010.
- [144] C. Cao and N. Hovakimyan, "Design and analysis of a novel adaptive control architecture with guaranteed transient performance," *IEEE Transactions on Automatic Control*, 53(2):586–591, 2008.
- [145] C. Cao and N. Hovakimyan, "Stability margins of adaptive control architecture," *IEEE Transactions on Automatic Control*, 55(2):480–487, 2010.

- [146] K. Kim and N. Hovakimyan, "Multi-criteria optimization for filter design of L1 adaptive control," *Journal of Optimization Theory and Applications*, 1–25, 2012.
- [147] E. Kharisov, N. Hovakimyan, and K. J. Åström, "Comparison of architectures and robustness of model reference adaptive controllers and L1 adaptive controllers," *International Journal of Adaptive Control and Signal Processing*, 2013.
- [148] H. Geng, G. Yang, D. Xu, and B. Wu, "Unified power control for PMSG-based wecs operating under different grid conditions," *IEEE Transactions on Energy Conversion*, 26:822–830, Sep. 2011.
- [149] M. N. Soltani, T. Knudsen, M. Svenstrup, R. Wisniewski, P. Brath, R. Ortega, and K. Johnson, "Estimation of rotor effective wind speed: A comparison," *IEEE Transactions on Control Systems Technology*, 21(4):1155–1167, 2013.
- [150] B. K. Bose, *Modern power electronics and AC drives*, Prentice-Hall, 2001.
- [151] W. Leonhard, *Control of electrical drives*, Springer, 2001.
- [152] Z. Lubosny and J. W. Bialek, "Supervisory control of a wind farm," *IEEE Transactions on Power Systems*, 22(3):985–994, 2007.
- [153] P. E. Sørensen, A. D. Hansen, F. Iov, F. Blaabjerg, and M. H. Donovan, "Wind farm models and control strategies," *Tech. Rep.*, 2005.
- [154] B. Biegel, D. Madjidian, V. Spudic, A. Rantzer, and J. Stoustrup, "Distributed low-complexity controller for wind power plant in derated operation," *IEEE International Conference on Control Applications (CCA)*, 146–151, IEEE, 2013.
- [155] D. Madjidian, K. Martensson, and A. Rantzer, "A distributed power coordination scheme for fatigue load reduction in wind farms," *American Control Conference (ACC)*, 5219–5224, 2011.
- [156] V. Spudić, M. Jelavić, and M. Baotić, "Wind turbine power references in coordinated control of wind farms," *Automatika—Journal for Control, Measurement, Electronics, Computing and Communications*, 52(2), 2011.
- [157] V. Spudic, M. Jelavic, M. Baotic, and N. Peric, "Hierarchical wind farm control for power/load optimization," *The Science of making Torque from Wind (Torque2010)*, 2010.
- [158] S. Teleke, M. Baran, S. Bhattacharya, and A. Huang, "Rule-based control of battery energy storage for dispatching intermittent renewable sources," *IEEE Transactions on Sustainable Energy*, 1(3), pp. 117–124, 2010.

- [159] H. Everett III, "Generalized Lagrange multiplier method for solving problems of optimum allocation of resources," *Operations research*, 11(3):399–417, 1963.
- [160] M. D. Doan, T. Keviczky, and B. De Schutter, "An iterative scheme for distributed model predictive control using fenchel's duality," *Journal of Process Control*, 21(5):746–755, 2011.
- [161] P. Giselsson, M. D. Doan, T. Keviczky, B. D. Schutter, and A. Rantzer, "Accelerated gradient methods and dual decomposition in distributed model predictive control," *Automatica*, 49(3):829–833, 2013.
- [162] P. Giselsson, "Improving fast dual ascent for MPC-Part I: The distributed case," arXiv preprint arXiv:1312.3012, 2013.
- [163] P. Giselsson, "Improving fast dual ascent for mpc-part ii: The embedded case," arXiv preprint arXiv:1312.3013, 2013.
- [164] M. Vasak, N. Hure, and N. Peric, "Identification of a discrete-time piecewise affine model of a pitch-controlled wind turbine," *MIPRO*, 2011 Proceedings of the 34th International Convention, 744–749, May 2011.
- [165] Y. T. Shi, Q. Kou, D. H. Sun, Z. X. Li, S. J. Qiao, and Y. J. Hou, "H fault tolerant control of WECS based on the PWA model," *Energies*, 7(3):1750–1769, 2014.
- [166] G. Ferrari-Trecate, M. Muselli, D. Liberati, and M. Morari, "A clustering technique for the identification of piecewise affine systems," *Automatica*, 39(2):205–217, 2003.
- [167] J. Jonkman, S. Butterfield, W. Musial, and G. Scott, "Definition of a 5 MW reference wind turbine for offshore system development," *Tech. Rep.*, National Renewable Energy Laboratory, 2009.
- [168] H. Zhao, Q. Wu, C. Rasmussen, and M. Blanke, "L1 adaptive speed control of a small wind energy conversion system for maximum power point tracking," *IEEE Transactions on Energy Conversion*, 29(3):576–584, 2014.
- [169] J. M. Maciejowski, *Predictive control: with constraints*. Pearson education, 2002.
- [170] G. Ferrari-Trecate, "Hybrid Identification Toolbox (HIT)," 2005.
- [171] M. Herceg, M. Kvasnica, C. Jones, and M. Morari, "Multi-Parametric Toolbox 3.0," *Proc. of the European Control Conference*, (Zürich, Switzerland), 502–510, Jul. 17–19 2013. <http://control.ee.ethz.ch/~mpt>.

- [172] J. D. Grunnet, M. Soltani, T. Knudsen, M. Kragelund, and T. Bak, "Aeolus toolbox for dynamic wind farm model, simulation and control," Proc. of the 2010 European Wind Energy Conference, 2010.
- [173] J. P. Barton and D. G. Infield, "A probabilistic method for calculating the usefulness of a store with finite energy capacity for smoothing electricity generation from wind and solar power," *Journal of Power Sources*, 162:943–948, Nov. 2006.
- [174] H. Bludszuweit, "Statistical analysis of wind power forecast error," *IEEE Transactions on Power Systems*, 23(3):983–991, 2008.
- [175] H. Bludszuweit and J. A. Domínguez-navarro, "A probabilistic method for energy storage sizing based on wind power forecast uncertainty," *IEEE Transactions on Power Systems*, 26(3):1651–1658, 2011.
- [176] T. Boutsika and S. Santoso, "Sizing an energy storage system to minimize wind power imbalances from the hourly average," *IEEE Power and Energy Society General*, 1–8, 2012.
- [177] X. Wang, D. M. Vilathgamuwa, and S. S. Choi, "Determination of battery storage capacity in energy buffer for wind farm," *IEEE Transactions on Energy Conversion*, 23(3):868–878, 2008.
- [178] T. Brekken and A. Yokochi, "Optimal energy storage sizing and control for wind power applications," *IEEE Transactions on Sustainable Energy*, 2(1):69–77, 2011.
- [179] S. Bose, D. F. Gayme, U. Topcu, and K. M. Chandy, "Optimal placement of energy storage in the grid," *IEEE 51st Annual Conference on Decision and Control (CDC)*, 5605–5612, 2012.
- [180] M. Ghofrani, A. Arabali, M. Etezadi-Amoli, and M. Fadali, "A Framework for Optimal Placement of Energy Storage Units Within a Power System With High Wind Penetration," *IEEE Transactions on Sustainable Energy*, 4(2):434–442, 2012.
- [181] Q. Li, S. Choi, Y. Yuan, and D. Yao, "On the determination of battery energy storage capacity and short-term power dispatch of a wind farm," *IEEE Transactions on Sustainable Energy*, 2(2):148–158, 2011.
- [182] D. Yao, S. S. Choi, K. J. Tseng, and T. Lie, "Determination of short-term power dispatch schedule for a wind farm incorporated with dual-battery energy storage scheme," *IEEE Transactions on Sustainable Energy*, 3(1):74–84, 2012.
- [183] H. V. Haghi, M. T. Bina, and M. A. Golkar, *Nonlinear modeling of temporal wind power variations*, 2013.

- [184] Y. Li, K. Xie, and B. Hu, “Copula-ARMA model for multivariate wind speed and its applications in reliability assessment of generating systems,” *Journal of Electrical Engineering & Technology*, 8(3):421–427, 2013.
- [185] R. Billinton, H. Chen, and R. Ghajar, “Time-series models for reliability evaluation of power systems including wind energy,” *Microelectronics Reliability*, 36(9):1253–1261, 1996.
- [186] L. B. Shi, Z. X. Weng, L. Z. Yao, and Y. X. Ni, “An analytical solution for wind farm power output”.
- [187] T. Ackermann et al., *Wind power in power systems*, Wiley Online Library, 2005.
- [188] J. Löfberg, “Yalmip : A toolbox for modeling and optimization in MATLAB,” *Proceedings of the CACSD Conference*, Taipei, Taiwan, 2004.
- [189] J. Sturm, “Implementation of interior point methods for mixed semidefinite and second order cone optimization problems,” *Optimization Methods and Software*, 17(6):1105 – 1154, 2002.
- [190] D. Kottick, M. Blau, and D. Edelstein, “Battery energy storage for frequency regulation in an island power system,” *IEEE Transactions on Energy Conversion*, 8:455 –459, Sep. 1993.
- [191] M. Ceraolo, “New dynamical models of lead-acid batteries,” *IEEE Transactions on Power Systems*, 15:1184 –1190, Nov. 2000.
- [192] DIgSILENT GmbH, “PowerFactory Application Manual: Battery Energy Storing Systems in PowerFactory,” *Tech. Rep.*, 2010.
- [193] Y. Chen, P. Pillay, and A. Khan, “Pm wind generator topologies,” *IEEE Transactions on Industry Applications*, 41(6):1619–1626, 2005.
- [194] K. Tan and S. Islam, “Optimum control strategies in energy conversion of PMSG wind turbine system without mechanical sensors,” *IEEE Transactions on Energy Conversion*, 19(2):392–399, 2004.
- [195] F. Valenciaga and P. Puleston, “High-order sliding control for a wind energy conversion system based on a permanent magnet synchronous generator,” *IEEE Transactions on Energy Conversion*, 23(3):860–867, 2008.
- [196] A. Grauers, “Efficiency of three wind energy generator systems,” *IEEE Transactions on Energy Conversion*, 11(3):650–657, 1996.
- [197] A. D. Hansen and G. Michalke, “Multi-pole permanent magnet synchronous generator wind turbines’ grid support capability in uninterrupted operation during grid faults,” *IET Renewable Power Generation*, 3(3):333–348, 2009.

- [198] F. Bianchi, H. De Battista, and R. Mantz, "Wind turbine control systems: Principles, modelling and gain-scheduling design (advances in industrial control)," Lavoisier Ed, 2006.
- [199] M. Ruh, G. Andersson, and A. Borer, "Micro-grid operation of inverter based distributed generation with voltage and frequency dependent loads," IEEE Power & Energy Society General Meeting, 2009.
- [200] M. Rasheduzzaman, S. N. Bhaskara, and B. H. Chowdhury, "Implementation of a microgrid central controller in a laboratory microgrid network," North American Power Symposium (NAPS), 2012, 1–6, 2012.
- [201] J. Peas Lopes, C. Moreira, and A. Madureira, "Defining control strategies for microgrids islanded operation," IEEE Transactions on Power Systems, 21(2):916–924, 2006.
- [202] M. Hussein, T. Senjyu, M. Orabi, M. Wahab, and M. Hamada, "Control of a variable speed stand alone wind energy supply system," IEEE International Conference on Power and Energy (PECon), 71–76, 2012.
- [203] C. Colson and M. Nehrir, "Load-following for wind turbines with permanent magnet synchronous generators," North American Power Symposium (NAPS), 1–8, 2010.
- [204] A. D. Hansen and G. Michalke, "Modelling and control of variable-speed multi-pole permanent magnet synchronous generator wind turbine," Wind Energy, 11(5):537–554, 2008.
- [205] H. Geng, D. Xu, B. Wu, and G. Yang, "Active damping for torsional vibrations in pmsg based wecs," Applied Power Electronics Conference and Exposition (APEC), 2010 Twenty-Fifth Annual IEEE, 2126–2131, 2010.
- [206] H. Geng, G. Yang, D. Xu, and B. Wu, "Unified power control for pmsg-based wecs operating under different grid conditions," IEEE Transactions on Energy Conversion, 26(3):822–830, 2011.
- [207] M. Shahabi, M.-R. Haghifam, M. Mohamadian, and S. Nabavi-Niaki, "Microgrid dynamic performance improvement using a doubly fed induction wind generator," IEEE Transactions on Energy Conversion, 24(1):137–145, 2009.
- [208] P. C. Loh and D. Holmes, "Analysis of multiloop control strategies for LC/CL/LCL-filtered voltage-source and current-source inverters," IEEE Transactions on Industry Applications, 41(2):644–654, 2005.
- [209] W. Qiao, "Dynamic modeling and control of doubly fed induction generators driven by wind turbines," Power Systems Conference and Exposition, 2009. PSCE '09. IEEE/PES, 1–8, 2009.

- [210] F. Gonzalez-Longatt, P. Wall, and V. Terzija, "A simplified model for dynamic behavior of permanent magnet synchronous generator for direct drive wind turbines," *IEEE PowerTech*, 1–7, 2011.